NASA-CR-192354

NASA-UVA LIGHT AEROSPACE ALLOY AND STRUCTURES TECHNOLOGY PROGRAM

LA^{2}ST

Program Director:

Richard P. Gangloff

Co-principal Investigators:

Richard P. Gangloff
John K. Haviland
Carl T. Herakovich
Walter D. Pilkey
Marek-Jerzy Pindera
John R. Scully
Glenn E. Stoner
Earl A. Thornton
Franklin E. Wawner, Jr.
John A. Wert

NASA-LaRC Grant Monitor:

Dennis L. Dicus

University of Virginia
Thornton Hall
Charlottesville, VA 22903

UNIVERSITY OF VIRGINIA
School of Engineering and Applied Science

The University of Virginia's School of Engineering and Applied Science has an undergraduate enrollment of approximately 1,500 students with a graduate enrollment of approximately 600. There are 160 faculty members, a majority of whom conduct research in addition to teaching.

Research is a vital part of the educational program and interests parallel academic specialties. These range from the classical engineering disciplines of Chemical, Civil, Electrical, and Mechanical and Aerospace to newer, more specialized fields of Applied Mechanics, Biomedical Engineering, Systems Engineering, Materials Science, Nuclear Engineering and Engineering Physics, Applied Mathematics and Computer Science. Within these disciplines there are well equipped laboratories for conducting highly specialized research. All departments offer the doctorate; Biomedical and Materials Science grant only graduate degrees. In addition, courses in the humanities are offered within the School.

The University of Virginia (which includes approximately 2,000 faculty and a total of full-time student enrollment of about 17,000), also offers professional degrees under the schools of Architecture, Law, Medicine, Nursing, Commerce, Business Administration, and Education. In addition, the College of Arts and Sciences houses departments of Mathematics, Physics, Chemistry and others relevant to the engineering research program. The School of Engineering and Applied Science is an integral part of this University community which provides opportunities for interdisciplinary work in pursuit of the basic goals of education, research, and public service.

A Progress Report

July 1, 1992 to December 31, 1992

NASA-UVA LIGHT AEROSPACE ALLOY AND STRUCTURES TECHNOLOGY PROGRAM (LA^2ST)

NASA-LaRC Grant NAG-1-745

Submitted to:

National Aeronautics and Space Administration
Langley Research Center
Hampton, Virginia 23665

Attention:

Mr. Richard J. Siebels
Grants Officer
MS 126

For Review by:

Mr. Dennis L. Dicus
Grant Monitor
Metallic Materials Branch, MS 188A

Submitted by:

Richard P. Gangloff
Professor
Department of Materials Science and Engineering
School of Engineering and Applied Science
University of Virginia

Report No. UVA/528266/MSE93/112
March 1993

Copy No. __

TABLE OF CONTENTS

TABLE OF CONTENTS (continued)

NASA-UVA LIGHT AEROSPACE ALLOY AND STRUCTURES TECHNOLOGY PROGRAM

EXECUTIVE SUMMARY

The NASA-UVa Light Aerospace Alloy and Structures Technology (LA^2ST) Program continues a high level of activity, with projects being conducted by graduate students and faculty advisors in the Departments of Materials Science and Engineering, Civil Engineering and Applied Mechanics, and Mechanical and Aerospace Engineering at the University of Virginia. This work is funded by the NASA-Langley Research Center under Grant NAG-1-745. Here, we report on progress achieved between July 1 and December 31, 1992.

The objective of the LA^2ST Program is to conduct interdisciplinary graduate student research on the performance of next generation, light weight aerospace alloys, composites and thermal gradient structures in collaboration with NASA-Langley researchers. Specific technical objectives are presented for each research project. We generally aim to produce relevant data and basic understanding of material mechanical response, corrosion behavior, and microstructure; new monolithic and composite alloys; advanced processing methods; new solid and fluid mechanics analyses; measurement advances; and critically, a pool of educated graduate students for aerospace technologies.

The accomplishments presented in this report are as follows.

- oo Four research areas are actively investigated, including: (1) Mechanical and Environmental Degradation Mechanisms in Advanced Light Metals and Composites, (2) Aerospace Materials Science, (3) Mechanics of Materials and Composites for Light Aerospace Structures, and (4) Thermal Gradient Structures.

- oo Fifteen research projects are being conducted by 10 PhD and 6 MS level graduate students, 10 faculty members, and 1 research associate from three departments in the Engineering School at UVa. Each project is planned and executed in conjunction with a specific branch and technical monitor at NASA-LaRC.

- oo Seven undergraduates successfully conducted research at NASA-LaRC during the summer of 1992. This work was wholly supervised by NASA staff. Recruiting of undergraduates for the 1993 Summer program was initiated during this reporting period. Two undergraduates are participating in LA^2ST research at UVa.

- Reporting accomplishments between July and December of 1992 include 10 journal or proceedings publications, 1 NASA progress report, 1 NASA Contractor Report, and 7 presentations at technical meetings. The LA^2ST totals since 1986 are 63 publications (34 archival journal or book publications), 8 PhD dissertations or MS theses, 68 external technical presentations, 13 NASA progress reports and 1 NASA Contractor Report. Since 1986, 25 graduate students, including 24 citizens of the United States, have been involved with LA^2ST research and 8 have received MS or PhD degrees. The average grade point average for NASA LA^2ST graduate students is above 3.4 on a scale of A equals 4.0. Four post-doctoral research associates have been involved with LA^2ST research.

- ***Research on environmental fatigue of Al-Li-Cu alloys*** has fully developed an SEM technique to define fracture surface facet crystallography based on the coupling of electron back scatter pattern (EBSP) analysis and quantitative tilt fractography. AA2090 inert environment fatigue facets are essentially parallel to {111} planes, independent of microstructure and texture, and consistent with localized slip band decohesion. Aqueous NaCl fatigue facets are not crystallographic for AA2090, being 15 to 30° from {100} "cleavage" planes. Work is in progress to explain these damage mechanisms based on intersecting slip, hydrogen trapping and normal stress.

  (Project 1)

- ***Research on mechanisms of localized corrosion and environmental fracture in Al-Cu-Li-Mg-Ag alloy X2095 and compositional variations*** is examining the electrochemical behavior of subgrain boundary phases under conditions intended to simulate mechanical and electrochemical stresses encountered at the tip of a stress corrosion crack. Data suggest that a copper depleted region may be responsible for an anodic dissolution based mechanism for SCC in the Al-Li-Cu alloys under study.

  (Project 5)

- ***Research on the effect of zinc additions on the precipitation and stress corrosion cracking behavior of alloy 8090*** demonstrates that electrochemically precharged hydrogen degrades the initiation toughness of alloy 2090, as determined by direct current electrical potential monitoring of compact tension specimens. A particularly strong hydrogen degradation was observed for recrystallized fine grain size sheet of 2090, with fracture being intergranular.

  (Project 6)

- ***Research on hydrogen interactions with Al-Li-Cu alloy 2090 and complimentary model alloys*** unambiguously shows that dissolved hydrogen induces damage, and degrades the tensile ductility of AA2090. The experimental procedures developed to date will make it possible to develop a fundamental understanding of the damage mechanisms

present for hydrogen affected cracking for these alloys.

(Project 7)

oo ***Research on metastable pitting of Al Alloys*** has analyzed pit current transients to determine that metastable pits can grow to a maximum size of about 2 μm before repassivating. Stable pits are sized at approximately 18 μm for the same growth times. The mechanism for the survival of metastable pits, leading to the formation of stable pits, is unclear. This work is enabled by a NASA Graduate Student Researchers Program Fellowship (Under-Represented Minority Focus).

(Project 8)

oo ***Research on the cryogenic fracture of Al-Cu-Li-In alloys*** shows that J-integral measures of plane strain crack initiation toughness (K_{IC}) are independent of thickness at -185°C and when a single transgranular shear/delamination fracture mode operates on both the macroscopic and microscopic scales. In contrast at 25°C, higher toughness is observed for the thinner specimen because of a fracture mode transition from delamination/macroscopic shear to flat fracture with decreasing specimen thickness. Polarized light microscopy and SEM back-scatter electron imaging were successfully employed to estimate grain orientation differences near a fracture surface.

(Project 3)

oo ***Research on the fracture toughness of Weldalite™*** determined that compositions at the extremes of the X2095 specification exhibit different microstructures; the low Cu-Li case is generally unrecrystallized, while high Cu-Li X2095 is recrystallized for plate. K_{IC} for the high copper case is low compared to low copper X2095 at both ambient and cryogenic temperatures, and for any aging condition. K_{IC} is constant with decreasing temperature for the high copper case, and for the low copper alloy at aging times up to 20 hours at 143°C. K_{IC} for low Cu X2095 (aged at 30 to 72 hours) may decrease with decreasing temperature, as predicted by micromechanical modeling.

(Project 4)

oo ***Research on elevated temperature cracking of advanced I/M aluminum alloys*** conducted initial R-curve fracture toughness experiments on Mg + Ag modified 2519 (from Alcoa) and on conventional 2618. The compact tension characterization method was successfully tested and potential problem areas were identified. The plane strain initiation and plane stress growth toughnesses of the modified 2519 are excellent at ambient temperature, and are consistent with the results of wide middle cracked tension plate specimens. Alloy 2650 has been obtained from Pechiney.

(Project 2)

- oo ***Research on Ti alloy matrix-SiC fiber reinforced composites*** has thoroughly investigated the factors that were found to contribute to the property degradation of Ti-100/SCS-6 following thermal exposure. These include matrix-ply debonding from poor fabrication quality, matrix embrittlement at high temperatures in moist air, and transport of embrittling species from air along the fiber-matrix interface.

  (Project 9)

- oo ***Research on superplastic forming of Weldalite™*** emphasized microstructure and microtexture analyses of two Weldalite alloys, 049 and X2095, after annealing alone and after superplastic elongation. Annealing does not significantly alter the boundary misorientation distribution, while concurrent straining and annealing strongly decreases the fraction of low-angle boundaries. To understand the mechanisms for this behavior, three simulative models of microstructure/microtexture evolution during concurrent straining and annealing were formulated. Application of the models to experimentally determined initial microstructure/microtexture states shows that a combination of the boundary sliding subgrain rotation model and the subgrain neighbor switching model most closely reproduces the boundary misorientation distributions found experimentally. (Project 10)

- oo ***Research to incorporate environmental effects into fracture mechanics fatigue life prediction codes such as NASA FLAGRO*** substantially expanded a literature review that identified crack growth rate data and predictive models for light aerospace alloys and environments. Fatigue and monotonically rising load crack growth experiments have been designed to characterize the fracture behavior of Ti-6Al-4V (ELI) and of 7075 (T651 and T7X1 aging treatments) plates in aqueous chloride compared to vacuum. Three undergraduates are developing Fortran programs to aid in the NASA FLAGRO implementation of a linear superposition model for predicting environmental da/dN versus ΔK behavior. (Project 11)

- oo ***Research on the deformation of SCS-6/Ti-15-3 metal matrix composite tubulars under biaxial loading*** has developed a theoretical model capable of predicting the inelastic response of an MMC, due to plasticity and damage, and for arbitrary loading. [0] tubes have been subjected to biaxial loading including internal pressure. The time dependent inelastic response has been separated from the time independent inelastic response of a $[\pm 45]_s$ tube subjected to axial/torsional loading.

  (Project 12)

- oo ***Research on finite element analysis of the effect of temperature on cylindrical shell structures*** determined, for a single bay model, the variations of thermal stresses and of buckling temperatures for several skin thicknesses, ring spacings, and stringer

spacings. These calculations reveal that achievable temperature gradients can cause thermal buckling. The considerable inaccuracy of the traditional strength of materials solution for a thermally loaded beam can be overcome by a simple and efficient solution of thermoelasticity. (Project 13)

oo ***Research on the thermoviscoplastic behavior*** of high temperature alloy panels demonstrated material and geometric nonlinearities. Tests of Hastelloy-X panels heated by quartz lamps provided temperature, displacement, and strain data for validation of finite element analysis. Material tests provided parameters for a Bodner-Partom constitutive model. Material tests for constitutive modeling of 8009 aluminum alloy are in progress. Future research includes tests of stiffened Hastelloy-X and 8009 alloy panels. (Project 14)

viii

INTRODUCTION

Background

In 1986 the Metallic Materials Branch in the Materials Division of the NASA-Langley Research Center initiated sponsorship of graduate student engineering and scientific research in the Department of Materials Science and Engineering at the University of Virginia[1]. This work emphasized the mechanical and corrosion behavior of light aerospace alloys, particularly Al-Li-Cu based compositions, in aggressive aerospace environments[2-4].

In the Fall of 1988, the scope of this program was increased to incorporate research at UVa on the development and processing of advanced aerospace materials[5]. Additional funding was provided by the Metallic Materials and Mechanics of Materials Branches at NASA-LaRC. In early 1989 the program was further enhanced to include interdisciplinary work on solid mechanics and thermal structures, with funding from several Divisions within the Structures Directorate at NASA-LaRC[6]. The Departments of Civil Engineering and of Mechanical and Aerospace Engineering at UVa participated in this expanded program. With this growth, the NASA-UVa Light Aerospace Alloy and Structures Technology Program (or LA^{2}ST Program) was formed within the School of Engineering and Applied Science at UVa.

Since 1989, the LA^{2}ST program has operated with full participation from about 10 faculty and 15 graduate students, as outlined in the last seven progress reports[7-13] and four grant renewal proposals[14-17]. Three 2-day Grant Review Meetings were held in June of 1990, 1991 and 1992 at the Langley Research Center, with over 25 faculty and graduate students from UVa participating. Each student presented the results of his or her research. Additionally, undergraduates have been involved in research projects at both NASA-LaRC and at UVa.

In October of 1991, Dean E.A. Starke proposed a substantial enhancement to the base LA^{2}ST Program[18,19]. The objective of this supplement is to involve UVa faculty with engineering scientists from aluminum alloy producers and airframe manufacturers in a broad research program to develop aluminum alloys and composites for elevated temperature high speed civil transport applications. This research began in January of 1992 and the results are separately reported.

Problem and Needs

Future aerospace structures require high performance light alloys and metal matrix composites with associated processing and fabrication techniques; new structural design

methods and concepts with experimental evaluations; component reliability/durability/damage tolerance prediction procedures; and a pool of masters and doctoral level engineers and scientists. Work on advanced materials and structures must be interdisciplinary and integrated. The thermal and chemical effects of aerospace environments on light metals and composites are particularly important to material performance. Nationally, academic efforts in these areas are limited. The NASA-UVa LA^{2}ST Program addresses these needs.

LA^{2}ST Program

As detailed in the original proposal[6] and affirmed in the most recent renewal[17], faculty from the Departments of Materials Science and Engineering, Mechanical and Aerospace Engineering, and Civil Engineering and Applied Mechanics at UVa are participating in the LA^{2}ST research and education program focused on high performance, light weight, aerospace alloys and structures. We aim to develop long term and interdisciplinary collaborations between graduate students, UVa faculty, and NASA-Langley researchers.

Our research efforts are producing basic understanding of materials performance, new monolithic and composite alloys, advanced processing methods, solid and fluid mechanics analyses, and measurement advances. A major product of the LA^{2}ST program is graduate students with interdisciplinary education and research experience in materials science, mechanics and mathematics. These advances should enable various NASA technologies.

The scope of the LA^{2}ST Program is broad. Four research areas are being investigated, including:

- oo Mechanical and Environmental Degradation Mechanisms in Advanced Light Metals and Composites,
- oo Aerospace Materials Science,
- oo Mechanics of Materials and Composites for Light Aerospace Structures,
- oo Thermal Gradient Structures.

Fifteen specific research projects are ongoing within these four areas and are reported here. These projects currently involve 10 faculty, 1 research associate and 17 graduate students. The majority of the graduate students are at the doctoral level (11 of 17), all are

citizens of the United States, and 2 are supported by the NASA Minority Grant Program. In each case the research provides the basis for the thesis or dissertation requirement of graduate studies at the University of Virginia. Each project is developed in conjunction with a specific LaRC researcher. Research is conducted at either UVa or LaRC, and under the guidance of UVa faculty and NASA staff. Participating students and faculty are closely identified with a NASA-LaRC branch.

A primary goal of the LA^{2}ST Program is to foster interdisciplinary research. To this end, many of the research projects share a common focus on the same next generation light alloys and composites, and on light and reusable aerospace structures which will be subjected to aggressive terrestrial and space environments. Emphasis is placed on both cryogenic and elevated temperature conditions, with severe thermal gradients typical of tankage structures.

Organization of Progress Report

This progress report first provides LA^{2}ST Program administrative information including statistics on the productivity of faculty and graduate student participants, a history of current and graduated students, refereed or archival publications, and a list of ongoing projects with NASA and UVa advisors.

Fifteen sections summarize the technical accomplishments of each research project, emphasizing the period from July 1st to December 31, 1992. Each program section contains a brief narrative of objective, recent progress, conclusions and immediate milestones.

Appendices document grant-sponsored publications, conference participation and citations of all LA^{2}ST Progress Reports.

References

1. R.P. Gangloff, G.E. Stoner and M.R. Louthan, Jr., "Environment Assisted Degradation Mechanisms in Al-Li Alloys", University of Virginia, Proposal No. MS-NASA/LaRC-3545-87, October, 1986.

2. R.P. Gangloff, G.E. Stoner and R.E. Swanson, "Environment Assisted Degradation Mechanisms in Al-Li Alloys", University of Virginia, Report No. UVA/528266/MS88/101, January, 1988.

3. R.P. Gangloff, G.E. Stoner and R.E. Swanson, "Environment Assisted Degradation Mechanisms in Advanced Light Metals", University of Virginia, Report No. UVA/528266/MS88/102, June, 1988.

4. R.P. Gangloff, G.E. Stoner and R.E. Swanson, "Environment Assisted Degradation Mechanisms in Advanced Light Metals", University of Virginia, Report No. UVA/528266/MS89/103, January, 1989.

5. T.H. Courtney, R.P. Gangloff, G.E. Stoner and H.G.F. Wilsdorf, "The NASA-UVa Light Alloy Technology Program", University of Virginia, Proposal No. MS NASA/LaRC-3937-88, March, 1988.

6. R.P. Gangloff, "NASA-UVa Light Aerospace Alloy and Structures Technology Program", University of Virginia, Proposal No. MS NASA/LaRC-4278-89, January, 1989.

7. R.P. Gangloff, "NASA-UVa Light Aerospace Alloy and Structures Technology Program", University of Virginia, Report No. UVA/528266/MS90/104, August, 1989.

8. R.P. Gangloff, "NASA-UVa Light Aerospace Alloy and Structures Technology Program", University of Virginia, Report No. UVA/528266/MS90/105, December, 1989.

9. R.P. Gangloff, "NASA-UVa Light Aerospace Alloy and Structures Technology Program", UVa Report No. UVA/528266/MS90/106, June, 1990.

10. R.P. Gangloff, "NASA-UVa Light Aerospace Alloy and Structures Technology Program", UVa Report No. UVA/528266/MS91/107, January, 1991.

11. R.P. Gangloff, "NASA-UVa Light Aerospace Alloy and Structures Technology Program", UVa Report No. UVA/528266/MS91/108, July, 1991.

12. R.P. Gangloff, "NASA-UVa Light Aerospace Alloy and Structures Technology Program", UVa Report No. UVA/528266/MS92/109, January, 1992.

13. R.P. Gangloff, "NASA-UVa Light Aerospace Alloy and Structures Technology Program", UVa Report No. UVA/528266/MS93/111, July, 1992.

14. R.P. Gangloff, "NASA-UVa Light Aerospace Alloy and Structures Technology Program", University of Virginia, Proposal No. MS-NASA/LaRC-4512-90, November, 1989.

15. R.P. Gangloff, "NASA-UVa Light Aerospace Alloy and Structures Technology Program", University of Virginia, Proposal No. MS-NASA/LaRC-4841-91, September, 1990.

16. R.P. Gangloff, "NASA-UVa Light Aerospace Alloy and Structures Technology Program", University of Virginia, Proposal No. MS-NASA/LaRC-5219-92, October, 1991.

17. R.P. Gangloff, "NASA-UVa Light Aerospace Alloy and Structures Technology Program", University of Virginia, Proposal No. MSE-NASA/LaRC-5691-93, November, 1992.

18. R.P. Gangloff, E.A. Starke, Jr., J.M. Howe and F.E. Wawner, "NASA-UVa Light Aerospace Alloy and Structures Technology Program: Supplement on Aluminum Based Materials for High Speed Aircraft", University of Virginia, Proposal No. MS NASA/LaRC-5215-92, October, 1991.

19. R.P. Gangloff, E.A. Starke, Jr., J.M. Howe and F.E. Wawner, "NASA-UVa Light Aerospace Alloy and Structures Technology Program: Supplement on Aluminum Based Materials for High Speed Aircraft", University of Virginia, Proposal No. MSE NASA/LaRC-5691-93, November, 1992.

SUMMARY STATISTICS

Table I documents the numbers of students and faculty who participated in the LA^{2}ST Program, both during this reporting period and since the program inception in 1986. Academic and research accomplishments are indicated by the degrees awarded, publications and presentations. Specific graduate students and research associates who participated in the LA^{2}ST Program are named in Tables II and III, respectively.

TABLE I: LA^{2}ST Program Statistics

	Current 7/1/92 to 12/31/92	Cumulative 1986 to 12/31/92
PhD Students--UVa:	9	15
--NASA-LaRC:	1	1
MS Students--UVa:	5	5
--NASA:	1	1
--VPI:	0	1
Undergraduates--UVa:	2	6
--NASA-LaRC:	7	11
Faculty--UVa:	10	11
--VPI:	0	1
Research Associates--UVa:	1	4
PhD Awarded:	0	5
MS Awarded:	0	3

TABLE I: LA^{2}ST Program Statistics (continued)

	Current 7/1/92 to 12/31/92	Cumulative 1986 to 12/31/92
Employers--NASA:	0	1
--Federal:	0	2
--University:	0	0
--Industry:	0	2
--Next degree:	0	2
Publications:	10	63
Presentations:	7	68
Dissertations/Theses:	0	8
NASA Reports:	2	14

TABLE II

GRADUATE STUDENT PARTICIPATION IN THE NASA-UVa LA^{2}ST PROGRAM

January, 1993

POS #	GRADUATE STUDENT EMPLOYER	ENTERED PROGRAM	DEGREE COMPLETED	LANGLEY RESIDENCY	RESEARCH TOPIC	UVa/NASA-LaRC ADVISORS
1.	R. S. Piascik NASA-Langley	6/86	Ph.D. 10/89		Damage Localization Mechanisms in Corrosion Fatigue of Aluminum-Lithium Alloys	R. P. Gangloff D. L. Dicus
2.	J. P. Moran NIST	9/88	Ph.D. 12/89		An Investigation of the Localized Corrosion and Stress Corrosion Cracking Behavior of Alloy 2090	G. E. Stoner W. B. Lisagor
3.	R. G. Buchheit Sandia National Laboratories	6/87	Ph.D. 12/90		Measurements and Mechanisms of Localized Aqueous Corrosion in Aluminum-Lithium Alloys	G. E. Stoner D. L. Dicus
4.	D. B. Gundel Ph.D.-UVa	9/88	M.S. 12/90		Investigation of the Reaction Kinetics Between SiC Fibers and Titanium Matrix Composites	F. E. Wawner W. B. Brewer
5.	F. Rivet (VPI)	9/88	M.S. 12/90		Deformation and Fracture of Aluminum-Lithium Alloys: The Effect of Dissolved Hydrogen	R. E. Swanson (VPI) D. L. Dicus
6.	C. Copper Ph.D.-UVa	4/89	M.S. 12/90		Design of Cryogenic Tanks for Space Vehicles	W. D. Pilkey J. K. Haviland D. R. Rummler M.J. Shuart
7.	J. A. Wagner NASA-Langley	6/87	Ph.D.	PhD Research @ LaRC	Temperature Effects on the Deformation and Fracture of Al-Li-Cu-In Alloys	R. P. Gangloff W. B. Lisagor J. C. Newman
8.	W. C. Porr, Jr. David Taylor Naval R&DC	1/88	Ph.D. 6/92		Elevated Temperature Facture of an Advanced Powder Metallurgy Aluminum Alloy	R. P. Gangloff C. E. Harris

TABLE II (continued)
GRADUATE STUDENT PARTICIPATION IN THE NASA-UVa LA^{2}ST PROGRAM
(continued)

POS #	GRADUATE STUDENT EMPLOYER	ENTERED PROGRAM	DEGREE COMPLETED	LANGLEY RESIDENCY	RESEARCH TOPIC	UVa/NASA-LaRC ADVISORS
9.	J. B. Parse Private Consultant	9/88	Ph.D. 6/92		Quantitative Characterization of the Spatial Distribution of Particles in Materials	J. A. Wert D. R. Tenney
10.	D. C. Slavik	9/89	Ph.D.		Environment Enhanced Fatigue of Advanced Aluminum Alloys and Composites	R. P. Gangloff D. L. Dicus
11.	C. L. Lach NASA-Langley	9/89	M.S.	MS Research @LaRC	Effect of Temperature on the Fracture Toughness of Weldalite^{TM} 049	R.P. Gangloff W. B. Lisagor
12.	R. J. Kilmer	11/89	Ph.D.		Effect of Zn Additions on the Environmental Stability of Alloy 8090	G. E. Stoner W. B. Lisagor
13.	M. F. Coyle	12/89	Ph.D.		Visoplastic Response of High Temperature Structures	E. A. Thornton J.H. Starnes, Jr.
14.	C.J. Lissenden	9/90	Ph.D.		Inelastic Response of Metal Matrix Composites Under Biaxial Loading	C.T. Herakovich M.J. Pindera W.S. Johnson
15.	C. Cooper	1/91	Ph.D.		Shell Structures Analytical Modeling	W. D. Pilkey J. K. Haviland M. Shuart J. Stroud

TABLE II (continued)

GRADUATE STUDENT PARTICIPATION IN THE NASA-UVa LA^{2}ST PROGRAM

(continued)

16.	Douglas Wall	4/91	Ph.D.		Measurements and Mechanisms of Localized Corrosion in Al-Li-Cu Alloys	G. E. Stoner D. L. Dicus
17.	S. W. Smith	4/91	Ph.D.		Hydrogen Interactions with Al-Li Alloys	J. R. Scully W. B. Lisagor
18.	D. B. Gundel	4/91	Ph.D.		Effect of Thermal Exposure on the Mechanical Properties of Titanium/SiC Composites	F. E. Wawner W. B. Brewer
19.	K. McCarthy	5/91	M.S.		Shell Structures Analytical Modeling	W. D. Pilkey M. J. Shuart J. Stroud
20.	M. Lyttle	12/91	M.S.		Superplasticity in Al-Li-Cu Alloys	J. A. Wert T. T. Bales
21.	T. Johnson	12/91	Ph.D.	(NASA Minority Grantee)	Shell Structures Analytical Modeling	W. D. Pilkey M. J. Shuart J. Stroud
22.	S. T. Pride	12/91	Ph.D.	(NASA Minority Grantee)	Metastable Pitting of Al Alloys	J. R. Scully D. L. Dicus
23.	M. A. Rowley	1/92	M.S.	(UVa AEP Sponsored)	Viscoplasticity of Metals	E. A. Thornton J. H. Starnes, Jr.
24.	M. J. Haynes	9/92	M.S.		Elevated Temperature Fracture of Advanced IM Al Alloys	R. P. Gangloff TBD
25.	M. Mason	9/92	M.S.		Environmental Effects in Fatigue Life Prediction	R. P. Gangloff R. S. Piascik

TABLE III

Post-Doctoral Research Associate Participation

in NASA-UVA LA^2ST Program

Pos #	Res. Assoc.	Tenure	Research	Supervisor
1.	Yang Leng	3/89 to 12/91	Elevated Temperature Deformation and Fracture of PM AL Alloys and Composites	R. P. Gangloff
2.	Farshad Mizadeh	7/89 to 12/91	Deformation of Metal Matrix Composites	C. T. Herakovich and Marek-Jerzy Pindera
3.	A.K.Mukhopadhyay	6/91 to 6/92	Aluminum Alloy Development	E. A. Starke, Jr.
4.	Sang-Shik Kim	12/91 to 12/93	Environmental Fatigue Life Prediction	R. P. Gangloff

GRANT PUBLICATIONS: (REFEREED JOURNALS, ARCHIVAL PROCEEDINGS AND NASA CONTRACTOR REPORTS)

The following papers are based on research conducted under LA^{2}ST Program support, and are published in the referred or archival literature.

34. D.C. Slavik, J.A. Wert and R.P. Gangloff, "Determining Fracture Facet Crystallography Using Electron Back Scatter Patterns and Quantitative Tilt Fractography", Journal of Materials Research, in review (1992).

33. W.C. Porr, Jr. and R.P. Gangloff, "Elevated Temperature Fracture of RS/PM Alloy 8009: Part I-Fracture Mechanics Behavior", Metallurgical Transactions A, in review (1992).

32. J.B. Parse and J.A. Wert, "A Geometrical Description of Particle Distributions in Materials", Modeling and Simulation in Materials Science and Engineering, in review (1992).

31. J.B. Parse and J.A. Wert, "Effects of Deformation Processing on the Oxide Particle Distribution in PM Al Alloy Sheet", Metallurgical Transactions A, in review (1992).

30. R.S. Piascik and R.P. Gangloff, "Environmental Fatigue of an Al-Li-Cu Alloy: Part III - Modeling of Crack Tip Hydrogen Damage", Metallurgical Transactions A, in review (1992).

29. R.G. Buchheit, G.E. Stoner and G.J. Shiflet, "Corrosion Properties of a Rapidly Solidified $Al_{90}Fe_5Gd_5$ Alloy", Corrosion Science, in review (1992).

28. R.P. Gangloff and S.S. Kim, "Environment Enhanced Fatigue Crack Propagation in Metals: Inputs to Fracture Mechanics Life Prediction Models", NASA Contractor Report, in press (1992).

27. D.C. Slavik, C.P. Blankenship, Jr., E.A. Starke, Jr. and R.P. Gangloff, "Intrinsic Fatigue Crack Growth Rates for Al-Li-Cu-Mg Alloys in Vacuum", Metallurgical Transactions A, in press (1992).

26. D.C. Slavik and R.P. Gangloff, "Microscopic Processes of Environmental Fatigue Crack Propagation in Al-Li-Cu Alloy 2090", in Fatigue '93, J.P. Bailon, ed., EMAS, West Midlands, UK, in press (1992).

25. R.P. Gangloff, R.S. Piascik, D.L. Dicus and J.C. Newman, "Fatigue Crack Propagation in Aerospace Aluminum Alloys", Journal of Aircraft, in press (1992).

24. R.S. Piascik and R.P. Gangloff, "Environmental Fatigue of an Al-Li-Cu Alloy: Part II - Microscopic Hydrogen Cracking Processes", Metallurgical Transactions A, in press (1992).

23. R.G. Buchheit, J.P. Moran and G.E. Stoner, "The Electrochemical Behavior of the T_1 (Al_2CuLi) Intermetallic Compound and Its Role in Localized Corrosion of Al-3Cu-2Li Alloys", Corrosion, in press (1992).

22. E.A. Thornton, M.F. Coyle, and R.N. McLeod, "Experimental Study of Plate Buckling Induced by Spatial Temperature Gradients," Journal of Thermal Stress, in press (1992).

21. E.A. Thornton and J.D. Kolenski, "Viscoplastic Response of Structures with Intense Local Heating", Journal of Aerospace Engineering, in press (1991).

20. C.J. Lissenden, M-J. Pindera and C.T. Herakovich, "Response of SiC/Ti Tubes Under Biaxial Loading in the Presence of Damage," Damage Mechanics in Composites, D.H. Allen and D.C. Lagoudas, Eds., ASME-AMD-Vol. 150, pp. 73-90 (1992).

19. J.A. Wagner and R.P. Gangloff, "Fracture Toughness of Al-Li-Cu-In Alloys", Scripta Metallurgica et Materialia, Vol. 26, pp. 1779-1784 (1992).

18. J.P. Moran, R.G. Buchheit, Jr., and G.E. Stoner, "Mechanisms of SCC of Alloy 2090 (Al-Li-Cu) - A Comparison of Interpretations from Static and Slow Strain Rate Techniques", Parkins Symposium on Fundamental Aspects of Stress Corrosion Cracking, S.M. Bruemmer, E.I. Meletis, R.H. Jones, W.W. Gerberich, F.P. Ford and R.W. Staehle, eds., TMS-AIME, Warrendale, PA, p. 159 (1992).

17. R.G. Buchheit, Jr., J.P. Moran, F.D. Wall, and G.E. Stoner, "Rapid Anodic Dissolution Based SCC of 2090 (Al-Li-Cu) by Isolated Pit Solutions," Parkins Symposium on Fundamental Aspects of Stress Corrosion Cracking, S.M. Bruemmer, E.I. Meletis, R.H. Jones, W.W. Gerberich, F.P. Ford and R.W. Staehle, eds., TMS-AIME, Warrendale, PA, p. 141 (1992).

16. R.J. Kilmer, T.J. Witters and G.E. Stoner, "Effect of Zn Additions on the Precipitation Events and Implications to Stress Corrosion Cracking Behavior in Al-Li-Cu-Mg-Zn Alloys", Proceedings of the Sixth International Al-Li Conference, M. Peters and P.J. Winkler, eds., DGM Informationsgesellschaft, Verlag, pp. 755-760 (1992).

15. C.T. Herakovich and J.S. Hidde, "Response of Metal Matrix Composites with Imperfect Bonding", Ultramicroscopy, Vol. 40, pp. 215-228 (1992).

14. R.G. Buchheit, Jr., F.D. Wall, G.E. Stoner and J.P. Moran, "Stress Corrosion Cracking of Al-Li-Cu-Zr Alloy 2090 in Aqueous Cl^- and Mixed Cl^-/CO_3^{-2} Environments", CORROSION/91, Paper No. 99, NACE, Houston, TX (1991).

13. R.P. Gangloff, D.C. Slavik, R.S. Piascik and R.H. Van Stone, "Direct Current Electrical Potential Measurement of the Growth of Small Fatigue Cracks", in Small Crack Test Methods, ASTM STP 1149, J.M. Larsen and J.E. Allison, eds., ASTM, Philadelphia, PA, pp. 116-168 (1992).

12. R.J. Kilmer and G.E. Stoner, "The Effect of Trace Additions of Zn on the Precipitation Behavior of Alloy 8090 During Artificial Aging", Proceedings, Light Weight Alloys for Aerospace Applications II, E.W. Lee, ed., TMS-AIME, Warrendale, PA, pp. 3-15, 1991.

11. W.C. Porr, Jr., Anthony Reynolds, Yang Leng and R.P. Gangloff, "Elevated Temperature Cracking of RSP Aluminum Alloy 8009: Characterization of the Environmental Effect", Scripta Metallurgica et Materialia, Vol. 25, pp. 2627-2632 (1991).

10. J. Aboudi, J.S. Hidde and C.T. Herakovich, "Thermo-mechanical Response Predictions for Metal Matrix Composites", in Mechanics of Composites at Elevated and Cryogenic Temperatures, S.N. Singhal, W.F. Jones and C.T. Herakovich, eds., ASME AMD, Vol. 118, pp. 1-18 (1991).

9. R.S. Piascik and R.P. Gangloff, "Environmental Fatigue of an Al-Li-Cu Alloy: Part I - Intrinsic Crack Propagation Kinetics in Hydrogenous Environments", Metallurgical Transactions A, Vol. 22A, pp. 2415-2428 (1991).

8. W.C. Porr, Jr., Y. Leng, and R.P. Gangloff, "Elevated Temperature Fracture Toughness of P/M Al-Fe-V-Si", in Low Density, High Temperature Powder Metallurgy Alloys, W.E. Frazier, M.J. Koczak, and P.W. Lee, eds., TMS-AIME, Warrendale, PA, pp. 129-155 (1991).

7. Yang Leng, William C. Porr, Jr. and Richard P. Gangloff, "Time Dependent Crack Growth in P/M Al-Fe-V-Si at Elevated Temperatures", Scripta Metallurgica et Materialia, Vol. 25, pp. 895-900 (1991).

6. R.J. Kilmer and G.E. Stoner, "Effect of Zn Additions on Precipitation During Aging of Alloy 8090", Scripta Metallurgica et Materialia, Vol. 25, pp. 243-248 (1991).

5. D.B. Gundel and F.E. Wawner, "Interfacial Reaction Kinetics of Coated SiC Fibers", Scripta Metallurgica et Materialia, Vol. 25, pp. 437-441 (1991).

4. R.G. Buchheit, Jr., J.P. Moran and G.E. Stoner, "Localized Corrosion Behavior of Alloy 2090-The Role of Microstructural Heterogeneity", Corrosion, Vol. 46, pp. 610-617 (1990).

3. Y. Leng, W.C. Porr, Jr. and R.P. Gangloff, "Tensile Deformation of 2618 and Al-Fe-Si-V Aluminum Alloys at Elevated Temperatures", Scripta Metallurgica et Materialia, Vol. 24, pp. 2163-2168 (1990).

2. R.P. Gangloff, "Corrosion Fatigue Crack Propagation in Metals", in Environment Induced Cracking of Metals, R.P. Gangloff and M.B. Ives, eds., NACE, Houston, TX, pp. 55-109 (1990).

1. R.S. Piascik and R.P. Gangloff, "Aqueous Environment Effects on Intrinsic Corrosion Fatigue Crack Propagation in an Al-Li-Cu Alloy", in Environment Induced Cracking of Metals, R.P. Gangloff and M.B. Ives, eds., NACE, Houston, TX, pp. 233-239 (1990).

COMPLETED PROJECTS: (1986 to present reporting period)

1. DAMAGE LOCALIZATION MECHANISMS IN CORROSION FATIGUE OF ALUMINUM-LITHIUM ALLOYS
   Faculty Investigator: R.P. Gangloff
   Graduate Student: Robert S. Piascik
   Degree: PhD
   UVa Department: Materials Science and Engineering
   NASA-LaRC Contact: D. L. Dicus (Metallic Materials)
   Start Date: June, 1986
   Completion Date: November, 1989
   Employment: NASA-Langley Research Center

2. AN INVESTIGATION OF THE LOCALIZED CORROSION AND STRESS CORROSION CRACKING BEHAVIOR OF ALLOY 2090 (Al-Li-Cu)
   Faculty Investigator: Glenn E. Stoner
   Graduate Student: James P. Moran
   Degree: PhD
   UVa Department: Materials Science and Engineering
   NASA-LaRC Contact: W.B. Lisagor (Metallic Materials)
   Start Date: September, 1988
   Completion Date: December, 1989
   Co-Sponsor: ALCOA
   Employment: ALCOA Laboratories

3. MECHANISMS OF LOCALIZED CORROSION IN AL-LI-CU ALLOY 2090
   Faculty Investigator: G.E. Stoner
   Graduate Student: R.G. Buchheit
   Degree: PhD
   UVa Department: Materials Science and Engineering
   NASA-LaRC Contact: D.L. Dicus (Metallic Materials)
   Start Date: June, 1987
   Completion Date: December, 1990
   Cosponsor: Alcoa
   Employment: Sandia National Laboratories

4. DEFORMATION AND FRACTURE OF ALUMINUM-LITHIUM ALLOYS: THE EFFECT OF DISSOLVED HYDROGEN
   Faculty Investigator: R.E. Swanson (VPI)
   Graduate Student: Frederic C. Rivet
   Degree: MS
   VPI Department: Materials Engineering
   NASA-LaRC Contact: D.L. Dicus (Metallic Materials)
   Start Date: September, 1988
   Completion Date: December, 1990
   Employment: Not determined

5. INVESTIGATION OF THE REACTION KINETICS BETWEEN SiC FIBERS AND SELECTIVELY ALLOYED TITANIUM MATRIX COMPOSITES AND DETERMINATION OF THEIR MECHANICAL PROPERTIES
   Faculty Investigator: F.E. Wawner
   Graduate Student: Douglas B. Gundel
   Degree: MS
   UVa Department: Materials Science and Engineering
   NASA-LaRC Contact: D.L. Dicus and W.B. Brewer (Metallic Materials)
   Start Date: January, 1989
   Completion Date: December, 1990
   Employment: Graduate School, University of Virginia; PhD candidate on LA^{2}ST Program; Department of Materials Science

6. DESIGN OF CRYOGENIC TANKS FOR SPACE VEHICLES
   Faculty Investigators: W.D. Pilkey and J.K. Haviland
   Graduate Student: Charles Copper
   Degree: MS
   UVa Department: Mechanical and Aerospace Engineering
   NASA-LaRC Contact: D.R. Rummler (Structural Mechanics Division), R.C. Davis and M.J. Shuart (Aircraft Structures)
   Start Date: April, 1989
   Completion Date: December, 1990
   Employment: Graduate School, University of Virginia; PhD candidate on NASA-Headquarters sponsored program; Department of Mechanical and Aerospace Engineering

7. ELEVATED TEMPERATURE FRACTURE OF AN ADVANCED RAPIDLY SOLIDIFIED, POWDER METALLURGY ALUMINUM ALLOY
   Faculty Investigator: R.P. Gangloff
   Graduate Student: William C. Porr, Jr.
   UVa Department: Materials Science and Engineering
   NASA-LaRC Contact: C.E. Harris (Mechanics of Materials)
   Start Date: January, 1988
   Completion Date: June, 1992
   Employment: David Taylor Naval Ship R&D Center

8. QUANTITATIVE CHARACTERIZATION OF THE SPATIAL DISTRIBUTION OF PARTICLES IN MATERIALS: APPLICATION TO MATERIALS PROCESSING
   Faculty Investigator: John A. Wert
   Graduate Student: Joseph Parse
   UVa Department: Materials Science and Engineering
   NASA-LaRC Contact: D.R. Tenney (Materials Division)
   Start Date: September, 1988
   Completion Date: June, 1992
   Employment: Private Consultant

ADMINISTRATIVE PROGRESS

Faculty Participation

There were no changes in the faculty participants during this reporting period.

Brochure

The brochure prepared in March of 1991 was employed to advertise the LA^{2}ST program during this reporting period. About 150 copies were nationally distributed to stimulate graduate and undergraduate recruitment. All layout, printing and mailing costs were paid by the School of Engineering and Applied Science at UVa.

Graduate Student Recruitment

The LA^{2}ST Program has encountered no problems in recruiting the best graduate students entering the participating Departments at UVa, and in sufficient numbers to achieve our education and research objectives. There was no recruitment activity during this reporting period.

Undergraduate Research Participation

In April of 1990, the LA^{2}ST Program was increased in scope to include undergraduate engineering students[2]. While four students from North Carolina State and California Polytechnic State Universities, worked at NASA-LaRC during the Summer of 1990, there were no qualified applicants for the 1991 program. Efforts to recruit undergraduates for the Summer of 1992 were intensified and entrance criteria were stiffened. As a result, seven highly qualified undergraduates were recruited and successfully worked at the Langley Research Center. Each student was, at the time, a rising senior in an engineering or science major closely related to aerospace materials and mechanics. The students were from Harvard (2), Georgia Institute of Technology, Virginia Polytechnic Institute, Duke (2), and the University of Missouri.

Professor Glenn E. Stoner has assumed responsibility for the 1993 Summer Undergraduate Program.

Complementary Programs at UVa

The School of Engineering and Applied Science at UVa has targeted materials and structures research for aerospace applications as an important area for broad future growth. The LA^{2}ST Program is an element of this thrust. Several additional programs are of benefit to LA^{2}ST work.

The Board of Visitors at UVa awarded SEAS an Academic Enhancement Program

Grant in the area of Light Thermal Structures. The aim is to use University funds to seed the establishment of a world-class center of excellence which incorporates several SEAS Departments. This program is lead by Professor Thornton and directly benefits NASA.

The Light Metals Center has existed within the Department of Materials Science at UVa for the past several years under the leadership of Professor H.G.F. Wilsdorf, and after his retirement, under leadership of Dean Starke. A Virginia Center for Innovative Technology Development Center in Electrochemical Science and Engineering was established in 1988 with Professor G.E. Stoner as Director. Professors Pilkey, Thornton and Gangloff are conducting research under NASA-Headquarters Grant sponsorship to examine "Advanced Concepts for Metallic Cryo-thermal Space Structures"[3,4]. Research within this program is complementing LA^2ST studies, but will conclude in May of 1993.

References

1. R.P. Gangloff, E.A. Starke, Jr., J.M. Howe and F.E. Wawner, "NASA-UVa Light Aerospace Alloy and Structures Technology Program: Supplement on Aluminum Based Materials for High Speed Aircraft", University of Virginia, Proposal No. MS NASA/LaRC-5215-92, October, 1991.

2. R.P. Gangloff, "NASA-UVa Light Aerospace Alloy and Structures Technology Program: A Supplementary Proposal", University of Virginia, Proposal No. MS NASA/LaRC-4677-90, April, 1990.

3. W.P. Pilkey, "Advanced Concepts for Metallic Cryo-thermal Space Structures", University of Virginia Proposal No. MAE-NASA/HQ-4462-90, August, 1989.

4. W.P. Pilkey, "Advanced Concepts for Metallic Cryo-thermal Space Structures", University of Virginia Report No. UVA/528345/MAE91/101, February, 1991.

CURRENT PROJECTS

MECHANICAL AND ENVIRONMENTAL DEGRADATION MECHANISMS IN ADVANCED LIGHT METALS AND COMPOSITES

1. ENVIRONMENTAL FATIGUE CRACK GROWTH AND CRACKING MECHANISMS IN Al-Li-Cu Alloy 2090
   Faculty Investigator: R.P. Gangloff
   Graduate Student: Donald Slavik; PhD Candidate
   UVa Department: Materials Science and Engineering (MS&E)
   NASA-LaRC Contact: D.L. Dicus (Metallic Materials)
   Start Date: September, 1989
   Anticipated Completion Date: June, 1993
   Project #1

2. ELEVATED TEMPERATURE DAMAGE TOLERANCE OF ADVANCED INGOT METALLURGY WROUGHT ALUMINUM ALLOYS
   Faculty Investigator: R.P. Gangloff
   Graduate Student: Michael J. Haynes
   UVa Department: MS&E
   NASA-LaRC Contact: To be determined (Metallic Materials)
   Start Date: September, 1992
   Completion Date: December, 1994
   Project #2

3. CRYOGENIC TEMPERATURE EFFECTS ON THE DEFORMATION AND FRACTURE OF Al-Li-Cu and Al-Li-Cu-In ALLOYS
   Faculty Investigator: R.P. Gangloff
   Graduate Student: John A. Wagner; PhD candidate and NASA-LaRC employee
   UVa Department: MS&E
   NASA-LaRC Contacts: W.B. Lisagor (Metallic Materials) and J.C. Newman (Mechanics of Materials)
   Start Date: June, 1987
   Anticipated Completion Date: May, 1993
   Project #3

4. THE EFFECT OF CRYOGENIC TEMPERATURE ON THE FRACTURE TOUGHNESS OF WELDALITE™ X2095

Faculty Investigator: R.P. Gangloff
Graduate Student: Cynthia L. Lach; MS candidate and NASA-LaRC employee
UVa Department: MS&E
NASA-LaRC Contacts: W.B. Lisagor (Metallic Materials)
Start Date: August, 1990
Anticipated Completion Date: May, 1994
Project #4

5. MECHANISMS OF LOCALIZED CORROSION IN 2090 AND X2095

Faculty Investigator: G.E. Stoner
Graduate Student: Douglas Wall; PhD candidate
UVa Department: MS&E
NASA-LaRC Contact: M.S. Domack (Metallic Materials)
Start Date: April, 1991
Completion Date: May, 1994
Cosponsor: Reynolds Metals Company
Technical Contact: A. Cho
Project #5

6. EFFECTS OF Zn ADDITIONS ON THE PRECIPITATION AND STRESS CORROSION CRACKING BEHAVIOR OF ALLOY 8090

Faculty Investigator: Glenn E. Stoner
Graduate Student: Raymond J. Kilmer; PhD candidate
Department: MS&E
NASA-LaRC Contact: W.B. Lisagor (Metallic Materials)
Start Date: September, 1989
Anticipated Completion Date: December, 1992
Cosponsor: Alcoa
Project #6

7. HYDROGEN INTERACTIONS IN ALUMINUM-LITHIUM ALLOY 2090 AND SELECTED COMPLIMENTARY MODEL ALLOYS

Faculty Investigator: John R. Scully
Graduate Student: Stephen W. Smith; PhD Candidate
Department: MS&E
NASA-LaRC Contact: W.B. Lisagor and D.L. Dicus (Metallic Materials)
Start Date: April, 1991
Anticipated Completion Date: To be determined
Cosponsor: Virginia CIT
Project #7

8. METASTABLE PITTING OF Al ALLOYS IN HALIDE SOLUTIONS
Faculty Investigators: John R. Scully and J.L. Hudson
Graduate Student: Sheldon T. Pride; PhD Candidate
Department: Chemical Engineering
NASA-LaRC Contact: D.L. Dicus (Metallic Materials)
Start Date: September, 1991
Anticipated Completion Date: To be determined
Cosponsor: NASA Graduate Student Researchers Program; Under Represented Minority Emphasis
Project #8

AEROSPACE MATERIALS SCIENCE

9. INVESTIGATION OF THE EFFECT OF THERMAL TREATMENT ON THE MECHANICAL PROPERTIES OF Ti-1100/SCS-6 COMPOSITES
Faculty Investigator: F.E. Wawner
Graduate Student: Douglas B. Gundel; PhD candidate
UVa Department: MS&E
NASA-LaRC Contact: D.L. Dicus and W.B. Brewer (Metallic Materials)
Start Date: April, 1991
Anticipated Completion Date: June, 1993
Project #9

10. PROCESSING AND SUPERPLASTIC PROPERTIES OF WELDALITE™ SHEET
Faculty Investigator: John A. Wert
Graduate Student: Mark Lyttle; MS Candidate
UVa Department: MS&E
NASA-LaRC Contact: T.T. Bales (Metallic Materials)
Start Date: September, 1991
Anticipated Completion Date: September, 1993
Project #10

MECHANICS OF MATERIALS FOR LIGHT AEROSPACE STRUCTURES

11. ENVIRONMENTAL EFFECTS IN FATIGUE LIFE PREDICTION: MODELING CRACK PROPAGATION IN LIGHT AEROSPACE ALLOYS
    Faculty Investigator: R.P. Gangloff
    Graduate Student: Mark Mason; MS Candidate
    Post Doctoral Research Associate: Dr. Sang-Shik Kim
    UVa Department: MS&E
    NASA-LaRC Contact: R.S. Piascik (Mechanics of Materials)
    Start Date: January, 1992
    Anticipated Completion Date: December, 1994
    Project #11

12. INELASTIC DEFORMATION OF METAL MATRIX COMPOSITES UNDER BIAXIAL LOADING
    Faculty Investigators: Carl T. Herakovich and Marek-Jerzy Pindera
    Graduate Student: Mr. Clifford J. Lissenden, PhD Candidate
    UVa Department: Civil Engineering and the Applied Mechanics Program
    NASA-LaRC Contact: W.S. Johnson (Mechanics of Materials)
    Start Date: September, 1990
    Anticipated Completion Date: May, 1993
    Project #12

THERMAL GRADIENT STRUCTURES

13. EFFECT OF TEMPERATURE ON THE RESPONSE OF METALLIC SHELL STRUCTURES
    Faculty Investigators: W.D. Pilkey and J.K. Haviland
    Graduate Student: Karen McCarthy; MS candidate
    Graduate Student: Theodore Johnson; PhD candidate (NASA Minority Grantee)
    Graduate Student: Charles Copper; PhD Candidate
    UVa Department: Mechanical and Aerospace Engineering
    NASA-LaRC Contact: Drs. M.J. Shuart and Jeffrey Stroud (Aircraft Structures)
    Start Date: April, 1991
    Anticipated Completion Date: May, 1993 for McCarthy and Copper
    Project #13

14. EXPERIMENTAL STUDY OF THE NONLINEAR VISCOPLASTIC RESPONSE OF HIGH TEMPERATURE STRUCTURES

Faculty Investigator: Earl A. Thornton
Graduate Student: Marshall F. Coyle; PhD candidate
Undergraduate Student: Ms. Yool Kim
UVa Department: Mechanical and Aerospace Engineering
NASA-LaRC Contact: James H. Starnes, Jr. (Aircraft Structures)
Start Date: January, 1990
Anticipated Completion Date: To be determined
Project #14

RESEARCH PROGRESS AND PLANS (July 1st to December 31, 1992)

Research progress, recorded during the period from July 1, 1992 to December 31, 1992, is summarized for each project in the following sections. Each project section presents the program objective, brief background, recent progress, conclusions and immediate milestones. Appendices I, II and III summarize Grant publications and technical presentations during the reporting period.

Project #1 Environmental Fatigue Crack Growth and Cracking Mechanisms in Al-Li-Cu Alloy 2090

Donald C. Slavik and Richard P. Gangloff

Objective

The objectives of this PhD research are to: (a) characterize the effect of microstructure on environmental fatigue crack propagation (FCP), and (b) quantitatively define the microscopic damage mechanisms involved in vacuum and environmental FCP; in each case for Al-Li-Cu alloys.

Background

Environment and FCP Rates

Microstructure sensitive extrinsic crack closure has been broadly studied as a dominant factor that affects rates of FCP in aluminum-lithium alloys exposed to moist air[1-3]. The similarly important influences of environment[1,2,4], microstructure[5] and texture on FCP kinetics and microscopic cracking modes[6] have received considerably less attention. When evaluated, the influences of environment on FCP of Al-Li-Cu alloys are considerable[1,2,4]. For Al-Li-Cu alloy AA2090, moist air accelerates fatigue crack growth rate (da/dN) up to 6-fold, while fatigue in aqueous NaCl is accelerated up to 35-fold, with both cases compared to FCP in vacuum[4].

Grain or Subgrain Size and FCP Rates

Grain and subgrain boundaries are thought to influence FCP behavior for Al-Li alloys in both inert and aggressive environments[5-7]. Da/dN-ΔK slope transitions were correlated with the stress intensity range (ΔK) where the cyclic plastic zone size exceeded

microstructural distances such as the subgrain size[6,7]. In this instance atomic hydrogen may be trapped at subgrain boundaries localizing damage. Grain size effects were examined for moist air fatigue[8] and stress corrosion cracking[9], but the influences of grain and subgrain size on inert and aggressive environment da/dN have not been evaluated and are not fully understood. A need in this regard is to systematically vary the grain size of Al-Li-Cu alloys.

Inert Environment Cracking Modes

Microscopic fatigue cracking modes in Al-Li alloys have only been qualitatively identified. Al-Li-Cu alloy FCP is facetted and tortuous in moist air and inert environments[1-3,5,6,8]. Facets are thought to be parallel to {111} persistent slip bands due to coherent shearable δ' (Al_3Li) precipitates that localize slip[1-3,5,6,8]. Facet crystallographic orientations have not been measured with conventional diffraction techniques, since probe sizes exceed subgrain sizes in unrecrystallized Al-Li-Cu alloys[10]. Persistent slip band fatigue cracking was instead identified for AA2090 based on etch pit fractography[6], as well as with combined global x-ray texture measurements and facet intersecting angles from metallographic sections perpendicular to the transverse direction (T-plane)[2,3]. These techniques are informative, but are not conclusive, as detailed elsewhere[10]. Additionally, shear bands in fatigue of an Al-Li-Cu-Mg alloy were recently observed to cross grain boundaries and move from a {111} to a {331} trace, suggesting that facet formation may be more complex than simple {111} slip plane decohesion[11]. New diffraction experiments are needed for precise facet crystallography determination.

Aqueous NaCl Environment Cracking Modes

The crack tip fatigue damage mechanisms for Al-Li-Cu alloys in aggressive environments, capable of hydrogen production and localized dissolution/passivation, are controversial. T_1 (Al_2CuLi) precipitates in alloys such as AA2090 are electrochemically active relative to the matrix[12], decorate subgrain boundaries to possibly block slip[5], and were proposed to promote environmental FCP by anodic dissolution[12] or hydrogen trapping and embrittlement[6]. Additional potential environmental cracking modes include brittle Al-Li hydride cracking[13], hydrogen enhanced localized plasticity[14,15], and {100}/{110} "cleavage"[6].

Embrittlement and cleavage[6,16,17] or dislocation based mechanisms[14,18,19] have been introduced to explain {100} and {110} cracking in aluminum alloys. {100} cleavage facets were identified for large grain Al-Cu-Mg alloys in liquid metal environments[16]. For less

aggressive moist air, {100} facets were observed only when {100} planes were oriented normal to the applied tensile loading axis[17]. An alternating slip mechanism was proposed where two {111} slip systems persist, and crack tip microvoid formation leads to {100} or {110} macroscopic cracking[18]. It is not known if this mechanism operates for textures and crack tip stress states where one or three unbalanced slip systems are active. Precise grain orientations, slip system predictions, and facet crystallography measurements are required to understand how slip, environment, and texture interact. More generally, fatigue facet crystallography would help to establish the appropriate damage mechanism, but as discussed above, this has not been quantitatively determined with a local diffraction probe.

Technical Approach

The influences of environment on global intrinsic fatigue crack growth rates were measured for Al-Li-Cu alloy 2090 in highly purified vacuum and an aggressive aqueous NaCl solution. Commercial Vintage III AA2090 plate and sheet products from Alcoa were studied in the unrecrystallized and peak aged condition. Extrinsic crack closure was minimized with high mean stress constant K_{max} experiments[4].

Different subgrain sizes, recrystallized grain sizes, and texture-types were produced with thermo-mechanical processing techniques applied to the 2090 plate. Precipitates and subgrain sizes were imaged with the transmission electron microscope (TEM), and grain sizes were measured from optical metallography. Tensile properties, pitting potentials, and global textures were identified from smooth bar tensile experiments, electrochemical polarization scans, and {111} x-ray diffraction measurements, respectively.

Microscopic fatigue cracking modes were qualitatively determined as a function of environment, microstructure, and ΔK with scanning electron microscope (SEM) fractography. Grain and subgrain misorientations were measured with electron back scatter patterns (EBSPs); fatigue facet crystallography was identified with EBSPs coupled with quantitative tilt fractography measurements[10].

Results

Summary of Previous Results

Inert and environmentally enhanced da/dN for unrecrystallized AA2090 plate (URP), unrecrystallized sheet (URS), recrystallized fine grain sheet (RFS, from 2090 plate), and

recrystallized coarse grain sheet (RCS, from 2090 plate) were reported in previous NASA reports under this grant[20,21]. Intrinsic da/dN were similar for AA2024, AA8090, AA2090, and X2095 in inert environments when compared on a $\Delta K^2/E\sigma_{ys}$ basis, approximating the local crack tip strain range. For AA2090 in aqueous NaCl, da/dN was reduced for the RCS compared to other AA2090 microstructures on a ΔK and a $\Delta K^2/E\sigma_{ys}$ basis.

Fatigue cracking modes are shown for URP and RCS with combined metallographic sections and fractographs in Fig. 1. The crack growth direction is indicated with an arrow, and the grain structure is shown on the etched T-plane section which is perpendicular to the cracking direction. Similar tortuous tent-shaped fatigue facets formed in vacuum for unrecrystallized and recrystallized AA2090, as shown in Figs. 1a and 1b. In aqueous NaCl parallel and repeating stepped facets formed in URP, particularly at low ΔK as shown in Fig. 1c. These facets were similarly oriented within single grains and were not tortuous in contrast to vacuum facets. Aqueous NaCl fatigue facets for RCS AA2090 were larger and more varied in orientation, consistent with the random texture of this microstructure, as shown in Fig. 1d.

Summary of Recent Results

EBSPs are used to measure grain boundary misorientations for a single facet viewed from a transverse metallographic section. High angle boundary misorientations are given near grain boundaries as shown in Fig. 2a. The fractured sample coordinate system (**L** = plate longitudinal direction, **S** = plate short direction, and **T** = plate transverse direction which points out from the page), a typical 60° facet included angle, and the grain crystallographic directions for a brass-type texture variant are shown in Fig. 2b. Grain boundaries are high angle within a single facet viewed from the **T**-plane, as shown in Fig. 2a. Furthermore, {111} and {100} facets are equally possible given the brass-type texture and **T**-plane sections alone, as shown in Fig. 2b. Global measurements are not conclusive in identifying local facet crystallography.

To overcome shortcomings of global measurements, and to understand grain and facet orientations, techniques were developed under this grant to measure fracture facet crystallography for individual grains and with a local probe[10]. Fatigue facet orientations for typical AA2090 grains are shown in Figs. 3a and 3b for inert environmental FCP, and in Fig. 3c and 3d for aqueous NaCl cracking. Clustered symbols (▵,□,○) represent subgrain orientations in a single grain, and x or ▲ represent average facet plane normals. For AA2090

URP, multiple {111} vacuum fatigue facets formed in a single grain with the brass-type texture, as shown in Fig. 3a. Inert environment {111} fatigue facets were also predominately observed for the recrystallized microstructure, as shown in Fig. 3b for a single grain.

Two NaCl facet poles in unrecrystallized grains of the same brass-type texture variant of URP AA2090 are shown in Fig. 3c. Cracking did not occur along a single low index crystallographic plane; facets were 15° from a plane perpendicular to the primary crack tip stress axis (σ_{yy}). Aqueous NaCl facet crystallography for AA2090 (RCS) is shown in Fig. 3d. Facets in Figs. 3c and 3d only occasionally formed along {100} planes, even when a {100} plane was exactly parallel to the Mode I crack plane and normal to σ_{yy}.

Discussion of Recent Results

Inert Environments

Da/dN was enhanced up to 3-fold for the RCS compared to other AA2090 microstructures when correlated on a ΔK or $\Delta K/E$ basis. This difference was largely accounted for by the σ_{ys} influence on $\Delta K^2/\sigma_{ys}E$, which is related to the crack tip strain range[5]. Since da/dN was a single power-law function of $\Delta K^2/\sigma_{ys}E$, subgrain boundaries do not play a role in FCP of AA2090. Either T_1 decorated subgrain boundaries do not impede slip in URP AA2090, or slip distance does not affect transitions in inert environment intrinsic da/dN-ΔK behavior[5-7].

Vacuum fatigue facet crystallographic measurements are summarized in Table I, where reported angular deviations are measured between fracture facet and crystallographic poles. Roughly 80% of all vacuum facets are nearly parallel to {111} planes (within 10°), confirming the semi-quantitative results of etch pit(6) and x-ray texture experiments[2,3]. The appearance of single facets extending beyond high angle boundaries can be understood by considering the orientation of {111} facets and multiple variants of the brass-type texture. For two grains with different brass-type textures, {111} facets move out-of-plane, which can be deduced from Fig. 3a. The fatigue crack front could link together by grain boundary delamination, which is not observed, or by multiple {111} facets within a single grain, which is observed. Small stepped facet features (Fig. 1a) can lead to the inaccurate conclusion of single facets crossing grain boundaries when viewed from the T-plane section alone. These features were not previously identified since facet three dimensional orientations and crystallography measurements were not performed.

Aqueous NaCl Environments

Enhanced growth rates and complex ΔK dependencies of da/dN were observed for AA2090 in aqueous NaCl fatigue. Near threshold FCP rates decreased for RCS in aqueous NaCl compared to the other higher strength AA2090 microstructures; multi-sloped transitions were not due to subgrain size/plastic zone behavior[6], but may be due to dislocation substructure which is produced by crack tip cyclic deformation. The ΔK-da/dN dependencies for unrecrystallized AA2090 do not correlate with unique microscopic damage modes or with plastic zone interactions with the T_1 decorated subboundaries[6]. The low ΔK transition (at 2.0 MPa$\sqrt{m}$) and the intermediate power-law behavior (for $2.0 < \Delta K < 5$ MPa$\sqrt{m}$) correlate with a cyclic plastic zone of approximately 0.4 to 3.0 μm. Subgrains are larger than this for both microstructures, so the plastic zone and subgrain sizes are not singular features controlling transition behavior.

The aqueous NaCl fatigue crack crystallographic orientation measurements are summarized in Table II. The average facet orientation is a high index plane, {1 1.8 5} from the average of the aqueous NaCl fracture facet results. The lack of a unique low index crystallographic cracking plane provides insight into the damage mechanism for environmental FCP in Al-Li-Cu alloys. EBSP analysis established that facets were: a) not along {100} crystallographic planes as expected based on lattice decohesion[6], b) not along {100} planes expected for brittle $AlLiH_4$ hydride cracking[13], c) not along {111} planes due to localized dissolution of matrix T_1[12], d) not parallel to {111} planes due to hydrogen enhanced localized plasticity and slip plane decohesion[14,15], e) not oriented precisely normal to the maximum crack tip stress σ_{yy}, and f) not consistent with any single high index cracking plane.

A combined multiple slip and hydrogen-tensile failure criteria, which is not strictly crystallographic in nature, may be appropriate for AA2090 in aqueous NaCl. Absorbed hydrogen may enhance crack tip dislocation nucleation[18] and mobility within the plastic zone[14]. Multiple slip systems are activated, even at very low ΔK, and intersect with two consequences. Intersections may concentrate tensile stress and cause vacancy or microvoid formation[19], and atomic hydrogen may be readily delivered to such defects, which are strong trap sites. Process zone fatigue failure ensues when sufficient hydrogen is localized to satisfy a normal stress-hydrogen concentration criterion. σ_{yy}, within one to two crack tip opening displacements from the crack tip and equaling 3 to 5 σ_{ys}, is critical in this regard and may

determine the average local crack plane. The plane is nearly perpendicular to the **L** direction, as shown in Figs. 3c and 3d, but is not precisely normal since multiple slip plays a role in the distribution of fatigue damage, normal stress and hydrogen within the cyclic plastic zone. Normal stresses are highest in the unrecrystallized alloy (higher σ_{ys}), requiring fewer load cycles to accumulate hydrogen before crack extension, and consequently increased average da/dN. This mechanism is clearly speculative and requires further development.

This work was reported in three publications that were prepared and submitted during this reporting period. The abstracts for these papers are presented in Appendix II.

Conclusions

1. Compared to FCP in vacuum, aqueous NaCl increases intrinsic da/dN (particularly near-threshold), alters the microscopic cracking mode, and causes a complex ΔK-da/dN dependence for several microstructures of Al-Li-Cu alloy AA2090.

2. Elimination of the subgrain microstructure does not affect the basic cracking modes for AA2090. FCP rates are equal for unrecrystallized and recrystallized microstructures in vacuum, based on $\Delta K^2/(E\sigma_{ys})$; while for aqueous NaCl, da/dN is increased and da/dN-ΔK transitions are more significant when subgrains are present and σ_{ys} is higher.

3. Large fatigue facets form essentially parallel to highly shear-stressed multiple {111} slip planes, confirming persistent slip band decohesion as the dominant fatigue damage mechanism for AA2090 in vacuum. Texture is not a prerequisite for facetted FCP.

4. FCP in aqueous NaCl is facetted, particularly at low ΔK. Facets are not crystallographic on a low index plane, and are not normal to the Mode I direction. Anodic dissolution of T_1, hydrogen enhanced slip plane cracking, and lattice "cleavage" by decohesion are not supported. Intersecting slip damage and hydrogen trapping within the crack tip process zone is a possible failure mechanism.

Immediate Future Direction

This project will be completed by June of 1993. Remaining work will emphasize the crack tip damage mechanisms for FCP in vacuum and NaCl environments. The Phd

dissertation is being prepared.

References

1. K.V. Jata and E.A. Starke, Jr., Metall. Trans. A, Vol. 17A, 1986, pp. 1011-1026.
2. K.T. Venkateswara Rao and R.O. Ritchie, Int. Matls. Rev., Vol. 37, 1992, pp. 153-185.
3. G.R. Yoder, P.S. Pao, M.A. Imam, and L.A. Cooley, Scripta Metall., Vol. 22, 1988, pp. 1241-1244.
4. R.S. Piascik and R.P. Gangloff, Metall. Trans. A, Vol. 22A, 1992, pp. 2415-2428.
5. D.C. Slavik, C.P. Blankenship, Jr., E.A. Starke, Jr., and R.P. Gangloff, "Intrinsic Fatigue Crack Growth Rates for Al-Li-Cu-Mg Alloys in Vacuum", submitted to Metall. Trans. A, 1992.
6. R.S. Piascik and R.P. Gangloff, "Environmental Fatigue of an Al-Li-Cu Alloy: Part II-Microscopic Hydrogen Cracking Processes", submitted to Metall. Trans. A, 1992.
7. G.R. Yoder, L.A. Cooley and T.W. Crooker, Scripta Metall., Vol. 16, 1982, pp. 1021-1025.
8. J.M. Neumann, P.J. Gregson, P.D. Pitcher, and P.J.E. Forsyth, in Aluminum-Lithium Alloys V, eds. T.H. Sanders Jr. and E.A. Starke Jr., Vol. 2, Materials and Component Engineering Publications Ltd., Wardley Heath, UK, pp. 1042-1052 (1988).
9. R.C. Dorwood, Corrosion, vol. 46, No. 4, 1990, pp. 348-325.
10. D. C. Slavik, J.A. Wert, and R.P. Gangloff, "Determining Fracture Facet Crystallography Using Electron Back Scatter Patterns and Quantitative Tilt Fractography", to be submitted to J. of Materials Research, 1993.
11. Y.B. Xu, L. Wang, Y. Zhang, Z.G. Wang, and Q.Z. Hu, Metall. Trans. A, 1991, Vol. 22A, pp. 723-729.
12. R.G. Buchheit, J.P. Moran, and G.E. Stoner, Corrosion, Vol. 46, 1990, pp. 610-617.
13. R. Balasubramaniam, D.J. Duquette, and K. Rajan, Acta. Metall., Vol. 38, No. 11, 1991, pp. 2597-2612.
14. H.K. Birnbaum, in Hydrogen Effects on Material Behavior, eds., N.E. Moody and A.W. Thompson, TMS-AIME, Warrendale, PA, 1990, pp. 639-660.
15. G.S. Chen and D.J. Duquette, Metall. Trans. A, Vol. 23A, 1992, pp. 1563-1572.

16. A.P. Reynolds and G.E. Stoner, Metall. Trans. A, Vol. 22A, 1991, pp. 1849-1855.

17. D. N. Fager, M.V. Hyatt, and H.T. Diep, Scripta Met., Vol. 20, 1986, pp. 1159-1164.

18. S.P. Lynch, Acta Metall., Vol. 36, No. 10, 1988, pp. 2639-2661.

19. G.G. Garrett and J.F. Knott, Acta Metall., Vol. 23, 1975, pp. 841-848.

20. D.C. Slavik and R.P. Gangloff, "NASA-UVA LA^{2}ST Progress Report", Univ. of Virginia, Report No. UVA/528266/MS92/109, Jan. 1992, pp. 23-44.

21. D.C. Slavik and R.P. Gangloff, "NASA-UVA LA^{2}ST Renewal Proposal", Univ. of Virginia, Report No. MSE-NASA/LaRC-5669-93, Nov. 1992, pp. 19-32.

Table I: Summary of Vacuum Fatigue Facet Crystallography

Plane	Material	0° to 5°	5° to 10°	> 10°
{111}	URP[1]	44%	40%	16%
{111}	RCS[2]	38%	38%	23%
{100}	URP	None	8%	92%
{100}	RCS	None	None	100%

[1] 25 facets for URP
[2] 13 facets for RCS

Table II: Aqueous NaCl Fatigue Facet Crystallography

Plane	Material	0° to 5°	5° to 10°	> 10°
{111}	URP[1]	None	None	100%
{111}	RCS[2]	None	None	100%
{100}	URP	None	None	100%
{100}	RCS	10%	None	90%
{1 1.8 5}[3]	URP	50%	37%	13%
{1 1.8 5}	RCS	30%	20%	50%

[1] 8 facets analyzed for URP
[2] 10 facets analyzed for RCS
[3] Average Aqueous NaCl Facet Crystallography

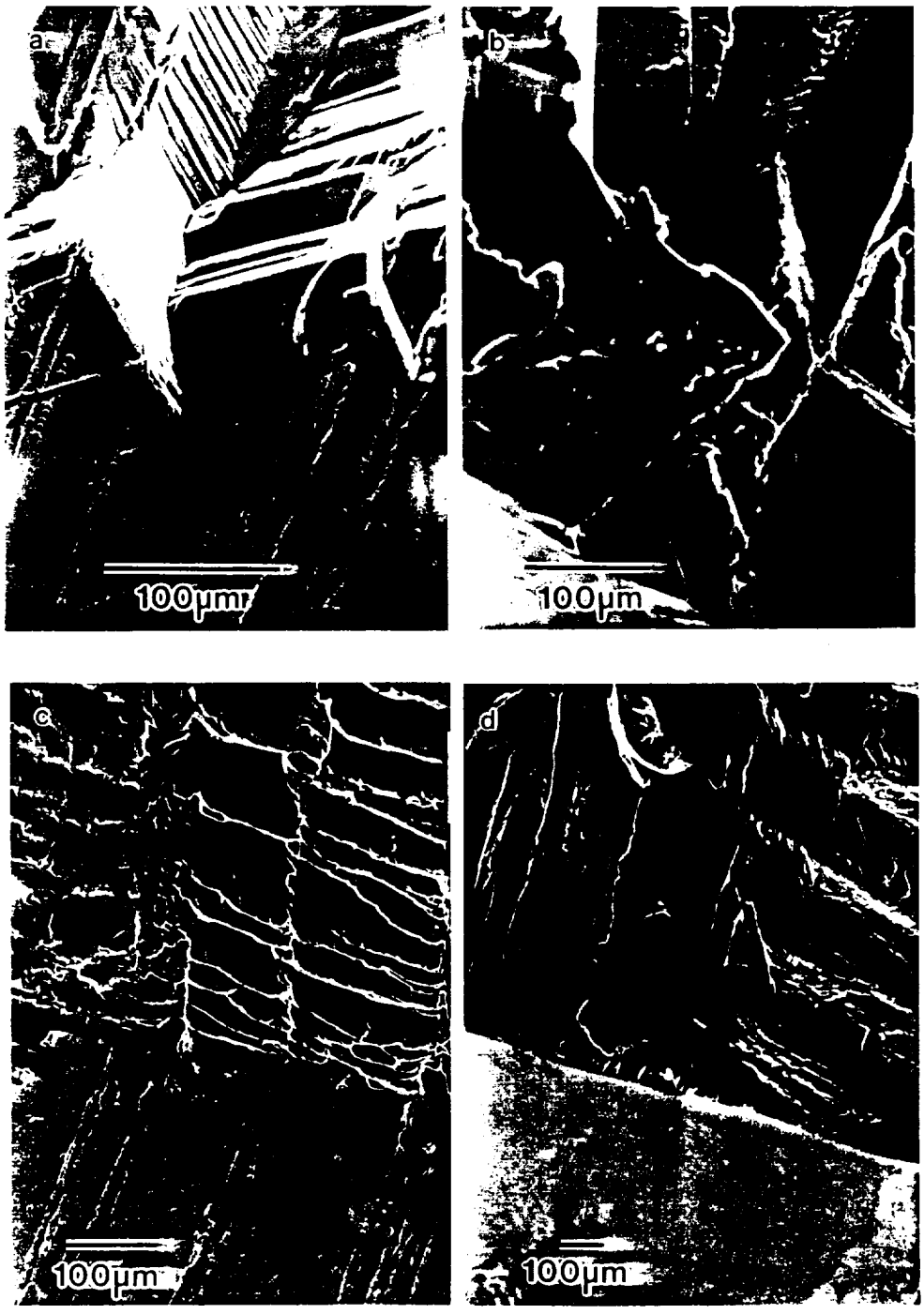

Figure 1 Metallographic T-plane sections and fatigue fracture facets for a) URP in vacuum, b) RCS in vacuum, c) URP in aqueous NaCl, and d) RCS in aqueous NaCl.

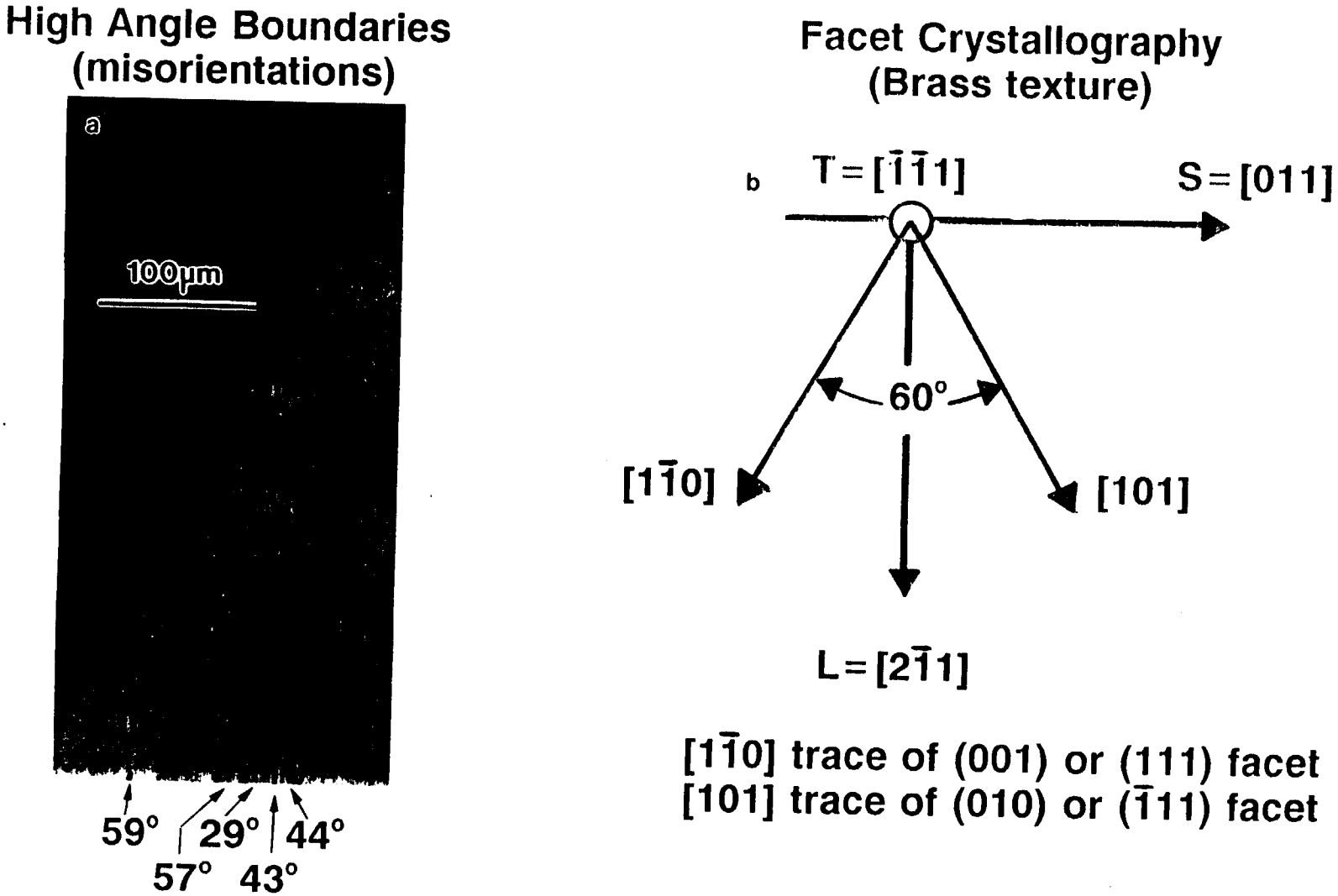

Figure 2 Unrecrystallized AA2090 vacuum fatigue fracture facets: a) high angle grain boundary misorientation measurements, and b) facet geometry and crystallographic directions for a brass-type texture variant.

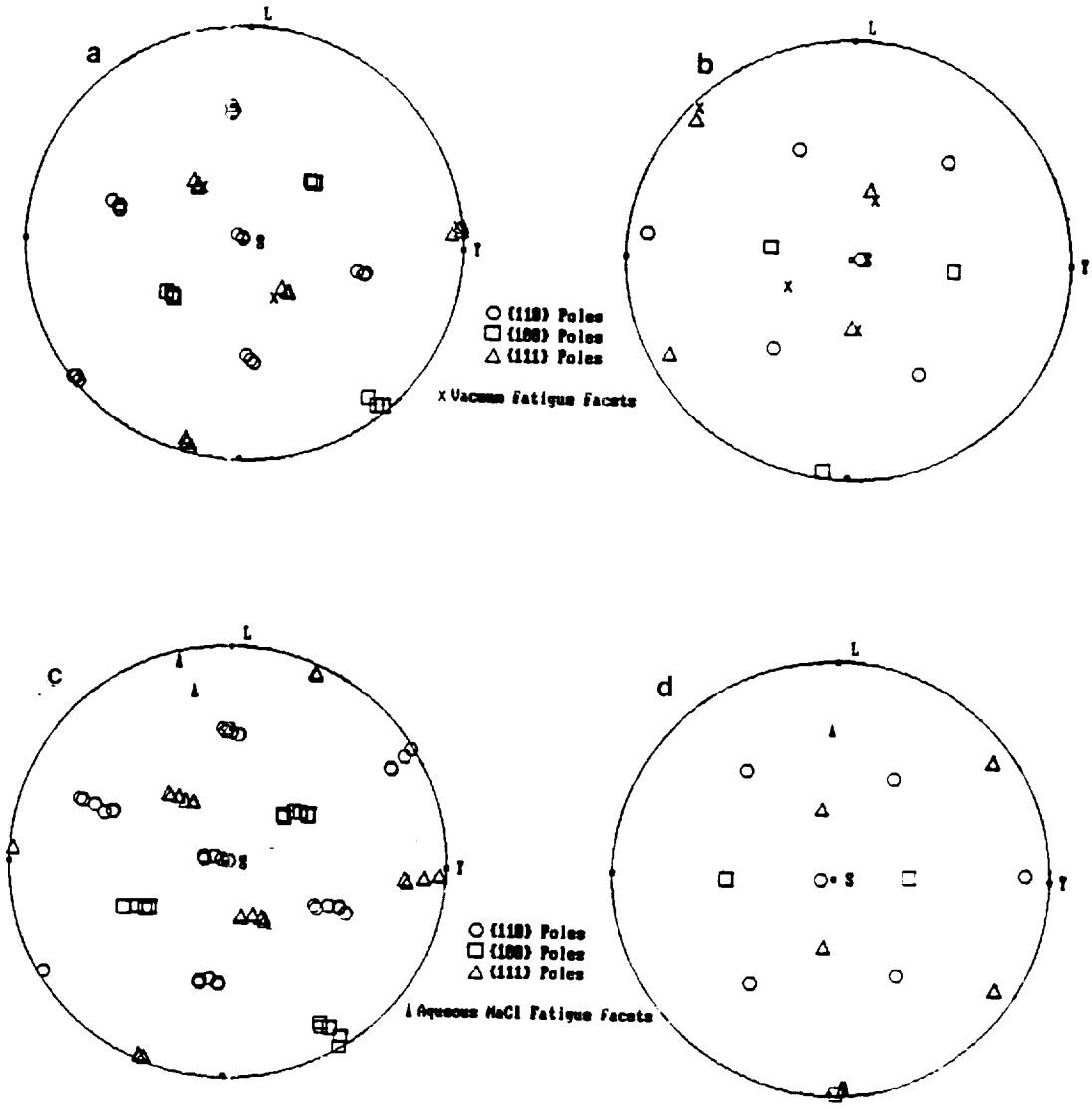

Figure 3 Microtexture and fatigue fracture facet poles for a) URP in vacuum, b) RCS in vacuum, c) URP in aqueous NaCl, and d) RCS in aqueous NaCl.

Project #2 **Elevated Temperature Damage Tolerance of Advanced Ingot Metallurgy Wrought Aluminum Alloys**

Michael J. Haynes and Richard P. Gangloff

Background and Problem Statement

A significant effort is currently aimed at developing advanced aluminum alloys for elevated temperature aerospace applications, particularly for high speed airframes such as the civil transport[1]. Since existing precipitation hardened aluminum alloys (e.g., 2024, 7075/7475 and 2090/8090) may not be sufficient to meet microstructural stability combined with strength/toughness requirements, new compositions of both wrought ingot metallurgy (I/M) and rapidly solidified powder metallurgy (RS/PM) alloys are under development. As promising compositions are determined, it is necessary to characterize the critical effects of loading rate and temperature on fracture toughness and creep-fatigue damage tolerance, and to establish micromechanical mechanisms and predictive models for such properties.

Objective

The objective of this MS research project is to characterize the flaw damage tolerance, particularly the tensile fracture toughness, of emerging ingot metallurgy wrought aluminum alloy sheet as a function of temperature, loading rate and environment. The underlying mechanisms for time-temperature dependent fracture will be physically defined and micromechanically modeled.

Technical Approach and Results During this Reporting Period

Michael J. Haynes began graduate studies at UVa in the Fall of 1992, and has worked on this project for 4 months. The following directions are being pursued and initial experimental results have been obtained.

Material

The proposed Task emphasizes advanced I/M aluminum alloys and is being coordinated with alloy development studies in a parallel ongoing NASA-funded research[1].

I/M 2519 (Al-5.8Cu-0.2Mg-0.3Mn-0.15Zr by wt%) and I/M 2618 (Al-2.7Cu-1.6Mg-

1.1Fe-1.2Ni-0.23Si by wt %) with alloy chemistry modifications, were chosen for this study. Dr. L.M. Angers and the Alcoa Laboratories recently supplied 3.2 mm thick sheet of two modified 2519 alloys. The compositions in Table I show that these alloys are based on the additions of 0.3 wt% Mg or 0.3 wt% Mg + 0.5 wt% Ag to the baseline 2519 composition. These additions are intended to promote Ω strengthening and microstructural stability[2,3].

Table I - Modified I/M 2519 Alloy Chemistries

Alloy ID#	Composition (wt %)							
	Cu	Mg	Ag	Mn	Zr	V	Fe	Si
689247	5.85	0.50	----	0.30	0.15	0.10	0.05	0.04
689248	5.85	0.50	0.50	0.30	0.15	0.10	0.05	0.04

Alloy heat treatment; consisting of solution treatment, cold water quench, stretching and peak aging at 177°C for 3 hours (T87 condition); was performed by Alcoa on each sheet. The Mg and Ag + Mg additions increased the room temperature yield strengths to 476 MPa and 485 MPa, respectively[4]. Plane stress fracture toughnesses of these two conditions were reported to equal 117 MPa$\sqrt{m}$ and 121 MPa$\sqrt{m}$, respectively, based on experiments with 16 cm wide and 3.1 mm thick middle cracked tension specimens[4]. One goal of the study is to characterize the effect of Ω formation on temperature dependent fracture toughness. Preliminary TEM provided by Alcoa indicates that Ω phase, forming on {111} habit planes, is present in the high Mg + Ag composition.

I/M 2618 with reduced Fe and Ni content (I/M 2650) was chosen for the study due to claims of increased fracture toughness at ambient temperature; most likely due to the decreased size and heterogeneity of typically micron sized Al_2FeNi intermetallic constituents. Pechiney Aluminum has agreed to provide a 6 mm thick plate of 2650-T6; this material is reported to exhibit a 15% in K_{IC} relative to more conventional 2618.

Fracture Mechanics Characterization Methods

Recent work at UVa demonstrated the application of fracture mechanics and micromechanics approaches to characterize and understand time-temperature dependent fracture in an advanced elevated temperature aluminum alloy RS/PM 8009[5-7]. These methods will be employed here. The basic experiment will be the rising load R-curve

method, measured in terms of the applied J-integral (equal to $(K^2/E)_{ELASTIC} + J_{PLASTIC}$) versus crack extension (Δa). A 3 mm thick, fatigue precracked compact tension specimen of 7 to 10 cm width will be employed for all experiments. Load, load line displacement, crack length from direct current electrical potential and temperature will be measured as a function of time for the specimen contained within a large convection furnace/cryogenic chamber mounted on a computer automated closed-loop servoelectric test machine. From these measurements, the J-Δa R-curve will be calculated, and both the crack initiation toughness (K_{IC}) and tearing modules will be determined. This method will be applied to 2024 in conjunction with the NASA-LaRC sponsored round robin program on fracture toughness characterization.

Room temperature J-Δa curves, at crosshead displacement rates of 2.5×10^{-3} and 1.8×10^{-6} mm/sec, were determined for two unmodified I/M 2618-T851 alloys (Figures 1 and 2). These experiments were conducted to: (a) provide a baseline for fracture toughness determinations of the modified I/M 2618 and I/M 2519 alloys, (b) confirm previously obtained results for I/M 2618[5], (c) explore the effect of slow loading rate (1.8×10^{-6} mm/sec) fracture. The following observations were made:

- The R-curve method successfully characterized the fracture toughness of 2618. K_{IC} and T_R (Tearing Modulus) values were reasonably close to previous results (See Table II). Both the plane strain crack initiation toughness (K_{IC}) and the tearing modulus (T_R) of this heat of 2618 are relatively low and are reproducible.

Table II - Room Temperature Fracture Properties of I/M 2618 Plate*

	Displacement Rate (mm/s)	K_{IC}** (MPa$\sqrt{m}$)	T_R
Present Results	1.80×10^{-6} 2.54×10^{-3}	21.2 21.5	0.6 1.8
Previous Results (Porr[5])	2.54×10^{-3}	20.1	0.5

* All data were obtained from 7.7 mm thick compact tension specimens that were side grooved to a reduced total thickness of 6.4 mm.

** Determined from J_i with direct current electrical potential measurements of initial fatigue crack tip damage.

- Based on sustained load crack growth rate data, it was hypothesized that a slow crack tip strain rate might produce a reduced fracture toughness and some intergranular cracking[8]. The data in Table II shown that this is not the case. SEM observations demonstrated failure entirely by microvoid coalescence. It is likely that reduced toughness, due to slow loading rate, will be encountered at higher temperatures. It is encouraging that the slow rate experiment, requiring four days to complete, was successful.

A room temperature J-Δa curve was determined for an LT oriented thin (3.16 mm) compact tension specimen (width, W, of 76.2 mm) of I/M 2519, modified with Mg and Ag additions (alloy ID# 689248). This curve, determined at a crosshead displacement rate of 6.5×10^{-5} mm/sec, was converted to a K-R curve (See Figure 3) by:

$$\sqrt{\frac{JE}{1-\nu^2}}$$

where E is the elastic modulus (73 GPa), and υ is Poisson's ratio (0.3). The following observations were obtained:

- The plane strain fracture initiation toughness (K_{IC}) is approximately 40% higher than the K_{IC} values for I/M 2618 (compare Figure 4 to Table II).
- J_{IC} is four-fold higher than J_i due to the substantial amount of plane stress typical of crack growth in this thin sheet. It is none-the-less likely, that crack initiation occurred under dominant plane strain and is characterized by K_{IC}; such is probably not the case for K_{JIC} from J_{IC}. Recall that the thickness requirement for plane strain J-based crack growth is a value in excess of $25J/\sigma_o$, where σ_o is the average of the yield and ultimate strengths. For J equalling 50 kJ/m^2 (near J_{IC} in Figure 3) and σ_o of 500 MPa, thickness (B) must exceed 2.5 mm. For J equalling 15 kJ/m^2 (near J_i in Figure 3), B must exceed 0.8 mm. Since the CT specimen thickness was 3.16 mm, J_i and the associated K_{IC} is most likely a plane strain value. For J levels near 50 kJ/m^2, however, significant plane stress will increase the measured toughness and compromise the attainment of a geometry independent plane strain initiation value. Since the J-integral thickness criterion is approximate, additional work is required to

analyze R-curves of the sort presented in Figure 3.

- The C(T) specimen represented in Figure 3 buckled and data were not taken beyond the estimated point where this complication occurred. Accordingly, cracking was not characterized over the full range of allowable Δa (Δa_{max} = 10% of the uncracked ligament, W - a, or 3.8 mm for the case in Figure 3). Since the exact point of buckling is unknown, the validity of the R-curve is suspect. Future tests will employ anti-buckling fixtures. Note, however, that the toughness of the modified 2519 is such that J_{max} was exceeded at a relatively small Δa of about 1.4 mm. (According to ASTM Standard 1152, J_{max} is given by the smaller of (W - a) or B times $\sigma_o/20$. Thickness resulted in the limitation plotted in Figure 3.) There is no analytical basis for the J_{max} criterion and the data in Figure 3 appear to obey a relationship that is not affected by the suggested violation. This issue will be addressed as additional data are obtained.

To alleviate buckling, the fatigue precrack in a similar 2519 specimen was grown an additional 0.1 a/W (to a/W of 0.6), and a room temperature fracture toughness experiment was performed (Figure 5). The specimen did not buckle. An aberration in the direct current electrical potential measurements was observed, corresponding to a deviation in the J-Δa data. The origin of this abnormality is unknown, but it may be either a material property or due to a temperature change during the test. It was estimated that a 1 to 2°C change in temperature could account for the deviation. Further tests will be performed under controlled temperature conditions (i.e., room temperature tests in a furnace controlled at 30°C) and will utilize a reference probe pair. In spite of the irregular J-Δa data, the K_{IC} value from Figure 5 agrees with the result of the previous experiment with 2519 as shown in Figure 4.

The fracture toughness of this thickness of modified 2519 is substantial. Angers previously reported that K_c, from a 16 cm wide middle cracked tension specimen of the same thickness (B = 3.1 mm) as the current experiments, equalled 121 MPa$\sqrt{m}$[4]. If the results in Figures 3 and 5 are extrapolated to this toughness level, the corresponding amounts of crack extension are 3.8 mm and 3.4 mm. This rough comparison suggests that the UVa compact tension experiments and the Alcoa middle crack tension experiments yielded similar high levels of plane stress fracture toughness. Quantitative comparisons of this sort must await the measurement of complete K-Δa R-curves for wide panels of alloys such as 2519.

In order to understand the details of the J-Δa analysis, the graduate student has carefully examined various methods for calculating J. A difference in the calculation of the J-integral from load versus load line displacement and crack length data was found between ASTM Standard E1152 and our computer program calculation technique. A typical discrepancy is shown in Figure 6. The squares were calculated with a spread sheet implementation of the ASTM standard equations, while the triangles were determined by our computer program. The spreadsheet method was employed to confirm the numerical accuracy of our computerized procedure. The difference indicated in Figure 6 was isolated to the calculation of the so-called "plastic area" used to determine J-plastic. The UVa technique preforms a numerical integration of the total area under the load versus load line displacement data, then subtracts the "elastic area" defined by the calculated compliance for a given crack length. The ASTM procedure calculates the plastic area by rectangular elements that appear to underestimate the correct area. This issue will be pursued during the next reporting period.

Proposed Research for the Next Reporting Period

We propose to achieve the following:

- oo Establish the rising load J-Δa relationships for the two modified compositions of AA2519 and for AA2650, as a function of temperature from -90°C to 250°C, at a constant loading rate that produces several millimeters of crack growth in 3 hours, and for the moist air environment.
- oo For a single alloy and temperature (probably AA2519 with Mg + Ag at 130°C), selected based on the above experiments, define the effect of loading time on cracking resistance.
- oo Define the microscopic fracture processes for the alloys examined in the temperature and time experiments.
- oo The plastic deformation of aluminum alloys is central to the evolution of fracture. In order to define work hardening resistance without complications due to necking, and to produce specimens for TEM characterizations of dislocation structures, we will develop a compression method.
- oo We plan to participate in the NASA-LaRC sponsored interlaboratory experimental program to characterize the room temperature fracture toughness of AA2024 sheet.

We will employ the small compact tension J-Δa R-curve method to define the initiation and growth toughnesses of both 3.2 mm thick and 1.6 mm thick sheet provided by LaRC. These materials were recently received by UVa. By comparing our results to the work from other participating laboratories, we will be able to assess the accuracy and relevance of the small specimen method.

References

1. R.P. Gangloff, E.A. Starke, Jr., J.M. Howe and F.E. Wawner, Jr., "Aluminum Based Materials for High Speed Aircraft", University of Virginia, Proposal No. MS-NASA/LaRC-5215-92, October (1991).

2. E.A. Starke, Jr., "University of Virginia HSR Aluminum Based Materials Grant Review", Hampton, VA, August (1992).

3. L.M. Angers, "Effects of Dispersoids and Precipitates on the Elevated Temperature Performance of 2519-Based Experimental Materials", ALTC Division Report 56-90-AK91, Alcoa Laboratories, Alcoa Center, PA (1990).

4. E.A. Starke, Jr., "NASA-UVa Light Aerospace Alloy and Structures Technology Program Supplement: Aluminum-Based Materials for High Speed Aircraft", UVa Progress Report to NASA-LaRC for the period from July to September (1992).

5. W.C. Porr, Jr., "Elevated Temperature Fracture of Advanced Powder Metallurgy Aluminum Alloy 8009", PhD Dissertation, University of Virginia (1992).

6. W. C. Porr, Jr., Y. Leng, and R. P. Gangloff, in Low Density, High Temperature P/M Alloys, W. E. Frazier, M. J. Koczak, and P. W. Lee, Eds., TMS-AIME, Warrendale, PA, (1991), pp. 129-156.

7. W. C. Porr, Jr, A. P. Reynolds, Y. Leng, and R. P. Gangloff, Scripta Metallurgica et Materialia, Vol. 25 (1991) pp. 2627-2632.

8. Y. Leng, W. C. Porr, Jr., and R. P. Gangloff, Scripta Metallurgica et Materialia, 25, (1991), pp. 895-900.

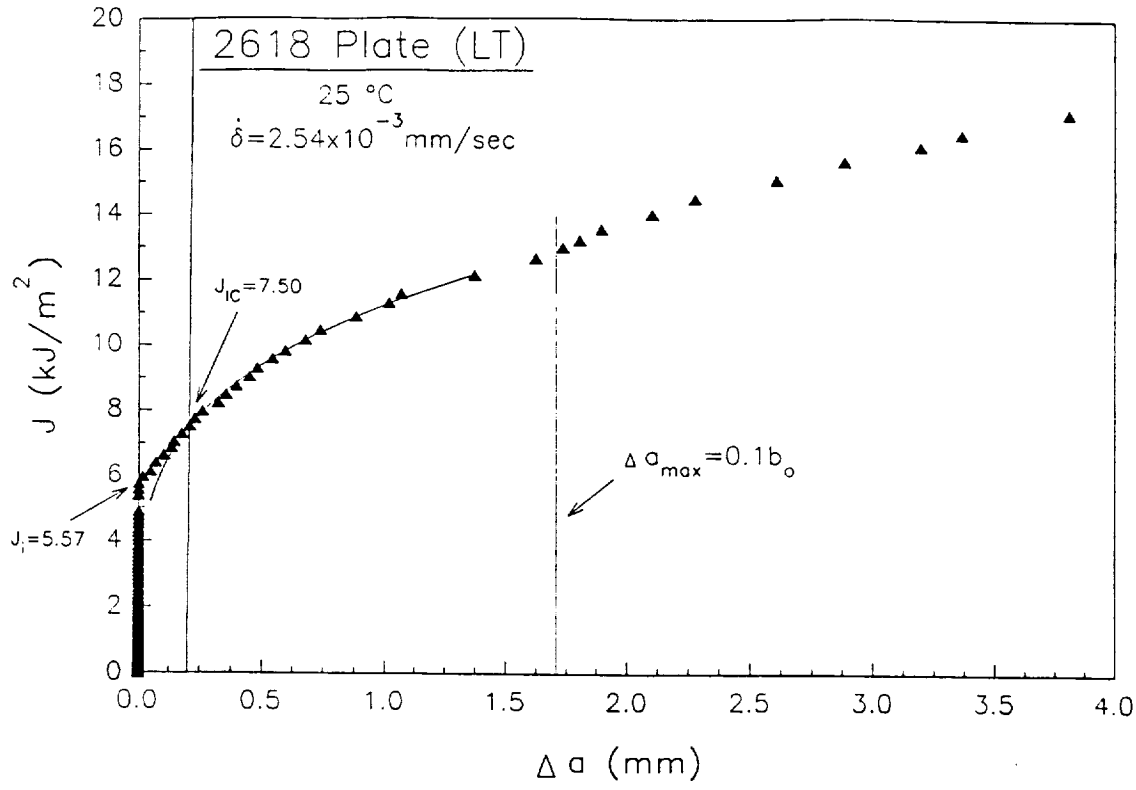

Figure 1 Applied J versus crack extension for I/M AA2618 at 25°C and a grip displacement rate of 2.5 x 10^{-3} mm/sec showing the determinations of J_i and J_{IC}.

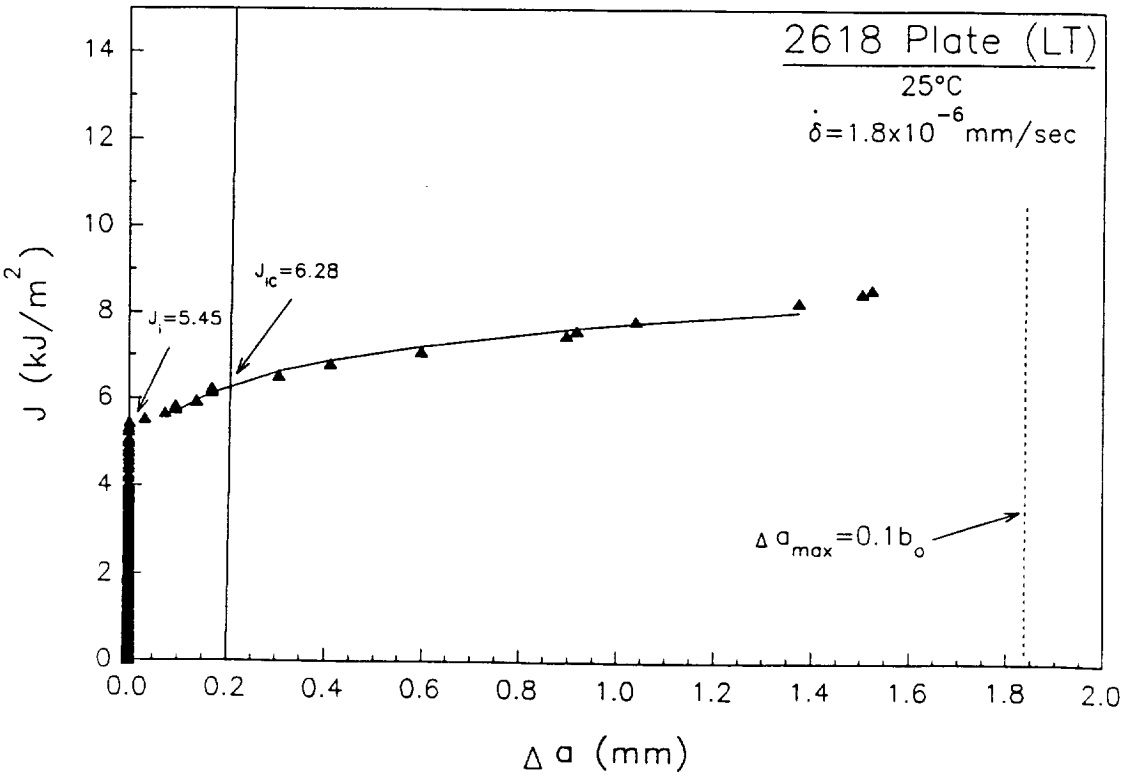

Figure 2 Applied J versus crack extension for I/M AA2618 at 25°C and a grip displacement rate of 1.8 x 10^{-6} mm/sec.

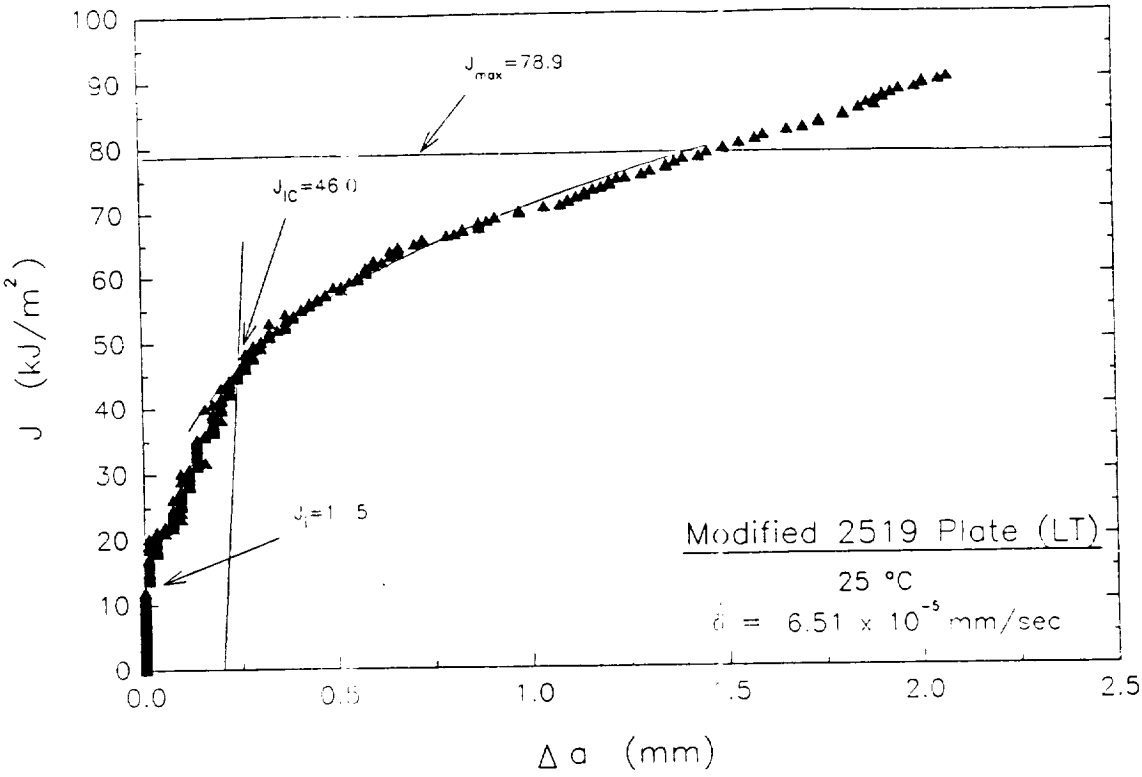

a

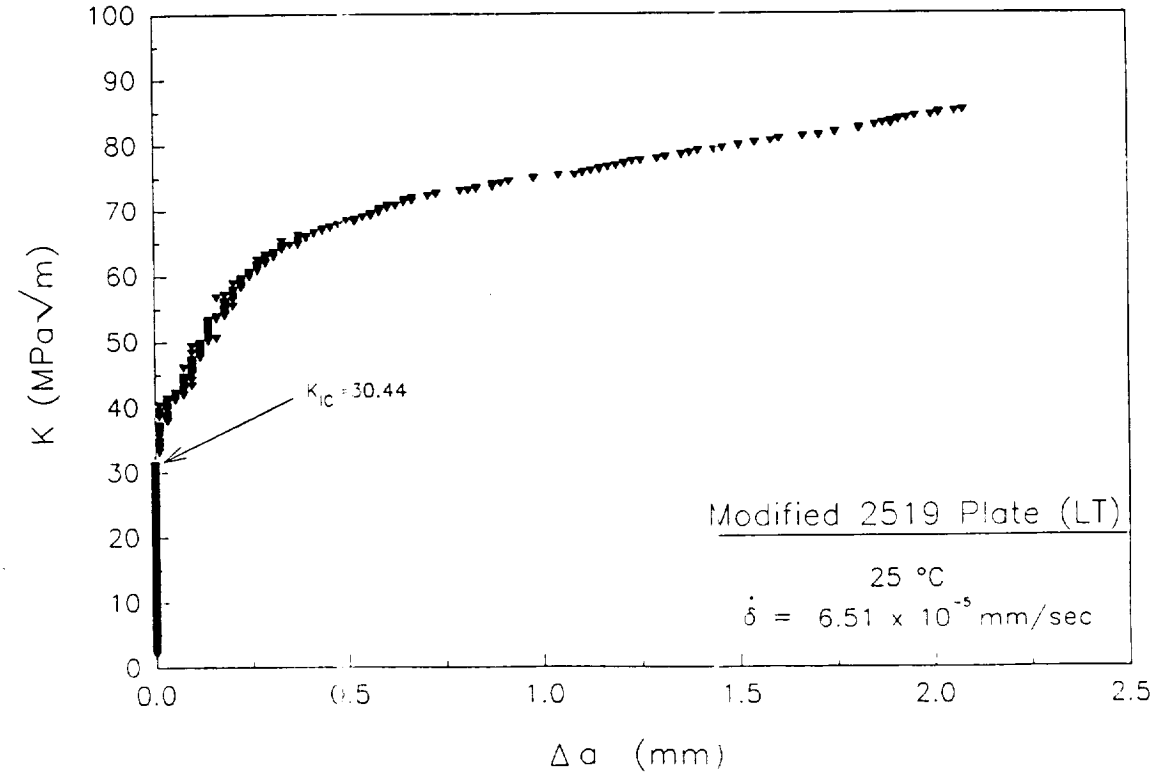

b

Figure 3 (a) J versus Δa, and (b) K versus Δa R-curves for Mg + Ag modified AA 2519 loaded at a displacement rate of 6.5 x 10^{-5} mm/sec at 25°C.

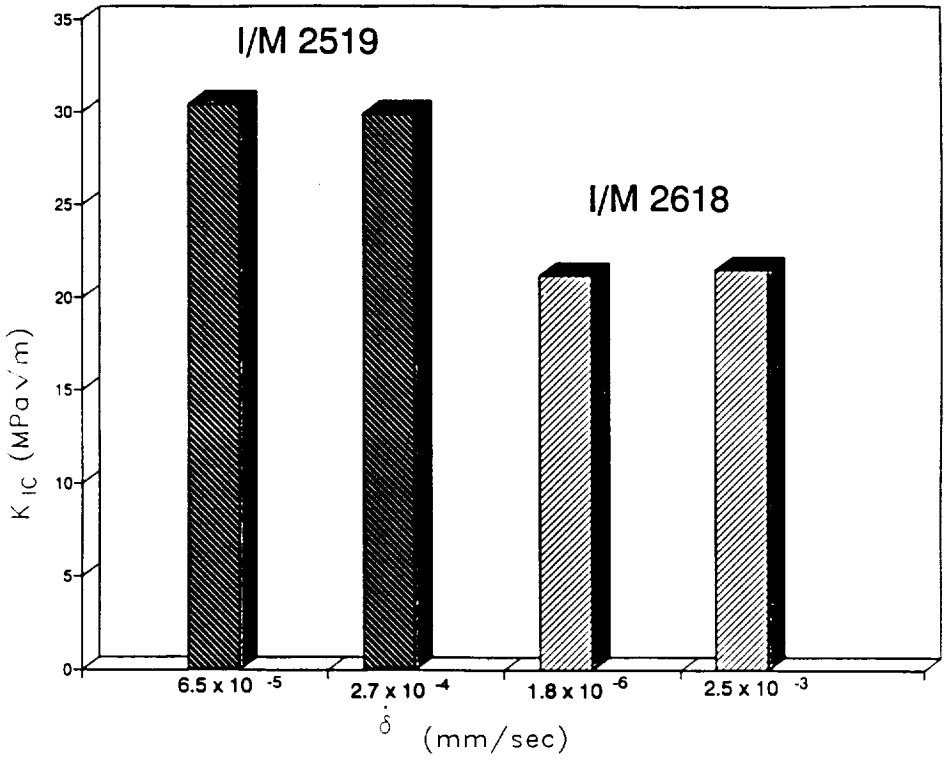

Figure 4 Plane strain crack initiation fracture toughness, K_{IC}, determined from J_i for I/M AA2618 and Mg + Ag modified AA2519.

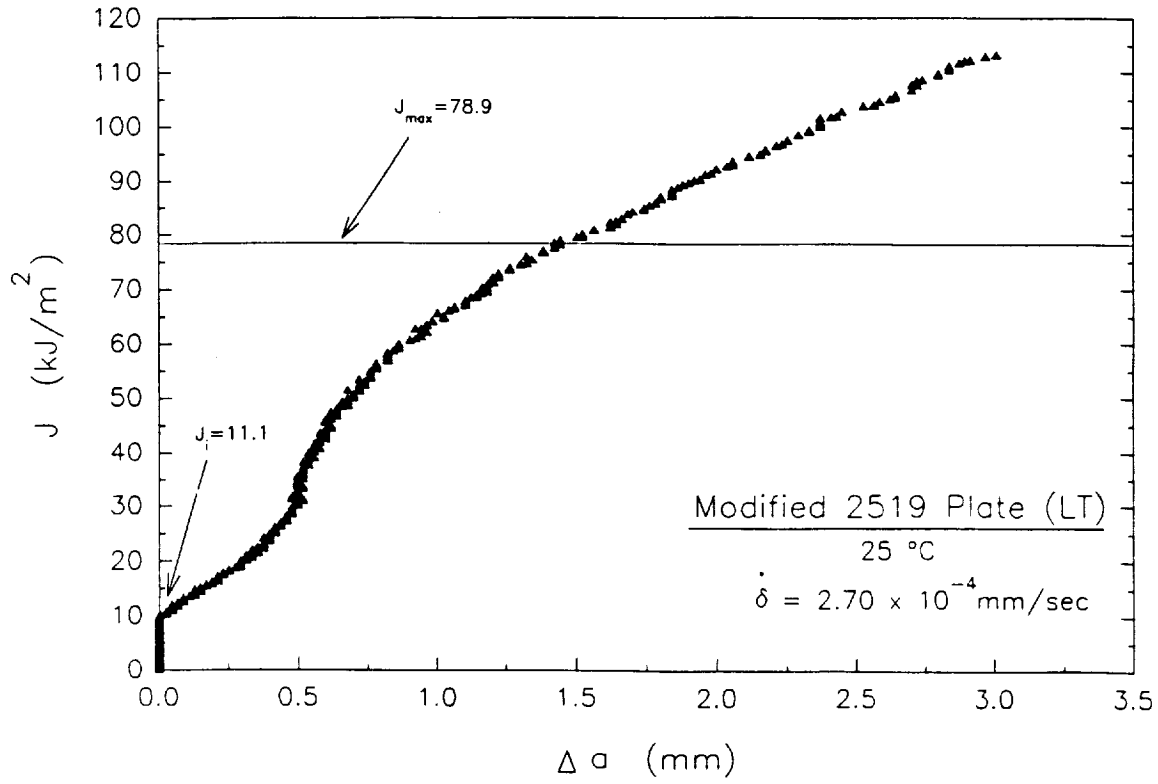

Figure 5 Applied J versus crack extension for Mg + Ag modified I/M AA2519 at 25°C and a grip displacement rate of 2.7 x 10^{-4} mm/sec.

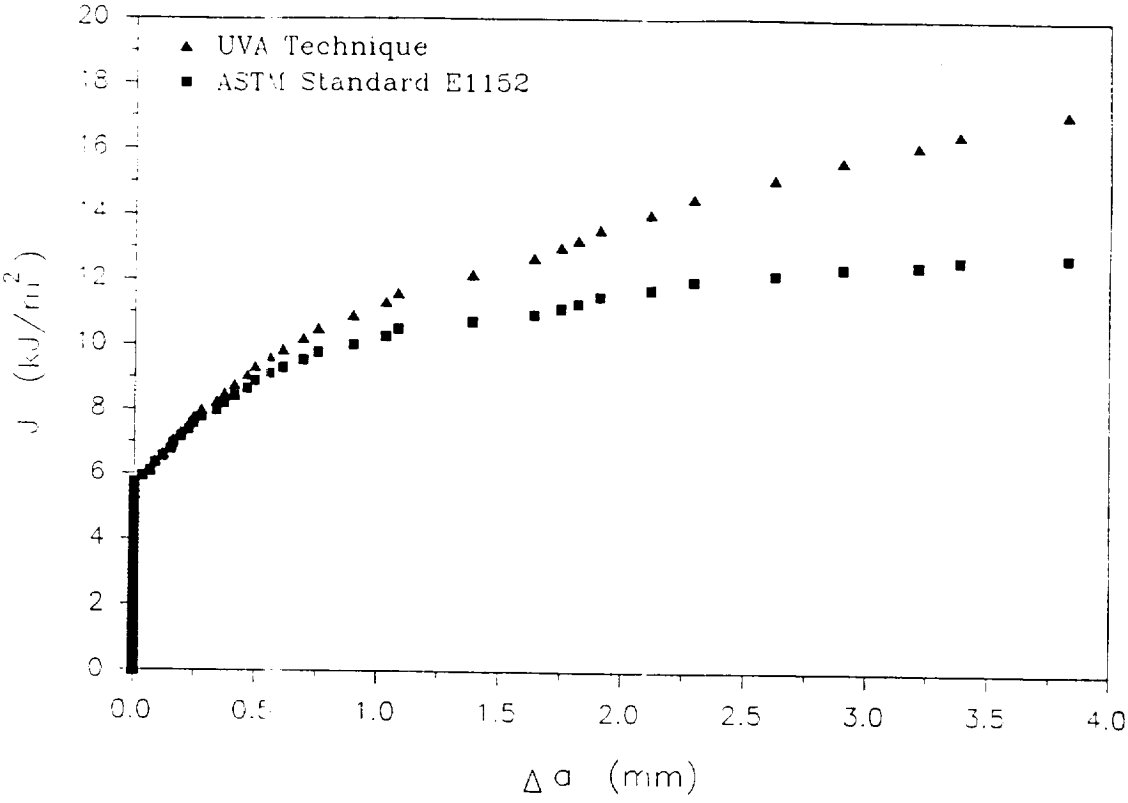

Figure 6 Comparison of J versus Δa results for a single experiment with AA2618, but calculated by two methods; ASTM Standard 1152 compared to a procedure employed at UVa.

Project #3 **Cryogenic Temperature Effects on the Deformation and Fracture of Al-Li-Cu and Al-Li-Cu-In Alloys**

John A. Wagner and R.P. Gangloff

Objective

The objective of this PhD research is to characterize and optimize the crack initiation and growth fracture resistances of Al-Li-Cu and Al-Li-Cu-In alloys for possible cryogenic propellent tank applications. The aim of the program is to understand microscopic fracture mechanisms as influenced by temperature, stress state and microstructure.

Approach

The approach to this objective was outlined in the proposal for the 1992 LA^2ST Program[1]. In summary our approach focuses on several areas including: (1) produce experimental Al-Li-Cu-Zr alloys with and without indium additions, (2) characterize both experimental Al-Li-Cu-Zr alloys and commercially available 2090-T81 plate, (3) implement J-integral fracture mechanics methods to measure crack initiation and propagation resistance for plane stress and plane strain conditions at ambient and cryogenic temperatures, (4) establish the effect of temperature, stress state and microstructure on fracture toughness, (5) analyze fracture surfaces and correlate fracture features with grain structure, and (6) develop and apply advanced mechanical test and metallographic techniques to investigate the deformation and fracture processes that are relevant to crack initiation and growth toughnesses.

Research Progress and Results

As documented in the last progress report[2], TEM of indium modified 2090 in the T6 condition indicated that, qualitatively, indium additions increased the number density of the T_1 strengthening phase, but indium had no measurable effect on 0.2% offset yield strength. Furthermore, work hardening, elongation and crack initiation and growth toughnesses decreased at cryogenic temperatures for 2090+In-T6. Fracture was characterized by intersubgranular (ISG) failure. Therefore, because of the insensitivity of yield strength to indium additions and the low cryogenic ductility and toughness of 2090+In-T6, the research

conducted during this reporting period focused on mechanisms of fracture for 2090-T81 plate under varying levels of crack tip constraint at 25 and -185°C. Progress over the last year is summarized below.

Recent Results

Mechanical Testing

Uniaxial tensile tests were conducted on 6.35 mm diameter specimens according to ASTM Standard E8-87. Specimens were machined about the plate midplane thickness in the longitudinal direction and had a 30.2 mm gage length. Elongation over a 25.4 mm gage length was determined using back-to-back extensometers. Work hardening exponents were determined according to ASTM standard E646-78 over the stress-plastic strain range prior to the onset of necking.

Fracture toughness behavior was determined by conducting elastic-plastic J-Integral fracture toughness experiments which conformed to ASTM Standards E 813-89 and E 1152-87, and employed the single specimen unloading compliance technique. Compact tension specimens 1.6 mm and 12.0 mm thick, the latter with 1.2 mm deep side grooves, were machined from the midplane of the plate in the LT orientation. The J-Integral technique was first applied to steels specimens exhibiting large scale plasticity to determine initiation toughness[3]. This technique assumes that in specimens primarily under plane stress constraint, the initiation toughness is under plane strain conditions if (W-a) and B are both greater than $25(J_{Ic}/\sigma_{ys})$ where W is specimen width, a is crack length, B is specimen thickness and σ_{ys} is uniaxial yield strength. It was speculated that applying the J-Integral technique to 2090-T81 Al-Li alloys would result in the same initiation toughness for 1.6 mm and 12.0 mm thick specimens. Further details of the test procedures have been reported previously[4].

Uniaxial Tensile Properties

Table I presents the results of uniaxial tensile tests at ambient and cryogenic temperatures. Each test represents an average of a minimum of two tests. The longitudinal tensile properties of 2090-T81 at 25°C are outstanding and consistent with the results of an independent investigation on the same lot of material[5,6]. At -185°C, there is an increase in strength, elongation, modulus and work hardening typical of 2090 type alloys in the near peak aged (T81) condition. The increase in elongation at -185°C is associated with an increase in stable deformation and work hardening prior to necking since the strain to failure

after geometric instability only slightly increases from ambient to cryogenic temperatures[7]. Specimens tested at -185°C also exhibited significantly more delamination along grain boundaries parallel to the loading direction compared to tests conducted at 25°C.

The reported values for work hardening exponent are in reasonable agreement with other investigations[8]. The increase in work hardening at -185°C has generally been associated with wider, more closely spaced slip bands and therefore more homogeneous, less intense deformation[9,10]. More homogeneous deformation allows for more strain to be accumulated in the deformation process, thus postponing the onset of localized plastic instability and fracture.

Fracture Toughness Results

Table II summarizes the results of fracture toughness testing at 25°C and -185°C for 1.6 and 12.0 mm thick specimens of AA2090 in the LT orientation. Again the values represent the average of at least two tests. Figure 1 presents typical R-curves for the two thicknesses and two test temperatures. K_{Ic} values were calculated from measured J_{Ic} using the relationship $K_{Ic}=(J_{Ic}E/(1-v)^2)^{1/2}$ where E is Young's modulus and v is Poisson's ratio. Tearing modulus, T_R, was used to assess the materials resistance to stable crack growth after crack initiation and was determined from the relationship $T_R=(E/\sigma_o)dJ/d\Delta a$ where σ_o is the flow stress and $dJ/d\Delta a$ is the slope of the J-Δa curve in the region of stable crack growth[11].

Effect of Stress State: With reference to Table II and Figure 1, at ambient temperature 1.6 mm thick specimens exhibit higher initiation and growth toughnesses compared to 12.0 mm thick specimens. The more steeply rising R-curve, which is reflected in a higher tearing modulus for the 1.6 mm thick specimen, is expected and is attributed to thin sheet "plane stress" fracture during stable crack growth. The difference in the initiation toughness of the two thicknesses was not, however, expected since $25(J_{Ic}/\sigma_{ys}) \approx 0.6$ mm which implies that 1.6 mm thick specimens were of sufficient thickness to provide valid J_{Ic} results typical of plane strain constraint.

The higher initiation toughness of the 1.6 mm specimen can be attributed to a change in fracture mode, and possibly microscopic mechanism, compared to the thicker 12.0 mm specimen. Figure 2a is a full thickness cross section of a 12.0 mm thick fracture toughness specimen tested at 25° C. The primary fracture mode is transgranular shear (TGS) which crosses numerous grains before arresting at a delamination. The presence of the delaminations promotes the TGS fracture mode which is typified by the "apparent K_{IC}" of

33.7 MPa$\sqrt{m}$. This toughness is not a geometry independent value typical of predominant plane strain constraint, and would not be produced in a thicker specimen (viz, without delamination). Delaminations which are perpendicular to the primary crack growth plane occur along high angle boundaries, presumably prior to the initial crack advance[8], and relieve some of the triaxial constraint in the thick specimen. Such delaminations may also provide the geometry necessary for highly localized shear instability in a planar slip alloy such as Al-Li-Cu.

For the 1.6 mm specimen, Figure 2b, through thickness stresses are lower and there are no delaminations along high angle boundaries. Failure in the center of the specimen is flat compared to the macroscopic TGS near the free surface, suggesting plane strain crack initiation at the onset of stable cracking. It is possible that the microscopic fracture mechanism for the flat mode is different from that of TGS. This flat fracture process is probably well described by a plane strain initiation toughness (K_{IC}) of 30.4 MPa$\sqrt{m}$. It appears that the 1.6 mm specimen was of sufficient size to provide a valid J_{Ic} and K_{IC}. It is not possible to compare the initiation toughnesses from the two specimen thicknesses because of the delamination induced fracture mode (and microscopic mechanism) transition to the localized shear process. This complication is not observed for steels which fracture by microvoid processes for both the flat and slant modes, albeit at different local strains for the different stress states.

At -185°C, the initiation and growth toughnesses of 2090-T81 specimens of two different thicknesses are almost identical. The average J_{Ic} for 1.6 mm specimens was 16.8 kJ/m^2 compared to 16.1 kJ/m^2 for 12.0 mm specimens, and the average T_R for 1.6 mm specimens was 3.1 compared to 2.8 for the 12.0 mm specimens. The similarity in crack initiation and growth toughnesses of the two thicknesses is associated with a similarity in macroscopic fracture mode. Both specimens exhibited delaminations and TGS fracture, Figures 2c and 2d. It is probable that the microscopic fracture mechanism is identical for each thickness at the low temperature. Accordingly, the J-integral determination of plane strain crack initiation toughness is independent of thickness for the range examined.

Effect of Temperature on Toughness (1.6 mm thick specimen): For 1.6 mm thick specimens, there is a modest increase in both J_{IC} and T_R for fracture at -185°C compared to 25°C. These results are in contrast to work by Rao et. al.[12] who observed a decrease in the initiation toughness of 1.6 mm thick 2090-T83 sheet compared to 12.7 mm plate when testing

at cryogenic temperatures, however, the microstructure of the sheet was recrystallized making it difficult to compare to the results of unrecrystallized plate. In the current investigation, 1.6 mm specimens machined from unrecrystallized plate exhibited a slight increase in toughness at -185°C and the fracture mode changed to one of TGS with some small delaminations, Figure 2d. The occurrence of some delaminations along with TGS fracture at -185°C may be related to the increased cryogenic yield strength promoting elevated through thickness stresses and to weakened boundaries at the cryogenic temperatures[13]. This effect may have been countered, insufficiently, by increasing work hardening and therefore decreasing tendency for shear localization with decreasing temperature.

Effect of Temperature on Toughness (12.0 mm thick specimen): Similar to the results for 1.6 mm specimens, 12.0 mm specimens exhibit an increase in both the initiation and growth toughnesses at cryogenic temperatures. However, the magnitude in the increase of J_{Ic} and T_R for the 12.0 mm specimens from 25°C to -185°C is significantly greater compared to 1.6 mm specimens. J_{Ic} increased by about 55% and T_R increased by 115% when tests were conducted at -185°C. The large increase in the crack initiation and growth toughnesses of 12.0 mm specimens was accompanied by a significant increase in the number and depth of delaminations along grain boundaries, Figure 2c compared to Figure 2a, similar to observations of others[8]. Furthermore, at the cryogenic temperature there was more of a tendency for deformation and fracture to be more "localized" within individual grains as explained below.

Fracture Morphology

The 2090-T81 plate studied in this investigation exhibited four fracture modes when tested at -185°C: intersubgranular (ISG) fracture, slip band cracking (SBC), delaminations, and TGS fracture which are shown in Figures 3 and 4. Figure 3 shows matched pairs of SEM fractographs together with the corresponding etched cross sections of the grain structure with 3b being a higher magnification of 3a. On the left side of each cross section in Figure 3 is a region of heavily decorated substructure as suggested by the etched boundaries. Fracture in areas which had a well defined substructure, in general, was characterized by ISG fracture and is consistent with the results of Dorward who observed a propensity for ISG fracture near the surface of 2090 sheet where substructure was most pronounced[14,15]. TEM analysis of the boundary particles revealed that they were primarily the T_1 (Al_2Cu Li) phase.

On the right side of the cross sections in Figure 3 is a region where fracture has been

confined to a single grain in which the subboundaries are, in comparison, not decorated. The "shear" failure which occurs within individual grains is most probably slip band cracking generally parallel to {111} planes[10,16]. There is more of a tendency for this type of fracture to occur in 2090-T81 at cryogenic temperature. Precise identification of slip band cracking during fracture toughness loading is lacking, and the "facets" are substantially rougher compared to fatigue cracking which was unambiguously shown to form {111} facets; see Project #1. The rough facets in Figure 3 may be due to the high level of crack tip deformation that accompanies crack growth.

Delaminations and a broad TGS fracture are shown in Figure 4. The location marked A in the photomicrograph shows a single grain with a fracture surface facet ending at a small delamination associated with a high angle boundary. This facet may be a {111} slip plane crack. Location B is a region of TGS fracture and the shear fracture propagates across several boundaries before arresting. The initiation of TGS fracture in this alloy probably occurred when slip bands within a single grain strain hardened internally to such a degree that the ductility of the band material is exhausted[17]; fracture occurs within the band or at the band-matrix interface. Once initiated, the driving force for continued propagation is high and TGS fracture propagates across several grains. The probability of the majority of grains within a TGS region having the same orientation is low and suggests that the propagation of localized deformation and cracking in the TGS region does not occur by cooperative SBC solely parallel to {111} planes within individual but highly textured grains.

Metallographic Examination

To qualitatively examine the orientation of grains in the region of fracture where TGS was the dominate fracture mode, cross sections of 12 mm specimens tested at 25°C were electroetched and examined in cross-polarized light, or electropolished and examined in the SEM backscattered electron (BSe-) mode. Electroetched specimens were prepared by hand polishing with 0.05 micron colloidal silica, and electroetching in boric acid modified Barker's reagent. Electropolished specimens were prepared by hand polishing to a 0.05 micron finish and electropolished in a mixture of 33 volume percent nitric acid in methanol.

Differences in grain orientation appear as differences in the color of the grains for the polarized light case[18] and as differences in contrast for the BSe- mode[19]. Figure 5 presents BSe- and polarized light photomicrographs of the intersection of a TGS fracture surface with the underlying grain structure. The figure shows that in the region of TGS fracture, several

grains of apparently differing orientation are traversed by a shear crack. This observation lends credence to the hypothesis that failure in this region occurred primarily by macroscopic shearing and not microscopic SBC.

Recent Conclusions

1. Tensile strength, elongation, elastic modulus and work hardening behavior of 2090-T81 increase at -185°C.
2. The difference in the J_{IC} initiation toughness of 1.6 and 12.0 mm thick specimens at 25°C is associated with a change in macroscopic and microscopic fracture modes. Specimens 12.0 mm thick exhibit delamination coupled with transgranular localized shear fracture behavior. Flat fracture is observed for the thinner specimens which did not delaminate.
3. Equal initiation and growth toughnesses are observed for the thick and thin specimens of 2090 at -185°C; here, a common fracture mode is operative.
4. Both 1.6 and 12.0 mm specimens from peak aged 2090 plate exhibit an increase in crack initiation and growth toughnesses at -185°C. The magnitude of the increase in toughness is much greater for 12.0 mm specimens.
5. Fracture in 2090-T81 is characterized by four fracture modes: intersubgranular, slip band cracking, delamination and transgranular shear fracture.
6. At -185°C, there is an increased incidence of delamination fracture and increased tendency for fracture to be confined within individual grains.

Future Direction

Interrupted notched tensile tests will be conducted at 25 and -185°C to examine the progression of localized SBC and TGS fracture in 2090-T81. Mechanisms which govern the nucleation of slip band cracking and transgranular shear fracture in 2090-T81 plate will be investigated. Results will be reported in an appropriate journal.

References

1. R.P. Gangloff, "NASA-UVA Light Aerospace Alloy and Structures Technology Program", University of Virginia, Proposal No. MS NASA/LaRC-5219-92, October, 1991.

2. R.P. Gangloff, "NASA-UVA Light Aerospace Alloy and Structures Technology Program", University of Virginia Report No. UVA/528266/MS91/108, July, 1991.

3. J.D. Landes and J.A. Begley: in Developments in Fracture Mechanics Test Methods Standardization, ASTM STP 632, ASTM, Philadelphia, PA, 1976, pp. 57-81.

4. J.A. Wagner and R.P. Gangloff: Scripta Metall., 1992, vol. 26, pp. 1779-1784.

5. P.T. Purtscher and E.S. Drexler: in Light-Weight Alloys for Aerospace Application II, E.W. Lee and N.J. Kim, eds., TMS-AIME, Warrendale, PA, 1991, pp. 65-75.

6. R.P. Reed et al.: Phillips Laboratory Report No. PL-TR-91-3073, Boulder, CO, 1991.

7. D. Yao, D. Chu and J.W. Morris, Jr.: in Light-Weight Alloys for Aerospace Application II, E.W. Lee and N.J. Kim, eds., TMS-AIME, Warrendale, Pa, 1991.

8. K.T. Venkateswara Rao and R.O. Ritchie: Acta Metall., vol. 38, No. 11, 1990, pp. 2309-2326.

9. J. Glazer, S.L. Verzasconi, R.R. Sawtell and J.W. Morris, Jr.: Metall. Trans. A, 1987, vol. 18A, pp. 1695-1701.

10. K.V. Jata and E.A. Starke: Metall. Trans. A, 1986, vol. 17A, pp. 1011-1026.

11. P.A. Paris, H. Tada, A. Zahoor and H. Ernst: in Elastic-Plastic Fracture, ASTM STP 668, Philadelphia, PA, 1979, pp. 5-36.

12. K.T. Venkateswara Rao and R.O. Ritchie: Scripta Metall., vol. 23, 1989, pp. 1129-1134.

13. R.C. Dorward: Scripta Metall., 1986, vol. 20, pp. 1379-1383.

14. R.C. Dorward: J. Mater. Sci. Let., 1986, vol. 5, pp. 1015-1018.

15. R.C. Dorward: in Advances in Fracture Research, K. Salama, et al., eds., Pergamon Press, Oxford, UK, 1989, pp. 2413-2422.

16. K.V. Jata and E.A. Starke, Jr.: Scripta Metall., 1988, vol. 22, pp. 1553-1556.

17. G. Terlinde and G. Luetjering: Metall. Trans. A, vol. 13A, p. 1283.

18. P.N. Kalu and F.J. Humphreys: in Proc. Int. Conf. on Aluminum Technology, 1986, pp. 197-203.

19. R. Crooks, P.N. Kalu and T.R. McNelley: Scripta Metall., 1991, vol. 25, pp. 1321-1325.

Table I. Longitudinal tensile properties of 2090-T81 at 25°C and -185°C

	25°C	-185°C
Ultimate strength (MPa)	605	727
Yield strength (MPa)	577	632
% elongation	7.0	8.7
Modulus (GPa)	77.9	87.6
Work hardening exponent, n $\sigma = K\varepsilon_p^n$	0.047	0.091

Table II. Fracture toughness of 2090-T81

	B = 1.6 mm		B = 12.0 mm	
	25°C	-185°C	25°C	-185°C
J_{IC} (kJ/m^2)	14.4	16.8	10.4	16.1
K_{IC} (MPa$\sqrt{m}$)	33.7	37.1	30.4	38.4
T_R	2.9	3.1	1.3	2.8

R-CURVES FOR 2090-T81 SPECIMENS

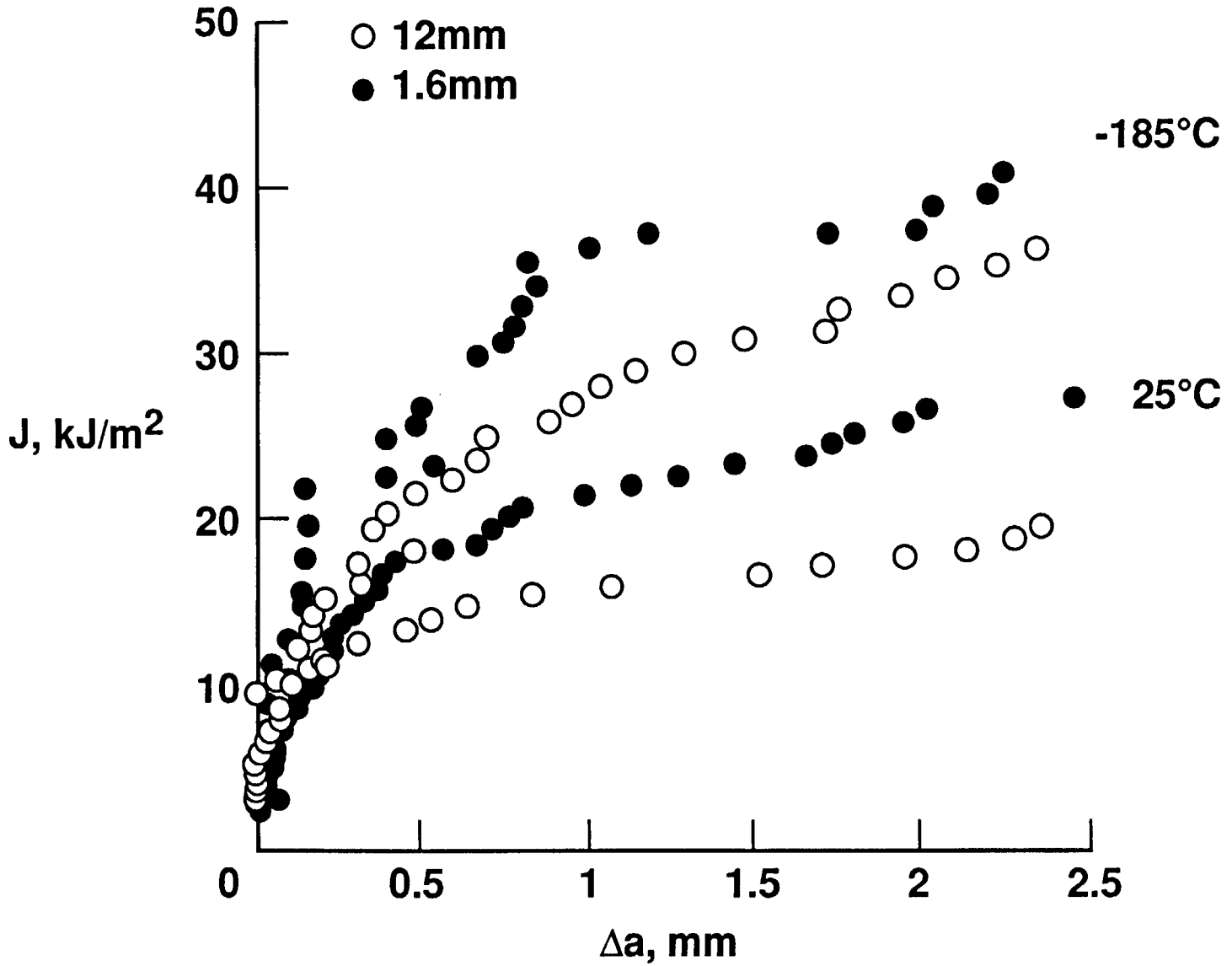

Figure 1

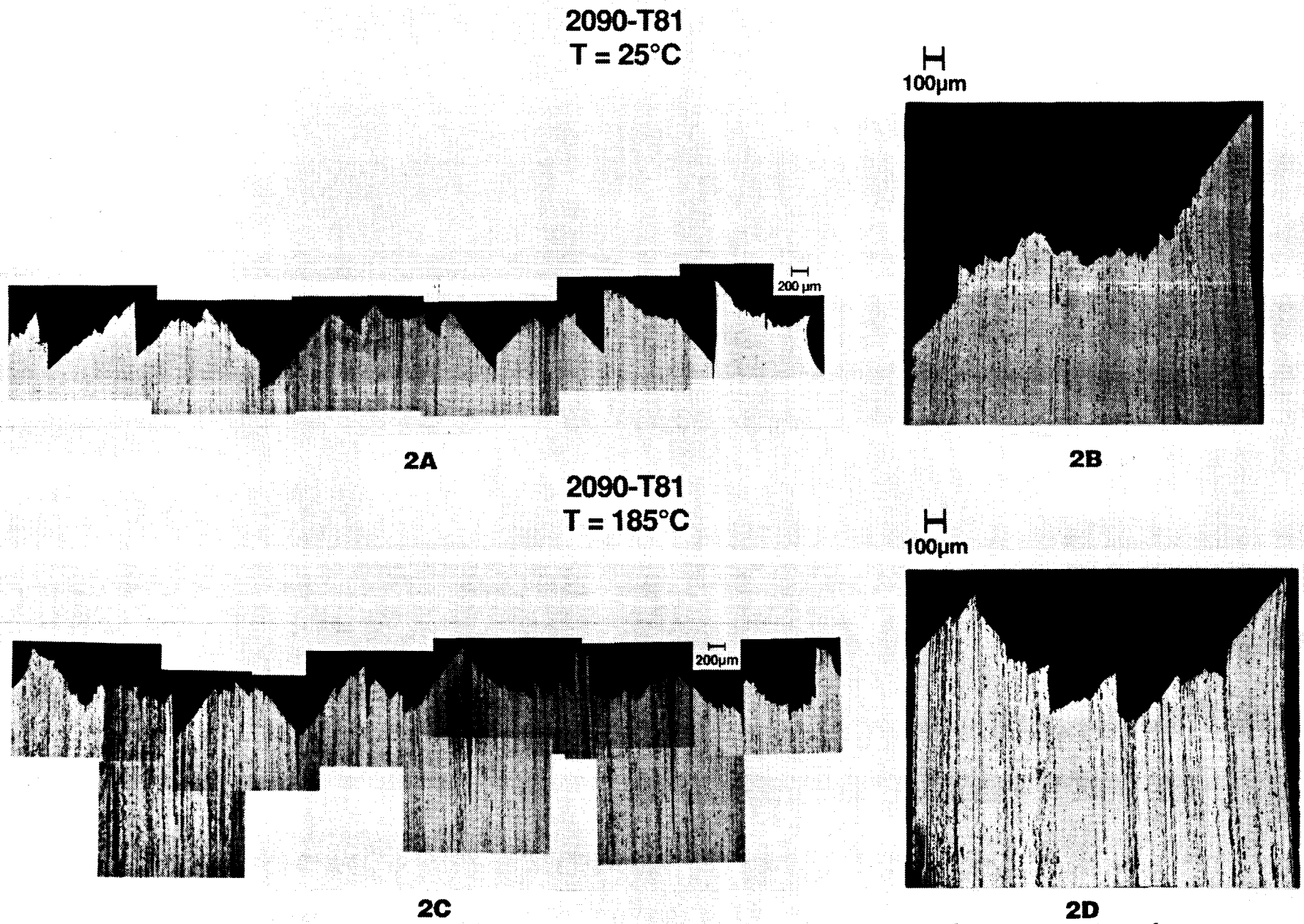

Figure 2. Metallographic sections of 2090-T81 perpendicular to crack growth direction.

INTERSUBGRANULAR FRACTURE AND AND SLIP BAND CRACKING 2090-T81

3A

40µm

3B

10µm

Figure 3

TRANSGRANULAR SHEAR FRACTURE IN 2090-T81 AT -185°C

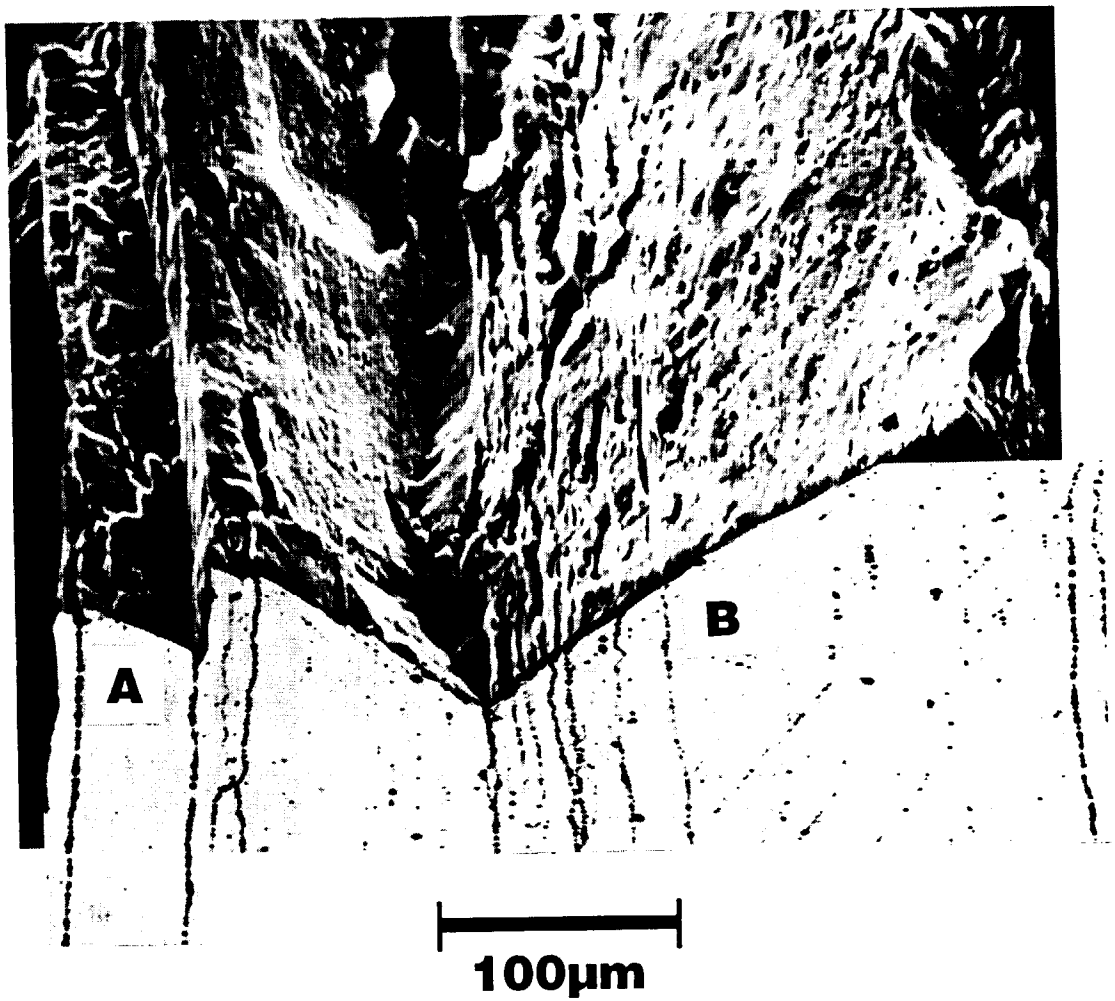

Figure 4

paste up Fig 4

CROSS SECTIONS OF TRANSGRANULAR SHEAR FRACTURE REGION IN 2090-T81

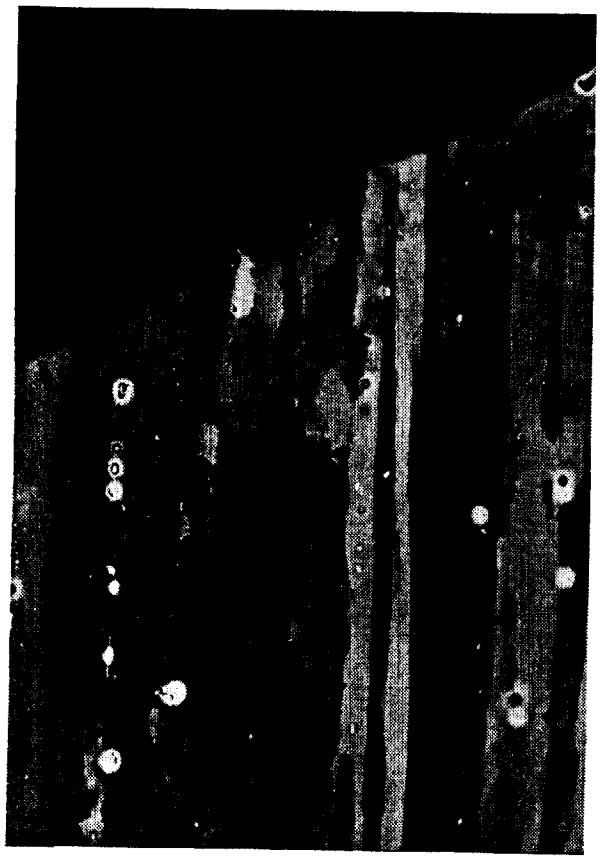

20μm

Backscattered electron image

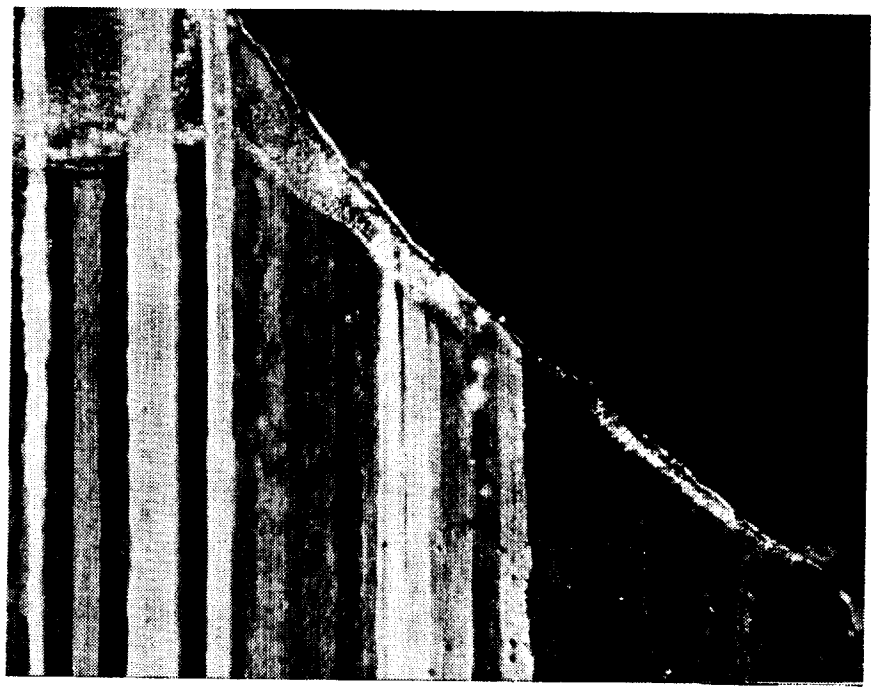

10μm

Cross polarized light image

Figure 5

Project #4 **The Effect of Cryogenic Temperature on the Fracture Toughness of Weldalite™ X2095**

Cynthia L. Lach and Richard P. Gangloff

Objective

The objective of this research is to characterize the effect of cryogenic to mildly elevated temperature on the tensile fracture toughness of an emerging composition of Weldalite™-type alloys. We will determine quantitative initiation and growth fracture toughness data, and associated microscopic fracture mechanisms.

Background

Aluminum-lithium-copper alloys are being developed to replace conventional 2XXX and 7XXX aluminum alloys in aerospace structures. Al-Li-Cu alloys such as 2090 offer increased stiffness and decreased density due to lithium, and exhibit increased strength and potentially increased fracture toughness with decreasing temperature from room to cryogenic levels[1-4]. Increasing toughness at cryogenic temperatures facilitates fracture mechanics damage tolerant designs because cold proof-testing is not required; a room temperature evaluation suffices. With the addition of elements such as Ag, Al-Li-Cu alloys exhibit exceptionally high yield strength, that further increases with decreasing temperature[5], without the necessity for post-solution treatment stretch deformation[6]. The fracture toughness of such alloy compositions must be understood.

Technical Approach

The approach to this research was outlined in past renewal proposals[7,8].

Material

Two Weldalite™ X2095 compositions were selected for study to examine the limits of the Li and Cu levels for the alloy designated X2095. Specifically, a high Cu-Li alloy (Al-4.64Cu-1.53Li-0.34Ag-0.37Mg-0.17Zr; wt%) and a low Cu-Li alloy (Al-4.04Cu-1.00Li-0.37Ag-0.36Mg-0.15Zr; wt%) were chosen for evaluation.

The expectation is that the selected alloys will contain substantially different amounts of primary phase to enable examination of the effect of this feature on temperature dependent

fracture toughness. Several artificial aging conditions, conducted at NASA-LaRC, will be employed to vary yield strength, work hardening rate, and the volume fraction and distribution of the δ' and T_1 strengthening precipitates. Metallurgical effects on toughness will be assessed for similar flow properties.

Deformation and Fracture

The approach of the proposed research will follow that developed by Wagner in Project #3. Measurements will produce uniaxial tensile stress-strain relationships and J-Integral based crack initiation and growth fracture toughness. This latter method will enable determination of plane strain fracture toughness data from relatively thin plates (eg. 3.9 mm thick). Yield strength, work hardening rate, K_{IC} and R-curve data will be obtained. Microstructural effects on the complete crack initiation and growth resistance relationship will be studied.

Proposed Research

With these Weldalite™ compositions and the compact tension J-Δa method, two of the original three areas will be sequentially examined. Initially, fracture toughness measurements with each X2095 variant will be obtained at 25°C and a single cryogenic temperature. The effect of alloy composition and aging treatment will be determined in this phase. The original research plan proposed to study the effect of compact tension (C(T)) specimen thickness on the R-curve. However, due to the inhomogeneity of the low Cu-Li alloy plate, this portion of the investigation was eliminated. The final phase of the work will emphasize a detailed characterization of the effect of temperature from -185°C to about 125°C for a single composition and heat treatment of X2095.

Fracture Toughness at 25°C and -185°C

The goal of these experiments is to characterize the crack initiation and growth resistance, and associated microscopic fracture modes, for Weldalite™ X2095 at ambient and a single cryogenic temperature of -185°C. Both K_{IC}, from J at the onset of crack growth, and the tearing modulus from $dJ/d\Delta a$ will be measured with the 3.9 mm thick C(T) specimen. The R-curve will be determined for each of the two Weldalite™ X2095 compositional variants; aged at 143°C for 10, 20, 30 and 72 hours; to determine the interactive effects of yield strength, work hardening, subgrain boundary T_1 and δ' precipitation (for the high Cu-Li alloy).

Effect of Cryogenic Temperature on Fracture Toughness

The objective of these experiments is to determine the effect of cryogenic temperature on the fracture toughness and microscopic fracture processes for Weldalite™ X2095. The low Cu-Li alloy will be tested at the aging condition that provides the best toughness (according to Reynolds Metals, 143°C for 20 hours). The full J-Δa relationship will be measured, with 3.9 mm thick C(T) specimens at several temperatures (viz, -185, -125, -75, -25, 25, 75, and 125°C). Tensile yield strength, work hardening and fracture strain will be characterized as a function of temperature for the constant alloy composition and age of the toughness-temperature study. The fracture surfaces will be examined by SEM and quantitative analysis.

Progress During The Reporting Period

The as-received microstructure of the 4.0%Cu-1.0%Li and the 4.6%Cu-1.5%Li variants of Weldalite™ X2095 were characterized using polarized light microscopy. The through thickness grain structures of the rolled 12.7 mm thick plates of each composition are shown in Figure 1. The thickness direction in the plate is vertical. The following observations are made:

- oo The through-thickness grain structure of the low Cu-Li alloy is inhomogeneous. The mid-plane microstructure of the plate is completely unrecrystallized. From the mid-plane toward the outer surfaces, the plate exhibits a mixture of unrecrystallized and recrystallized grain structures. At the outer surfaces, the microstructure is completely recrystallized.
- oo The microstructure of the high Cu-Li alloy is essentially recrystallized throughout the entire cross-section of the plate. This is unexpected given the presence of Zr in the alloy and the general result that hot rolled Al-Li-Cu alloys such as 2090 are typically unrecrystallized.
- oo Previous X-ray pole figure results[9] provided by the Alcoa Technical Center showed the presence of strong brass-type texture components, at least at the plate mid-plane. These data lead to the initial conclusion that each plate was similarly unrecrystallized[9]. Considering the metallographic results in Figures 1 and 2, only the low Cu-Li variant is unrecrystallized.

The two Weldalite™ X2095 plates were commercially produced and presumably underwent identical thermomechanical processing procedures; thus, a modest change in chemistry and perhaps processing (e.g., time, temperature and reduction schedule) produced a completely different plate microstructure. This behavior, as well as the metallographic and pole figure observations, can be rationalized. A significant amount of primary copper rich phase was probably present during hot rolling of the higher copper alloy. Such particles could cause localized plastic deformation in the adjacent matrix, and hence act as nucleation centers for recrystallization during heating or rolling. Since the volume fraction of such sites depends on copper content and temperature, differences in the degree of recrystallization between the two alloys are reasonable. The higher copper alloy is more likely to recrystallize. Rather than a recrystallization texture, the deformation texture for the high copper variant may have been produced by one or more near-final rolling passes at relatively low temperatures. Such rolling would produce the textured grain orientations; optical metallography would not resolve the dislocation cell structures and low angle grains likely from this type of processing. In fact local areas of identical contrast for more than one "recrystallized grains" are present in Figure 2, consistent with the development of the deformation texture.

All 3.9 mm C(T) specimens were machined from the mid-plane of the 12.7 mm plates. Figure 2 shows the mid-plane grain structure for each alloy variant at 200X magnification. The mid-plane microstructure of the high Cu-Li alloy, Figure 2(a), is entirely composed of recrystallized grains. As shown in Figure 2(b), the low Cu-Li alloy had an unrecrystallized mid-plane microstructure. The cross-section of the 4.0%Cu1.0%Li C(T) specimens was entirely composed of unrecrystallized grains. Thus, the C(T) specimens for both alloy variants were homogeneous throughout their 3.9 mm cross-sectional thickness. Since the low Cu-Li alloy has an inhomogeneous through-thickness grain structure, the initial plan of examining the effect of C(T) specimen thickness on the R-curve characterization is eliminated from the research proposal.

The microstructures shown in Figure 2 are notable in that each has a similar strong deformation texture, but substantially different grain and perhaps boundary precipitate characteristics. These recrystallized and unrecrystallized microstructures may exhibit different deformation and fracture behaviors; apart from constituent particle, work hardening and yield strength differences.

The 4.6%Cu-1.5%Li and the 4.0%Cu-1.0%Li variants of Weldalite™ X2095 were characterized in terms of fracture toughness at 25 and -185°C. To investigate the effect of strength level, both alloy variants were aged at 143°C for 10, 20, 30 and 72 hours. The initial tensile and fracture toughness results were reported in Reference 8; selected fracture experiments were repeated because of uncertainties in single specimen values that clouded interpretation[8]. The following observations were obtained during the current reporting period.

- oo For the 4.6%Cu-1.5%Li alloy variant at 25°C, the plane strain fracture initiation toughnesses (K_{IC}) determined by the thin (3.9 mm) specimen R-curve method, are 31.6 and 18.2 MPa$\sqrt{m}$ for the 20 and 72 hour ages, respectively. The corresponding tearing moduli are 4.0 and 1.2. (See Table I).
- oo For the 4.6%Cu-1.5%Li alloy variant at -185°C, the plane strain fracture toughnesses (K_{IC}) are 32.1 and 23.1 MPa$\sqrt{m}$ for the 20 and 72 hour ages, respectively. The corresponding tearing moduli are 4.1 and 0.3.
- oo While good reproducibility is observed for the lower toughness, 72 hour aging condition, substantial K_{IC} variability is indicated in Table I for the 20 hour age at each fracture temperature.
- oo Considering average toughnesses, K_{IC} and T_R of the 4.6%Cu-1.5%Li alloy decrease with increasing aging time at each temperature. For each aging condition, these toughnesses are essentially constant with decreasing temperature from 25 to -185°C. There is no evidence for decreased toughness with decreasing temperature.
- oo For each temperature and aging condition, the fracture toughnesses of the low Cu variant are substantially higher than the values for the high Cu X2095. The initiation toughnesses, K_{IC}, of the low copper X2095 are very high compared to other wrought aluminum alloys at the 550 to 700 MPa yield strength levels[9].
- oo For the 4.0%Cu-1.0%Li alloy variant at 25°C, the plane strain fracture toughnesses (K_{IC}) are 59.2, 51.9, 73.0 MPa$\sqrt{m}$ for the 20, 30 and 72 hour ages, respectively. The corresponding tearing moduli are 5.9, 14.5 and 5.4.
- oo For the 4.0%Cu-1.0%Li alloy variant at -185°C, K_{IC} equals 84.8 MPa$\sqrt{m}$ for the 20 hour age. The corresponding tearing modulus is 2.0.
- oo At 25°C, K_{IC} and T_R are broadly constant with increasing aging time and hence σ_{ys}. The expected decline in K_{IC} due to increased precipitation hardening may have been

obscured by variability in the data.

- oo At -185°C the fracture toughness and tearing resistance of the 4.0%Cu-1.0%Li alloy variant decrease with increasing aging times.
- oo For the short aging times (10 and 20 hours), the toughnesses of the low Cu variant of X2095 do not appear to decrease with decreasing temperature. This undesirable trend is suggested for the longest aging time and, critically, for the 30 hour age.

Selected fracture toughness experiments were conducted during this reporting period and compared to previous results. Figure 3 shows two 25°C J-Δa R-curves for the low Cu-Li alloy aged at 143°C for 20 hours. The recent results are plotted by open squares and are compared to the previous test results depicted by open circles. The blunting line, given by $J = 2\sigma_{ys}\Delta a$, and the arbitrary 0.2 mm offset blunting line are shown. The higher K_{IC} value of 59.2 MPa$\sqrt{m}$ compared with the initial result of 41.2 MPa$\sqrt{m}$ is not understood. Similar differences are indicated in Table I for replicate experiments with other aging conditions and for each alloy. Significant toughness variability is observed for both test temperatures. Further analysis of the fracture surface and microstructure will be conducted. Additionally, JΔa procedures were standardized largely based on laboratory experience with ductile steels. Subtle experimental factors, unique to moderate toughness aluminum alloys, may not as yet be sufficiently controlled to guarantee reproducible data. It may be notable that toughnesses, determined during the current reporting period and contained in parentheses in Table I, were in all cases but one higher than the values obtained earlier in the research[9].

Some of the experiments that were repeated showed good agreement with the previous results. As shown in Figure 4, the 25°C fracture toughness results for the low Cu-Li alloy aged at 143°C for 30 hours, the R-curves are very similar and lead to K_{IC} values of 29.0 and 33.2 MPa$\sqrt{m}$, respectively.

Due to the inconsistencies in the data presented in Table I, the fracture toughness trends that were previously cited are preliminary speculations for both alloys and test temperatures.

Tasks for the Next Reporting Period

Fracture surfaces will be examined, and the details of the J-integral test procedure and associated data analysis methods will be reviewed in order to determine the source(s) of the

variability in the fracture toughness data obtained to date.

The fracture toughness experiments will measure the J-crack growth response, based on the automated unloading compliance method, for cryogenic to ambient temperatures and above (125°C) for a single alloy composition and microstructure. Results to date indicate that the 4.0Cu-1.0Li composition aged at 30 hours provides excellent strength-toughness properties at 25°C. The 20 hour age may be more desirable considering strength and toughness at -185°C. The data in Table I suggest that toughness increases with decreasing temperature for the 20 hour age, but decreases for the 30 hour treatment. This speculation must be confirmed, once the source of the data variability is identified and eliminated, before a final condition is selected for study of the temperature effect.

The uniaxial tensile deformation behavior of Weldalite™ X2095 will be characterized at selected temperatures spanning the range from -185 to 125°C. The stress-strain relationship based on the Ramberg-Osgood power-law relation will be used to identify work hardening characteristics for uniform deformation prior to necking.

References

1. S. Suresh, A.K. Vasudevan, M. Tosten and P.R. Howell, "Microscopic and Macroscopic Aspects of Fracture in Lithium-containing Aluminum Alloys", Acta Metall., Vol.35, pp. 26-46 (1987).

2. J. Glazer, S.L. Verzasconi, R.R. Sawtell and J.W. Morris, Jr., "Mechanical Behavior of Aluminum-Lithium Alloys at Cryogenic Temperatures", Metall. Trans. A., Vol. 18A, pp. 1695-1701, (1987).

3. K.T. Venkateswara Rao, Y. Weikang and R.O. Ritchie, "Cryogenic Toughness of Commercial Aluminum-Lithium Alloys: Role of Delamination Toughening", Metall. Trans. A., Vol. 20A, pp.485-487 (1989).

4. K.V. Jata and E.A. Starke, Jr., "Fracture Toughness of Al-Li-X Alloys at Ambient and Cryogenic Temperatures", Scripta Metall., Vol. 22, pp. 1553-1556 (1988).

5. W.T. Tack and L.W. Loechel, "Weldalite TM 049: Applicability of a New High Strength, Weldable Al-Li-Cu Alloy", in Proceedings of the Fifth International Aluminum-Lithium Conference, T.H. Sanders, Jr. and E.A. Starke, Jr., eds., Vol. III, MCEP Ltd., Birmingham, UK, pp. 1457-1467 (1989).

6. Alex Cho and W. A. Cassada, "Effect of Cu and Cu:Li Ratio on T6 and T8 Temper Properties of Al-Cu-Li-Mg-Ag Alloys", Presented at Aero Mat 91, Long Beach, CA, May (1991).

7. R.P. Gangloff, "NASA-UVa Light Aerospace Alloy and Structures Technology Program", Proposal No. MS-NASA/LaRC-4841-91, University of Virginia, Charlottesville, VA (1990).

8. R.P. Gangloff, "NASA-UVa Light Aerospace Alloy and Structures Technology Program", Proposal No. MSE-NASA/LaRC-5691-93, University of Virginia, Charlottesville, VA (1992).

9. R.P. Gangloff, "NASA-UVa Light Aerospace Alloy and Structures Technology Program", UVa Report No. UVA/528266/MS93/111, July, 1992.

Table I. Fracture Toughness of Weldalite™ X2095 Alloy Variants

		25°C				-185°C			
ALLOY	143°C Age Time, hrs	JQ (E813-87), KJ/m^2	Modulus, GN/m^2	KIC, MPa m$^{1/2}$	Tearing Resistance	JQ (E813-87), KJ/m^2	Modulus, GN/m^2	KIC, MPa m$^{1/2}$	Tearing Resistance
4.6%Cu 1.5% Li	10	10.1	73.8	28.9	5.1	8.0	84.8	27.6	5.0
4.6%Cu 1.5% Li	20	6.6 (11.8) Avg=9.2	75.2	23.6 (31.6) Avg=27.6	2.4 (4.0) Avg=3.2	4.2 (10.9)	84.1	19.9 (32.1) Avg=26.0	1.8 (4.1) Avg=3.0
4.6%Cu 1.5% Li	72	2.8 (3.8) Avg=3.3	77.9	15.6 (18.2) Avg=16.9	1.0 (1.2) Avg=1.1	4.3 (5.5*)	86.2	20.4 (23.1) Avg=21.8	0.3 (0.3) Avg=0.3
4.0%Cu 1.0% Li	10	107.3*	73.1	93.8	18.1	89.8*	84.1	92.1	36.4
4.0%Cu 1.0% Li	20	20.9 (43.2) Avg=32.1	72.4	41.2 (59.2) Avg=50.2	10.0 (5.9) Avg=8.0	17.9 (77.3) Avg=47.6	82.8	40.8 (84.8) Avg=62.8	7.7 (2.0) Avg=4.9
4.0%Cu 1.0% Li	30	29.0, 15.3, 38.1 48.3 (33.2) Avg=32.8	72.4	48.5, 35.3 55.6, 62.6 (51.9) Avg=50.8	12.2, 7.0 9.4, 10.7 (14.5) Avg=10.8	17.8, 16.3 Avg=17.1	83.5	40.8, 39.1 Avg=40.0	3.4, 3.4 Avg=3.4
4.0%Cu 1.0% Li	72	(65.5)	72.4	73.0	5.4	10.5	82.8	31.2	2.9

* Calculated from JQ(Power)
(retested)

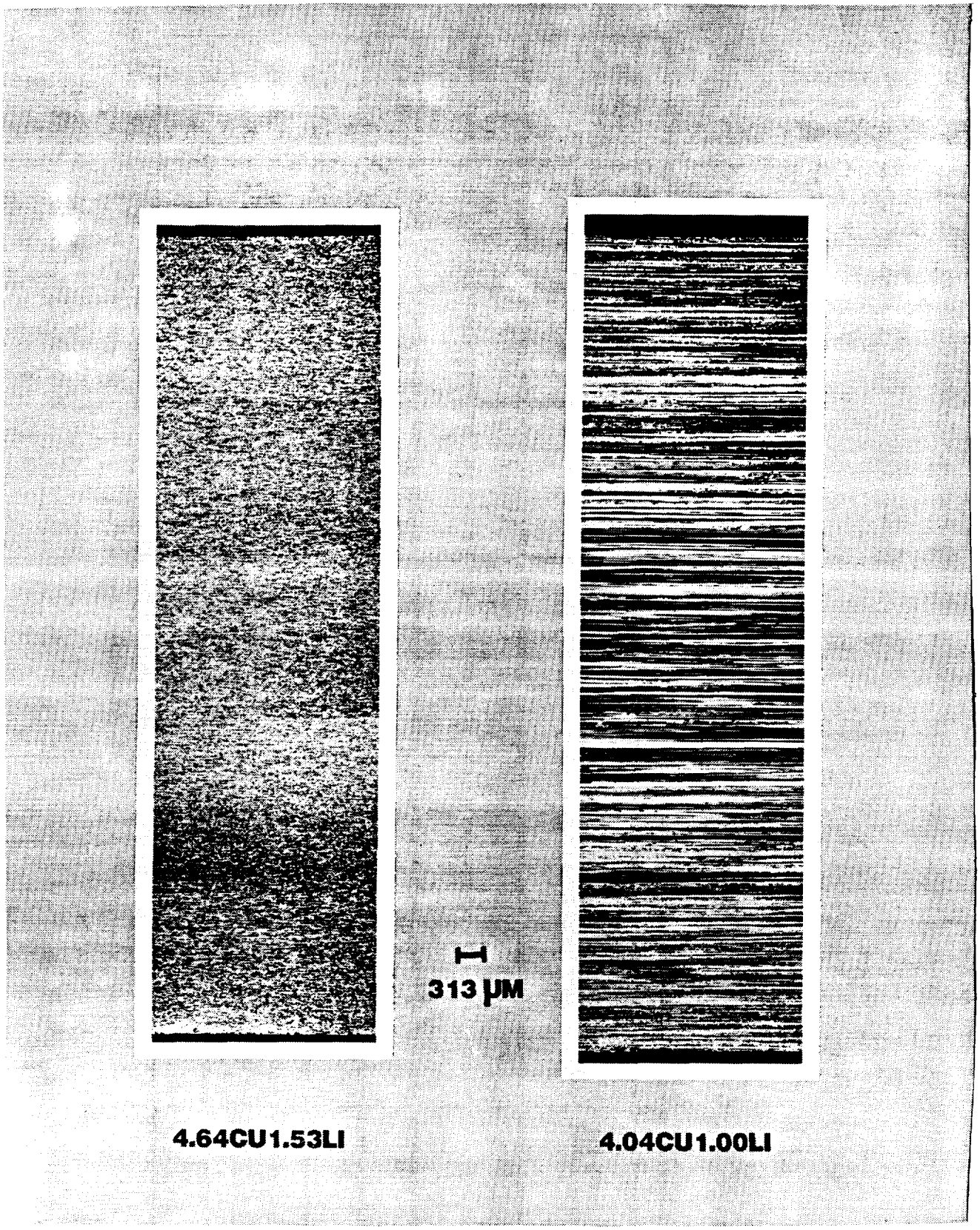

Figure 1: Through thickness grain structure of Weldalite™ X2095 alloy variants using polarized light microscopy.

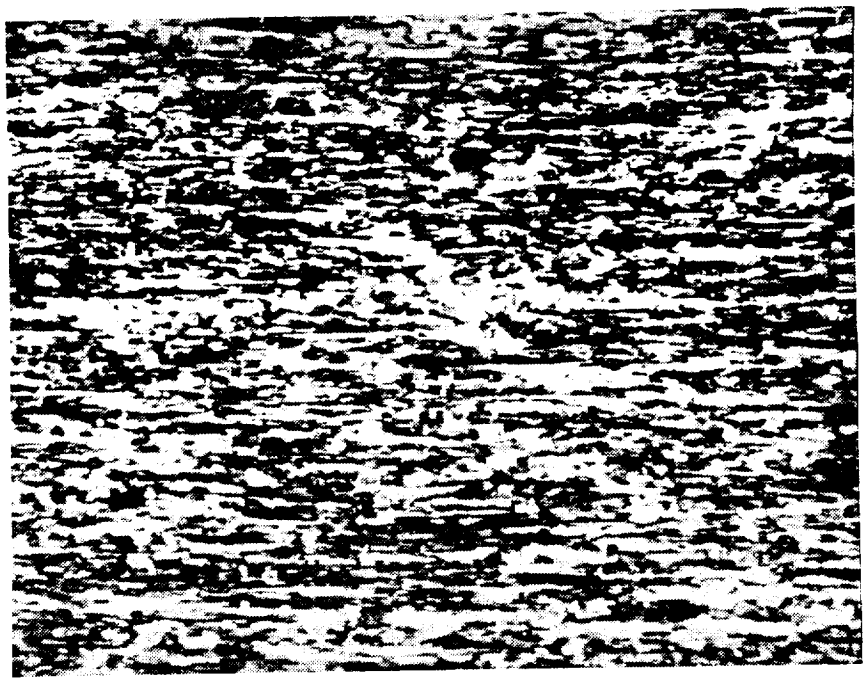

a) 100% recrystallized mid-plane grain structure of 4.6%Cu1.5%Li alloy.

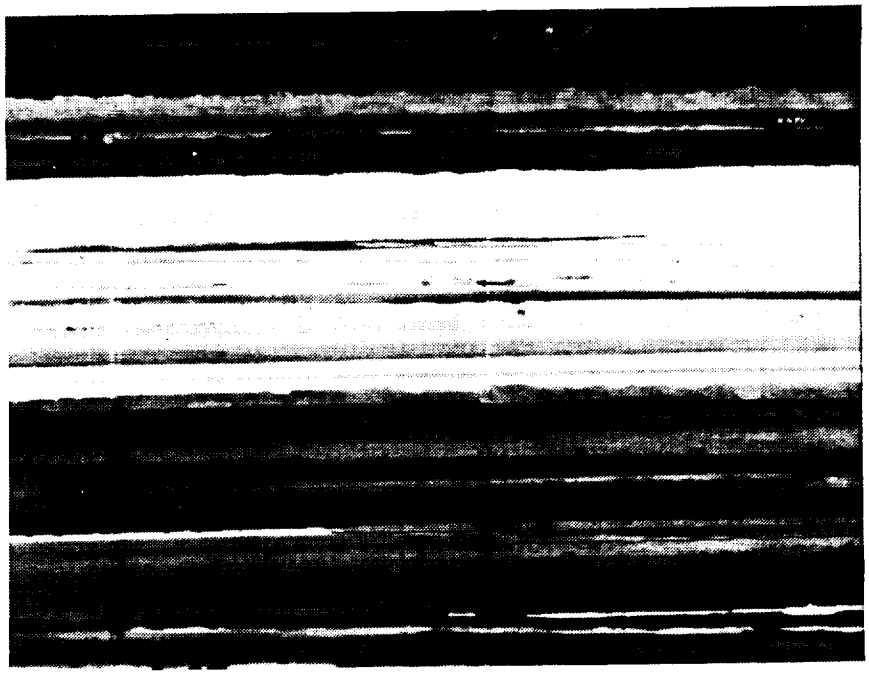

b) 100% unrecrystallized mid-plane grain structure of 4.0%Cu1.0%Li alloy.

Figure 2: Mid-plane grain structure of Weldalite™ X2095 alloy variants using polarized light microscopy (200X).

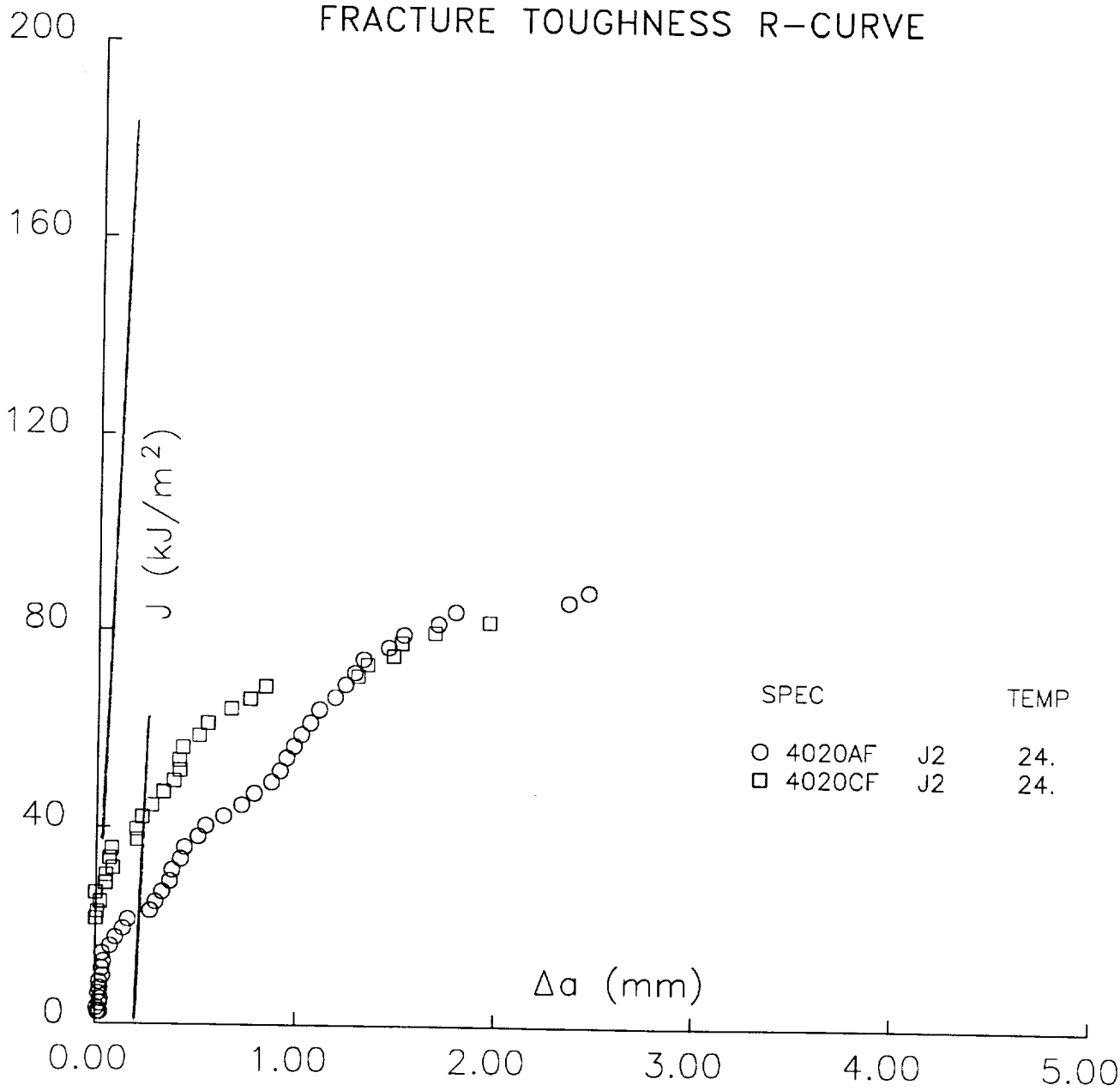

Figure 3: Fracture toughness J-Δa R-curves for 4.0%Cu-1.0%Li Weldalite™ alloy (aged at 143°C for 20 hrs) loaded at 25°C.

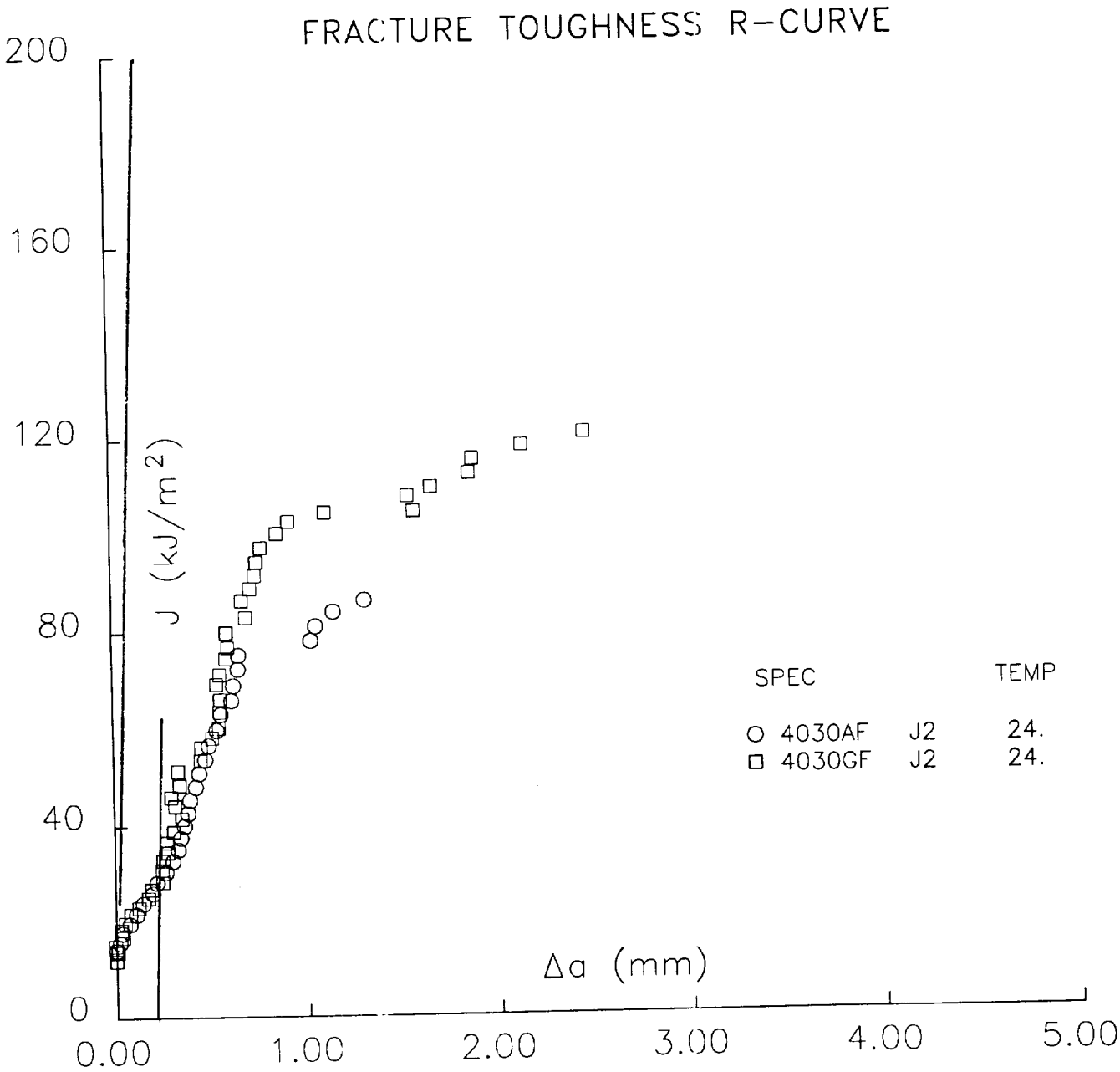

Figure 4: Fracture toughness J-Δa R-curves for 4.0%Cu-1.0%Li Weldalite^{TM} alloy (aged at 143°C for 30 hrs) loaded at 25°C.

Project #5 Mechanisms of Localized Corrosion in Alloys 2090 and X2095

F. Douglas Wall and Glenn E. Stoner

Objective

The objective of this research project is to identify the roles of microstructure and environment in the stress corrosion cracking (SCC) failure of Al-Li-Cu alloys 2090 and X2095. The recent focus has been on examination of the crack environment and the electrochemistry of subgrain boundary phases.

Background and Approach

Proposed mechanisms for the environmentally assisted cracking of high strength Al-Cu-Li alloys include embrittlement by adsorbed hydrogen[1,2] and anodic dissolution of an activated pathway[3-6]; the latter being addressed by this project.

For a sharp, active crack to propagate along a grain or subgrain boundary there must be an inhomogeneity in the microstructure which when interacting with the proper crack environment, causes some phase or region to preferentially dissolve. Likely candidates in peak-aged material include active precipitate phases, matrix material surrounding noble precipitates, copper or other solute depleted zones and precipitate free zones. Work on 2090 (Al-2 Li-2.5 Cu) by Buchheit[7] has indicated that the subgrain boundary phase T_1 (Al_2CuLi) is highly active suggesting that it may provide an active path for SCC. In order to test this supposition, constant load time-to-failure experiments were performed as a function of applied potential in a sodium chloride/lithium carbonate environment[4]. In the presence of lithium carbonate the breakaway potential (E_{br}) of the matrix phase is shifted to a more noble value while E_{br} of the T_1 phase remains essentially unaffected. It was observed that samples polarized cathodic to E_{br} of T_1 did not fail for the duration of the test whereas samples polarized anodic to this potential exhibited rapid corrosion rates and failed in less than one day. The sharp change in behavior was attributed to an activation of an anodically dissolving, subgrain boundary T_1 pathway. A criterion for rapid SCC failure was proposed as:

$$E_{br,T1} < E_{applied} < E_{br,matrix}$$

Initial work on X2095 (Al-4 Cu-1 Li-0.25 Mg-0.25 Ag) was intended to determine if this alloy was susceptible to the rapid failure criterion observed for 2090. The more homogeneous distribution and finer size of T_1 in X2095 versus that in 2090 suggested that active T_1 may be either less continuous or less confined to a sharp pathway in this alloy. Smooth short transverse tensile samples of peak aged and over aged X2095 (designated X2095-A and X2095-B respectively) were used in constant load TTF experiments in two inhibiting environments: 0.6M NaCl + 0.1M Li_2CO_3 and 0.1M NaCl + 0.1M Na_2CrO_4. Despite microstructural differences, these tempers of X2095 behaved almost identically to 2090 in terms of TTF vs applied potential.

The original constant load experiments were slightly modified for subsequent samples in that once a sample was stable (showing no signs of localized corrosion) at a given potential, mechanical flaws were initiated via scratching the metal surface with a glass rod. The result of these experiments (performed in the chromate environment) was that samples showed high corrosion rates and rapid failures after scratching at potentials where they had remained passive in the initial testing. Also from these experiments it was determined that the critical potentials where flaws would propagate differed by approximately 15 mV for the two tempers of X2095. If the active path were due to T_1 corrosion, the critical potentials for the two tempers should be indistinguishable. Also contradictory to the T_1 based active path mechanism is that the flawed samples showed rapid failures at potentials up to 65 mV cathodic to the E_{br} of T_1 reported by Buchheit[4].

A type of pathway that might exhibit a change in breakaway potential with aging time is a copper depleted zone. Galvele showed that the E_{br} of aluminum could be shifted in the noble direction, approximately 100 mV, through copper additions up to 5 w/o[3]. Thus, with the X2095 containing 4 w/o Cu, a depleted region approaching pure aluminum in the limit could have a much more active E_{br} than the surrounding matrix. Continued aging of a material might tend to further lower the Cu content in a depleted region. This may correspond to the lowering of the no failure to failure transition potential in overaged X2095 versus the underaged temper.

Initially, mechanisms based on a Cu depleted zone were discounted on the basis of potentiodynamic polarization experiments performed on 99.99 Al (to simulate the worst case of solute depletion). Polarizations performed in the chromate environment showed the E_{br} of Al to be approximately 400 mV more noble than the critical potential for transition in TTF

behavior. Likewise, in the lithium carbonate environment the E_{br} of Al was 150 mV more noble than the critical TTF potential. However, potentiodynamic polarizations on static, flat specimens may not yield the electrochemical information that is pertinent at a deforming crack tip. To better approximate the condition of material at a crack tip (bare metal exposed to solution) scratching electrode experiments were performed on potentiostatically polarized samples of 99.99 Al and solution heat treated 2090 and X2095. In these experiments the samples were held at a constant potential until stable, then scratched with a glass rod. In this manner critical potentials were observed where material changed behavior from spontaneous repassivation to propagation of corrosion. The critical potential for pure aluminum was approximately 10 to 50 mV more cathodic than the potentials where the transition in time-to-failure response occurred for all alloys tested. These data indicate that a copper depleted zone may play a role in the anodic dissolution based SCC failures of alloys 2090 and X2095.

Although the scratching electrode experiments provide a better indication of the electrochemistry of deformed material than potentiodynamic polarizations, they do not truly represent the electrochemistry of a dynamically straining material. Therefore, to compliment the scratching electrode data, straining electrode experimentation has been initiated and will be discussed in the following section of this report.

Two other areas of experimentation have been initiated during this reporting period: (1) A study of occluded environments in Al-Li-Cu alloys in an attempt to model the solution chemistry of an SCC crack, (2) Time-to-failure testing on a variety of 2090 tempers as well as on a non-lithium containing alloy to better define microstructural features which may be contributing to anodic dissolution based SCC failures.

Progress this Reporting Period

This section is divided into four subsections each addressing a particular branch of experimentation that has been performed during this reporting period.

Straining Electrode Experiments

Straining electrode experiments were performed to assess the electrochemical behavior of the matrix phase and a copper depleted region during plastic deformation. These experiments were intended to approximate the mechanical and electrochemical conditions experienced by a material at a growing SCC crack. Smooth tensile samples machined from solution heat treated 2090 were used to simulate the matrix phase and 99.99 Al was used to

represent the extreme case of copper depletion. The objective was to determine critical potentials where the materials no longer spontaneously repassivated under conditions of plastic deformation. These potentials could then be compared with critical potentials from TTF experiments for aged 2090 and X2095.

A complete matrix of experiments has not been completed at this time although representative experiments have been performed. Figure 1 shows the load and current density vs time data for both SHT 2090 and pure aluminum at an approximate strain rate of 5×10^{-5} sec^{-1} in a chloride/chromate environment at an applied potential of -0.550 V_{SCE}. The SHT material remains passive throughout the experiment, whereas the aluminum sample becomes highly active at the onset of plastic deformation and continues to rapidly corrode for the duration of the experiment. Therefore, a Cu depleted zone in an Al-Li-Cu alloy under these conditions would provide an active crack path. Consistent with these data is the previously determined result that all alloys tested in constant load under these same environmental and applied potential conditions exhibit rapid SCC failures.

Investigation of Occluded Chemistries

The electrochemical and SCC data presented thus far have been obtained in inhibiting environments. In order to substantiate the conclusions drawn from these data it is necessary to demonstrate that an inhibiting environment can be generated within an occluded cell. The data presented here represent an initial look at occluded environments with more sophisticated and comprehensive experiments to follow in the coming months.

To study pH changes in occluded chemistries Buchheit[8] used pH probes inserted into small diameter holes in 2090 filled with sodium chloride solution. The solution was observed to stabilize at an alkaline pH. Current research is aimed at beginning with similar experiments, but then performing analysis of the resulting alkaline solutions using ion chromatography (IC) and capillary electrophoresis (CE).

To generate an occluded solution chemistry, a small cylindrical hole was bored in a block of either X2095-A,B or T8 2090. The hole was filled with either 0.6M or 0.1M NaCl and a microelectrode was inserted into the hole forming a tight geometry with the cylinder wall. The pH was then monitored over time until a stable value was obtained. Figure 2 shows three hours of exposure for three test materials. Although the final pH for the materials appears to be significantly different, no explanation has been proposed to account for this phenomenon. At the end of the experiment (3 to 30 hours of exposure) solution was

removed from the hole using a glass capillary then analyzed. To date analysis has been performed using both IC and CE, but has been hindered due to large sodium peaks in the spectra. Efforts are being made to circumvent this problem. Despite the presence of sodium, it has also been possible to identify lithium ions in solution from an occluded environment. Although it has not been possible to accurately quantify the concentration of lithium ions, their detection in conjunction with the observed trends in pH lends credence to the use of the lithium carbonate environment in SCC experimentation.

TTF Behavior of Various 2090 Tempers

Electrochemical behavior of both T_1 and a simulated Cu depleted zone qualifies either phase as an active pathway for SCC propagation. In order to separate the contributions of these phases it is necessary to isolate microstructures containing one without the other. This goal is approached by the experiments described in this subsection as well as the one following.

Several microstructures of 2090 were produced by solution heat treating material at 545°C for one hour followed by cold water quench and isothermal aging at 160°C. The aging times used were 1.5, 3 and 7 hours. For each temper, smooth tensile samples were machined and used in constant load TTF experiments in 0.6M NaCl + 0.1M Li_2CO_3 solution under an applied potential. Due to a shortage of samples it was difficult to accurately determine the critical potentials at which each temper underwent the no failure to rapid failure transition. However, it was determined that the critical potentials for these tempers as a whole ranged between 60 and 85 mV more noble than the critical potential observed for material in the T8 condition.

These data indicate that a path for rapid anodic dissolution exists in extremely underaged material. Unfortunately, the microstructures of these tempers are unknown at this time. If T_1 is not found in the underaged material it will be a strong indication that this phase is not necessary for the rapid anodic dissolution based failure to occur.

TTF Behavior of a Non-lithium Containing Alloy

Constant load TTF experiments on alloy 2124 were intended to provide a comparison with an aluminum alloy that does not contain lithium, hence no T_1, but does contain copper and therefore may develop a copper depleted zone. In the chromate environment, alloy 2124 underwent the no failure to rapid failure transition at approximately -0.575 V_{SCE} which is within several millivolts of the critical potential for some aluminum-lithium-copper alloys.

This experiment suggests that a rapid SCC path can exist without the presence of T_1. It is possible that there exists a precipitate phase in 2124 that becomes active at this specific combination of environment and potential; however, the similarity in potentials between alloy systems strongly favors the existence of a common feature. It is possible that this feature is a copper depleted zone.

Conclusions

The following list represents the major conclusions that can be drawn from research performed within the past report period:

(a) Straining electrode experiments performed on 99.99 aluminum and SHT 2090 indicate that the electrochemical behavior of these materials at the crack tip may dictate the potentials required for rapid SCC failure in alloys 2090 and X2095.

(b) Preliminary analysis of occluded environments in Al-Cu-Li alloys indicates the presence of Li in the solution and an alkaline chemistry. A more accurate description of the solution has not been proposed at this time.

(c) Constant load experiments performed on under aged 2090 indicate that the microstructural features necessary for rapid SCC failure are present early in the tempering process.

(d) Experiments performed on alloy 2124 show that an aluminum alloy which does not contain lithium is susceptible to the criteria for rapid SCC failure which has previously been attributed to the presence of T_1. It is possible that a microstructural feature common to this alloy and lithium containing alloys is responsible for the rapid failures.

Tasks for Next Reporting Period

In the following research period, efforts will be made to quantify the occluded cell chemistry associated with aluminum-lithium-copper alloys. Ion chromatography and capillary electrophoresis will be used as complementary tools in the identification of ions in solution. Both of these methods are extremely sensitive, being able to detect ions such as lithium and copper in concentrations in the parts per million range. Efforts will be made to identify the significance of solution volume to metal surface area ratios, isolated crevices versus those with an external bulk solution and the effect of dissolved oxygen availability. Also, various

molarities of NaCl solution will be used as initial environments in the occluded cells to determine the aggressive ion effect on final solution chemistry. The ultimate goal in this area of the research project is to correlate the solution chemistry from contrived occluded cells to that of real propagating SCC cracks. If this can be accomplished, the electrochemistry of pertinent subgrain boundary phases can be evaluated in true crack tip chemistries. The proposed procedure to accomplish this is analysis of crack solutions from double cantilever beam (DCB) specimens.

Bolt loaded DCB specimens in the S-L orientation, machined from both tempers of X2095 as well as 2090 T8, will be used in either alternate immersion and/or drop-wise addition testing. The purpose of these experiments will be twofold. As mentioned in the previous paragraph, attempts will be made to analyze solution chemistry from SCC cracks growing in these specimens. The crack growth rate information from this type of testing is also of interest. It will be used to quantitatively distinguish the SCC behavior of X2095-A, X2095-B and PKA 2090. Since these three materials differ in terms of T_1 distribution and size, it may be possible to find a correlation if any between crack growth rates and this microstructural feature.

Finally, transmission electron microscopy (TEM) will be used to identify prominent microstructural features in the alloys and tempers employed in this research project. Information from TEM studies when correlated with TTF data should provide insight into which features affect the anodic dissolution process.

References

[1] R. Balasubramaniam, D.J. Duquette and K. Rajan, Acta Metall. Mater., **39**, 2597, 1991.

[2] E.I. Meletis and Weiji Huang, Materials Science and Engineering, **A148**, 197, 1991.

[3] J.R. Galvele and S.M. de De Micheli, Conf. Proc. NACE, Localized Corrosion, Williamsburg, VA, December, 1971.

[4] R.G. Buchheit, Jr., F.D. Wall, G.E. Stoner and J.P. Moran, Corrosion 1991, Cincinnati, OH, Paper No. 99, March, 1991.

[5] R.G. Buchheit, Jr., J.P. Moran, F.D. Wall and G.E. Stoner, Parkins Symposium on Stress Corrosion Cracking, Fall TMS meeting, Cincinnati, OH, October, 1991.

[6] J.P. Moran and G.E. Stoner, Aluminum Lithium V, Eds. T.H. Sanders and E.A. Starke Jr., Williamsburg, VA, 1989, pp. 1187-1196.

[7] R.G. Buchheit Jr. and G.E. Stoner, "The Corrosion Behavior of the T_1 (Al_2CuLi) Intermetallic Compound in Aqueous Environments", Proceedings of the Fifth Al-Li Conference, Williamsburg, VA, March, 1989.

[8] R.G. Buchheit, Jr., Ph.D. Dissertation, University of Virginia, January, 1991.

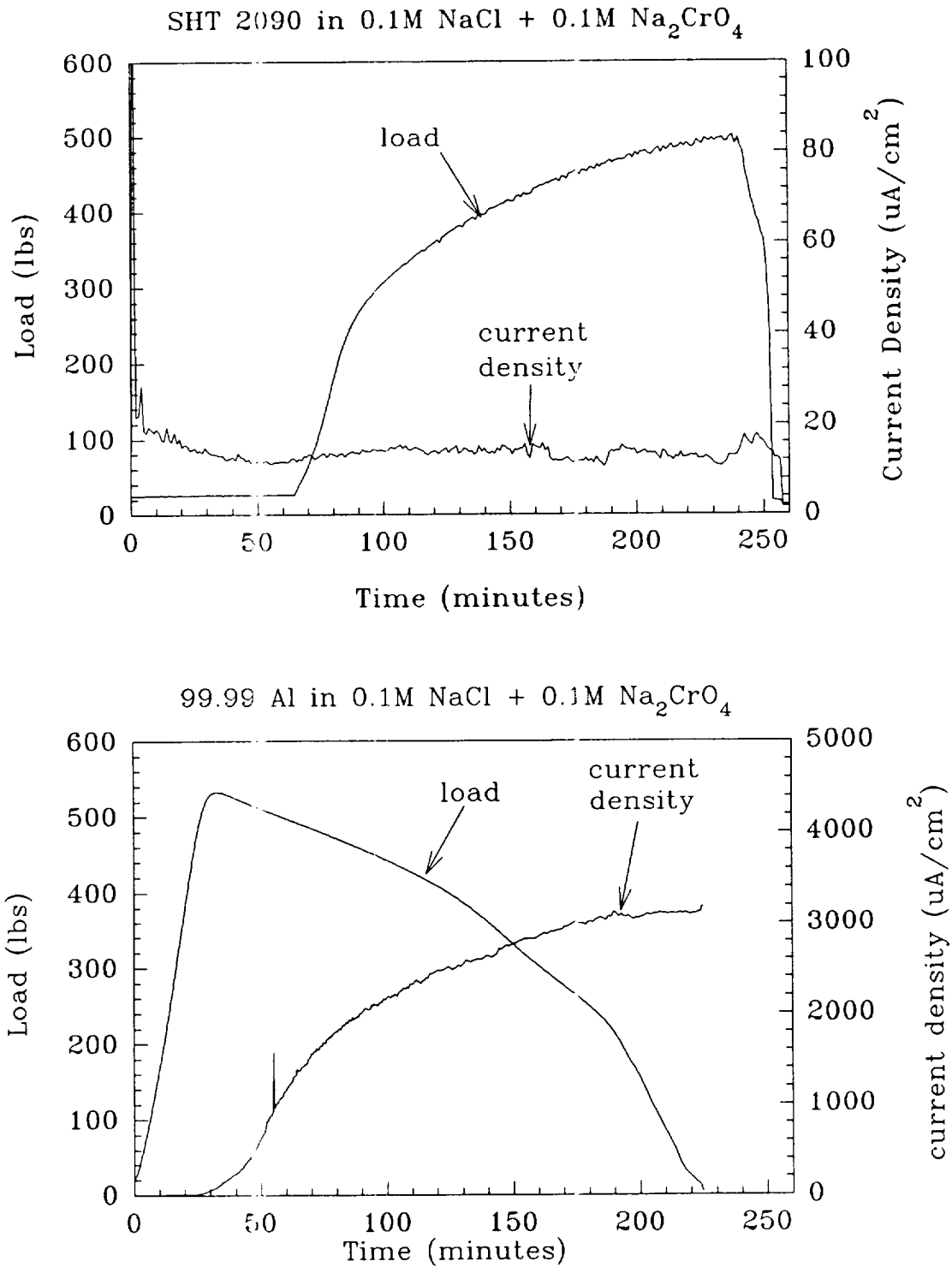

Figure 1. Results of straining electrode experiments

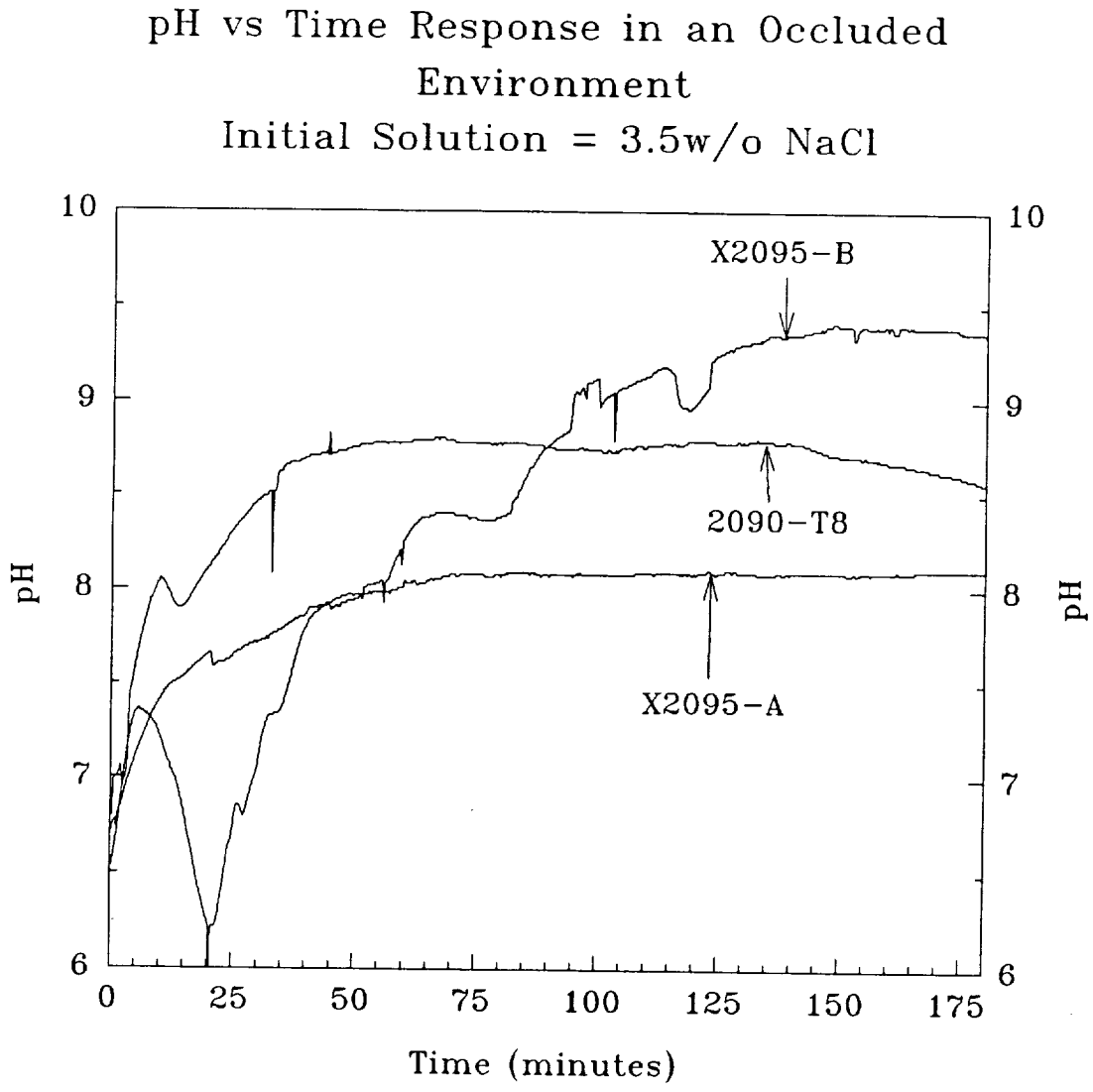

Figure 2. pH results from occluded chemistry experiment

Project #6 The Effects of Zinc Additions on the Precipitation and Stress Corrosion Cracking Behavior of Alloy 8090

Raymond J. Kilmer and G.E. Stoner

Objectives

The objectives of this Ph.D. research are to: (a) document the effect Zn additions have on the precipitation events in Al-Li-Cu-Mg alloys, (b) identify the conditions necessary for SCC in the model Al-Li alloys, and (c) demonstrate the mechanism(s) by which Zn additions alter the baseline 8090 alloys' SCC behavior.

Specific goals are to: (a) identify the pertinent precipitate phases seen in the alloys in the T3 to T3 + 100 hrs at 160°C aging period, (b) assess the interrelationship between specific solute content (i.e., Li, Mg, Cu and Zn) and final properties, (c) identify the salient microstructural features (i.e., SCC pathway) and determine the role of Zn in imparting an improved SCC resistance, and (d) assess the anodic dissolution behavior of the precipitates, comment on their role in this environmental fracture process, and determine the susceptibility of the alloys to hydrogen embrittlement.

Background and Problem Statement

Alloy 8090 is an Al-Li-Cu-Mg alloy demonstrating good strength/weight properties, but SCC resistance is relatively poor. Zn additions[1,2] have been shown to result in alloys displaying significantly longer time-to-failure lifetimes in aged conditions. The issues involved in trying to gauge alloy resistance to environmental fracture via alternate immersion time-to-failure experiments are complex. Smooth tensile samples lump SCC initiation and propagation events; to obtain a true measure of an environmentally assisted crack velocity, precracked, high constraint samples must be employed. The issues of SCC propagation and how they pertain to 8090 and 8090 + Zn will be addressed in this research, with emphasis on understanding the roles of anodic dissolution and hydrogen embrittlement in the phenomenon.

Approach

Transmission Electron Microscopy, Differential Scanning Calorimetry, Guinier Phase

Analysis, as well as tensile and toughness testing were employed to characterize the microstructure and properties of the alloys. These results have been presented previously[3,4].

Alternate immersion time to failure testing in the standard 3.5 w/o aqueous NaCl environments was employed to initially identify general trends in SCC behavior as a function of aging time at 160°C. As previously reported[3], these results indicated a marked improvement in SCC resistance in the Zn containing alloys when aged greater than 20 hrs at 160°C. This transition in SCC behavior occurred earlier for the higher Zn content alloy.

Current research focusses on a more quantitative evaluation and determination of the SCC behaviors in the alloys. To accomplish this a constant displacement rate test employing environmentally exposed compact tension (CT) specimens is being developed. A schematic of the environmental cell is included in Figure 1. The S-L orientation was chosen as it is the most susceptible orientation to SCC. The tests will be run potentiostatically at -800 mV_{SCE} (below E_{Br}) to minimize the effects of pitting and the environment will be 3.5 w/o NaCl + 0.5 w/o Na_2CrO_4. The chromate is added to inhibit general corrosion and to protect the fracture surfaces during the tests. From both ionic size and valency considerations the Cr^{-2} should not effect the corrosion behavior at the crack tip.

To investigate the susceptibility of the alloys to hydrogen embrittlement, a number of model alloys were fabricated at UVa. These model alloys were a series of recrystallized 2090 sheet alloys, recrystallized to differing grain sizes. To address the role of subgrain boundaries, an unrecrystallized commercial sheet alloy was also included for study. The recrystallized grain sizes varied from approximately 35 μm equiaxed (fine grained alloy) to approximately 1 mm by 300 μm (coarse grained alloy). All alloys were aged to one of two tempers; an underage (UA) temper (5 hrs at 160°C) where the alloy is known to be most susceptible to SCC, and a peak age temper (PA) (25 hrs at 160°C). Compact tension samples were machined from the alloys such that the direction of cracking was transverse to the direction of rolling (LT). The thickness of each CT specimen was 2.4 mm. Two specimens were run at each condition, one charged and one uncharged, and the resultant J-R curves analyzed. Specimens were fractured at a constant actuator displacement rate of 6.3 x 10^{-4} mm/sec.

Charging was accomplished by S.W. Smith and this aspect of the research is a collaborative effort with J.R. Scully and S.W. Smith. The technique used for charging was developed by them and the details have been previously reported (see Project #7). The goal

of this test matrix is to gain insight into the role of hydrogen on specific fracture processes. The coarse grained alloy fails by transgranular shear and the fine grained alloy fails by intergranular fracture. Under equivalent charging conditions, with knowledge of the microstructure, insight can be obtained with regards to the relative strength of traps. Coupling this work with the future TDS work by Smith should yield a plethora of information. Armed with insights from this research, S-L CT samples from the 8090 and 8090 + Zn J-R testing will be performed on charged and uncharged samples in the SCC susceptible and SCC resistant tempers. In all cases alternate immersion time-to-failure tests will be performed to validate susceptibility of the specific alloys.

Results

J-R curves have been generated for the underaged alloys; hydrogen charged and uncharged, and are presented in Figure 2. The J_i values for the uncharged alloys correlate well with grain size, with the highest J_i value for the recrystallized alloys being the fine grained alloy and the lowest J_i for the coarse grained material. The results of the hydrogen charging indicate that the greatest degradation in material properties is seen for the fine grained alloy, and little or no effect is seen in either the coarse grained recrystallized or the unrecrystallized alloys. Fractography will provide the answers as to the role of hydrogen on specific fracture modes as the coarse grained alloys (in air) and the unrecrystallized alloy fail predominately by transgranular shear while the fine grained alloy fails predominately by intergranular fracture. The results of the peak age material, along with a complete fractographic analysis of all CT specimens, should provide more information.

To confirm that the hydrogen charging method is indeed resulting in the introduction of hydrogen, 7075-T6 CT specimens will be tested both charged and uncharged. The deleterious effects of hydrogen on this material are well documented[6,7,8] and should provide a basis for evaluation of the test technique.

The aqueous testing should be completed in the next couple of months. A few modifications have been made to the cell including the substitution of a chloridized silver wire as the reference electrode. Load-displacement curves, with and without the clamped cell indicate a negligible effect of the clamping pressure on the results. The v-K relationships for 8090 underage, 8090 + Zn underage, 8090 peak age and 8090 + Zn peak age will be determined via testing at a displacement rate of approximately 2.5×10^{-7} mm/sec with CT

samples preloaded to a K of approximately 5 MPa$\sqrt{m}$. This should save a significant amount of time and the stress intensity should be well below the knee in the v-K curve, as most aluminum alloy plateau crack growth rates begin at a K level of about 10 MPa$\sqrt{m}$.

References

1. A. Gray, N.J.H. Holroyd and J. White, Proceedings of the Fifth Al-Li Conference, Williamsburg, VA (E.A. Starke and T.H. Sanders, eds.) MCE publications, Birmingham, pp. 1175-1186.

2. R.J. Kilmer, J.J. Witters and G.E. Stoner, Proceedings of the Sixth Al-Li Conference, Garmisch-Partenkirchen, FRG, pp. 755-760.

3. R.J. Kilmer, G.E. Stoner, NASA-UVA Light Aerospace Alloy and Structures Program, NASA-LaRC Grant NAG-1-745, Jan, 1992, pp. 101-110.

4. R.J. Kilmer, G.E. Stoner, NASA-UVA Light Aerospace Alloy and Structures Program, NASA-LaRC Grant NAG-1-745, July, 1992, p. 60.

5. S.W. Smith, J.R. Scully, NASA-UVA Light Aerospace Alloy and Structures Program, NASA-LaRC Grant NAG-1-745, July, 1992, p. 61.

6. J. Albrecht, A.W. Thompson and I.M. Bernstein, Met. Trans. A, Vol. 10A November, 1979, pp. 1759-1766.

7. M. Taheri, J. Albrecht, I.M. Bernstein and A.W. Thompson, Scripta Met., Vol. 13 pp. 871-875.

8. D.A. Hardwick, A.W. Thompson and I.M. Bernstein, Met. Trans. A, Vol. 14A, December, 1983, pp. 2517-2526.

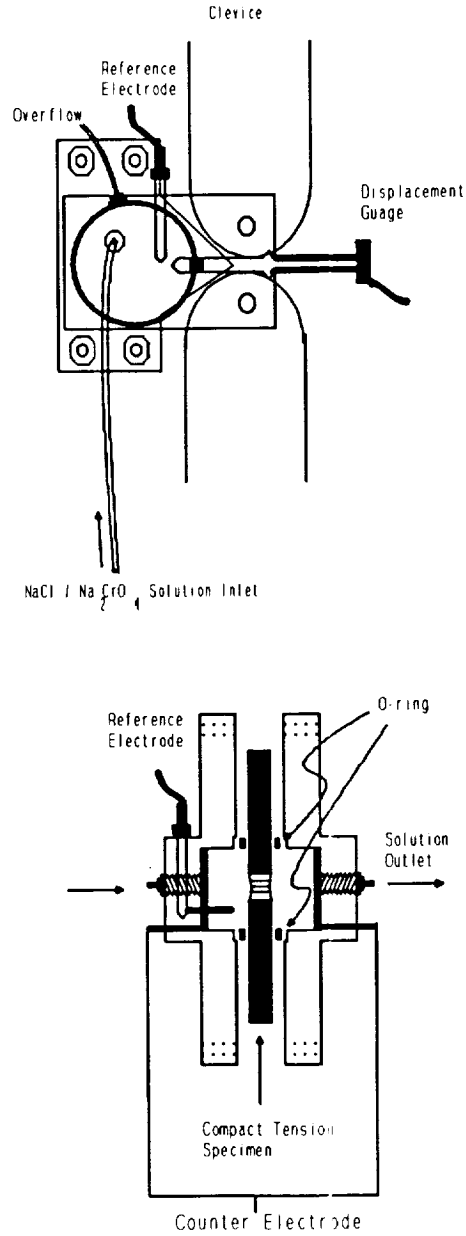

Figure 1. Schematic of environmental cell.

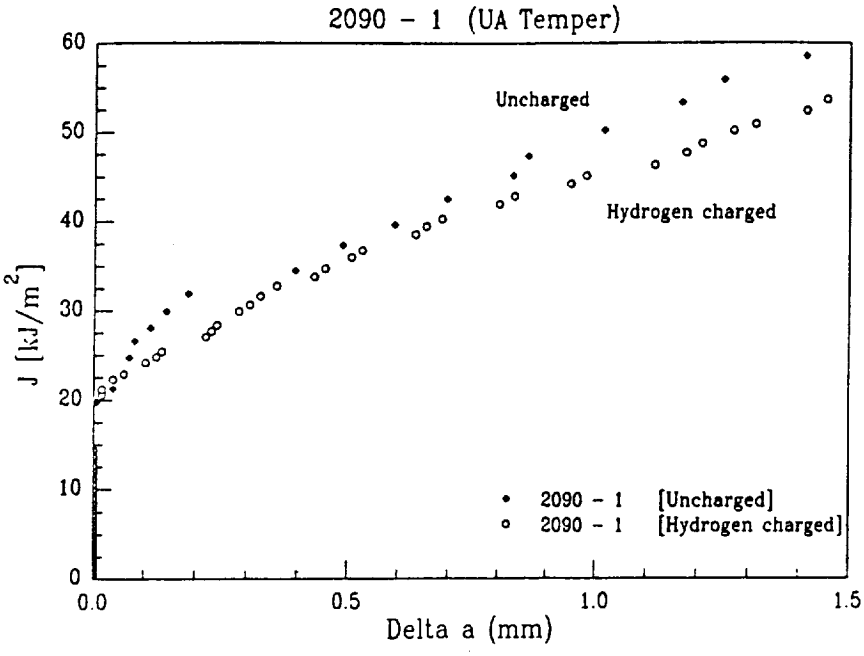

(a) Unrecrystallized 2090 sheet. LT orientation

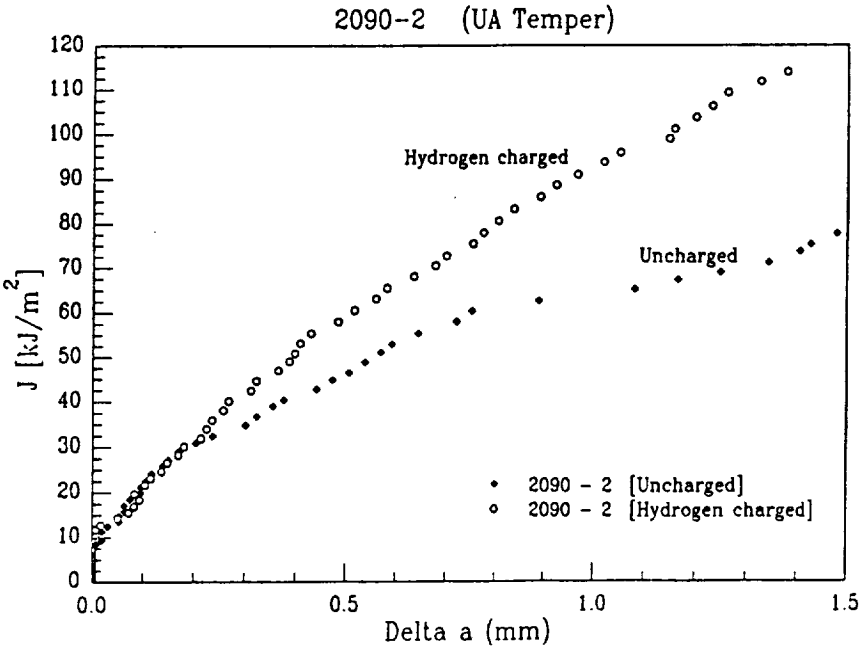

(b) Coarse grained recrystallized 2090 sheet. LT orientation.

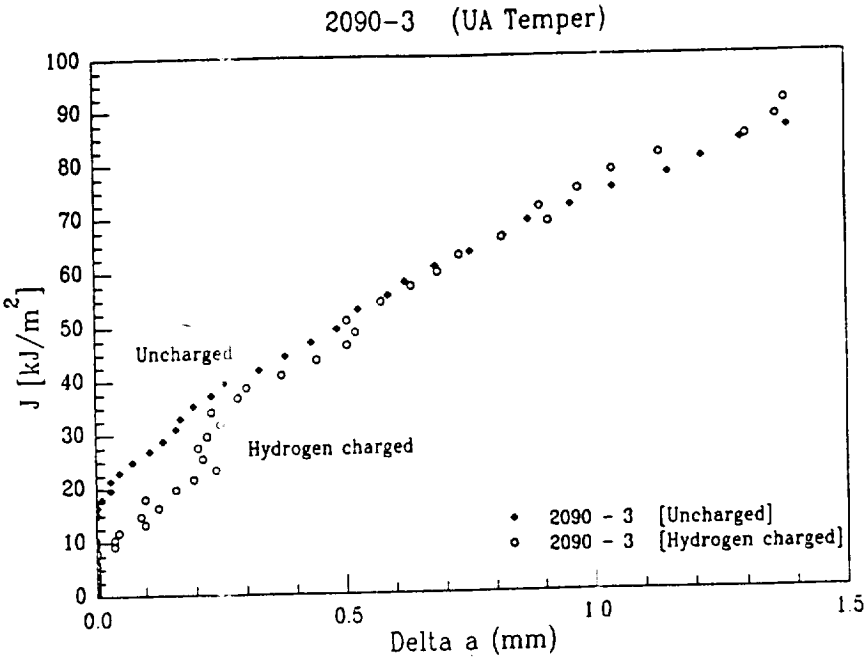

(c) intermediate grained recrystallized 2090 sheet. LT orientation.

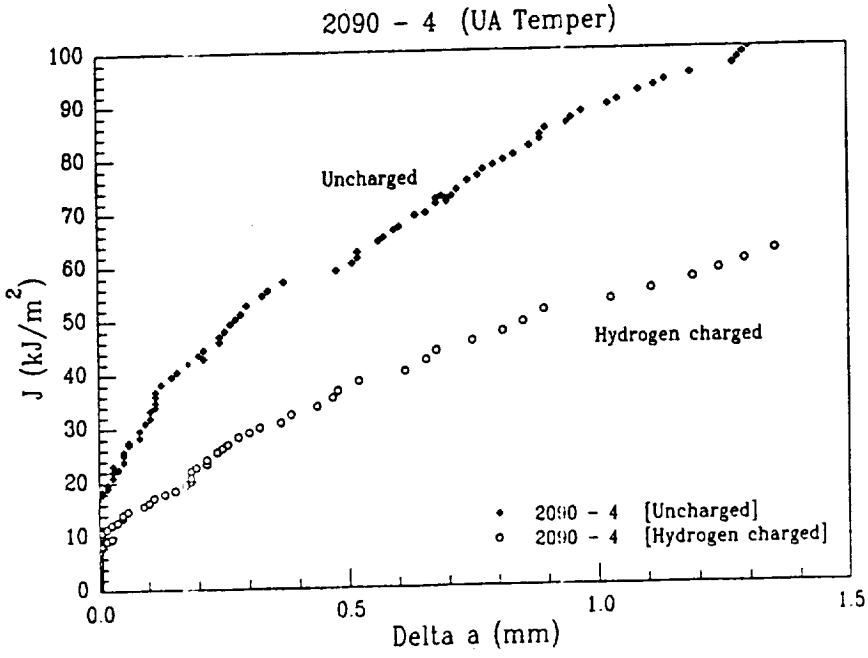

(d) Fine grained recrystallized sheet. LT orientation

Figure 2. J-R curves for four 2090 alloys.

Project #7 **Hydrogen Interactions in Aluminum-Lithium Alloy 2090 and Selected Complimentary Model Alloys**

S.W. Smith and J.R. Scully

Background and Problem Statement

Al-Li-Cu-X alloys are susceptible to both intergranular and transgranular environmentally assisted cracking (EAC). To date several theories have been proposed to account for the EAC of these materials. These theories include subgrain boundary T_1 dissolution,[1] preferential T_1 dissolution with accelerated hydrogen uptake,[2] brittle $AlLiH_4$ hydride cracking,[3,4] hydrogen induced lattice decohesion,[5] and hydrogen induced localized plasticity and slip plane decohesion.[6] In our present work we hope to develop deterministic models defining Al-Li-Cu-X behavior by quantifying the role of hydrogen interactions in these materials and relating this to subsequent fracture paths. To be successful in studying hydrogen affected environmentally assisted cracking (HEAC), hydrogen must be introduced into the alloys as a noncompetitive process relative to anodic dissolution processes. The procedures being developed on this project will produce a series of diagnostic tests for studying hydrogen interactions in structural materials. Although the present study will focus on conventional 2090 sheet and several complementary alloys, the protocol can be used to study other materials. We also seek to develop deterministic models to understand the effects of internal hydrogen on ambient and cryogenic temperature mechanical properties for emerging Al-Li-Cu-X alloys. By developing a comprehensive understanding of the role hydrogen plays in these materials, the reliability of previously fabricated systems and potential applications of these materials can be evaluated.

Several problems are encountered when performing traditional EAC tests on Al-Li-Cu-X alloys, making it difficult to unambiguously determine the influence of hydrogen on the mechanical properties. Three major problems, which have impeded progress in this area have been identified in the literature.[7] These are: (i) intersubgranular fracture in Al-Li alloys when tested in the ST orientation in air or vacuum make it difficult to readily detect hydrogen induced fracture based on straight forward changes in fractography, (ii) the inherently low hydrogen diffusivity and solubility in Al alloys is further compounded by a native oxide which acts as a hydrogen permeation barrier; these factors complicate hydrogen,

ingress, detection and quantification, and (iii) hydrogen effects are masked by dissolution assisted processes associated with T_1 precipitates on subgrain boundaries when mechanical testing is performed in aqueous solutions. The experimental procedures developed here make it possible to overcome these barriers, thereby allowing us to develop a better understanding of the role hydrogen plays during EAC of these alloys than that which is available in the literature. In order to produce these results we are considering hydrogen uptake and the effect of hydrogen on mechanical behavior as noncompetitive processes. Although this is not the most common approach, this methodology makes it possible to separate the effects of HEAC from dissolution controlled EAC. The procedures by which this will be performed, the results to date and the status of this project will be reviewed.

Objective

The goal of this project is to develop a fundamental understanding of the effects of dissolved and trapped hydrogen on the mechanical properties of selected Al-Li-Cu-X alloys in the T3, underaged and peak aged tempers. The present program will focus on alloy 2090. We propose to: (a) distinguish HEAC from aqueous dissolution controlled EAC, (b) correlate hydrogen induced EAC susceptibility with mobile and trapped hydrogen concentrations, and (c) identify significant trap sites and hydride phases (if any) through utilization of model alloys and phases. The specific objectives for 1993 are discussed below.

Technical Approach

Materials

The ultimate objective of this research project is to create a well developed understanding of the role hydrogen plays in the EAC of Al-Li-Cu-X alloys. In order to reach this goal it is necessary to study what effect various microstructures play in these processes. Testing has been performed on 2090 sheet using three different tempers and machining mechanical tests specimens in the LT and TL orientations. We have chosen not to study the ST orientation for two reasons. Firstly, Al-Li alloys fracture intersubgranularly when tested in the ST orientation, even when tested in vacuum, thereby making it difficult to distinguish any changes in fracture mode after introducing hydrogen to the specimen. Secondly, if we are to study the effects of hydrogen on different microstructures, we should use a material having a uniform microstructure through-thickness. This led us to select a sheet product,

0.125 inches in thickness, making it impossible to study the ST orientation.

The three different tempers are produced from the same sheet. This insures us that the bulk composition of the specimens will be the same. The material was received in the T3 condition (σ_{ys} = 39.3 ksi) , which denotes a material that has been solution heat treated, cold worked and then allowed to age naturally. From this material the other two tempers are produced by artificially aging the material at 160°C for differing times. The temper which will be referred to as underaged (UA) was aged for five hours (σ_{ys} = 66.0 ksi). The final temper is labelled as T8, this material was aged for 25 hours, which produces a material very close to the peak aged condition (σ_{ys} = 77.2 ksi). These three tempers were chosen since EAC susceptibility is known to be a function of aging condition.

Hydrogen Uptake

The native oxide on aluminum alloys possesses an extremely low hydrogen diffusion coefficient. This results in the oxide behaving as a hydrogen diffusion barrier. During exposure of these materials to an aqueous environment,with mechanical or chemical destabilization of the passive film, hydrogen adsorption is facilitated by local breakdown in the passive film and acceleration of the reduction of water reaction. Hydrogen adsorbed onto the bare metal can then absorb into the bulk before the repassivation of the exposed site. In this case the exact role hydrogen plays in the materials being tested is difficult to quantify since HEAC and dissolution controlled EAC act as competitive processes. It was therefore necessary to develop a process by which we could remove the hydrogen diffusion barrier to facilitate hydrogen uptake, while protecting the material from any aqueous dissolution. This is accomplished by loading specimens into a vacuum system, sputter etching the native oxide from the surface and subsequently sputter depositing a thin nickel coating on the surface. This nickel coating allows for hydrogen adsorption and diffusion, while protecting the specimens from any dissolution. With the protective nickel film in place the specimens can then be placed into an aqueous solution and polarized to cathodic overpotentials with respect to the reversible potential for water reduction. This process makes it possible to vary the hydrogen concentration in a specimen by applying different overpotentials. Greater hydrogen concentrations can be achieved by using larger cathodic overpotentials. This makes it possible for us to also examine the effect of hydrogen concentration on the mechanical properties of these materials independent of anodic processes. Charging time can also be used as a test parameter affecting the hydrogen concentration profile.

A standard charging time was adopted by charging 2090-T3-LT tensile specimens for various times and performing continuous extension rate tests (Fig. 1). From these tests a charging time of 28 days was adopted as an adequate time to obtain a fairly uniform concentration profile. To insure the stability of the nickel coating during charging, the solutions used were buffered to a pH of 7.

Mechanical Testing - Continuous Extension Rate Tests

Slow extension rate tests were performed on hydrogen charged prenotched and smooth tensile specimens. These tests were performed in a cell containing magnesium perchlorate that is continuously purged with dry argon to provide a low humidity environment. By hydrogen charging specimens in a manner which does not promote aqueous dissolution and then removing the specimens from solution and performing mechanical testing in an environment free of water vapor it is possible to determine the effect of a quantified amount of absorbed hydrogen on these materials. As a control, specimens that were not hydrogen charged were tested to measure the mechanical properties of the alloys containing very low concentrations of hydrogen.

A test parameter of concern when attempting to identify hydrogen damage is strain rate. Figure 2 shows data produced from tests performed at two different strain rates: 2.5×10^{-3} and 2.5×10^{-6} sec^{-1}. The faster strain rate did not result in significant damage, while the slower rate proved to be satisfactory for our work. This result suggests that there must be a dynamic hydrogen redistribution to the fracture process zone, or when fracture is dominated by macroscopic shear, there is a dynamic hydrogen interaction with dislocations or shearable precipitates.

Mechanical Testing - Fracture Mechanics

Fracture testing using compact tension specimens, prepared in the same manner as the tensile specimens described in the preceding section, were performed to quantify HEAC under high constraint conditions. A J-Integral R-Curve analysis is being performed to evaluate the amount of embrittlement produced. The testing to date has been performed by Ray Kilmer and is discussed in Project #6 and in the literature[8]. In the future we will perform these tests on 2090 materials under the metallurgical conditions described above. Using the information obtained by the continuous extension rate test, we can select charging parameters that would allow us to most effectively evaluate the susceptible to embrittlement for these materials.

Hydrogen Analysis - Total Hydrogen Content

Charged 2090 sheet specimens have been sent to Alcoa Technical Center for hydrogen analysis using the Leco method. In this test method, specimens are placed into a small chamber that can be heated with an RF source. The specimen is heated for 60 seconds at 200°C to remove any surface contamination, and then allowed to cool. After cooling the specimen is heated very quickly above its melting point. Any gases that are evolved during this test are transported to an analysis chamber by purging with a carrier gas. The hydrogen partial pressure is then measured and the concentration of hydrogen in the specimen is calculated. Although, this testing procedure does not yield any information on how the hydrogen is partitioned, it indicates the amount of hydrogen introduced to the specimen by cathodic charging.

Hydrogen Analysis - Hydrogen Partitioning

We have recently completed assembly of a thermal desorption spectroscopy system. The design of this system is shown in Fig. 3. The vacuum system is designed to operate in the ultrahigh vacuum range ($< 1 \times 10^{-9}$ Torr). The specimen is loaded into a quartz specimen chamber located within a resistance tube furnace and the volume is evacuated. As the specimen is heated, all evolved gases are monitored using a quadrupole mass spectrometer. By measuring the H_2^+ fragmentation, the partial pressure of hydrogen in the analysis chamber can be determined. Measuring the hydrogen partial pressure as a function of specimen temperature makes it is possible to determine the amount of hydrogen present in the specimen.[9]

Unlike the Leco method previously reviewed, TDS makes it possible to identify how hydrogen is partitioned in a sample. Each hydrogen trap site will have a distinct hydrogen binding energy, therefore hydrogen from different trap sites will be released at different temperatures. This makes it possible to determine the concentration of hydrogen at each trap site and to calculate the binding energy of each trap site.[10] In order to determine the identity of each trap site, model alloys will be charged and analyzed. Since the model alloys will be simpler alloys, containing one or two phases, the potential number of different trap sites is limited and this will allow us to identify the trapping behavior of our selected alloys.

Summary of Important Conclusions

To date CERT testing has been performed on 2090-T3 and 2090-T8 specimens. The

results obtained for the T3 temper clearly show that the introduction of hydrogen into this alloy results in a deleterious effect, up to 75% decrease in the reduction in area (Fig. 4). Examination of failed 2090-T3-TL specimens showed a change in fracture mode with the introduction of hydrogen. Uncharged specimens failed by transgranular shear, while specimens charged at -1 V vs. SCE on nickel resulted in intersubgranular failure. There was no change in fracture path for specimens tested in the LT orientation. The fracture surfaces for charged specimens did appear different from those that were not charged, however, in all cases the specimens failed by transgranular shear. These results were shown in our previous progress report.[11]

We were concerned that by using flat tensile specimens there was not a great enough degree of mechanical constraint or large enough notch tip stress concentration to satisfy possible hydrogen-tensile stress criteria. Notches were machined into the gauge section normal to the tensile axis in several specimens to insure this criteria was met. When examining T3-LT notched specimens, it was possible to identify some intergranular failure near the notch tip, however the predominance of the fracture surface was caused by transgranular shear.

Mechanical testing of the T8 material has led to different conclusions. The results to date for CERT of 2090-T8 specimens are shown in Fig. 5. Testing of smooth tensile specimens in the LT and TL orientations did not result in any adverse effects with the addition of hydrogen. Notched 2090-T8-LT specimens charged at -1 V and -750 mV vs. SCE have not shown any hydrogen damage. However, a 2090-T8-LT specimen charging at -1.25 V has shown hydrogen embrittlement. Additional testing of notched specimens, including 2090-T8-TL, must be completed. This work does show that the degree of hydrogen damage present for peak aged 2090 is significantly lower than that seen in the T3 temper.

Fracture testing of underaged 2090 specimens in the LT orientation has been performed by Ray Kilmer (see Project 6). These tests were performed on the 2090 sheet product used in our CERT tests, as well as several recrystallized 2090 variants. Table 1 shows the results obtained for the unrecrystallized sheet used in the present study as well as the results for a fine grained recrystallized sheet. The fine grain recrystallized sheet shows a significant loss in fracture initiation toughness due to hydrogen while the unrecrystallized material does not indicate a significant change in properties with hydrogen. The fine grain

material is very close to having an equiaxed microstructure, therefore, the unfavorable orientation of high angle boundaries with respect to tensile stress for LT specimens is avoided. With the fine equiaxed structure an intergranular failure path normal to the loading axis is available. In order to prove the validity of this argument additional testing of the unrecrystallized sheet material in the TL orientation must be performed.

Figure 6 illustrates the hydrogen thermal desorption spectra for a palladium foil that has been electrochemically charged with hydrogen. The large peak labelled as number 1 is believed to be due to the decomposition of the remnants of a palladium hydride phase and the other peaks are for hydrogen associated with microstructural traps. This plot clearly distinguishes types of trap sites. The initial desorption experiments were done with palladium foil since the solubility of hydrogen in palladium is very large and will allow us to perfect our experimental procedure prior to advancing to the more complicated case of aluminum alloys.

Proposed Research Plan for 1993

Work for the next reporting period will be centralized around four major research tasks: (1) mechanical testing of hydrogen charged specimens, including J-Integral R-Curve methods and CERT testing of underaged materials, (2) fractographic analysis of mechanical test specimens, (3) hydrogen analysis of aluminum alloy 2090 and complementary alloys by thermal desorption spectroscopy, and (4) transmission electron microscopy of the alloys under study to obtain a better understanding of the microstructures of the materials being used.

References

1. R.G. Buchheit, J.P. Moran and G.E. Stoner, Corrosion, 46, pp. 610-617, 1990.

2. E.I. Meletis and W. Huang, Mater.Sci. and Eng., AI48, p. 197, 1991.

3. R. Balasubramaniam, D.J. Duquette and K. Rajan, Acta.Met., 39, pp. 2597-2605, 1991.

4. R. Balasubramaniam, D.J. Duquette and K. Rajan, Acta.Met., 39, pp. 2607-2613, 1991.

5. R.S. Piascik and R.P. Gangloff, Metall. Trans. A, in press.

6. H.K. Birnbaum, in "Hydrogen Effects on Material Behavior", eds., Moody and Thompson, TMS-AIME, Warrendale, PA, pp. 639-660, 1990.

7. T.D. Burleigh, Corrosion, 47, pp. 89-98, 1991.

8. ASTM Standard No. E 813, 1987.

9. R.A. Outlaw, D.T. Peterson and F.A. Schmidt, Scripta Metallurgica, 16, pp. 287-292, 1982.

10. J.Y. Lee, J.L. Lee and W.Y. Choo, in "Current Solutions to Hydrogen Problems in Steels", eds., C.G. Interrante and G.M. Pressouyre, ASM, pp. 423-427, 1982.

11. S.W. Smith and J.R.Scully, "NASA-Uva Light Aerospace Alloy and Structures Technology Program", UVa Report No. UVA/528266/MS93, October, 1992.

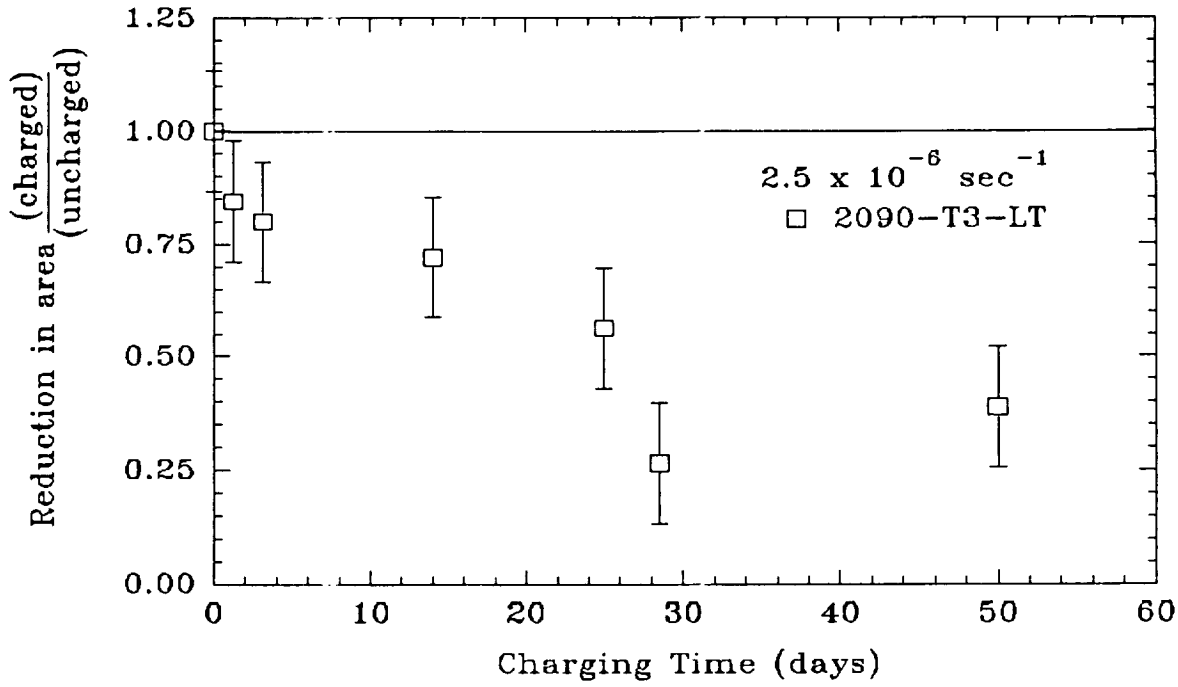

Figure 1. Continuous extension rate test results for charging at −1 V vs. SCE on nickel coated 2090−T3−LT.

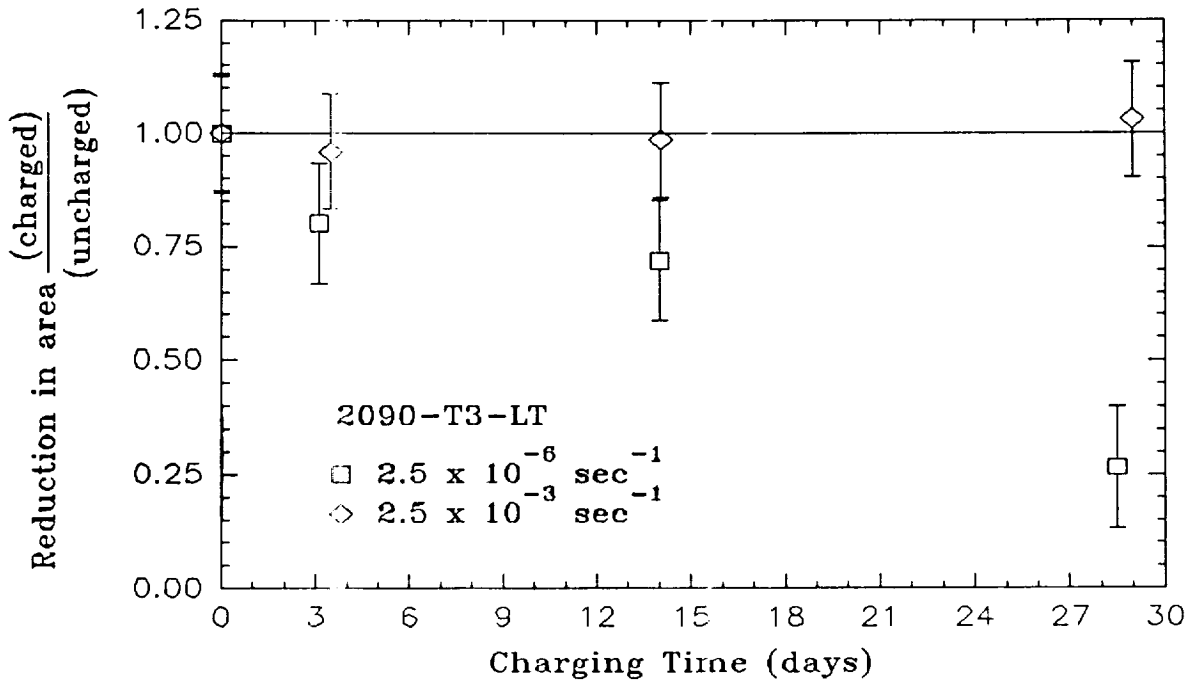

Figure 2. Continuous extension rate test results for charging at −1 V vs. SCE on nickel coated 2090−T3−LT.

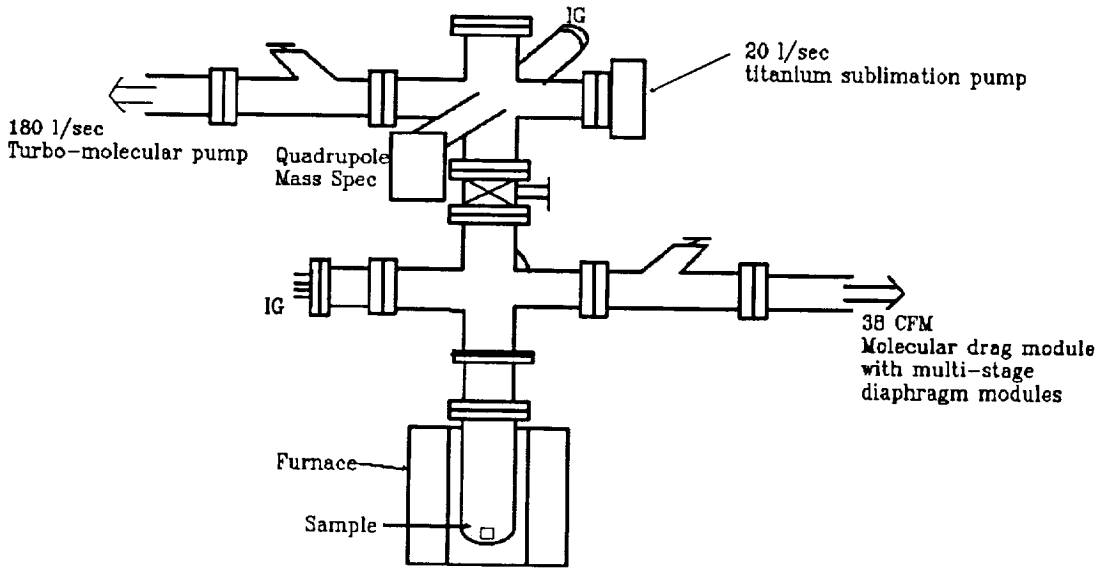

Figure 3. Schematic diagram of thermal desorption system.

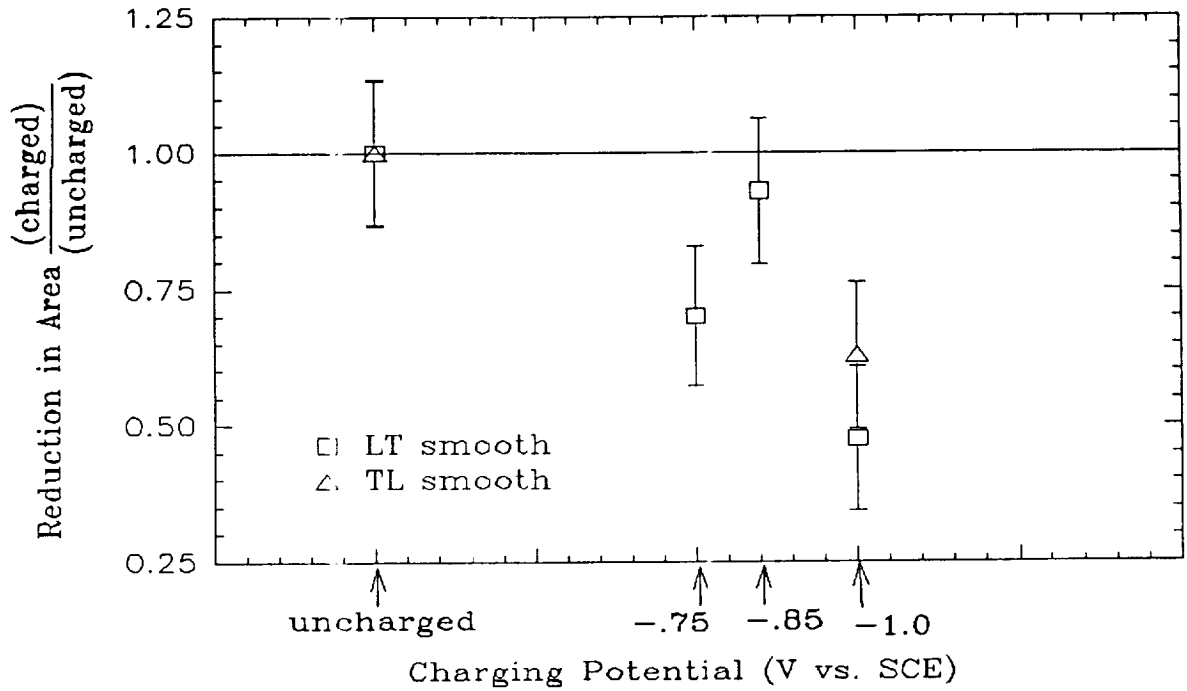

Figure 4. Continuous extension rate test results for 2090-T3. Charged at −1 V vs. SCE on nickel.

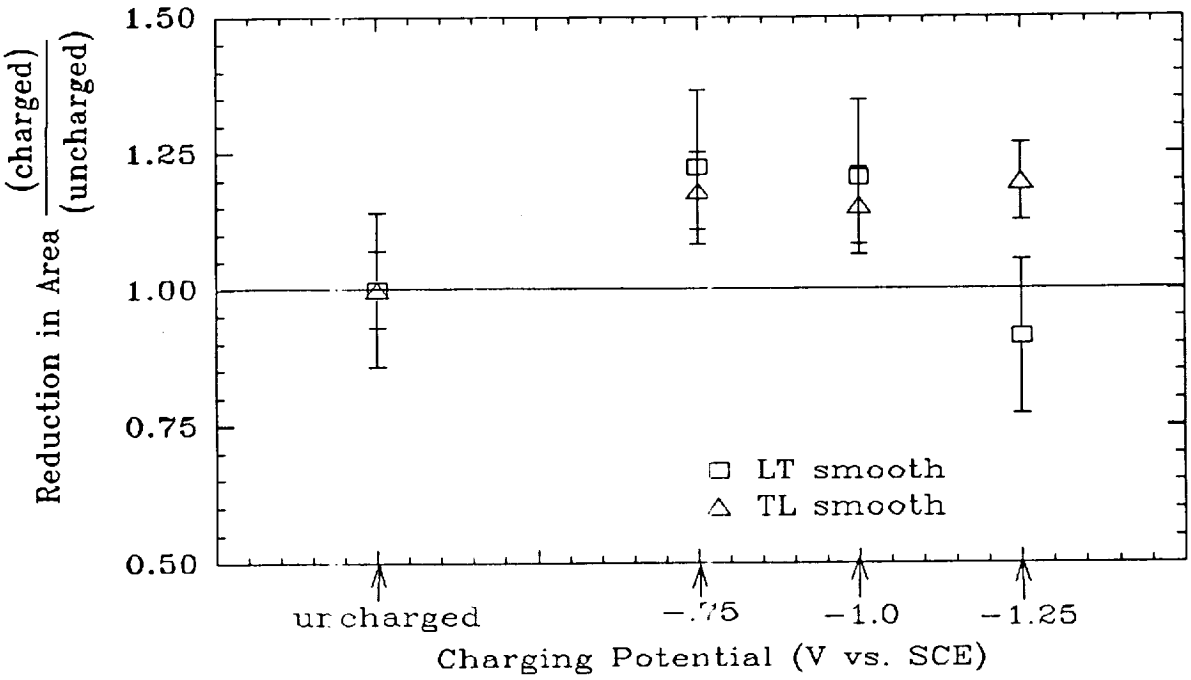

Figure 5. Continuous extension rate test results for 2090-T8. Charged at −1 V vs. SCE on nickel.

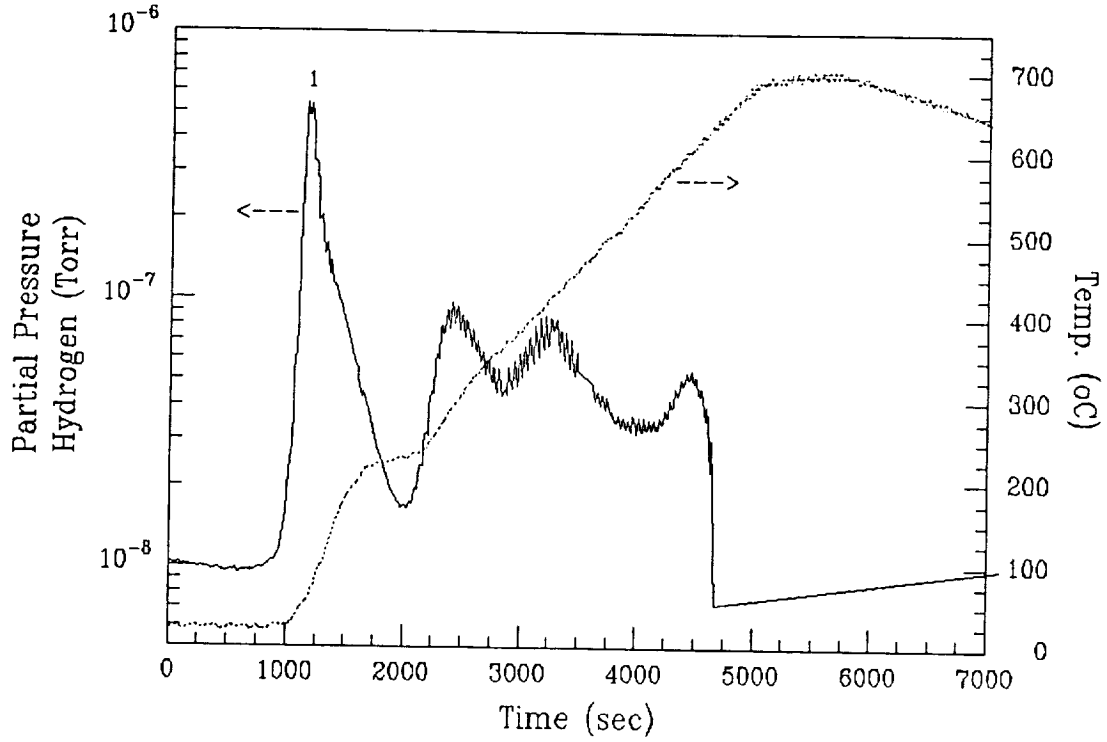

Figure 6. Thermal desorption of hydrogen from a palladium foil.

Table 1. Results from J-Integral R-Curve analysis for compact tension specimens.

Specimen	Charging Conditions	J_i (kJ/m^2)	K_i (Mpa$\sqrt{m}$)	J_{IC} (kJ/m^2)	K_{IC} (Mpa$\sqrt{m}$)
2090-UA-LT unrecrys.	uncharged	18.42	38.04	32.00	50.14
2090-UA-LT unrecrys.	-1 V vs. SCE 28 days	17.31	36.88	30.00	48.55
2090-UA-LT fine grain recrystallized	uncharged	15.59	35.00	51.00	63.30
2090-UA-LT fine grain recrystallized	-1 V vs. SCE 28 days	5.20	20.22	25.00	44.30

Project #8 **Metastable Pitting of Al Alloys in Halide Solutions**

S.T. Pride[1], J.R. Scully and J.L. Hudson[1]

Background and Problem Statement

Pitting corrosion of aluminum alloys has a number of detrimental effects on structural materials. These include creation of sites of stress concentration and localized occluded cell chemistry which, in turn, can lead to conditions favorable towards environmentally assisted cracking or fatigue[1-3]. One critical issue concerning aircraft aging is the pit size required to initiate a fatigue or stress corrosion crack. This program addresses pitting phenomena in Al alloys. In the case of aged Al-Cu binary alloys, pitting is induced by galvanic coupling between the θ-Al_2Cu phase and the aluminum rich (copper depleted) matrix or grain boundary zone[3-5].

It is well established that metastable pits form at potentials below the pitting potential[4-8]. However, these pits are believed to repassivate when the oxide remnant covering the pit mouth ruptures either due to hydrogen evolution[9,10], structural instability as the pit mouth widens[6], or osmotic pressure[8]. Hence, metastable pits have a low probability of surviving for long time periods. Pits which initiate above the pitting potential have a higher probability of growing for extended periods of time and of sustaining growth even after the oxide cover ruptures[6].

Most laboratory studies cited in the literature focus on stable pit propagation at high positive potentials[9-13]. Consequently, little is understood about pit nucleation and the factors responsible for stabilizing pit growth as a result of the galvanic cell formed by microstructural heterogeneities. For instance, factors that control the pit growth process and pit depth as well as govern the transition from metastable to stable pit growth remain unclear. What are the criteria for pit stabilization? Additionally, little is known about the dynamics of the pit initiation and growth process. Is pit initiation stochastic in nature, or is initiation of metastable pits spatially or temporally dependent on the "progress" of other pit sites? Is the high metal dissolution rate observed in metastable pits fundamentally different than that

[1] Department of Chemical Engineering, University of Virginia, Charlottesville, VA.

associated with stable pits, or do the differences lie elsewhere?

To obtain possible answers to these questions various electrochemical techniques will be used to at first examine pure Al, model bulk Al-Cu alloys, and Al-Cu alloy thin films. The dynamic behavior will be studied through analysis of the oscillations in the applied current at constant potential, or alternatively, the open circuit potential. More recently developed electrochemical methods based on the techniques of nonlinear dynamics will be employed in addition to more tradition approaches.

Objectives

The goal of the program is to improve the fundamental understanding of pitting nucleation and growth phenomena in Al alloy systems. Emphasis is placed on understanding the electrochemical factors controlling the nucleation, propagation, and repassivation of pit sites in model Al alloys. To accomplish these goals, conventional electrochemical methods have been augmented with nonlinear dynamic analysis methods suitable for characterizing electrochemical transient associated with metastable pitting. To date pitting has been investigated on artificially aged Al-Cu alloys. The goals for 1993 will be concentrated more on the analyses of the metastable pitting transients with nonlinear dynamic methods.

Technical Approach

Materials

Al-2%Cu will be used as a model alloy to study metastable pitting. This binary alloy (made from 99.999% Al and 99.999% Cu) provides a simpler system to study rather than commercial grade aluminum alloys or complex Al-Li-Cu alloys. Bulk and thin film (0.8 μm) Al-2%Cu alloys are used in this project. The thin film restricts pit dimensions in the direction perpendicular to the metal surface and provides a means to investigate the role of pit depth on factors possibly controlling pit growth and repassivation (such as ohmic and mass transport control). Preparation and properties of the thin films are described elsewhere[4,5]. The aging conditions for the bulk Al-2%Cu are: i) held at 510°C for 2 hours to completely dissolve the Cu into the Al matrix, ii) quenched to room temperature, and iii) held at 246°C for 24 hours to form θ-Al_2Cu phase at the grain boundaries.

Electrochemical Testing

Pure Al wire electrodes (99.999%, 0.25mm dia.) were used to simulate the Cu

depleted grain boundary zone of the aged alloy containing equilibrium θ-Al_2Cu precipitates. Since the currents associated with the metastable pits are in the 0.01 μA range, small surface areas (approximately 0.1 cm^2 to 0.01 cm^2) were used in order to minimize the background current associated with the passive response of the materials. Several types of experiments have been performed using Al-2%Cu and pure Al samples. Pitting potentials for pure Al, open circuit potential transient results for aged Al-2%Cu, as well as pertinent conclusions were reported in the 1993 renewal proposal.

Potentiostatic experiments were performed using pure Al wire electrodes. Potentials below the pitting potential for pure Al at the given Cl^- concentration were chosen to study metastable pitting transients. It is well established that current spikes correspond to the occurrence of a pitting event. Williams and coauthors found that the number of pits observed by scanning electron microscopy corresponded exactly with the number of transients observed in their system[6]. Individual pit current transients were analyzed to determine pit size using the following Faraday Law relationship and assuming hemispherical pits:

$$r_{pit} = (3AW/2\pi zF\rho)^{1/3}(\int(I_{app} - I_{ox})dt)^{1/3} \qquad (1)$$

where r_{pit} is the pit radius, AW is atomic weight, z is the valence, F is Faraday's constant, ρ is the density of Al, I_{app} is anodic current, I_{ox} is passive current, and t is time. Typically, current versus time data were analyzed up to the peak metastable pit anodic current. Apparent pit current densities were determined at the peak pit current by dividing the peak pit current by the area determined from the pit radius given by Equation (1). Note that this procedure underestimates pit current by an amount equal to the cathodic reaction rate in the pit as shown in the following equation:

$$I_{app} - I_{ox} = I(pit)_{an} - I(pit)_{cath} \qquad (2)$$

where $I(pit)_{an}$ is anodic pit current and $I(pit)_{cath}$ is the cathodic pit current.

Results During Reporting Period

Deterministic Analysis of Metastable Pitting of Pure Al

Constant potential experiments were conducted on high purity Al wire electrodes. The smallest observed current transients considered were greater than twice the background system noise of 0.3 nA. A current transient from a pure Al wire electrode in 10^{-3} M Cl^- solution and -0.65 V applied potential is shown in Figure 1. The average time to reach maximum peak current was 1 second and the average time for repassivation was 22 seconds

for pit current transients. These times are in reasonable agreement with metastable pitting observed in OCP transients for Al-2%Cu in Cl^- undergoing pit initiation and repassivation. A dynamic micropolarization experiment yielded a time for repassivation of approximately 100 seconds for Al in a solution with a pH of 6.9[13]. Hence, repassivation of pits in Al is a process that occurs within the order of tens of seconds. However, the charge associated with the metastable pit current decay is greater than the charge necessary to reform the approximately 2 nm thick Al_2O_3 passive film indicating a inefficient repassivation process in the pit environment.

In order to better understand metastable pitting phenomena, an aqueous phase inhibitor was added to Cl^- containing solutions. It is well established that inhibitors can raise the pitting potentials of Al based alloys. Hence, inhibitors are a logical variable to incorporate as a diagnostic for examining the relationship between metastable and stable pitting. Inhibitor efficiency ranged from NO_3^- > CrO_4^{-2} > acetate > benzoate > SO_4^{-2} [14]. It is generally accepted that the aqueous inhibitor concentration must exceed the halide concentration in order to be effective in raising the pitting potential. However, the influence of inhibitors on the metastable pit process is unclear. Figure 1 shows the metastable pitting present with nitrate inhibitor (10^{-2} M NO_3^-) added to the 10^{-3} M Cl^- solution as compared to 10^{-3} M Cl^-. It can be seen by comparing the two current-time series that the inhibitor decreased the number of metastable pitting events and decreased the amplitudes of the individual current spikes.

The average pitting potential for pure Al in 10^{-3} M Cl^- was -0.35 V (SCE) (see 1993 renewal proposal). By adding 10^{-2} M NO_3^- the pitting potential increased to 1.63 V (SCE). It can be seen in Figure 2 that number of pitting events with 10^{-2} M NO_3^- becomes significantly less as the exposure time increases. Metastable pit current transients were completely inhibited for the same experimental conditions as in Figure 1 with 0.1 M NO_3^- added. The diagnostic information presented here confirms the hypothesis proposed earlier that the greater the number of metastable pitting events, the higher the probability of forming a stable pit[6] (also see 1993 renewal proposal).

Analysis of the pitting transients in the absence of inhibitors showed that metastable pits which were formed at potentials (-0.5 V, -0.6 V, -0.75 V) less than the pitting potential (-0.25 V at 10^{-4} M Cl^-) have apparent current densities at the peak current that range from about 0.05 to 1 A/cm^2 (Figure 3). In contrast, apparent current densities at a peak current

of 1 to 10 A/cm^2 were found for metastable pits that formed in the pitting potential distribution range (-0.1 V, -0.35 V, -0.42 V). Moreover, more metastable pitting events were observed in this potential range, consistent with a higher probability of breakdown[6]. It should be noted in Figure 3 that stable pits formed at high potentials (0.1 V, 0.5 V, 1.0 V) also have pit current densities that range from 1 to 10 A/cm^2. The significance of this will be discussed later. These stable pit current densities were calculated assuming that the initial rise in the anodic current corresponded to the formation of a single stable pit. Current rise time periods approximately equal to the time required to achieve peak current for metastable pit were used to calculate the charge associated with the stable pits. Evaluation at equivalent times provides a common basis for comparison.

The current densities of metastable pits formed at the lower potentials are weakly dependent or independent on applied potential. This behavior can be seen more clearly in Figure 4 which is a plot of the averaged pit current density at peak current for a number of pit transients at a given applied potential. These averages are then plotted versus applied potential. Pistorius and Burstein also found that the pit current density was not strongly affected by the potential for AISI type 304 stainless steel in Cl^- solution[8]. Since the pit current density is weakly dependent on the applied potential, it can be argued that the metastable pit growth at these potentials may be under diffusion control. At higher potentials, averaged metastable pit current densities follow an approximately linear relationship with respect to applied potential, hence, may be ohmic controlled. Other researchers have reported pit growth in Al to be ohmic or diffusion controlled[5,8,10,12].

Metastable pit life-times were distributed between 0.2 second to 60 seconds. According to Frankel, the H_2 current density is probably 10% to 30% of the pit current density[10]. This result may indicate that repassivation of a pit is promoted by rupture of the pit oxide cover as a result of accumulated H_2 supplied by H_2 evolution. Once the pit cover is removed, dilution of the pit solution occurs. Scully argued that the calculated diffusional length associated with pit depths required to maintain a concentrated environment (1 M to 3 M) in open pits is 1.5 to 4.5 μm at 10 A/cm^2, 15 to 45 μm at 1 A/cm^2, and 150 to 450 μm at 0.1 A/cm^2 [5]. The calculated apparent metastable pit radii at peak current in Figure 3 (before repassivation begins) vary only from 0.2 μm to 2 μm. Hence it would appear that an oxide film or a salt film is required to discourage small open pits from repassivating. It should be noted the actual pit sizes may be slightly larger due to the anodic current being

higher than measured because of hydrogen evolution in the pits. Final pit sizes will be larger still due to additional growth during the anodic current decay.

Metastable pits with higher current densities may tend to repassivate faster due to greater H_2 production inside the pits. However, it can be shown that dilution of the pit solution due to mixing caused by H_2 bubbles is not a factor in stable pit survival *once the stable pit reaches a critical size*. This critical pit size may be estimated. N. Ibl reported an equation relating H_2 evolution (v in $cm^3/cm^2 \cdot sec$) to diffusion layer thickness (δ)[10]:

$$\delta = (D/A)v^{-0.53} \qquad (3)$$

where $D = 10^{-5}$ cm^2/s and $A = 0.0347$ $(cm/s)^{0.47}$. Taking the H_2 evolution current density to be 30% of either 1 or 10 A/cm^2, the corresponding diffusion layer thicknesses are approximately 17 and 5 μm, respectively. These calculated dimensions are approximately equal to or less than the size of stable pits once they reach a critical size which apparently is of the order of 15 μm for the current densities stated. The concentrated pit environment can still be maintained at the base of the pit with these diffusional layer thicknesses and current densities. These findings are in agreement with Figure 3 ($\odot$,x,$\Diamond$,+) which shows the current associated with four stable pits at a lifetime equal to that of metastable pits peak current rise times. The apparent pit sizes are approximately 18 μm.

However, this argument gives no explanation of how the pits survived long enough to achieve pit radii of nearly 18 μm for time periods approximately equal to metastable pit life-times. Possible explanations for stabilization of a pit are a combination of current densities considerably larger than 1 A/cm^2, a reentrant pit geometry, and a fast rise in pit current.

Conclusions

There is a distribution of pitting potentials due to the distribution of pit current densities and pit current rise times. Perhaps reentrant pit geometries favor stabilization of pits also. The cumulative number of pitting events increases with applied potential. Apparent metastable pit current densities ranged from 0.05 A/cm^2 to 10 A/cm^2. Stable pit current densities ranged from 1 A/cm^2 to 10 A/cm^2 with larger apparent pit radii formed for time periods approximately equal to metastable pits currents rise times.

Proposed Research Plan for 1993

For 1993, the OCP and potentiostatic experiments described in the Technical Approach section will be continued with a greater emphasis on the thin film samples. Another set of experiments planned for the next year are galvanic coupling experiments. In this case, two identical Al-2%Cu samples are galvanically coupled with a zero resistance ammeter. This arrangement will allow for both the current and potential fluctuations associated with metastable pitting to be recorded and analyzed. There will also be a greater focus on applying nonlinear dynamic techniques to analyze the pitting transients obtained from the various experimental methods. A discrete Legendre polynomials coordinate transformation method proposed by Gibson and et al.[15] has been determined to be a possible technique for analysis the pure Al current transient data. The discrete Legendre polynomials can increase the signal to noise ratio of time series data and give good state space reconstruction parameters (time delay and embedding).

References

1. K. Urushino and K. Sugimoto, Corrosion Science, 225, 19 (1979).

2. K. Sugimoto, K. Hoshino, M. Kageyama, S. Kageyama, and Y. Sawada, Corrosion Science, 709, 15 (1975).

3. J.R. Galvele and S.M. DE Micheli, Corrosion Science, 795, 10 (1970).

4. J.R. Scully, R.P. Frankenthal, K.J. Hanson, D.J. Siconolfi, and J.D. Sinclair, J. Electrochem. Soc., 137, 1365 (1990).

5. J.R. Scully, "Proceedings of the Symposium on Critical Factors in Localized Corrosion", G.S. Frankel and R.C. Newman, Editors, 144, Vol. 92-9 (1992).

6. D.E. Williams, J. Stewart, and P.H. Balkwill, "Proceedings of the Symposium on Critical Factors in Localized Corrosion", G.S. Frankel and R.C. Newman, Editors, 36, Vol.92-9 (1992).

7. R. Holliger and H. Bohni,"Proceedings of the Symposium on Computer Aided Acquisition and Analysis of Corrosion Data", M.W. Kendig, U. Bertocci, and J. Strutt, Editors, ECS PV 85-3, 200-209 (1985).

8. P.C. Pistorius and G.T. Burstein, "Concerning the Nature of Pitting as Studied by The Examination o Current Transients," In Proceedings of the 5th International Conference of the South African Corrosion Institute, Johannesburg, South Africa, August (1990).

9. T. Hagyard and J.R. Santhiapillai, J. Appl. Chem., 323, 9 (1959).

10. G.S. Frankel, Corrosion Science, 30 (12), 1203-1218, (1990).

11. H. Kaesche, "Localized Corrosion", R.W. Staehle, B.F. Brown, J. Kruger, (1974).

12. F. Hunkeler and H. Bohni, Corrosion, 37 (11), 645-650, (1981).

13. E. Kirowa-Eisner, C. Zollman, and E. Gileadi, J. Electrochem. Soc., 137, 1378 (1990).

14. H. Bohni and H.H. Uhlig, J. Electrochem. Soc., 116, 906, (1969).

15. J.F. Gibson, J.D. Farmer, M. Casdagli, and S. Eubank, Physica D, 57, 1-30, (1992).

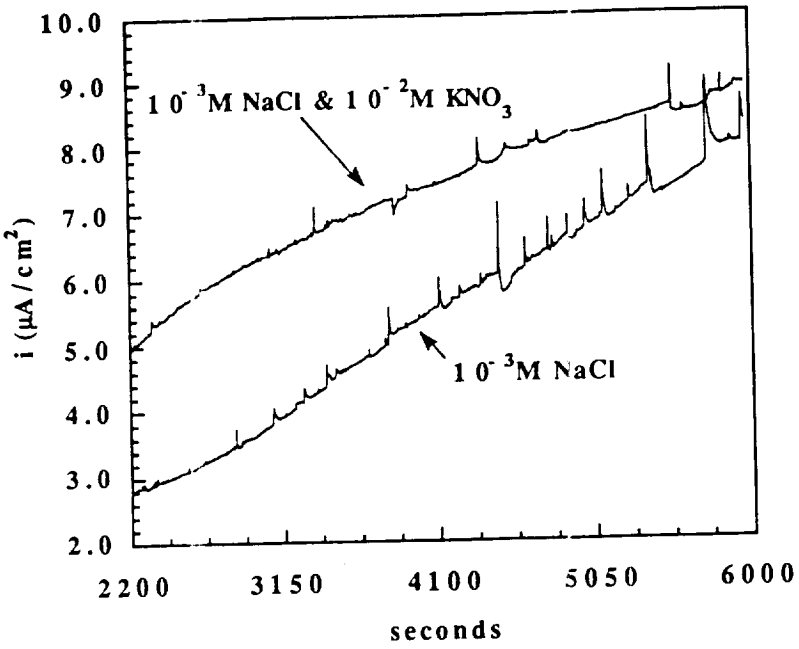

Figure 1: Anodic current time series from Al looped wire electrodes in the deaerated solutions shown in the figure. Applied potential = -0.65V (SCE).

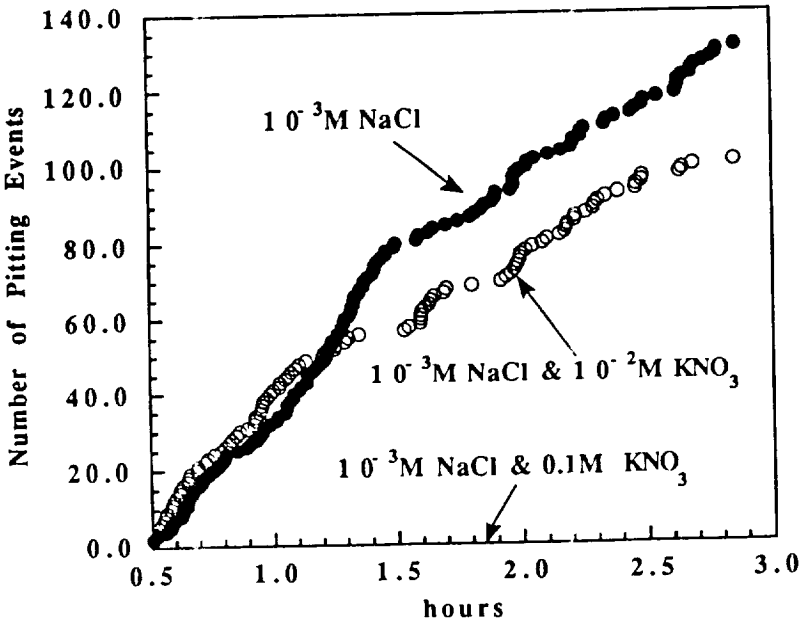

Figure 2: Cumulative number of pitting events from Al looped wire electrodes in the deaerated solutions shown in the figure.
Applied potential = -0.65V (SCE).

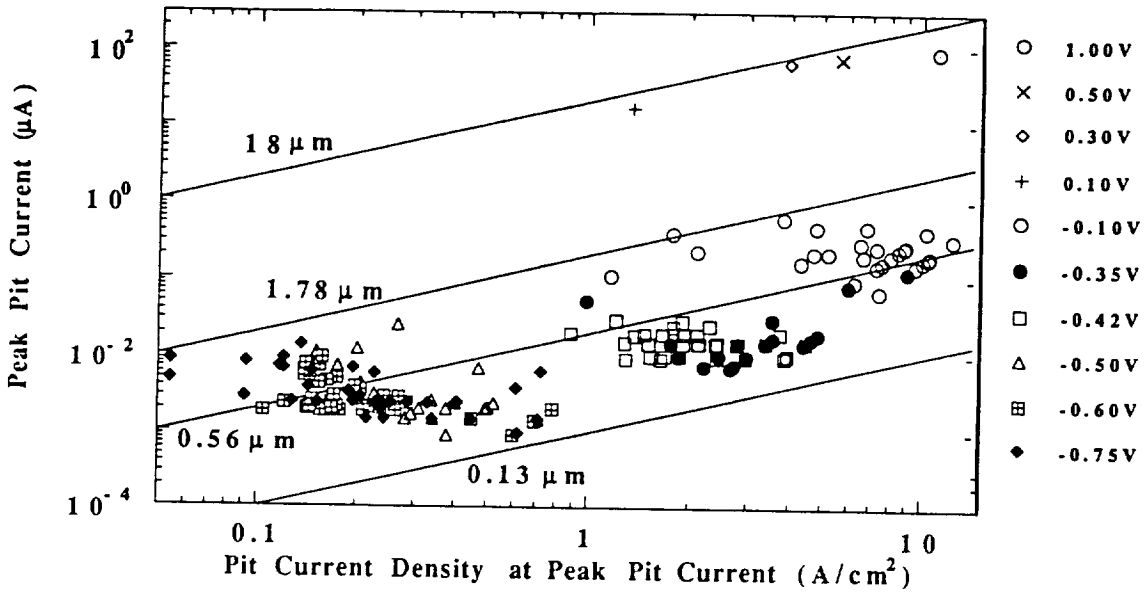

Figure 3: Relationship between peak currents and apparent pit current densities at peak current for metastable and stable pitting transients. Al looped wire electrodes in 10^{-4}M NaCl. The lines of constant slope represent lines of constant pit radii.

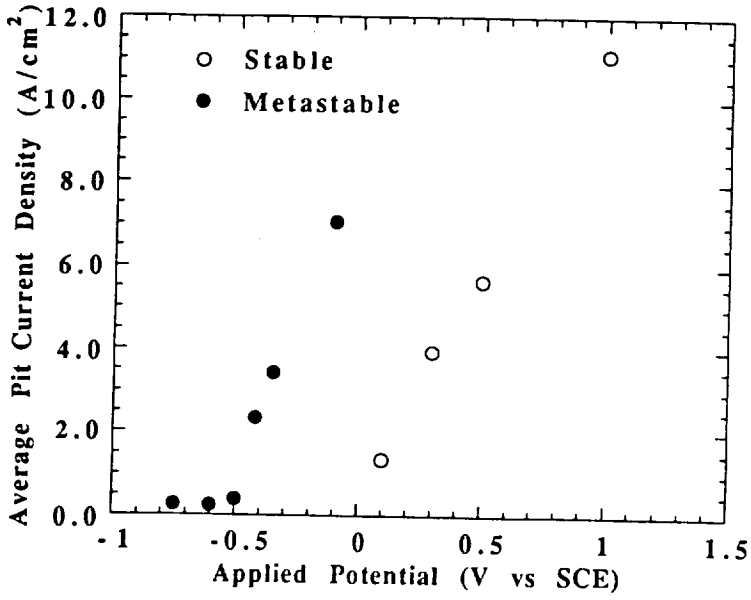

Figure 4: Relationship between average apparent pit current densities and applied potential. Taken from data shown in Figure 3.

Project #9 **Investigation of the Effect of Thermal Treatment on the Mechanical Properties of Ti-1100/SCS-6 Composites**

Douglas B. Gundel and F.E. Wawner

Objective

The objective of this study is to investigate the influence of thermal exposure, both isothermal and cyclic, on the microstructure, mechanical properties, and fracture characteristics of Ti-1100/SCS-6 fiber composites.

Approach

The Ti-1100/SCS-6 composites evaluated in this study will be fabricated at NASA Langley Research Center. These materials will be subjected to thermal exposure at UVa and evaluated for microstructural changes, tensile properties in the longitudinal and transverse directions, and fracture characteristics. Thermal cycling experiments will include both low to high temperature and ambient to cryogenic temperatures. Scanning and transmission electron microscopy will be utilized to delineate microstructure and any associated changes with environmental exposure. It is anticipated that an upper practical temperature limit will be defined for utilization of this composite system. Fracture analysis will be conducted by SEM to relate interface and microstructure contribution to the failure process.

The specific research plan has been outlined previously[1].

Research Progress

The important conclusions of the thermal cycling study have been previously reported[1,2] and will be summarized here briefly. Cycling of longitudinal samples from 150 to 800°C, 500 times, resulted in extensive damage to poorly fabricated samples (as determined by ultrasonic c-scans of the panel), whereas well-consolidated specimens exhibited only slight degradation. The degradation was attributed to matrix-ply debonding that led to increased matrix embrittlement and fiber-matrix debonding. The degradation of transverse samples during the same exposure was attributed to the rapid diffusion of matrix-embrittling species down the fiber-matrix interface and into the matrix. The studies of the current

reporting period focussed on some fundamental aspects of the factors that have been found to contribute to the strength degradation. These include matrix embrittlement, fabrication problems, and transport of species from the air down the fiber-matrix interface.

Matrix Embrittlement

The attack of the matrix by species from air (oxygen, nitrogen) is a critical contributor to the strength degradation of the composite in both orientations. Tensile testing and microscopic examination of the matrix following exposure in air were performed. Unreinforced 4-ply matrix samples were exposed in exactly the same manner as the composites, as were single matrix foils of varying thicknesses. The neat panels exhibited only slight degradation after isothermal exposure (735°C, 26.5 h), or the thermal cycling exposure, and strained to 1.0-3.0% before failing (just as in the as-fabricated condition). Individual matrix foils exhibited a dramatic decrease in strain to failure and strength. The ultimate strain of the foils was 0.7 to 0.8% if they were 240 μm thick (the thickness of the supplied foil), and 0.35% to 0.55% if they were 200 μm or thinner.

Figure 1a compares the stress-strain curves of three thicknesses of Ti-1100 following the thermal cycling exposure. The stress-strain curves of the thicker foils exhibited a reduction of slope at a strain of about 0.5%. Replica studies of the foil surfaces indicate that this change of slope was associated with the formation of cracks perpendicular to the tensile axis, which closed upon relief of the stress. Figure 1b is a micrograph showing the distribution and length of the surface cracks from a replica taken just after they had formed. The cracks were found to extend to a depth of about 25-50 μm into the titanium, and the stress-strain curves indicated that they grew to this length in a short range of stress at approximately 0.5%. Vickers microhardness traverses were performed on these specimens and an average value of VHN equalling 420 was found in the titanium at the tip of the cracks, as opposed to a VHN of 300 in the center of the 240 μm foils. As expected, after the brittle layer was removed a change in the slope of the stress-strain curve was not observed, but the composite still had an ultimate strain to failure of only 0.7 to 0.8%. This indicates that the exposure significantly altered the properties of the titanium in the core of the foil.

The effect of the environmental attack on the composite can now be addressed. The lack of significant damage to the neat matrix plies suggests that thick composite samples, where the attack is strictly confined to the composite surfaces, should likewise exhibit limited

degradation (as seen in the well-consolidated longitudinal composite). Extensive degradation of the composite occurred as a result of the exposure of increased matrix surface area to the environment. In the case of longitudinal composites, this was achieved via matrix ply debonding, and in the transverse composite the fiber-matrix interface allowed the rapid transport of oxygen into the matrix.

Fabrication

Matrix-ply debonding in the case of longitudinal composites exposed a larger matrix area to the environment, and destroyed the fiber-matrix bonds. The result was much lower strain-to-failure and strength of the samples. The matrix-matrix bonds are therefore critical to the performance of the material, and, therefore, it was necessary to investigate the reason for their weakness.

In the as-fabricated condition, the longitudinal composite exhibited some sensitivity to fabrication. The outer samples were often lower in strength than the center ones and had more pulled-out fibers on their fracture surfaces. Following tensile testing, however, even the center samples ("well-consolidated") sometimes contained cracks in the region corresponding to the matrix-ply interface. Polished cross-sections indicated slight microstructural variations and cracks at this interface (see Fig. 2). This evidence suggests that the fabrication process can lead to a matrix-ply bond that is unacceptably brittle throughout the composite panel.

Composites were fabricated in order to observe any cracking or changes in microstructure at the matrix-matrix interface. The hold time at the fabrication temperature was varied to study the effect of exposure to the hot-press environment. Individual matrix plies with and without fibers on them were also placed in the hot-press and held at the fabrication temperature (975°C) for extended periods, but not pressed. This was done in order to examine the foil surfaces which, upon consolidation, become the matrix-matrix interfaces.

Figure 3 is an SEM micrograph of the matrix-ply interface of a sample that had been held for two hours at the fabrication temperature prior to consolidation. The extensive cracking in the titanium immediately adjacent to the bond line is clear, as well as microstructural variations in this region. There was also a carbon-rich precipitate found at the matrix-matrix interface, whose presence indicates extreme carbon contamination of the titanium. This evidence points to some interaction of the hot-press environment with the

matrix that led to embrittlement. Careful observation of the matrix plies, consolidated without pressing, and an experiment done where the matrix did not directly touch the graphite parts in the furnace (with no binder present), revealed that the species causing the embrittlement was present as a gas. X-ray diffraction of these matrix foils revealed that there was a significant amount of titanium carbide on the surface of the foils. It was postulated that carbon bearing gases (CO or CO_2) were reduced by titanium on its surface, converted to the atomic species, then transported into the titanium. This phenomenon was observed by Outlaw et al.[3] under ultrahigh vacuum conditions using pure titanium.

Diffusion bonding of the composite is dependent upon the matrix surface undergoing deformation. A TiC-covered, carbon-rich, oxygen-rich surface layer on the foils will have a much larger flow stress than the pure alloy, and therefore the bonding will be inhibited compared to a matrix with clean surfaces. Of course, the composites that were exposed and tensile tested were made at NASA LaRC under slightly different conditions than in this study, but similar contamination can be expected. The gases evolved from the binder (in the tested composite) are C and O-rich, and at the high temperatures at which the binder was pyrolyzed (400-500°C), TiC can form (according to Outlaw et al.). The vacuum in which they were fabricated (10^{-3} torr) was not high and therefore contamination from adsorbed gases, even pump oil vapor, probably occurred.

Even if there was no hold time at the fabrication temperature, the TiC layer was still found to be present on the foils. In the AF Ti-1100 composites, however, when composites were pressed just after reaching the fabrication temperature, no TiC was apparent at the bond line. Presumably, the TiC dissolves into the titanium when the surfaces are no longer exposed to the hot-press environment.

A computer program was written to analyze the dissolution of TiC at the matrix-matrix boundary if the process is diffusion-controlled. The analysis required the temperature of fabrication, foil thickness, initial carbon concentration, and the predominant titanium phase of the alloy. It assumed a linear concentration gradient of carbon in the matrix and that the solubilities and diffusivities of carbon in the alloy are the same as those reported by Wagner et al.[4] for pure titanium. The phase boundaries from the Ti-C phase diagram were also utilized[5].

Figure 4 is a plot obtained from the model of the size of the TiC layer on the foil versus the time at exposure. The plot is interpreted as follows. The TiC layer present on

the titanium just prior to consolidation at the fabrication temperature has a certain thickness. Upon consolidation, two such layers come together, and the initial combined thickness is the value plotted as zero on the figure. This thickness is reduced during the high temperature exposure in the hot press due to dissolution of the TiC. The temperatures chosen were typical for diffusion bonding of beta (Ti-15-3 and BETA 21S) and alpha alloys (Ti-1100). For example, the model predicts that the thickness of the TiC layer between two 250 μm alpha alloy foils will be reduced by 17 μm after they are pressed together and held at the fabrication temperature for one hour. Therefore, if the TiC layer is 2.5 μm thick on each foil, and the sample is pressed, the TiC layer is predicted to dissolve completely in the alpha foils, but not in the beta alloys.

The thickness of the TiC prior to consolidation is not known for the beta alloys, but has been measured to be 8 μm for a Ti-1100 foil that had been ramped up to the fabrication temperature and then furnace-cooled. From the plot it can be seen that only the 250 mil thick alpha alloy is expected to be capable of completely dissolving this amount of TiC within an hour. The thickness of the TiC on the same alloy foil after a two hour hold at the fabrication temperature was measured to be about 12 μm. The model predicts that none of the systems investigated are capable of dissolving this thickness of TiC. The sample from Fig. 3 which still contained some TiC at the bond line following consolidation was composed of 240 μm Ti-1100 (alpha alloy) foils. The layup was held at the fabrication temperature for two hours, then pressed for 30 minutes. The model correctly predicts that the TiC formed will not completely dissolve. An important contributing factor, that this simple model does not take into account, is the dissolution of the TiC prior to applying pressure. The constant contamination of the titanium with carbon and oxygen during the two hour hold will reduce its ability to accept more, and therefore lessen the rate of TiC dissolution upon consolidation.

From the model it seems that the beta alloys have a much lower ability to absorb the contamination than the alpha alloys, and the foil thickness has a strong effect on the rate that the TiC is absorbed. The reason that for the difference between the two rates for the phases is mainly due to the disparity of the solubility of carbon in the two. The foil thickness is important because the dissolution rate proceeds rapidly until the carbon concentration in the center of the foil begins to increase; it then proceeds with a decreasing rate. Due to the various assumptions made in this model, and unknown quantities such as the amount and distribution of carbon and oxygen in the titanium, these calculations can only be regarded as

a rough comparison; however, the relative effect of the foil thickness, temperature, and alloy phase are expected to be accurate.

The decoration of the diffusion bond (DB) line that is observed in composites whose matrix alloys predominantly contain the beta phase (Ti-15-3, BETA 21S) of Ti may be explained by this contamination phenomenon. The precipitate phase on the DB line has been identified in the present research to be carbon-rich. Under normal fabrication procedures, the beta alloys have been observed to exhibit this effect, while the alpha alloys have not. Using Fig. 4 it can be seen that if similar thicknesses of TiC were on the foils of the two alloys prior to pressing, some may still remain in the beta composite as opposed to the alpha. The effect of the TiC layer in the beta composite is not known, but the matrix near the region did not contain cracks, as did the alpha composite when TiC remained (Fig. 3). This is probably due to the lower concentration of the interstitials in the beta phase, and possibly that it is not embrittled by them to the same extent as the alpha phase.

There are two important ways that foil surface contamination during fabrication can harm the composites. The surface layer can interfere with the diffusion bonding process by not allowing the necessary deformation of the matrix and the interdiffusion of titanium atoms from adjacent foils. Additionally, interstitial elements are detrimental to the fracture properties of the matrix, and a high concentration of them at the matrix-matrix bonds can cause the observed cracking, and matrix-ply delamination. For these reasons it is imperative to minimize this contamination.

Interfacial Transport of Oxygen

In order to evaluate the rate of the oxygen transport down the fiber-matrix interface, samples of specially-made composite were exposed to 800°C for 100 hours. These samples had a very low volume fraction of fibers to isolate each fiber and keep them from interacting.

After exposure, these samples were sectioned along the fiber axis to reveal the longitudinal cross section. Optical and scanning electron microscopic analyses were performed on the samples. The matrix region immediately adjacent to the fibers etched differently than the bulk matrix. This region was very thin near the center of the sample, and relatively thick near the original surface where the fiber end was exposed. It was attributed to oxygen that travelled down the fiber-matrix interface and stabilized the alpha phase thereby leading to all-alpha titanium near the interface, and the usual alpha phase with a small amount of beta elsewhere.

Fig. 5 is an SEM micrograph of the interfacial region approximately 0.8 mm from the fiber end. At least 1 mm into the composite there appeared to be a gap (about 1 μm thick) between the bulk SiC of the fiber and the adjacent layer. On the matrix side of the gap was a layer approximately 3-4 μm thick that was well-adhered to the matrix. EDS of this layer revealed that it only contained a large amount of silicon and oxygen and some carbon. The region just outside of this silicon-rich zone was a thin layer of severely cracked titanium, followed by the uncracked, bulk Ti of the composite.

The nature of the interface suggests that the fiber-matrix interface had undergone a severe amount of damage from interaction with the air. The oxygen appears to have reacted with the SCS layer and transformed it to SiO_2. The carbon that was initially present in this layer was largely gone after exposure, thereby resulting in the shrinkage of the SCS layer and the formation of the gap. The carbon may have been transported out of the composite in the form of CO or CO_2.

An effective diffusivity can be calculated from the angle that the boundary of the oxygen-affected matrix approaches the fiber-matrix interface, but the value obtained will have little meaning due to the significant alteration of the interface. It is assumed that the gap would have permitted a much greater flux of oxygen into the composite, as opposed to the unaffected interface; therefore, the transport rate down the interface probably changed significantly with time and distance into the material. This situation is therefore not one that can be evaluated by a boundary diffusion model.

Figure 6 compares the stress-strain curves of as-fabricated, isothermally exposed, and cycled transverse samples. The initially high modulus of the AF sample is not present in those that were exposed. As proposed by Nimmer[6], this high initial modulus in the unexposed transverse samples is due to residual stresses in the matrix that clamp down on the fibers and give the interface a false "tensile strength". A loss of some material around the interface will reduce the residual stresses present. Since a gap was present at room temperature it is apparent that there were no residual stresses present in that region because no interfacial bond remained. The initial modulus of that region, therefore, is expected to be equal to the secondary modulus of the unexposed composite. This can be observed in the Fig. 6 for the case of the composite cycled to 800°C, 500 times. Its stress-strain curve is nearly parallel to that of the unexposed composite after the "knee", thereby possibly indicating that the thermal stresses were relieved upon exposure. In the isothermally exposed

samples, the modulus was slightly higher, indicating that the damage accumulated was less severe. The amount of interfacial damage in specially-made (low volume fraction), thermally-exposed (cyclic and isothermal) samples is currently being evaluated.

The severity of interfacial degradation accumulated while isothermally exposing the samples is great, but it is possible that thermal cycling the composite may yield this amount of damage in a shorter time. The reason is that oxygen ingress may be accelerated by mechanical damage done to the interface. Slight oxygen attack in addition to thermal stresses may cause the SCS-layer and the matrix to crack and separate from the fiber, thereby opening a path for greater attack and advancement of the oxygen. In thermal cycling, therefore, it is expected that a greater volume of the matrix will be embrittled and the depth of oxygen penetration into the matrix will be larger.

Conclusions

The degradation to the composites following the high temperature exposures, isothermal and cyclic, has been found to stem directly from environmental interactions in both the transverse and longitudinal orientations. In the longitudinal orientation, extensive degradation was found to occur only when the samples were poorly fabricated. The reason for the poor fabrication of some samples might have been contamination of the composite during the ramp up to the press temperature. When the matrix-ply bonds delaminated during thermal cycling, more matrix was exposed to the environment and subsequently embrittled. This matrix was also not well bonded to the fibers and therefore it strained to a greater extent than the well-bonded matrix. Its low strain-to-failure caused it to fail at a low composite strain, thereby causing the composite to fail. The transverse samples allowed greater matrix attack by the environment via the many fiber-matrix interfaces that intersect the composite surface. This embrittlement lowered the strain-to-failure of the composite. The lower initial modulus of the exposed transverse samples may have been caused by erosion of the interface during exposure that led to a reduction of thermal stresses. Apparently, the transport down the interface does not occur fast enough to cause severe embrittlement in the gauge section of the longitudinal samples, but only affects the gripped sections.

Possible Approach to Solve Problems

The problem of the embrittlement of the titanium with interstitial elements does not

seem to be solvable, but the effect can be minimized by considering the other problems. In longitudinal samples, problems of fabrication quality need to be addressed, while in transverse samples the main cause of degradation is high diffusion rates of oxygen down the interface.

The effect of poor fabrication in the longitudinal composites will most likely overshadow any other fundamental processes that can lead to strength degradation. Cleanup of the environment of the hot-press will most likely help a great deal, but it is possible that it cannot be cleaned up completely due to the burnout of the organic binder necessary to hold the fibers in place. It is possible that poorly-bonded matrix-ply interfaces that have not yet cracked can be improved. Cracking at this interface is primarily due to the presence of interstitial atoms (O and C) and perhaps microscopic pores. It is expected that a long-term anneal at a high temperature in an inert atmosphere will promote coalescence of the voids, redistribution of the interstitials throughout the matrix, and, perhaps, titanium interdiffusion and grain growth across the bond line. This thermal exposure will also cause growth of the fiber-matrix reaction zone, but its kinetics are well known and the exposure time and temperature can be chosen with this in mind. The samples can be c-scanned before and after the heat treatment to determine if they are bonded more completely, and if so, exposure tests of annealed versus untreated samples can be done.

The problem of fast diffusion of the species from the air down the interface in the transverse orientation can be mitigated by using wide samples, protecting the fiber ends from oxygen, or possibly altering the interface. The use of wide samples will minimize the volume of the matrix that is embrittled. If they are made sufficiently wide, a different degradation mechanism may dominate. Protection of the fiber ends is a viable method to stop the damage related to diffusion down the fiber-matrix interface, and this may be how it will be avoided in service. It is possible that the erosion of the carbon-rich SCS-layer is responsible for allowing the oxygen into the composite at a high rate. This can be tested by measuring the diffusion of oxygen down a similar interface of an uncoated fiber.

Future Work

The main objective of this work is to note any property degradation following thermal exposure and to relate it to microstructural changes in the composite. Thus far the observed degradation has been ascribed to problems with fabrication for the longitudinal samples, and

diffusion down the fiber-matrix interface for transverse samples. It is of interest to solve these problems in order to find other factors that can lower the properties, and in doing so determine the upper exposure limit of this composite system. The most important item to address is therefore the problem of fabrication. New samples without weak matrix-ply interfaces are necessary. If it is not possible to change the fabrication procedure, then samples from the center of the panels can be studied, and/or a heat treatment can be performed to possibly improve the matrix-matrix bonds. When this is accomplished, the work outlined elsewhere can be resumed[1]. These include isothermal exposures and cycling for longer times at lower temperatures. Additional experiments using wide transverse samples (greater fiber aspect ratio) are also of interest because the volume of matrix affected will be reduced, and therefore another degradation mechanism might dominate. Although a great deal has already been learned, these proposed studies for both the transverse and longitudinal samples may uncover other, perhaps more fundamental, processes that lead to property degradation.

References

1. F.E. Wawner, D.B. Gundel, Renewal Proposal submitted to NASA, Grant No. NAG-1-745, November 1992.

2. D.B. Gundel, F.E. Wawner, Progress Report Presentation at NASA Langley, Grant No. NAG-1-745, July 1992.

3. R.A. Outlaw, W.S. Lee, S.N. Sankaran, D. Wu, R.K. Clark, *Scripta Met. et Mat.* **24** (1990) 171-176.

4. F.C. Wagner, E.J. Bucur, M.A. Steinberg, *Trans. ASM* **48** (1956) pp. 742-761.

5. R.I. Jaffee, *Prog. in Metal Physics* **7** (1958) pp. 65-163.

6. R.P. Nimmer, *J. Composites Technology and Research*, **12**, No.2, Summer 1990, pp. 65-75.

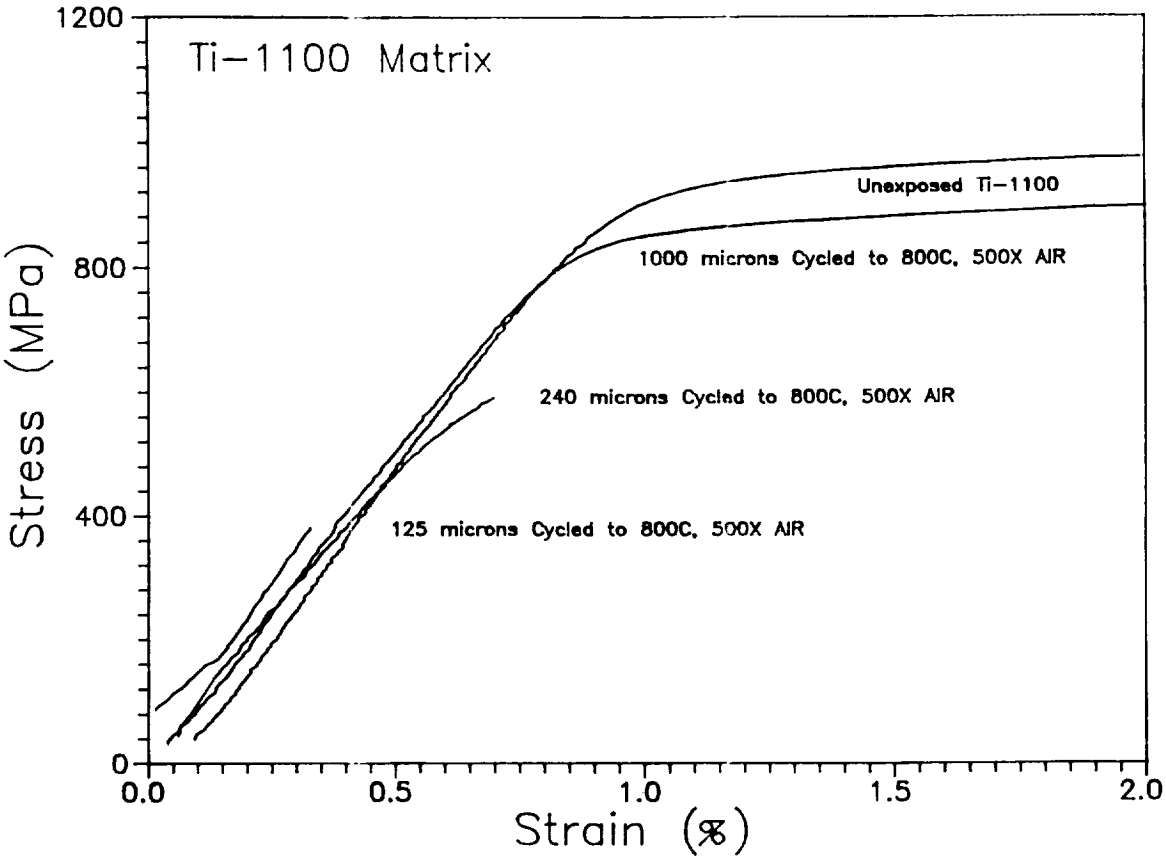

a

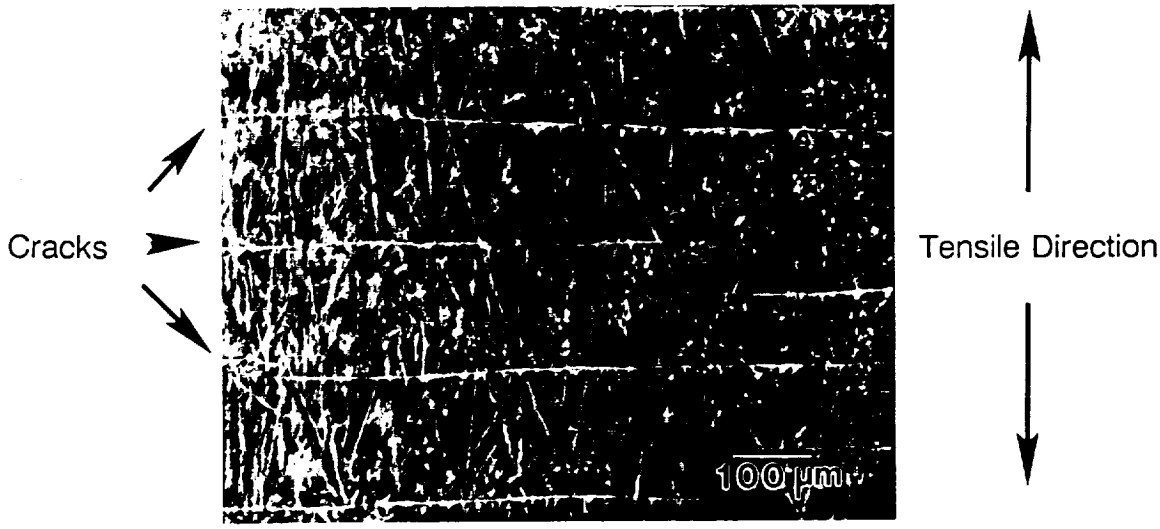

b

Figure 1. 1a is a comparison of the stress-strain curves of different thicknesses of the matrix alone. As expected, the initial thickness had a profound effect of the residual mechanical properties. 1b is an SEM micrograph of a replica of the titanium surface under stress after the cracks had formed.

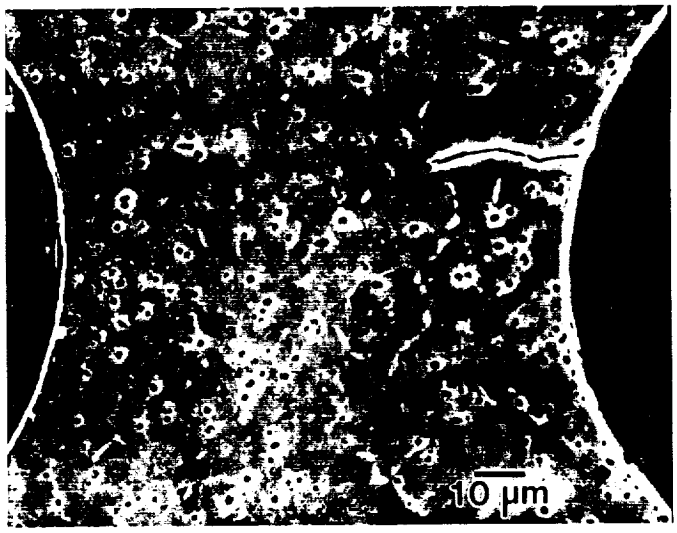

Figure 2. Polished and etched cross section of an as-fabricated longitudinal sample following the tensile test. Note the crack at the matrix-ply bond.

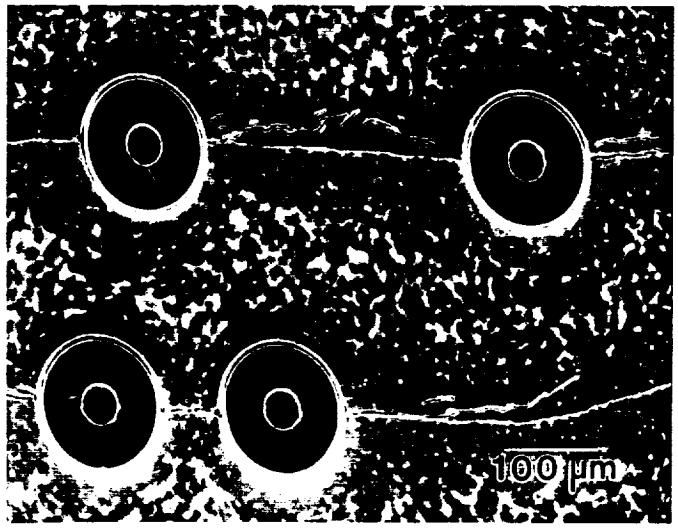

Figure 3. SEM micrograph of sample consolidated after a two hour hold time at the fabrication temperature. Note the matrix cracks and microstructural variations in addition to the bond-line precipitate.

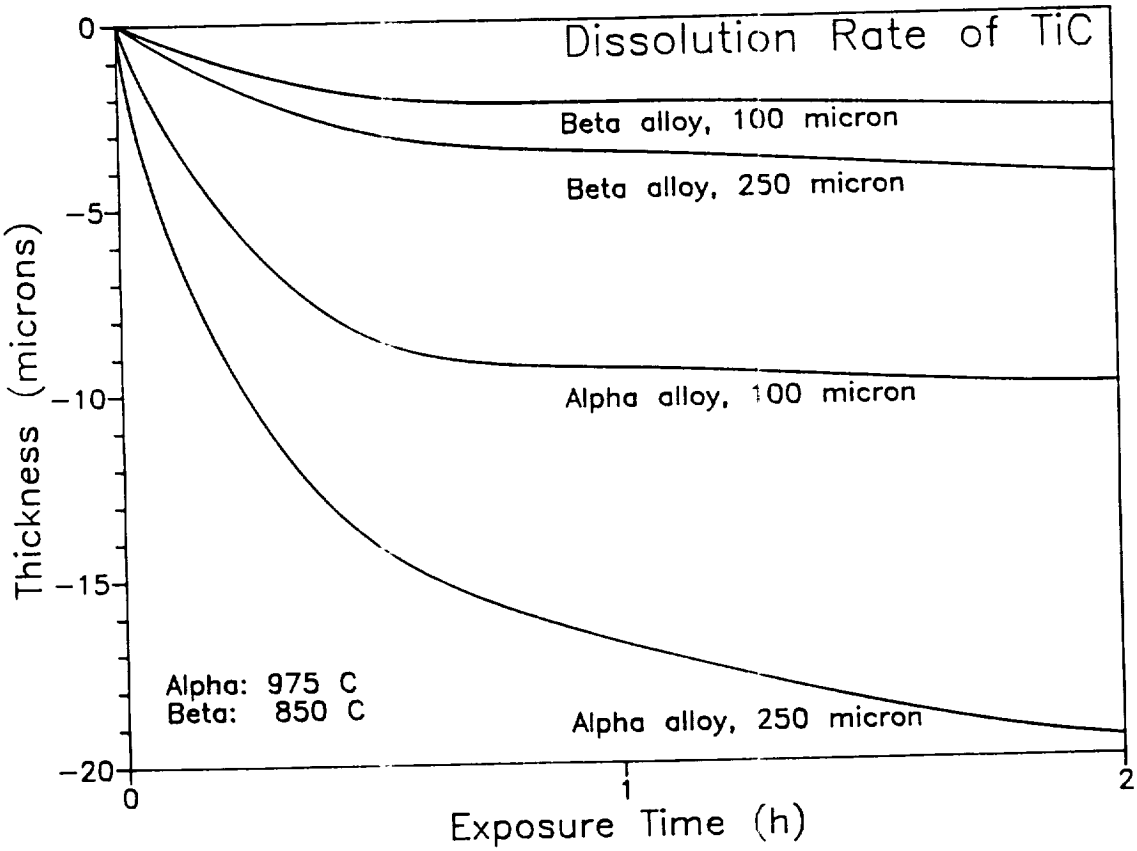

Figure 4. Plot of TiC thickness reduction at the bond line following consolidation. This was constructed using a simple model that assumed the dissolution rate is diffusion-controlled (see text). The rates for the two predominant alloy phases and two foil thickness are compared.

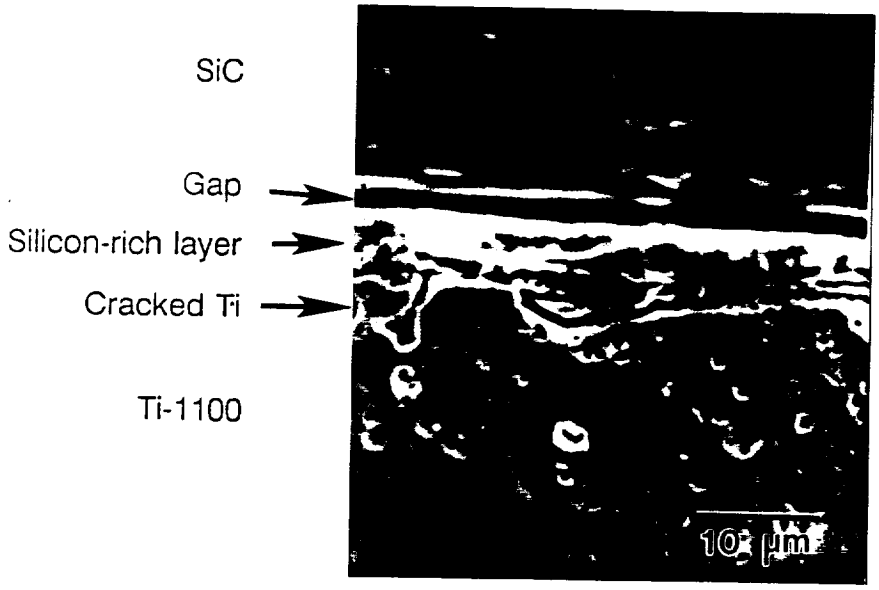

Figure 5. SEM micrograph of the interface of a sample exposed for 100 hours at 800°C. The region was about 0.8 mm from the fiber end. The important features are labelled.

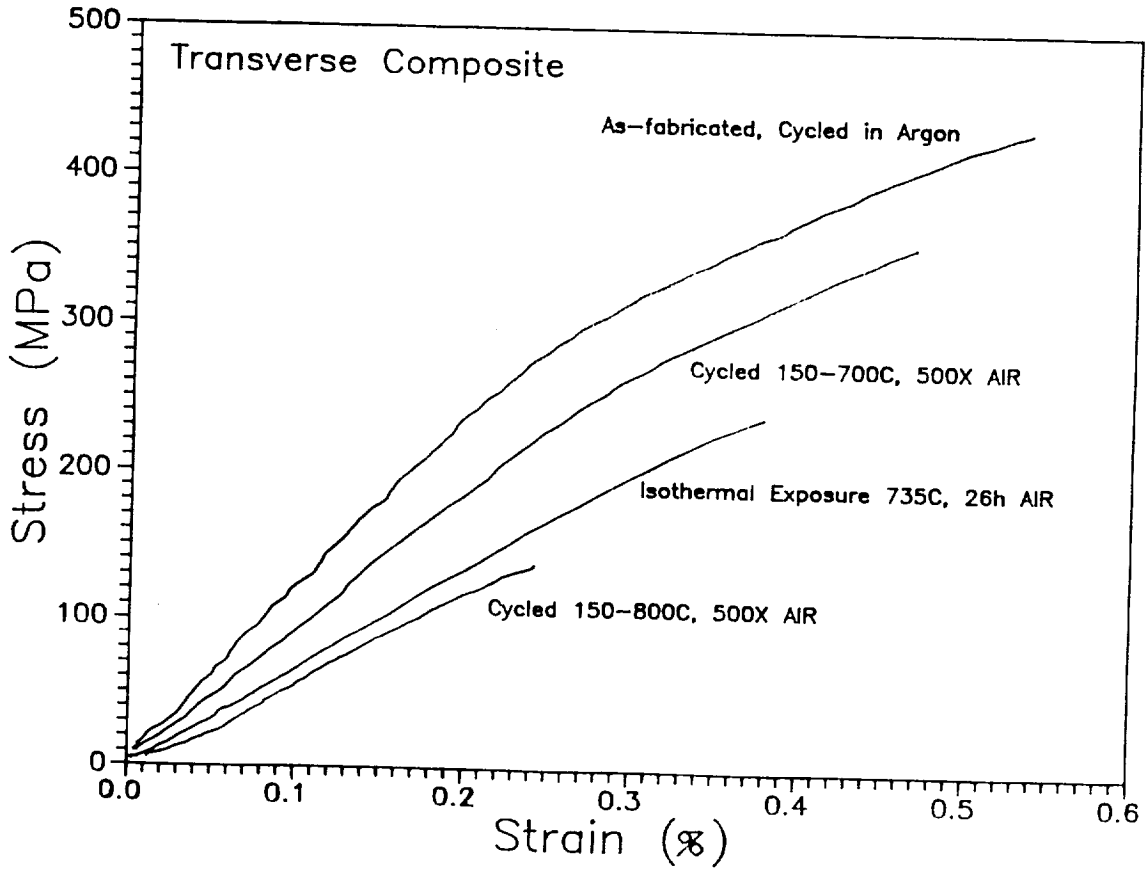

Figure 6. Stress-strain curves of exposed transverse composites. Following exposure the initial modulus was reduced.

Project #10 Processing and Superplastic Properties of Weldalite™ Sheet

Mark Lyttle and John A. Wert

Objectives

The objectives of this research project are to establish the cause of anisotropic and variable superplastic properties of Weldalite sheet, and to identify the thermomechanical processing steps that introduce the anisotropy and variability.

Progress During the Reporting Period

During 1992, two major tasks have been completed within the scope of the present project. First, analyses have been conducted for the two Weldalite alloys, designated 049 and X2095, to characterize evolution of the microstructure and microtexture during the initial stages of superplastic forming. These tests have shown that microstructure/microtexture changes during longitudinal uniaxial extension of the alloys are similar to changes previously observed in Al-Zr-Si and Al-Cu-Zr-Si alloys. High-temperature deformation (concurrent straining and annealing) gradually transforms boundaries that initially have low misorientation angles into boundaries with higher misorientation angles. The evolved microstructure is suitable for superplastic deformation, and large elongations are subsequently obtained.

Second, simulative models of microstructure/microtexture evolution during concurrent straining and annealing have been formulated. The three models involve subgrain rotation associated with boundary sliding, subgrain rotation associated with slip, and grain neighbor switching. A combination of the boundary sliding (sub)grain rotation model and the (sub)grain neighbor switching model most closely reproduces the boundary misorientation distributions found experimentally.

The results of this investigation have been summarized in a paper, entitled "Modeling of Continuous Recrystallization in Aluminum Alloys" by M.T. Lyttle and J.A. Wert, that was submitted to the *Journal of Materials Science*. Several sections of this paper, including all of the figures, are reproduced in the following pages. Copies of the complete paper are available from the authors.

Experimental Observations

Grain orientation and boundary misorientation data for Al-0.24Zr-0.1Si and Al-4.1Cu-0.28Zr-0.1Si alloys (compositions are given in weight percent) have been previously reported[20,21] and are included in the present paper for comparison with model results. Similar experimental observations have been made more recently for a Weldalite^{tm} alloy designated 049 (Al-4.76Cu-1.27Li-0.37Ag-0.33Mg-0.13Zr) and are reported for the first time in the present paper. The techniques used for concurrent straining and annealing experiments have been described previously[20,21], including specific temperatures, holding times, and initial strain rates for the Al-Zr-Si and Al-Cu-Zr-Si alloys. For the Al-Cu-Li-Ag-Mg-Zr alloy, tensile specimens with the tensile axis parallel to the rolling direction (L) were heated to the test temperature of 773 K in approximately 0.5 h, and were held at that temperature for 0.16 h prior to straining at an initial strain rate of 6.6×10^{-4} s^{-1}. Tests were interrupted at true strains (ϵ) of 0.11, 0.21 and 0.47; and the tensile specimens were rapidly quenched in water. TEM foils normal to the long transverse (T) direction were prepared, and measurements of grain orientation and boundary misorientation were performed as described previously[20,21].

Experimental results consist of lattice orientation data for individual, contiguous (sub)grains; from which the axis/angle pairs for individual boundaries are extracted. Figs. 1 - 3 show the distributions of boundary misorientation angles from various samples, represented in the form of histograms.

The as-rolled microstructure has been evaluated for the Al-Zr-Si alloy. Approximately 2/3 of the boundaries characterized have misorientations of 10° or less. The boundaries with misorientations near 55° are transition-band-type boundaries between deformation bands, and are nearly always parallel to the rolling plane. Similar features have been described by other authors for a variety of rolled aluminum alloys[28-36].

The grip section results are broadly similar for all three alloys investigated. More than 1/2 of the boundaries examined in each grip section have misorientations of 10° or less, similar to the as-rolled microstructure of the Al-Zr-Si alloy. Transition-band-type boundaries were observed in the Al-Cu-Zr-Si and Al-Cu-Li-Ag-Mg-Zr grip sections, but not in the Al-Zr-Si grip section. It is thought that this reflects the small number of observations and variable spacing of transition-band-type boundaries, rather than a fundamental difference between these microstructures. It has been previously reported that the boundary

misorientation distributions in samples of the Al-Zr-Si alloy annealed for extended periods (not grip sections of tensile specimens) were essentially the same as the boundary misorientation distributions in the grip sections[20]. Taken as a whole, these results suggest that, absent discontinuous recrystallization, annealing without concurrent deformation does not significantly alter the boundary misorientation distribution in any of the three alloys investigated.

Figs. 1 - 3 also show boundary misorientation distributions for the gauge sections of the tensile samples. These results are characterized by a marked decrease in the fraction of boundaries with misorientations of 10° or less, and a simultaneous increase in the fraction of higher-angle boundaries, as a function of elevated temperature strain. At strains near 0.45, for example, boundaries with 10° or less misorientation represent fewer than 1/3 of the boundaries in each alloy. There are two potential origins for the observed shift in the boundary misorientation distributions. Either:

i) some low-angle boundaries are transformed into high-angle boundaries as a result of (sub)grain rotation and (sub)grain switching processes, or

ii) some of the low-angle boundaries initially present are eliminated by (sub)grain growth so that the high-angle boundaries initially present comprise a larger fraction of the total boundary population.

Examination of the boundary locations and orientations in TEM micrographs shows that explanation i) is the dominant effect. For example, boundaries with misorientations between 10° and 20° and with the boundary plane approximately normal to the L direction are infrequently observed in the grip sections[20,21]. After concurrent straining and annealing to $\epsilon > 0.2$, such intermediate angle boundaries normal to the L direction are often observed. No evidence of discontinuous recrystallization was found in any of the grip or gauge sections.

While the boundary misorientation distributions provide a general picture of a shift from low misorientation angles to higher misorientation angles as a function of strain, the $\epsilon = 0.88$ result for the Al-Cu-Zr-Si alloy illustrates the opposite trend. In a previous paper[21], evidence was presented to show that this effect was caused by a significant contribution to plastic deformation from intra(sub)granular slip in the strain interval 0.44 to 0.88. This results in re-intensification of the original deformation texture and a shift of boundary misorientations back toward low angles. Modeling results pertinent to this case are presented later.

The combined experimental observations indicate that lattice rotations occur in all three of the alloys during the course of concurrent straining and annealing, but not during static annealing. This is consistent with the view of continuous recrystallization as a strictly dynamic process. However, the mechanism of lattice rotation is not clarified by these observations. In Section 3 of the paper (available from the authors), simulative models of lattice rotation mechanisms are described and are applied to experimentally determined microstructure/microtexture states. In the next section of this report, model results are compared with experimental observations.

Comparison of Experimental and Model Results

The effect of concurrent straining and annealing on boundary misorientation distributions has been established experimentally and through several simulative models. The purpose of this discussion section is to compare the experimental and modeling results, with the goal of identifying which models most closely reproduce the experimental results. The models for dislocation glide (sub)grain rotation and for (sub)grain neighbor switching are explicit functions of strain. The strain value used to obtain the modeling results shown in Figs. 5 - 7 is 0.41. It is therefore appropriate to compare the modeling results with the experimental results for tensile specimens deformed to a similar strain. Figs. 1 - 3 contain boundary misorientation distributions for tensile strains in the range 0.44 to 0.47 for the various alloys.

Boundary Sliding (Sub)grain Rotation (BSSR) Model Results

For all three alloys, the prominent effect of the BSSR model on the boundary misorientation distribution is to decrease the fraction of boundaries with misorientations of 10° or less. Thus, the BSSR model reproduces the principal characteristic of the experimental boundary misorientation distributions for tensile strains near 0.45. For the Al-Zr-Si alloy, a rotation of 10° yields better agreement between the BSSR model results and the experimental boundary misorientation distribution, while a 5° rotation yields better agreement for the other two alloys.

Although the BSSR model reproduces in a general way the principal characteristic of the experimental observations, a strong fundamental basis for selecting a particular value of (sub)grain rotation to associate with strains near 0.45 does not exist. Previously published micro-pole figures for the Al-Zr-Si and Al-Cu-Zr-Si alloys[20,21] show that initially similar (sub)grain orientations diverge during concurrent straining and annealing by rotations of up

to 10° or 15°. The classic marker line experiments described by Matsuki and coworkers[39,40] and others[41] also reveal grain rotations of similar magnitude for strains near 0.5. In addition, the simulative grain rotation model formulated by Beere[42,43] indicates that grain rotations of 10° or more are readily achieved at a strain of 0.5, provided that moderate differences in boundary sliding rate exist among the various boundaries in the material. Based on these observations, a rotation of 5° has been selected to represent the average subgrain rotation at a strain of 0.41.

Dislocation Glide (Sub)grain Rotation (DGSR) Model Results

Application of the DGSR model to the initial boundary misorientation distributions for the three alloys increases the fraction of boundaries with misorientations of 10° or less. This reflects convergence of (sub)grain orientations and intensification of the initial texture, a result that would be anticipated for deformation by slip. Since this result is contrary to experimental observations for strains near 0.45, we conclude that (sub)grain rotation during concurrent straining and annealing of the alloys studied in the present investigation is not a result of slip. This is consistent with an earlier report that the contribution of slip to the total strain was less than 10% during superplastic deformation of a continuously recrystallized Al-Cu-Zr alloy[25].

(Sub)grain Neighbor Switching Model Results

(Sub)grain neighbor switching produced only modest changes in the boundary misorientation distributions for the three alloys. This result can be anticipated from knowledge of the initial microstructure/microtexture states of the alloys. (Sub)grains of similar orientation are arranged in deformation bands oriented parallel to the rolling direction. Moderate elongation of deformation bands in the L direction maintains many (sub)grains of similar orientation in contact, with the result that (sub)grain neighbor switching does not strongly alter the boundary misorientation distributions.

Combined Boundary Sliding (Sub)grain Rotation and (Sub)grain Neighbor Switching Model Results

The BSSR model produced boundary misorientation distributions broadly similar to those found experimentally. However, since the (sub)grains remain approximately equiaxed during deformation (a salient characteristic of superplastic deformation[37-40]), (sub)grain neighbor switching must occur in conjunction with (sub)grain rotation. To model the combination of these processes, we have applied the individual BSSR and (sub)grain neighbor

switching models successively to the initial boundary misorientation distributions. Since the models are independent, the order of application is immaterial.

The last histogram in Figs. 5 - 7 shows the combined BSSR and (sub)grain neighbor switching model results. Comparing these distributions with the experimentally determined distributions for strains near 0.45 reveals broad similarities. Thus, we find that a combination of the boundary sliding (sub)grain rotation and (sub)grain neighbor switching models produces boundary misorientation distributions consistent with the experimental observations. This finding is consistent with a wide variety of previous observations concerning evolution of microstructure and texture during concurrent straining and annealing of superplastic aluminum alloys[12-25]. It also supports the idea that continuous recrystallization is strictly a dynamic process in which the applied stress drives (sub)grain rotation such that initial (sub)grain orientations diverge during concurrent straining and annealing.

Conclusions

This study of simulative modeling of microstructure/microtexture evolution during concurrent straining and annealing of three aluminum alloys has lead to the following conclusions.

1. The boundary misorientation distributions for the three alloys included in the present study are broadly similar after annealing alone and after concurrent straining and annealing. Annealing alone does not significantly alter the boundary misorientation distribution, while concurrent straining and annealing decreases the fraction of low-angle boundaries.
2. Three simulative models of microstructure/microtexture evolution during concurrent straining and annealing have been formulated. Application of the models to experimentally determined initial microstructure/microtexture states shows that the boundary sliding (sub)grain rotation model decreases the fraction of low-angle boundaries, the dislocation glide (sub)grain rotation model increases the fraction of low-angle boundaries, and the (sub)grain neighbor switching model modestly decreases the fraction of low-angle boundaries.
3. A combination of the boundary sliding (sub)grain rotation model and the (sub)grain neighbor switching model most closely reproduces the boundary misorientation

distributions found experimentally.

4. The experimental and modeling results are consistent with the view that continuous recrystallization is strictly a dynamic process.

Research Plan for 1993

The processing methods used to impart superplastic characteristics to the two Weldalite alloys under study give large superplastic elongations in the longitudinal (rolling) direction. In tensile tests, the two alloys exhibit lower superplastic elongations in the transverse direction than in the longitudinal direction. A major goal of the project is to discover the origin of reduced transverse elongation. Based on prior knowledge, it seems likely that the microstructure/ microtexture evolution process that converts the warm-rolled microstructure into a microstructure suitable for superplastic forming occurs somewhat differently when the material is strained in the transverse direction than in the longitudinal direction. In the past year, we have characterized the microstructure/ microtexture evolution for superplastic straining in the longitudinal direction, and developed models that simulate the evolutionary processes. In the final 9 month period of this project, we will experimentally characterize the microstructure and microtexture for tensile samples strained in the transverse direction, and use the models to understand the evolutionary processes.

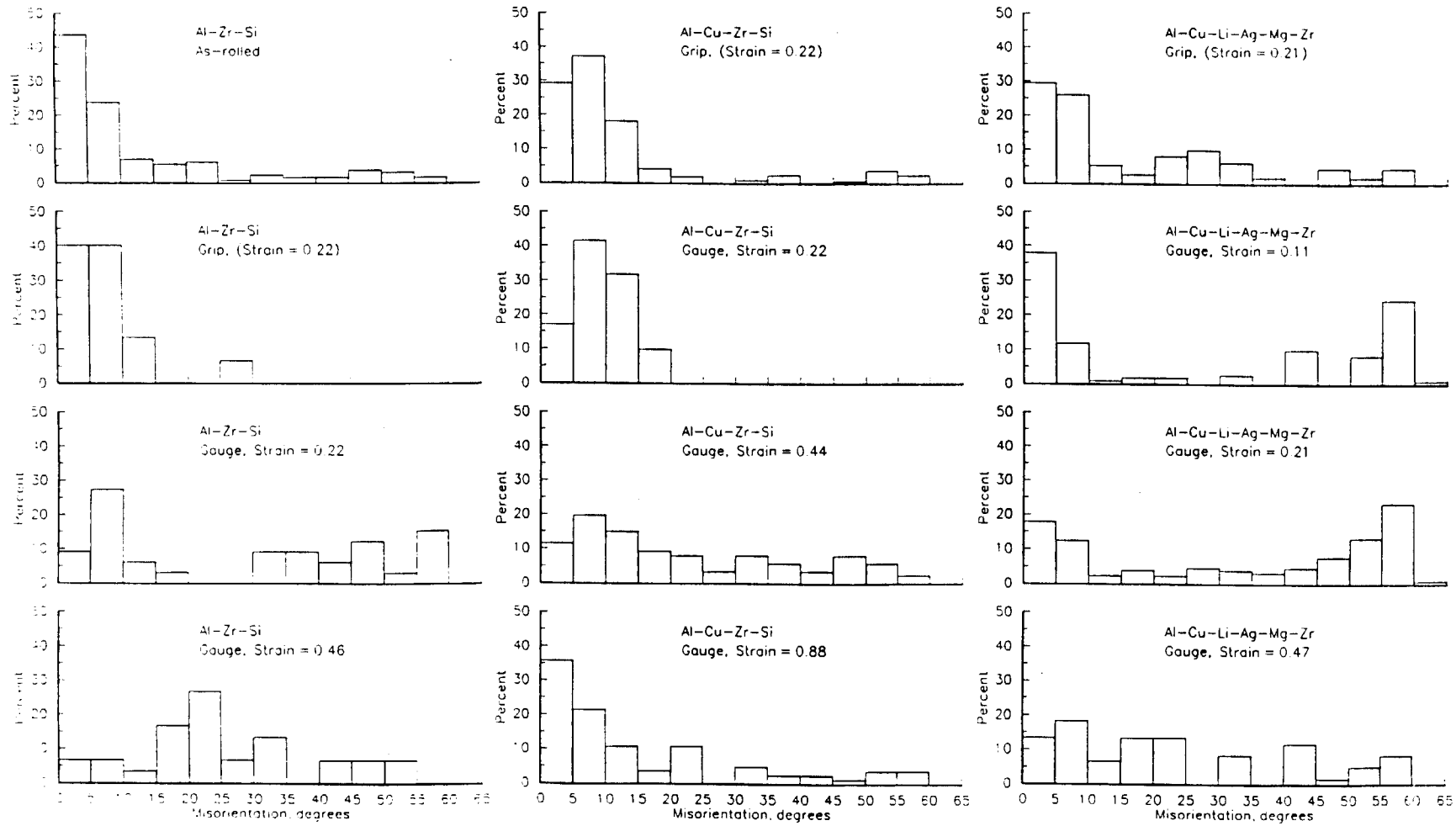

Figs. 1 - 3: Experimentally determined boundary misorientation distributions for the Al-Zr-Si, Al-Cu-Zr-Si and Al-Cu-Li-Ag-Mg-Zr (Weldalite 049) alloys. Strain history in indicated on the individual plots.

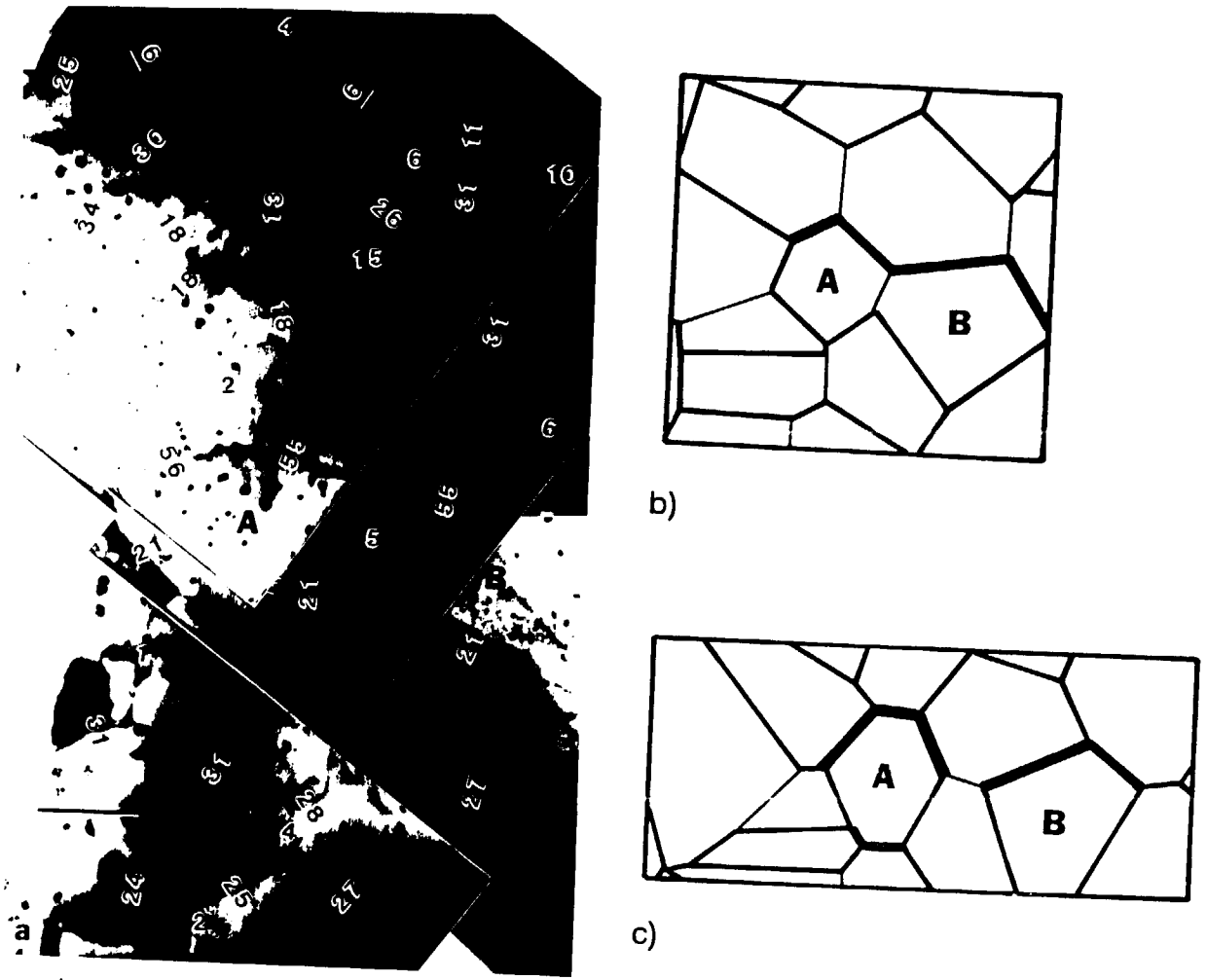

Fig. 4 Method used to define (sub)grain neighbors after (sub)grain neighbor switching. a) TEM micrograph of the grip section of an Al-Cu-Li-Ag-Mg-Zr tensile specimen (gauge section strain = 0.22). Numbers marked on the micrograph represent boundary misorientation angles. The scale marker represents 2 μm and is parallel to L; T is normal to the page. b) Dirichlet tessellation representing a portion of the microstructure in a). Line thickness indicates boundary misorientation: thin lines represent 10° or less misorientation, intermediate lines represent boundary misorientations between 10° and 50°, and thick lines represent boundaries with misorientations of 50° or greater. c) Dirichlet tessellation from b) with centroid of each grain mapped to a new location corresponding to a tensile strain of 0.41.

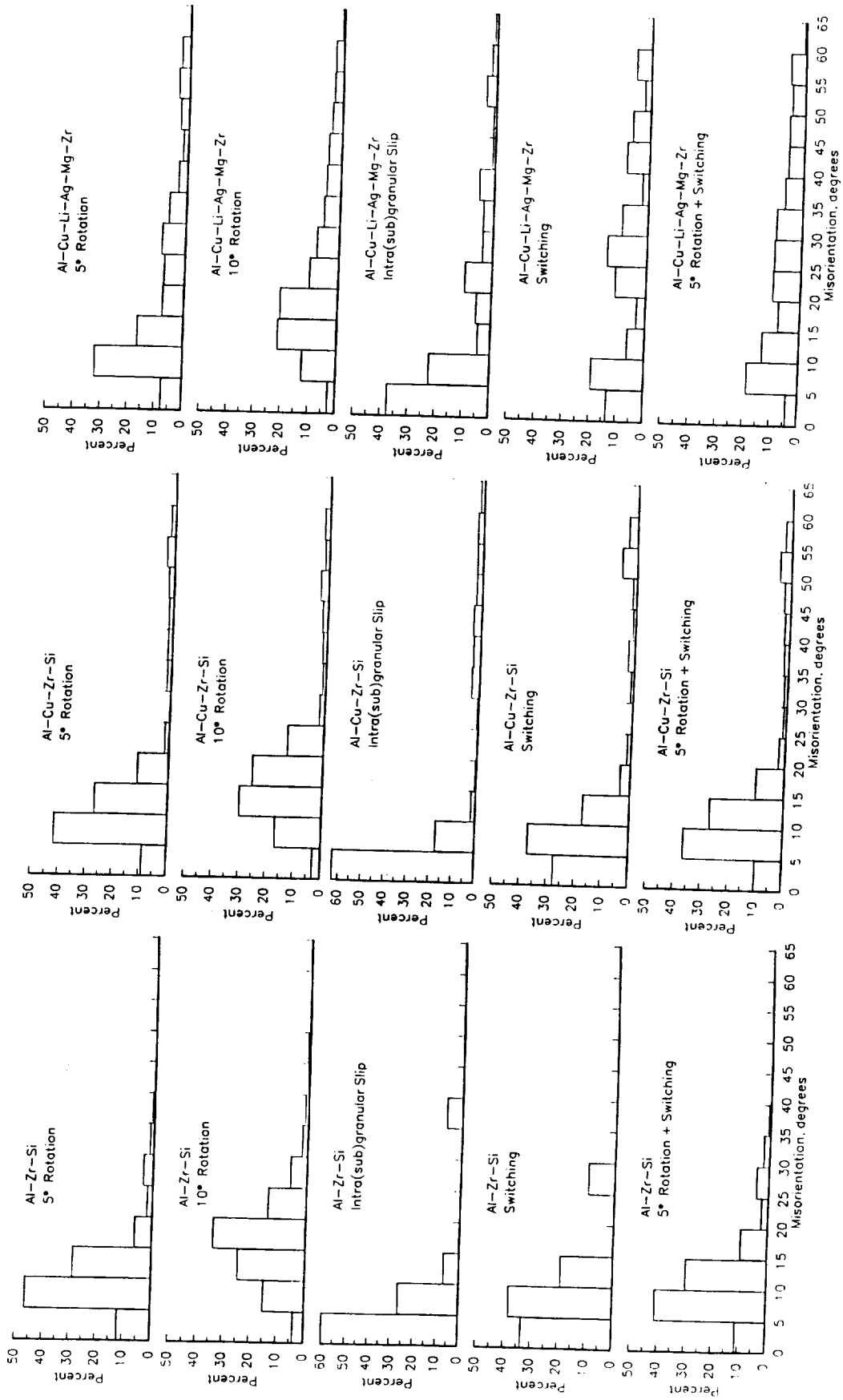

Figs. 5 - 7: Calculated boundary misorientation distributions for the Al-Zr-Si, Al-Cu-Zr-Si and Al-Cu-Li-Ag-Mg-Zr (Weldalite 049) alloys. Model parameters are indicated on the individual plots.

Project #11 Environmental Effects in Fatigue Life Prediction: Modeling Crack Propagation in Light Aerospace Alloys

Mark Mason, Sang-Shik Kim and Richard P. Gangloff

Problem Statement

Fracture mechanics-based fatigue crack propagation (FCP) rate data and predictive models are central elements of computerized life prediction codes such as NASA FLAGRO[1], however, work to date has necessarily focused on cracking in relatively benign moist air[2]. Since FCP rates in aerospace alloys are accelerated by many gaseous, aqueous and thermal environments[3], it is important to characterize and understand environment-alloy-loading interaction effects on da/dN-ΔK data, and to incorporate such information into a life prediction method for application to aerospace components. To date, this goal has not been accomplished.

The magnitude of the environmental effect on da/dN depends on interactive variables which do not influence FCP in inert environments[3]. For example, EFCP is strongly time-dependent[4]; it is extremely difficult to predict the long-life, slow loading frequency (f) performance of structural materials based on short-term laboratory da/dN-ΔK data. Secondly, the fracture mechanics formulation of da/dN-ΔK in an aggressive environment must account for compromises due to extrinsic factors; particularly crack closure, small crack mechanics, and crack geometry dependent local environment chemistry.

The challenge is to determine and predict the stress intensity dependence of environment-sensitive FCP rates, based on an understanding of the contributions of extrinsic crack closure and intrinsic crack tip damage mechanisms. Models are required to predict environmental FCP kinetics, well beyond necessarily limited laboratory data.

Objectives

The long term objective of this project is to establish data and models for predicting environment enhanced FCP kinetics for light aerospace structural alloys, particularly titanium and high strength aluminum alloys.

Specific goals are to:

1. Characterize da/dN versus ΔK for an α/β-titanium alloy, a β-titanium alloy, and a 7000 series aluminum alloy, in selected environments including vacuum, gaseous hydrogen and aqueous chloride;
2. Identify the effect of R ratio on environmentally-influenced crack closure and intrinsic process zone damage for one titanium alloy-environment system;
3. Characterize K_{th} and time-based cracking velocity (da/dt versus K); initially for the 7000 series high-strength aluminum alloy-aqueous environment system; as a function of crack tip strain rate, and compared to classic static load or crack mouth opening displacement methods;
4. Evaluate the applicability of empirical and linear superposition models for high strength titanium and aluminum alloys, and determine if dynamic load cracking data improve superposition modeling. Provide a linear superposition routine for incorporation into NASA-FLAGRO.
5. Develop mechanistic understanding of the microscopic crack tip damage processes in environmental FCP. For example, identify the effects of stress ratio and crack tip surface passive film on environmental fatigue and fracture in a selected titanium alloy-environment system and in the 7000 aluminum alloy-environment system.

Technical Approach

The technical approaches to the project objectives; including the rationale for material and environment selection, as well experimental fracture mechanics procedures; were detailed in the 1993 renewal proposal[5]. Dr. Sang Kim is responsible for Goals 1, 2 and 5; Mr. Mark Mason is responsible for Goals 3, 4 and 5, and three undergraduate students are working on elements of Goal 4.

Results During the Reporting Period

Literature Review

An unexpectedly large amount of time was expended during this reporting period to revise and improve a substantial literature review on those aspects of environmental fatigue crack propagation (EFCP) that must be understood in order to incorporate environmental effects into fatigue life prediction codes. The following Executive Summary describes the essence of this work. This document will be published as a NASA Contractor Report.

Environment Enhanced Fatigue Crack Propagation in Metals: Inputs to Fracture Mechanics Life Prediction Models [2]

Richard P. Gangloff and Sang-Shik Kim

The fatigue crack growth resistance of metallic alloys and structures is generally reduced by concomitant exposure to a wide range of aggressive environments. Notable examples are nickel-based superalloys in high pressure hydrogen gas, high strength alloy steels in water vapor and titanium or aluminum alloys in aqueous chloride. Despite substantial advances over the last 30 years, the fracture mechanics approach for damage tolerant fatigue life prediction has not been adequately developed to define deleterious environmental effects for use in computerized codes such as NASA FLAGRO.

The objective of this report is to review and critically evaluate both environment-enhanced fatigue crack propagation (FCP) data and the predictive capabilities of crack growth rate models to broadly extend laboratory data. This information provides the necessary foundation for incorporating environmental effects in NASA FLAGRO and will better enable predictions of aerospace component fatigue lives.

This review presents extensive literature data on "stress corrosion cracking" (more accurately monotonic load environmental cracking) and "corrosion fatigue" (more accurately environmental fatigue cracking). The linear elastic fracture mechanics approach, based on stress intensity range (ΔK) similitude with macroscopic crack propagation thresholds (ΔK_{TH}) and growth rates (da/dN), provides the basis for these data. The results of laboratory experiments demonstrate that gases (viz., H_2 or H_2O) and electrolytes (e.g., NaCl and H_2O) enhance FCP rates in aerospace alloys including: C-Mn and heat treated alloy steels, aluminum alloys, nickel-based superalloys and titanium alloys. Environment causes purely time-dependent fatigue cracking above the monotonic load cracking threshold (K_{IEAC}) and promotes cycle-time dependent cracking below K_{IEAC} where cyclic deformation is uniquely damaging. Crack growth in nickel based superalloys in elevated temperature oxidizing environments is phenomenologically similar to lower temperature "corrosion fatigue".

While mechanistic understanding is qualitative, environmental effects on FCP can be rationalized based on either an environmental hydrogen production/embrittlement mechanism, or on electrochemical film formation with repeated rupture and transient anodic dissolution.

---

[2] SEAS Report No. UVA/528266/MSE93/111; University of Virginia, Charlottesville, VA, December (1992).

For many aerospace alloys and environments, so-called Hydrogen Environment Embrittlement is the suspected failure mechanism. This process provides a framework for understanding the effects of variables on environmental fatigue crack growth. Electrochemical dissolution models are similarly useful for considering environmental effects on cracking.

The magnitude of environment enhanced FCP kinetics is determined by the synergistic interaction of a plethora of mechanical, microstructural and chemical variables. Environment activity (e.g., H_2, H_2O or O_2 pressure in addition to temperature and electrode potential), stress intensity range and mean level, and loading frequency are critical. Stress ratio (R) effects are qualitatively understood based on crack closure, but not based on intrinsic damage processes. The complex and multifaceted dependence of da/dN on ΔK and the dominant effect of fatigue loading time (viz., frequency and hold time), are particularly important. Environmental effects generally increase with decreasing frequency or increasing hold time; the exact dependence is determined by rate limiting mass transport and reaction processes. Environment enhanced fatigue crack growth models must be capable of predicting the effects of these critical variables in order to accurately scale laboratory data to component service conditions. For example, it is crucial to be able to extrapolate short term (of order weeks) laboratory data to predict long term (of order years) component cracking behavior.

The fracture mechanics stress intensity range correlates environmental fatigue crack propagation rates independent of load magnitude, crack size and geometry. Stress intensity-based similitude is, however, complicated by the effects of crack closure, small crack size and loading spectra. Several crack closure and small crack mechanisms are unique to external environments, and are not well understood based on data and modeling for FCP in moist air. Such complications to similitude must be considered in fatigue life prediction.

Approaches to predict da/dN-ΔK for environmental situations; including empirical interpolative equations, linear superposition of mechanical fatigue and time-based environmental cracking, and mechanism-based models; are presented. For several technologies, successes have been reported in evaluating the environmental fatigue contribution and were incorporated in fracture mechanics life prediction models. Considerable uncertainties are, however, associated with these models. The linear superposition analysis is emphasized; material-environment systems that are severely environment-sensitive should be adequately described by this method. Direct and indirect methods exist to define time-based crack growth rates for use in linear superposition predictions of da/dN. This approach is effective, but only for those cases where K_{IEAC} is on the order of stress intensity levels typical of components in service. Empirical curve-fit

models require an extensive environmental crack growth rate data base, are costly to develop, and are effective for interpolations but not predictions of FCP data. Mechanism based models for broad predictions of cycle-time dependent da/dN versus ΔK, and other variables such as frequency or hold time, are in an infant state.

Substantial work is required in order to effectively incorporate environmental effects in fatigue life prediction codes. For example, research is necessary in the areas of near-threshold environmental fatigue behavior, advanced alloy and composite cracking, experimental methods development, fundamental damage mechanism models, da/dN-ΔK modeling, crack closure, and small crack effects on similitude. The challenge to NASA is acute because of the wide range of materials and complex environments that are relevant to aerospace applications.

Specific recommendations for incorporating environmental effects on FCP in NASA FLAGRO include cataloging the data contained in this report, adapting a linear superposition computer program as a FLAGRO module, testing the linear superposition approach for a relevant material/environment system, experimentally defining the "below K_{IEAC}" behavior of a relevant material/environment system, and continuing to develop fundamental models of environment sensitive crack closure and intrinsic damage mechanisms.

Environmental Fatigue Crack Propagation

FCP kinetics will be characterized with advanced fracture mechanics methods utilizing the compact tension specimen. Crack growth rates will be defined for computer automated decreasing ΔK conditions, both as a function of constant stress ratio and separately for constant K_{MAX}. Crack length and crack closure will be measured by the global compliance technique with a standard gauge mounted across the notch mouth. Stress ratio, loading frequency and waveform are important variables.

EFCP experiments will be conducted on an α/β-titanium and on AA7075 (see next section). A plate (14.0 mm thick by 20.3 cm wide by 1.4 m long) of mill annealed Ti-6Al-4V (ELI, or Extra Low Interstitial) was purchased from President Titanium in Hanson, MA and is scheduled to arrive at UVa by April 1st. We proposed three environments for the EFCP experiments with titanium alloys; vacuum, gaseous hydrogen and 1% NaCl with HCl at pH 3[5]. For the aluminum alloy, we proposed a chromate inhibited 3.5% NaCl solution at a fixed potential somewhat cathodic to the free corrosion condition for aerated solution.

A chamber was designed to contain aqueous solutions about the crack in a compact

tension specimen. The aim of the design is to control the environment chemistry during EFCP, while enabling compliance-based measurement of fatigue crack closure without interference from the chamber. The machining of this apparatus is essentially partially completed, however, no data have been determined to date.

Rising Load Environmental Cracking

A monotonically rising load method will be employed to characterize the threshold stress intensity for the onset of environmental cracking and subsequent time-based crack growth rates[6]. This approach is a derivative of the J-integral fracture toughness (R-curve) procedure and will provide applied K versus crack extension (Δa) as well as subcritical crack extension versus time. This method enables an assessment of the effect of crack tip strain rate on K_{th} and da/dt, including the range of conditions from classical constant load or displacement crack arrest to programmed constant applied crack tip strain rate. Crack extension will be measured by a direct current electrical potential method, for all environments and without specimen unloading. Crack mouth opening displacement will be measured to calculate J. The chamber to contain the inhibited aqueous chloride solution is identical to that designed for the EFCP experiments.

Two aluminum alloy plates were donated by Mr. E.L. Colvin and the Alcoa Technical Center; 7075-T651 and 7075-T7X1. This 5.1 cm thick plate was originally purchased by Alcoa from a distributor for an ASTM interlaboratory test program on the breaking load characterization of stress corrosion cracking. Accordingly, extensive mechanical properties data exist[7,8]. The 7075 plate was received at Alcoa in the T651 condition (probably aged to peak strength at 121°C for 24 hours). A portion of the plate was given a second aging at 168°C for 5 hours to approximate the overaged T73 condition. The intent was to produce intermediate stress corrosion cracking resistance (T73) compared to the environmental cracking prone T651 condition. These two conditions will be ideally suited to assess the effect of dynamic strain on environmental cracking resistance for an alloy that is either prone or resistant to SCC under static loading.

The following properties were reported[7,8].

7075-T651: σ_{ys} = 471 MPa (short transverse)

σ_{uts} = 539 MPa (short transverse)

K_{IC} = 20.8 to 21.2 MPa$\sqrt{m}$ (S-L orientation)

7975-T7X1: σ_{ys} = 442 MPa (short transverse)

σ_{uts} = 520 MPa (short transverse)

K_{IC} = 20.8 to 21.3 MPa$\sqrt{m}$ (S-L orientation)

Breaking load experiments, conducted with statically loaded smooth tensile specimens in 3.5% NaCl with alternate immersion (10 minutes immersed + 50 minutes drying cycle), showed that the T7X1 temper substantially improved the resistance of this plate of 7075 compared to the T651 condition[7,8]. Environmental cracking was assessed for the short-transverse orientation. Fracture mechanics data presented by Holroyd and Speidel suggest that the threshold for environmental crack arrest in a fixed displacement cantilever beam experiment is 5 MPa$\sqrt{m}$ and the plateau crack growth rate is just above 10^{-5} mm/sec for 7075-T651 in 3.5% NaCl (constant immersion)[9,10]. The very SCC resistant T7351 temper results in a threshold stress intensity for NaCl environmental cracking of above 20 MPa$\sqrt{m}$ and a plateau crack velocity of about 4 x 10^{-7} mm/sec. The T7X1 temper is likely to be more environmental cracking prone compared to T7351, but certainly more resistant than T651. The T651 and T7X1 heat treatments of the same 7075 plate will provide two important cases to examine the effect of dynamic straining on environmental cracking resistance, to test the simple linear superposition concept, and to develop improved modeling relevant to EFCP.

This project will emphasize environmental cracking in the particularly susceptible short transverse crack plane. Given the relatively limited thickness of the two 7075 plates (5.1 cm), it is necessary to employ the so-called Wedge-Opening-Load (WOL) specimen for precracked fracture mechanics experiments. The height (H) to width (W) ratio of this specimen, 0.486, is less than that of the conventional compact tension geometry where H/W equals 0.60. The WOL specimen will be machined in the S-L orientation with H = 2.54 cm, W = 5.23 cm, and thickness (B) = 7.6 mm. Specimen machining is in progress and is scheduled to be completed by April 1st. WOL specimen grips will include ball bearing bushings to eliminate stress intensity errors due to loading pin friction and to provide improved load-displacement linearity. This latter feature, when coupled with high precision and high stability direct current electrical potential measurement, should improve the definition of the onset of crack growth

Linear Superposition Modeling

The linear superposition approach proposed by Landes and Wei, as well as by Bucci and Paris, provides a simple method to predict EFCP kinetics from inert environment FCP data and quasi static load/displacement environmental cracking data[11,12]. While this method is not applicable to a large number of material-environment systems where cyclic deformation interactively exacerbates environmental cracking below quasi static threshold levels[3], linear superposition provides a meaningful first step to incorporating environmental effects into NASA FLAGRO.

Three fourth year undergraduate students in the Mechanical and Aerospace Engineering Department at UVa have worked during the past four months on elements of the linear superposition approach. Mr. John Pope is working to develop an automated digitizing procedure to transfer literature data on either da/dN versus ΔK or da/dt versus K from a published plot to an ASCII file for analysis. This capability is necessary given the large number of data points that are typically present in such plots. The method has been largely debugged and a Fortran program has been written to relate linear digitized coordinates with full or semi-logarithmic axes.

Mr. Edward Richey is developing a Fortran program that provides least squares curve fitting of da/dN versus ΔK and da/dt versus K data. The forms of the curve fit relationships have been selected based on literature results. For example, a dual-power law relationship was programmed to relate da/dt and K. The modified Forman equation for the ΔK and R dependencies of da/dN will be employed for FCP data. The current version of FLAGRO was obtained from R.G. Forman, and the subroutine for determining the coefficients in the Forman equation will be incorporated into our Fortran program. The Richey program will operate on either UVa laboratory generated da/dN versus ΔK data, or on files of literature data from the Pope digitizing program.

Mr. Allen Wilson is developing a Fortran computer program that implements the classic linear superposition method[11,12]. The inputs to this program are da/dN versus ΔK for a specific alloy-inert environment system, da/dt versus K for the same alloy-aggressive environment system, and the time and stress ratio dependent applied K waveform. These data will be either in file or equation form. The latter will be the results of the Richey program. The output of the linear superposition program will be a prediction of the frequency, R and load waveform dependencies of EFCP rates.

These three undergraduates are conducting this work in conjunction with the senior thesis requirement of the School of Engineering and Applied Science. There is no cost to the LA^{2}ST Grant. The downside of this arrangement is that the students have limited time to both learn about a complex area and to assemble a useful program that is integrated with the work of their colleagues. The work is scheduled for completion by the end of May, 1993 when project reports must be submitted for degree credit. Any useful results will be incorporated into the UVa research in this project, and will be forwarded to both LaRC and the Johnson Space Flight Center for incorporation into NASA programs. It is possible that one of the three undergraduates will continue this work through the Summer of 1993 to fully integrate the three programs and to maximize the benefit to the LA^{2}ST Program.

Proposed Research

Consistent with the 1993 renewal proposal[5], we aim to achieve the following during the next two reporting periods:

- oo Measure the effect of ΔK and R on the EFCP kinetics for plate Ti-6-4 (mill-annealed, ELI) in 1% NaCl at a fixed electrode potential. R ratios of 0.1, 0.5, 0.7 and constant K_{max} of 24 MPa$\sqrt{m}$ will be employed for FCP experiments with a sinusoidal loading frequency of either 4 Hz, or a combined 0.1 Hz/10 Hz sequence for high and low da/dN, respectively. Limited FCP tests will be conducted in vacuum.
- oo Similarly characterize the EFCP kinetics for 7075-T651 (SL orientation) in the chromate inhibited chloride environment.
- oo Limited experiments will be conducted with loading frequencies of 0.05 to 30 Hz, in the moderate ΔK region and for the alloy-environment system that is most interesting from the linear superposition and NASA-FLAGRO perspectives.
- oo Measure crack closure in vacuum and the aqueous environment though use of global compliance. Da/dN will be expressed as a function of ΔK_{eff} and compared with high R da/dN-ΔK data.
- oo Analyze EFCP data with interpolative curve fitting models for possible application to NASA FLAGRO. This work will be carried out by an undergraduate and will begin by applying the NASA-FLAGRO routine for fitting da/dN-ΔK equations as proposed by Forman, Newman and others.
- oo Measure the threshold and time based crack growth rates for monotonic load cracking

of 7075-T651 and 7075-T7X1 in chromate inhibited 3.5% NaCl, as a function of loading rate and estimated crack tip strain rate.

- oo Measure the subcritical cracking kinetics, above threshold, for 7075-T651 in the aqueous environment. This will be accomplished by classic fracture mechanics constant load/displacement stress corrosion cracking methods, and by analysis of data on the effect of K_{max} hold-time on da/dN and the associated time-based rate of crack growth.
- oo Formulate the interpolative and linear superposition models for incorporation into NASA FLAGRO.

References

1. R.G. Forman, V. Shivakumar, J.C. Newman, Jr., S.M. Piotrowski and L.C. Williams, in Fracture Mechanics: 18th Symposium, ASTM STP 945, D.T. Read and R.P. Reed, eds., ASTM, Philadelphia, PA, pp. 781-803 (1988).

2. R.P. Gangloff, R.S. Piascik, D.L. Dicus and J.C. Newman, "Fatigue Crack Propagation in Aerospace Aluminum Alloys", Journal of Aircraft, in press (1993).

3. R.P. Gangloff, in Environment Induced Cracking of Metals, R.P. Gangloff and M.B. Ives, eds., NACE, Houston, TX, pp. 55-109 (1990).

4. R.P. Wei and R.P. Gangloff, in Fracture Mechanics: Perspectives and Directions, ASTM STP 1020, R.P. Wei and R.P. Gangloff, eds., ASTM, Philadelphia, Pa, pp. 233-264 (1989).

5. R.P. Gangloff, "NASA-UVa Light Aerospace Alloy and Structures Technology Program", University of Virginia, Proposal No. MSE-NASA/LaRC-5691-93, November (1992).

6. L.M. Hartman and R.P. Gangloff, "Hydrogen Environment Embrittlement of Beta Titanium Alloys", in Seventh World Conference on Titanium, F.H. Froes, ed., TMS-AIME, Warrendale, PA, in press (1993).

7. D.A. Lukasak, R.J. Bucci, E.L. Colvin and B.W. Lifka, in New Method for Corrosion Testing of Aluminum Alloys, ASTM STP 1134, V.S. Agarwala and G.M. Ugiansky, eds., ASTM, Philadelphia, PA, pp. 101-116 (1992).

8. E.L. Colvin and M.R. Emptage, "The Breaking Load Method; Results and Statistical Modifications from the ASTM Inter-Laboratory Test Program",in New Method for Corrosion Testing of Aluminum Alloys, ASTM STP 1134, V.S. Agarwala and G.M. Ugiansky, eds., ASTM, Philadelphia, PA (1992).

9. N.J.H. Holroyd, in Environment Induced Cracking of Metals, R.P. Gangloff and M.B. Ives, eds., NACE, Houston, TX, pp. 311-346 (1990).

10. M.O. Speidel, in Metall. Trans. A, Vol. 6A, pp. 631-651 (1975).

11. R.P. Wei and J.D. Landes, Matls. Res. Stds., pp. 25, July (1969).

12. R.J. Bucci, "Environment Enhanced Fatigue and Stress Corrosion Cracking of a Titanium Alloys plus a Simple Model for the Assessment of Environmental Influence on Fatigue Behavior", PhD Dissertation, Lehigh University, Bethlehem, PA (1970).

Project #12 Inelastic Deformation of Metal Matrix Composites Under Biaxial Loading

C.J. Lissenden, M.-J. Pindera and C.T. Herakovich

Objective

The long-term objective of this investigation is to attain a complete understanding of the inelastic response of metal matrix composites (MMC) subjected to arbitrary, biaxial load histories. The core of the research program is a series of biaxial tests conducted on different types of advanced metal matrix composite systems using a combined axial/torsional load frame. These tests involve primarily tubular specimens and include tension, compression, torsion, internal pressure, and combinations thereof in order to critically assess the inelastic response of advanced metal matrix composites in a wide temperature range.

Approach

The approach employed to characterize the inelastic response of advanced MMC over a wide temperature range and arbitrary biaxial loading consists of a combined experimental and analytical program. The analytical program involves the development of models to predict initial yielding and subsequent inelastic response of MMC using a combined micromechanics approach and laminated plate and tube analysis. The micromechanics approach is based on a repeating unit cell model that is capable of generating the effective response of MMCs in both the linear elastic and inelastic ranges in the presence of temperature-dependent constituent properties and imperfect bonding. Micromechanical predictions for the response of a unidirectional ply subsequently will be employed as input in macroscopic laminate analyses to predict the response of multidirectional composite tubes under combined loading. The analytical predictions will in turn be employed in identifying load histories aimed at critically assessing the predictive capabilities of the developed models under the most general loading conditions.

Progress during Reporting Period

Experimental Program

As indicated in previous progress reports unidirectional, $[0_4]$ and angle-ply, $[\pm 45]_s$

SCS-6/Ti-15-3 tubular specimens have been obtained for testing on a combined axial/torsional load frame. The immediate goal of the experimental program is to obtain a better understanding of the inelastic response of MMC, with the emphasis on distinguishing effects associated with matrix plasticity from those associated with damage. With this in mind, a test matrix of biaxial loadings was developed to accentuate inelastic features such as stiffness degradation, yielding, coupling and creep. The basic biaxial loadings chosen are represented schematically in Fig. 1. Type I loading is a sequence of axial load cycles to sequentially higher load levels, at the maximum axial load in each cycle a small increment of torque is applied. Both $[0_4]$ and $[\pm 45]_s$ tubes have been subjected to Type I loading and the results have been discussed in previous progress reports.

Type I tests were modified to study time dependent inelastic effects by the inclusion of hold times, where applied stresses are held constant immediately before the application of torque and at the maximum torque (points J and K in Fig. 1). This modified loading has been designated Type IA, and has been applied to $[\pm 45]_s$ tubes only. Type II loading is the inverse of Type I, in that the application of axial load and torque are simply reversed. Type II loadings have been applied to both $[0_4]$ and $[\pm 45]_s$ tubes, these experiments will be discussed subsequently.

Internal pressure was applied to a $[0_4]$ tube via Type III loading in order to study the transverse response of a unidirectional composite. These Type III tests turned out to be quite complicated to conduct, because it was desirable to have only one stress component, the transverse (hoop) stress present. This required that the longitudinal stress component due to internal pressure be eliminated by the application of an axial compression. Due to the type of hydraulic system used to apply the internal pressure, it was impossible to apply axial compression at a proportional rate to the internal pressure, thus incremental loading was used. So the internal pressure and compression were applied incrementally for each cycle, see Fig. 1. Also, at the maximum internal pressure, increments of axial tension and torque were applied. Type III loading has been applied to $[0_4]$ tubes only.

Experimental Results

Type II tests conducted on $[0_4]$ tubes exhibited a linear elastic response at low stress levels, however at higher stresses these tests revealed a sudden inelastic deformation once a critical shear stress had been surpassed (see Fig. 2a). Acoustic emissions (AE) were monitored by mounting a microphone on the surface of the tube. Low level AE was first

heard at a shear stress of 35 ksi in experiment #16, the AE increased in intensity as the stress increased. In the subsequent cycle (#17), AE was first heard at a shear stress of 37 ksi, and an abrupt knee occurred when the stress reached 39.5 ksi. This stress value lies inside the predicted yield surface for a perfectly bonded composite. After the knee, the response resembled that of a perfectly plastic material, and upon unloading the response was nonlinear and shear stiffness degraded. The final experiment (#18) displayed an initial stiffness that was degraded 10%, and a nonlinear response beginning at approximately 10 ksi, with AE starting at 38 ksi. Again, a knee occurred around 40 ksi, with a linear hardening type behavior afterward. Failure, in the form of a longitudinal crack running the length of the tube, occurred at a shear stress of 42 ksi.

The Type II tests conducted on $[\pm 45]_s$ tubes resulted in a linear response with only a small amount of stiffness degradation. It is noted that the amount of torque that could be applied to a $[\pm 45]_s$ tube was limited by the capacity of the load frame.

Some results from Type III tests on a $[0_4]$ tube are presented in Figs. 2b, 2c and 2d. As discussed above, the primary loading in Type III tests is internal pressure. Prior to the application of torque and axial tension, comparisons can be made with tension tests conducted on [90] coupons. These coupon tests were conducted on the same material by the McDonnell Douglas Corporation. The initial stiffnesses and ultimate strengths were in relatively good agreement, but the stress level at which the initial knee, characteristic of bond failure, and the strain to failure were much different. The initial knee in the Type III tests occurred at a stress approximately twice that of the coupon tests. The strain to failure in the Type III tests was just over 50% that of the coupon tests. These differences could be explained by the additional constraint of the grips necessary for the tubular specimens. The axial, transverse and shear stiffnesses were in excellent agreement with predictions from the method of cells micromechanical model[1]. After the initial knee occurred in Exp.(#13) at 40 ksi, the subsequent cycles (#14 and #15), exhibited knees at the lower values of 25 ksi and 21 ksi, respectively. This could be an indication of the mechanical bond being broken in cycle (#13), then the knees at lower stresses are associated with overcoming only the thermal residual stresses. Figure 2b shows the nonlinear, degraded transverse response and indicates that the initial stiffness is not degraded. This could be due to the thermal residual stresses closing the separation that occurs at the interface upon unloading. AE was first heard at a transverse stress of 39 ksi and followed the Kaiser effect[2], as it did for Type I and Type II

loadings. Figure 2c presents the axial response, under internal pressure, of cycles (#13 and #14), only minimal degradation in axial stiffness has occurred. The shear response, under internal pressure, of Exp.(#13 and #14) is depicted in Fig. 2d, inelastic shear deformation is evident in Exp.(#14). Although not shown in the figures, transverse strains were accumulated after the transverse stress was held constant and shear stresses were being applied and then removed.

Angle-ply $[\pm 45]_s$ tubes were subjected to Type IA loadings to assess the significance of time dependent components of the inelastic response to axial and combined axial/shear loadings. Figure 3a presents the axial response of a $[\pm 45]_s$ tube subjected to cyclic Type IA loading. Important features in the figure to note are:

- o the stiffness is degraded with each cycle (see also Fig. 3d),
- o the hysteresis type loading and unloading characteristic of slippage or cracks opening and closing,
- o the large accumulation of strain after the axial stress was held constant, this accumulation increased as the maximum applied stress in each cycle increased, and is permanent.

All of these features were also evident in the Type I tests conducted on $[\pm 45]_s$ tubes, but now it is possible to separate time dependent effects from time independent effects. This can be readily accomplished by plotting the strain accumulated after the axial stress was held constant, against time. Figure 4c does this, and shows that two phenomenon are present. Initially the strain accumulation is due to creep, because the axial stress is being held constant. The increased rate of strain accumulation between 400 and 600 seconds for most of the cycles is due to the application of shear stresses. Once the maximum shear stress is obtained, both axial and shear stresses are held constant and not much strain is accumulated until unloading. The tail, or increased rate of strain accumulation at the right end of the data, occurred during the removal of the shear stress. This axial strain accumulation during shear stress unloading could be an indication of kinematic hardening while loading on the current yield surface. At low values of constant axial stress (eg., 30 ksi and 36 ksi), the time independent accumulated axial strains associated with coupling during shear loading and unloading, are larger than the time dependent components. At an axial stress of 48 ksi, the time dependent and independent components are approximately the same. Above 48 ksi the time dependent strain component becomes larger than the time independent component, and

grows tremendously as the maximum axial stress level increases.

The shear response of one cycle of shear loading is shown in Fig. 3b, the response is seen to be mildly nonlinear with a small amount of permanent shear strain accumulated after the shear stress was held constant. Only a slight nonlinear response was anticipated because the shear response of a $[\pm 45]_s$ laminate is predicted to be only mildly nonlinear.

AE was monitored with a piezoelectric sensor and oscilloscope based data acquisition system, and again followed the Kaiser effect. This preserved a better record of the AE data, and verified that most of the relevant initial acoustic activity was being heard by the microphone. At high axial stresses acoustic activity was very intense and appeared to reach a saturation level, and further, once the axial stress was held constant, the AE continued at the same level of intensity for quite a while. Axial and shear stiffness degradation data are displayed in bar chart form in Fig. 3d, the degradation of both stiffnesses occurs in a roughly linear fashion after Exp.(#3), where the maximum axial stress was 24 ksi.

Analytical Modelling

Model Development

An analytical model capable of predicting the inelastic response of unidirectional MMC has been developed. The model includes matrix viscoplasticity, as well as damage in the form of fiber/matrix interfacial debonding. It was felt that debonding should be considered first, then other types of damage such as radial matrix microcracking will be included later. The primary assumption of the model is that a unidirectional composite can be represented by a repeating cell model. For predicting the response of the tubular specimens, a square repeating cell is used, because if the tubes were manufactured perfectly the fiber spacing would be the same radially and circumferentially. In reality, micrographs show uneven fiber spacing in both directions. Studies conducted during the reporting period showed that the aspect ratio (1.0 for a square cell) of the unit cell can greatly effect the predicted effective response, particularly if a debonded interface is present. Due to these considerations, a square repeating unit cell analysis seemed to be the best choice. It is pointed out that the use of a square, or rectangular unit cell does not yield a transversely isotropic composite response, but there is no need to place this kind of restriction on the model.

The unit cell is considered to be in a state of generalized plane strain such that the stress and strain fields are the same on any cross-section cut perpendicular to the continuous

fiber. Thus, a two dimensional finite element model can be used to represent the response of the composite to any loading. To date, axial, transverse, axial shear and thermal loads have been considered, because they are the loading conditions applied in the experimental program.

Fiber/matrix debonding is modelled using the theory originally developed by Needleman[3] and modified by Tvergaard[4]. The theory describes interfacial tractions in terms of interfacial displacement discontinuities. Debonding is allowed to occur normal to the interface and in both tangential directions. Once the interface has failed, tractions may still be transmitted by Columbic friction. Four properties are used to physically describe the interface, however at this time these properties are treated as parameters, since no attempt has been made to experimentally determine the actual properties for these constituents. The properties are as follows: σ_0, the maximum traction carried by the interface undergoing a purely normal separation; α, the ratio of shear to normal interfacial strengths; δ, the characteristic length which is a function of the work of separation; and μ, the coefficient of friction. Thermal residual stresses are explicitly included by subjecting the unit cell to a temperature change representative of that used in processing the composite.

Model Implementation

Analysis of the repeating unit cell is performed numerically using the finite element method. Generalized plane strain triangular elements are formulated with three degrees of freedom at each of the three corner nodes. An extra node, common to all elements, with one degree of freedom in the fiber direction is added for constant axial strain. The unified theory of viscoplasticity of Bodner and Partom[5] is currently used in the constitutive calculations. Interface elements, based on the debonding theory discussed above, are used between fiber and matrix elements. Like the solid triangular elements, these elements are two dimensional with three degrees of freedom at each of the four nodes. The interface element stiffness matrix is formed by taking derivatives of the tractions with respect to the displacements. A commercially available program (ABAQUS) is used to assemble and solve the global system of equations. The Newton method is used to solve the nonlinear system of equations.

Model Predictions

To demonstrate the capabilities of the analytical model, the effective axial, transverse and axial shear responses of a [0] SCS-6/Ti-15-3 composite with a 0.40 fiber volume fraction are presented in Fig. 4. Three different interfacial conditions are shown; perfect bonding

between the fiber and matrix, the debonding model discussed above, and no bond between the fiber and matrix but with tangential tractions transmitted by Columbic friction. An effective temperature change of -1000 °F is used to obtain the thermal residual stresses from processing. The interface properties used, were chosen somewhat arbitrarily to be $\sigma_0 = 40$ ksi, $\alpha = 1.2$, $\delta = 0.008$ in, and $\mu = 0.4$, these properties may or may not be realistic. Figure 4a shows that the condition of the fiber/matrix bond has no effect on the effective axial response of a [0] composite. On the other hand, the effective axial shear response shown in Fig. 4b is greatly effected by the condition of the fiber/matrix bond. However, there is not much difference between the perfect bond prediction and that predicted using the debonding model. This indicates that bond failure does not occur in this strain range, and that matrix plasticity is the prominent inelastic mechanism. The predicted response from the debonding model can readily be changed by reducing any combination of σ_0, α and δ, in this case the predicted response will lie somewhere between the perfect and no bond cases. Both transverse tensile and compressive responses are presented in Fig. 4c. Again, the condition of the bond greatly effects the predicted response. The debonding model prediction starts out close to that for perfect bonding, then debonding occurs and the response approaches that of the no bond prediction. In order for this to occur, an unstable response, or falling stress/strain diagram, is predicted. This type of behavior has not been experimentally observed, and implies that unrealistic interface properties may have been used, it does however verify that the debonding model is permitting the interface to debond.

Conclusions

Results from Type II tests on a [0] SCS-6/Ti-15-3 composite reveal a sudden loss of stiffness at a shear stress of 40 ksi. This appears to be caused by damage accelerated plasticity. Type III tests on a [0] tube indicate that transverse loading degrades the stiffness after the residual thermal stresses have been overcome, and that damage precedes plasticity. Type IA tests on a $[\pm 45]_s$ tube suggest that at low axial stress levels time independent effects (coupling), are more important than time dependent effects (creep). As the axial stress level increases, the time dependent effects become much more prominent and short term creep strains become quite large.

The first step has been taken in the development of a theoretical model capable of predicting the inelastic response of laminated structural components. To date, the inelastic

response of unidirectional composites can be predicted using a two-dimensional model. Arbitrary thermomechanical loading may be applied, and both fiber/matrix debonding and matrix viscoplasticity are included.

Future Work

Future work will focus on the extension of the current model to laminate analysis. The method to be used is the incorporation of the current model, as the constitutive model for a ply in a laminate. Classical lamination theory with the inclusion of nonlinear terms for plasticity and damage will then be used to determine the laminate response. Comparisons between already obtained experimental data, and model predictions will be made to judge the validity and accuracy of the model, for both unidirectional and laminated composites.

References

1. J. Aboudi, "Closed Form Constitutive Equations for Metal Matrix Composites," Int. J. Eng. Sci., Vol. 25, No. 9, pp. 1229-1240 (1987).

2. J. Kaiser, "Untersuchungen uber das Auftreten Gerauschen Biem Zugversuch," PhD thesis, Technisch Hochschule, Munich (1950).

3. A. Needleman, "A Continuum Model for Void Nucleation by Inclusion Debonding," ASME Trans. J. Appl. Mech., Vol. 54, pp. 525-531 (1987).

4. V. Tvergaard, "Effect of Fibre Debonding in a Whisker-reinforced Metal," Mat. Sci. Eng., A125, pp. 203-213 (1990).

5. S.R. Bodner, "Review of a Unified Elastic-Viscoplastic Theory," Unified Constitutive Equations for Creep and Plasticity, A.K. Miller, Ed., Elsevier, London (1987).

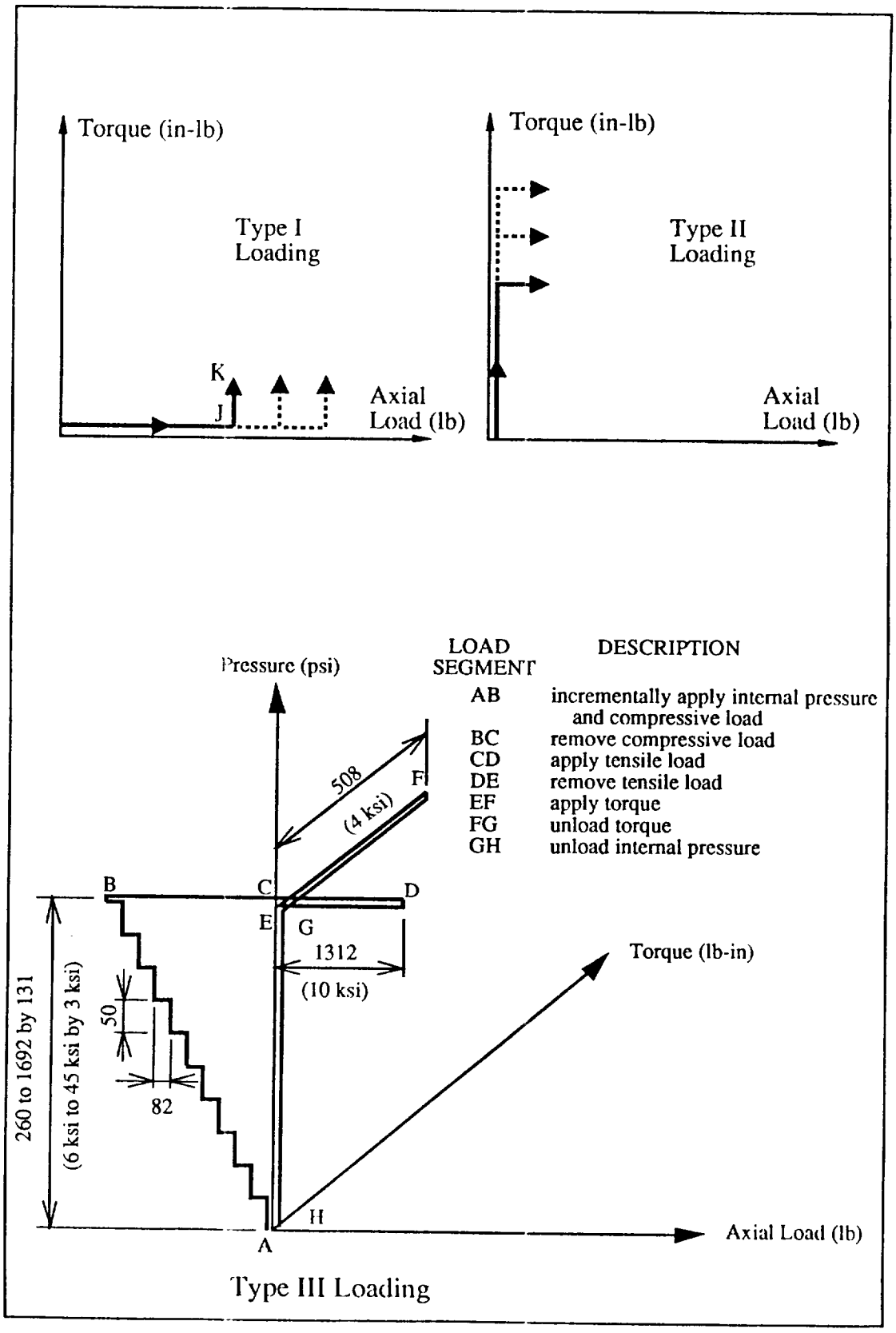

Figure 1: Biaxial Loading Schematics

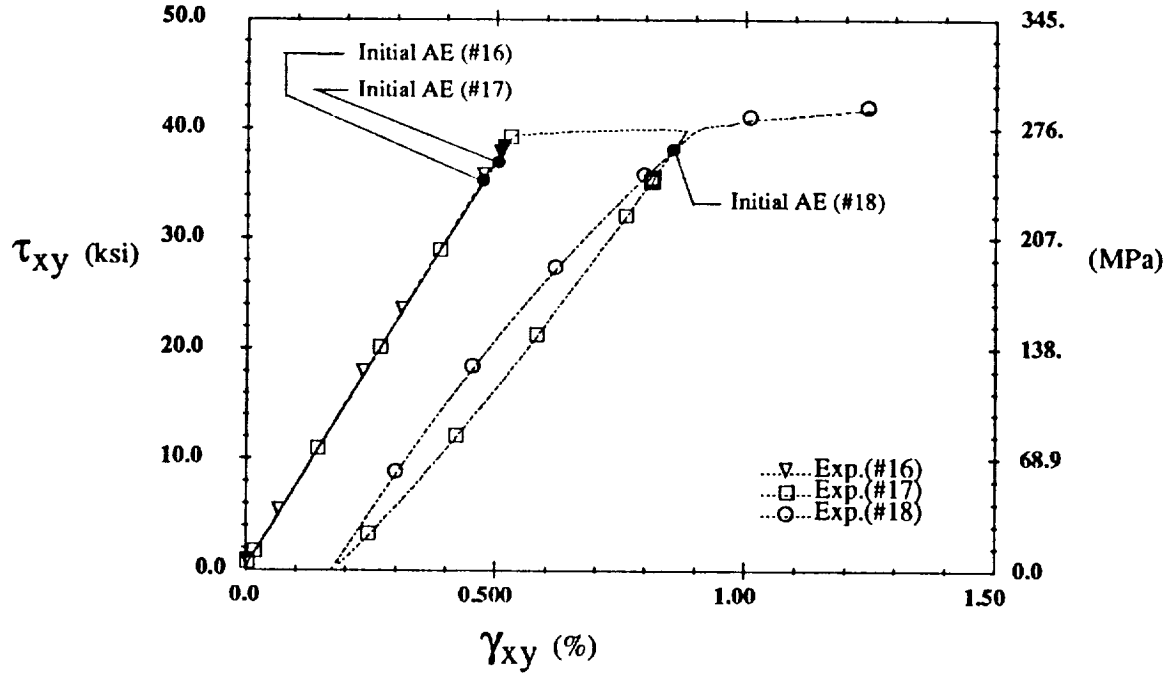

(a) Type II Loading Shear Response

nasa.fig.2a

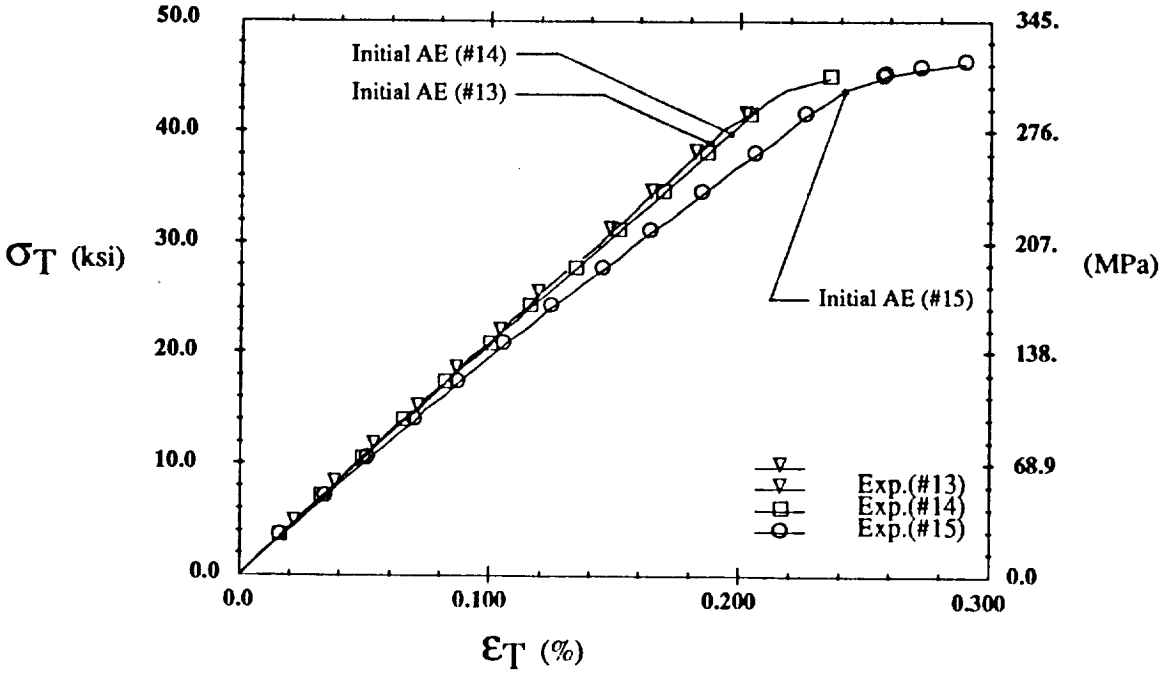

(b) Type III Loading Transverse Response

nasa.fig.2b

Figure 2: $[0_4]$ Experimental Results

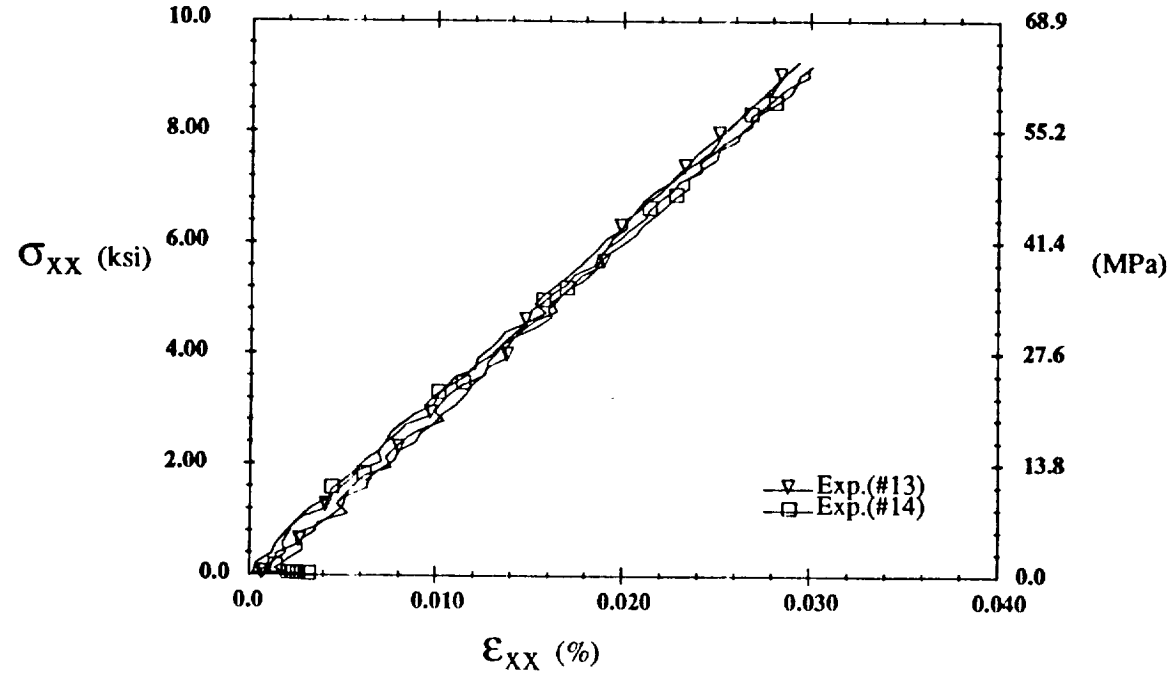

(c) Type III Loading Axial Response

nasa.fig.2c

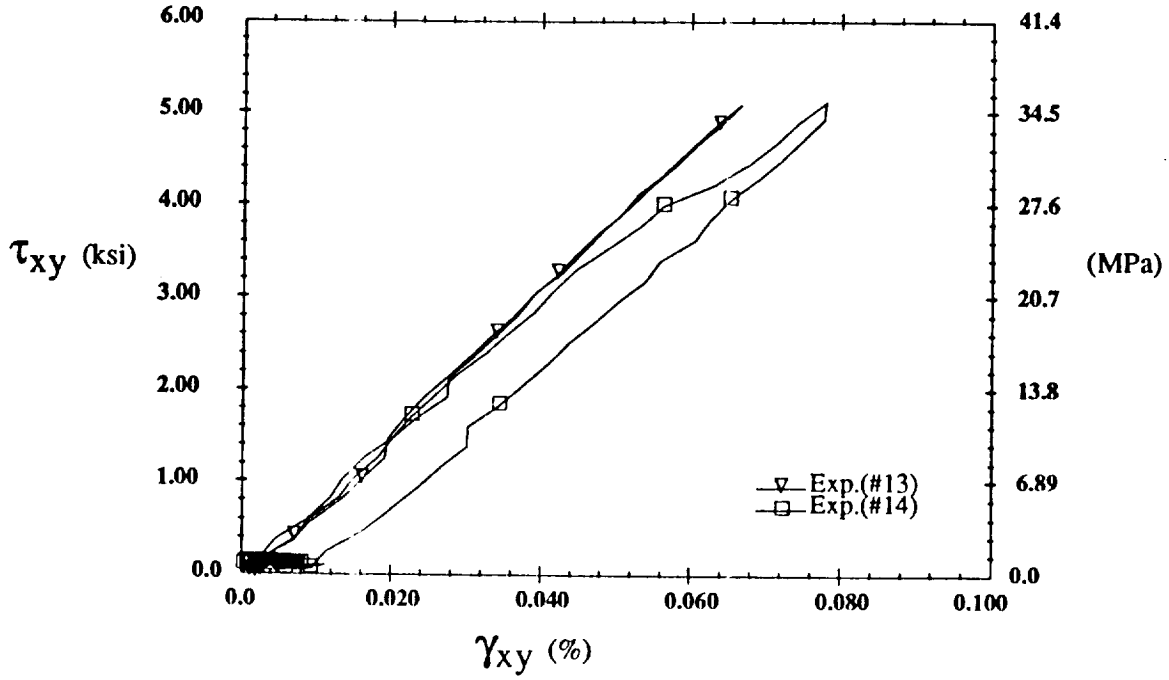

(d) Type III Loading Shear Response

nasa.fig.2d

Figure 2: $[0_4]$ Experimental Results

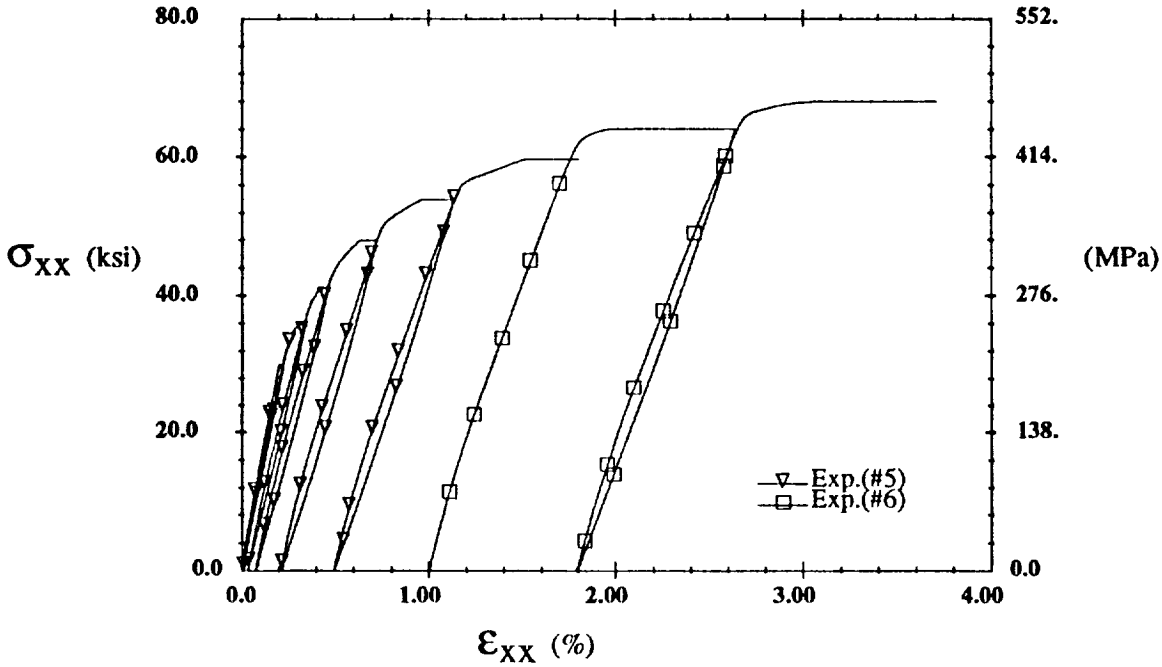

(a) Type IA Loading Axial Response

nasa.fig.3a

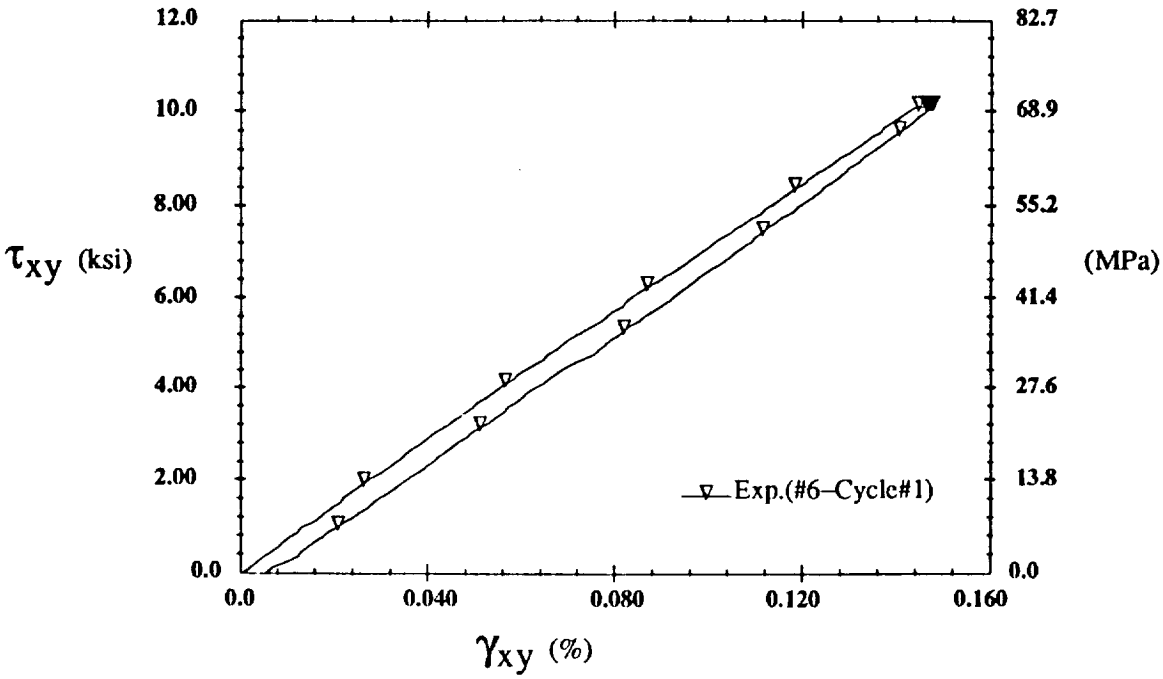

(b) Type III Loading Shear Response

nasa.fig.3b

Figure 3: $[\pm 45]_s$ Experimental Results

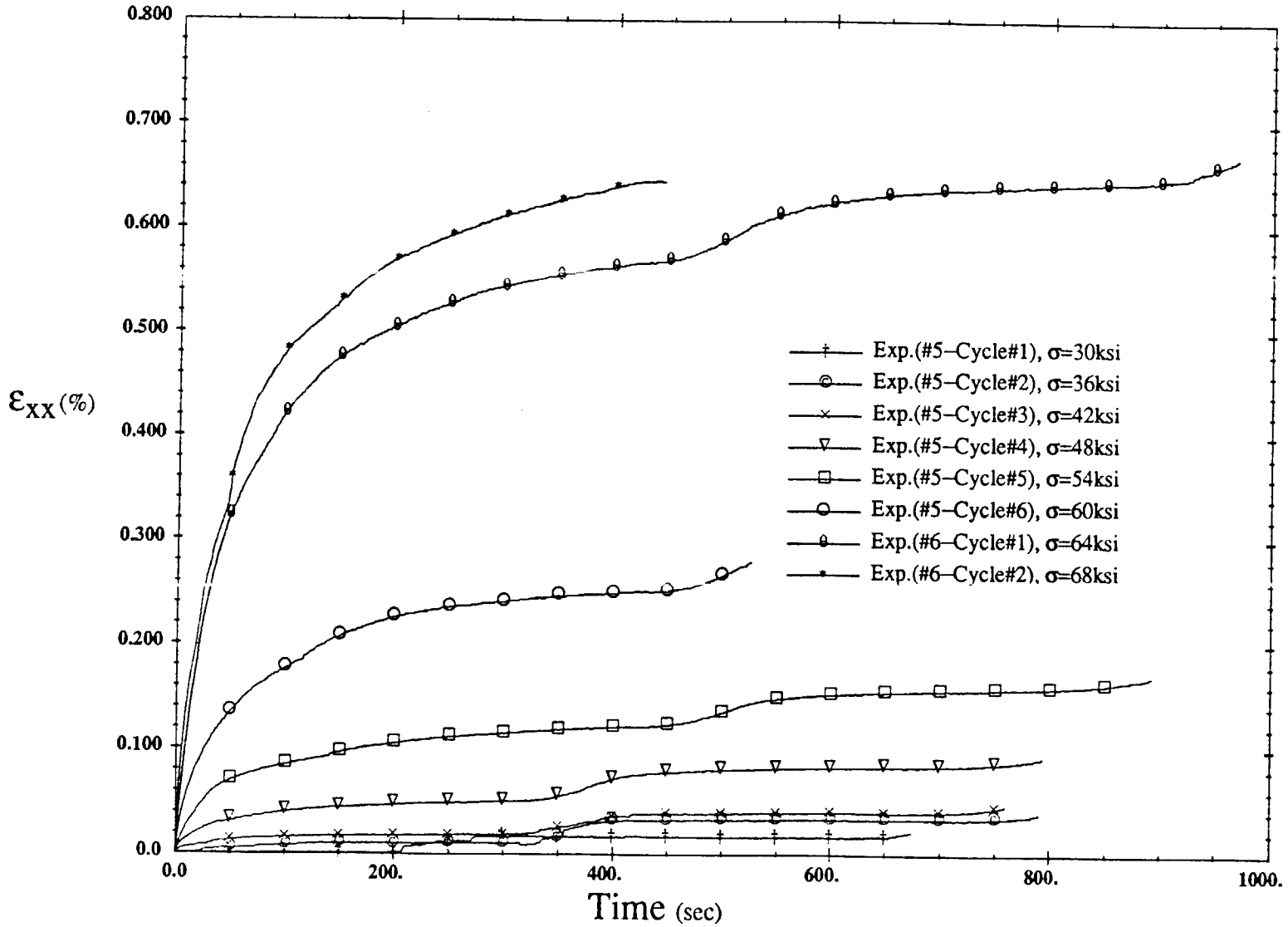

(c)Type IA Loading Creep Response

nasa.fig.3c

Figure 3: $[\pm 45]_s$ Experimental Results

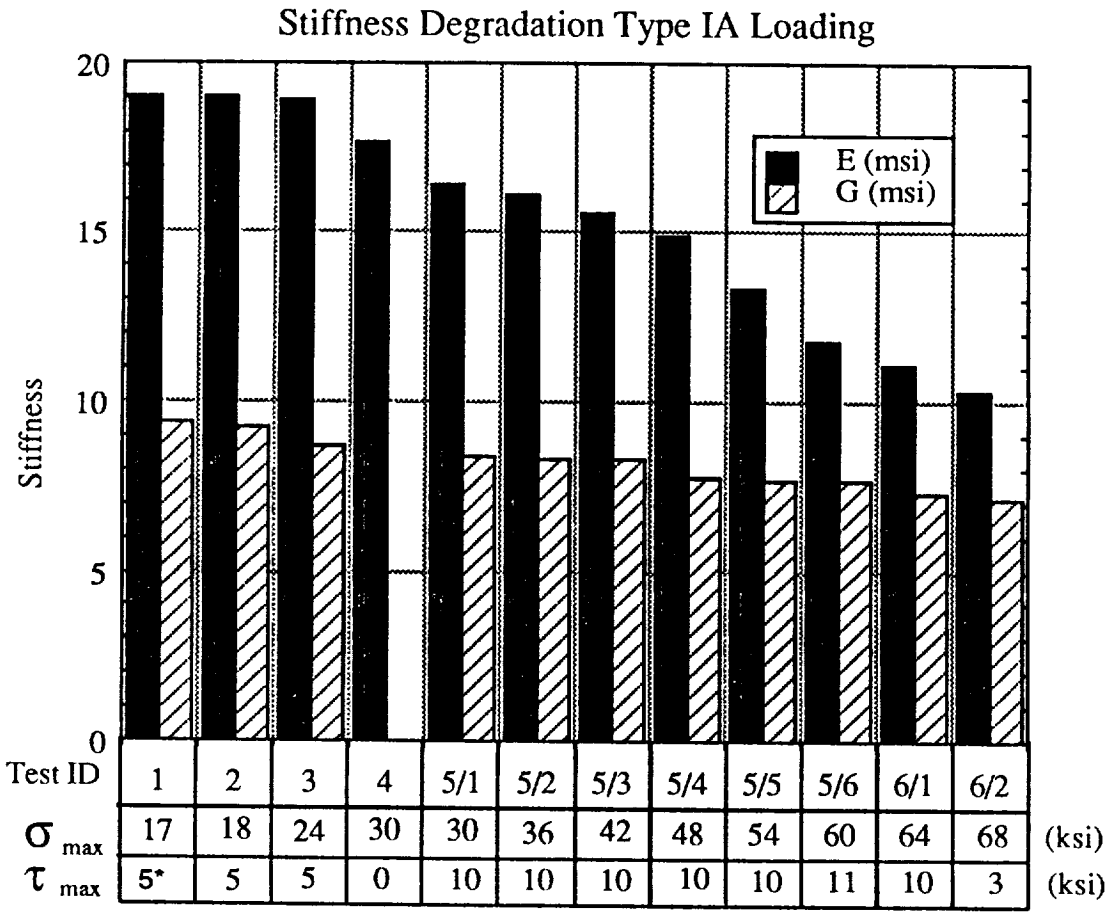

Figure 3(d): $[\pm 45]_s$ Experimental Results

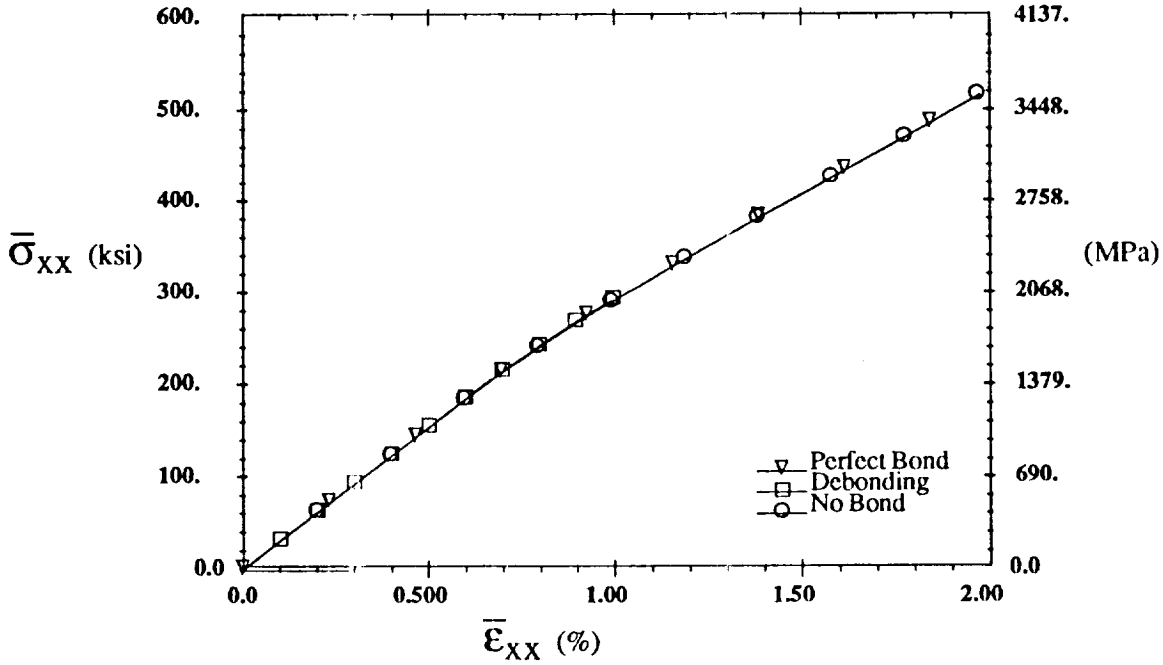

(a) Effective Axial Response

nasa.fig.4a

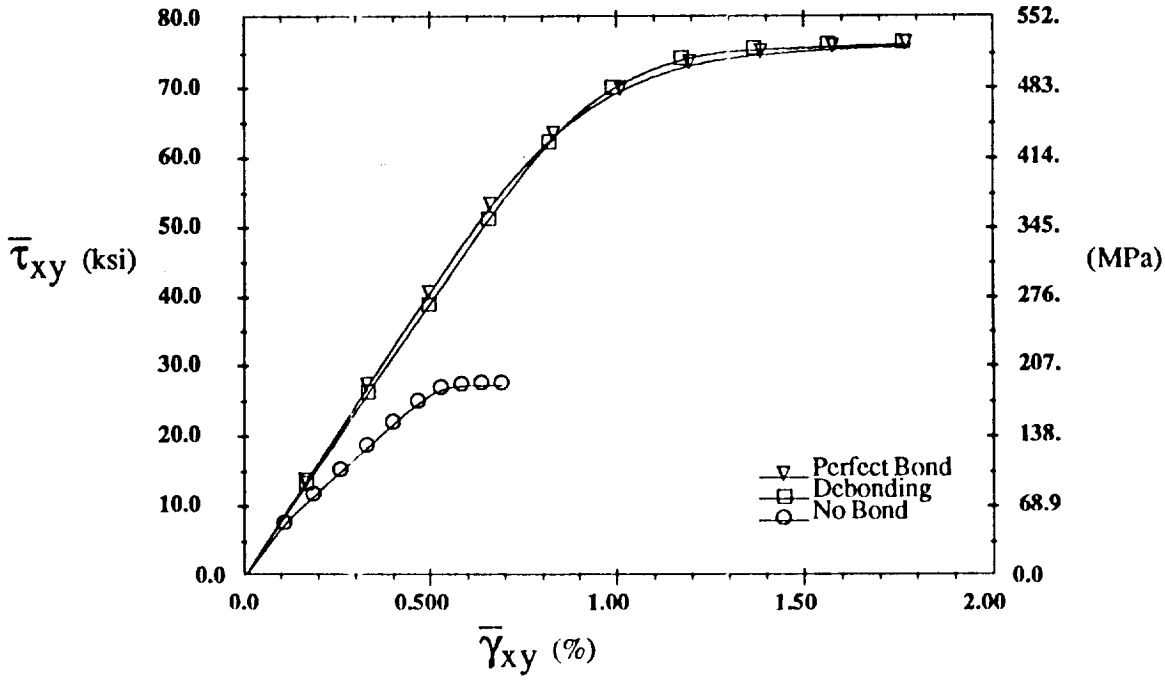

(b) Effective Shear Response

nasa.fig.4b

Figure 4: Analytical Model Predictions

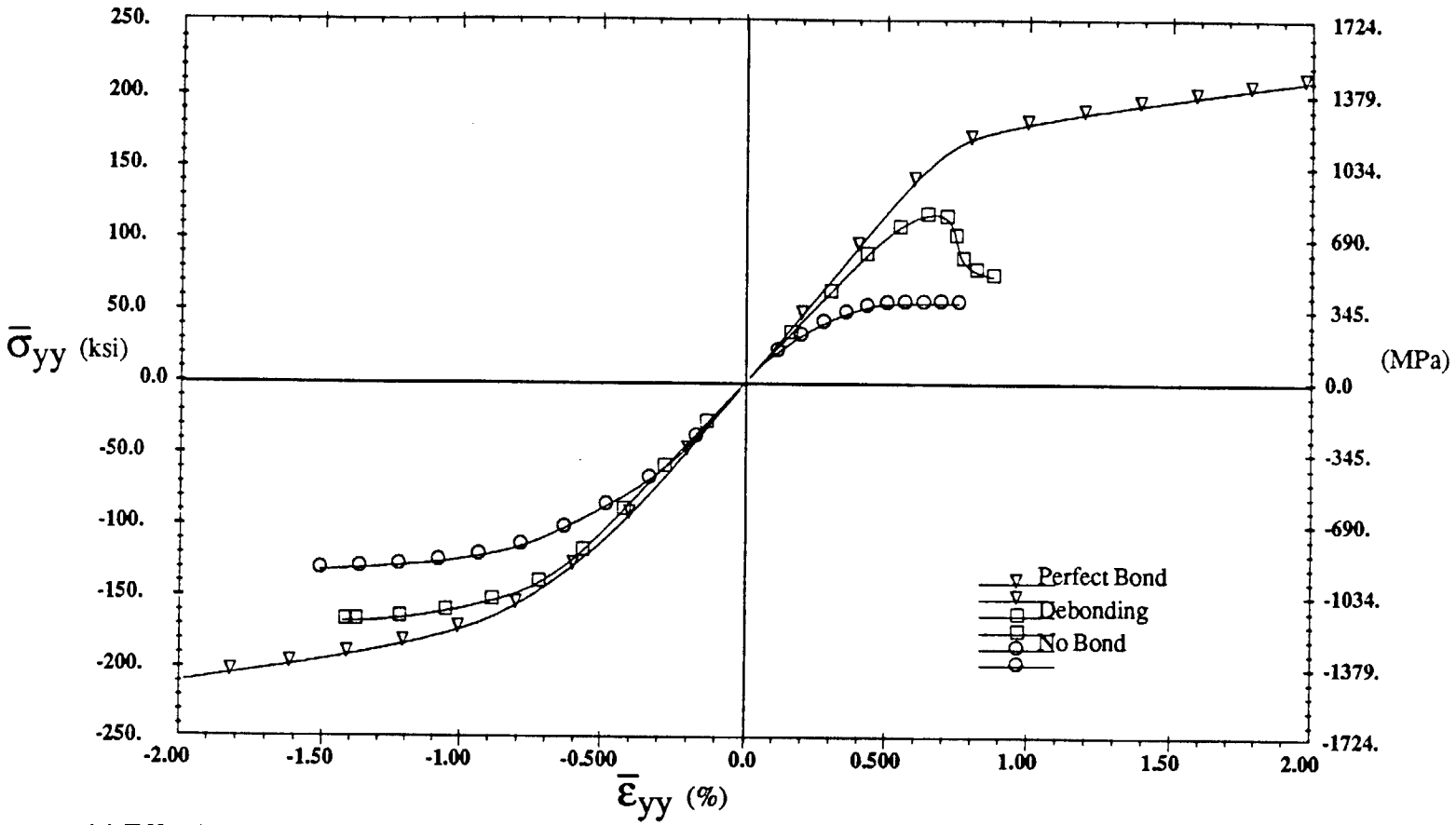

(c) Effective Transverse Response

nasa.fig.4c

Figure 4: Analytical Model Predictions

Project #13 Effect of Temperature on the Response of Metallic Shell Structures

C. Copper, K. McCarthy, W.D. Pilkey and J.K. Haviland

Research Objectives

The objective of this research is to investigate the effects of nonuniform temperature distribution on the response of unstiffened and stiffened cylindrical shells. The focus of the study has shifted from an application to the cryogenic fuel tanks of the National Aerospace Plane (NASP) to fuselage sections of high speed transports (HST).

There are severe temperature variations around or along the fuselage of high speed vehicles. Thermal stresses develop as the heated, expanding skin is constrained by the cooler stiffeners. Due to the severe nonuniform temperature distributions faced by the HST, these thermal stresses are expected to cause buckling of the fuselage. This research purports to gain an understanding of the response of shell structures to thermal gradients.

An additional objective is to develop a method to solve the thermoelasticity equations for prismatic beams with isotropic or orthotropic material properties and arbitrary cross-section shape. This is intended to overcome the considerable inaccuracies of the traditional strength of materials solution.

Approach

The Response of Shell Structures

The principal method of analysis has been computational finite element analysis. The COMPUTATIONAL ANALYSIS TESTBED (COMET) program at NASA-LaRC and an educational version of ANSYS were used for initial investigations. However, Engineering Analysis Language (EAL) was used for the principal analyses because of its flexibility, easy accessibility, and thermal stress analysis capabilities. During the school year, the computational work was done remotely using TELNET, both to send inputs to the CONVEX computer at NASA-LaRC and to recover results for plotting by PATRAN at the University. During the summer, the literature search and the computational work was done by K. McCarthy at NASA-LaRC.

Thermoelastic Beam Solution

The approach to solve the thermoelasticity equations for the prismatic beam is to reduce the solution of the straight beam into the solution of simpler problems. Due to the availability of modern numerical solutions on the commercial market, these simpler problems are easily solved.

Progress During the Reporting Period

The Response of Shell Structures

Preliminary analyses of unstiffened cylinders showed that the Von Mises stresses on the inner skin surface agreed closely with the theoretical value of:

$$\sigma = \frac{\Delta T A E}{2 (1 - \nu)} .$$

The axial displacement of unstiffened cylinders and stringer-stiffened cylinders agreed with a one-dimensional equation. Thus the code was yielding accurate results.

A cylindrical structure 240 inches long and 120 inches in diameter was modelled using shell and/or beam elements. The skin and stiffeners were made of aluminum. A 200-degree thermal gradient was placed through the thickness of the skin. The temperatures of the surfaces (which were -100 °F and 100 °F) are not important, only the gradient through the skin. The skin thickness, ring spacing, and stringer spacing varied from model to model. The five models which will be discussed had a skin thickness of 0.25 inches, a stringer spacing of 18 degrees, and a ring spacing of 24 inches. The structure was first modelled by placing dome caps on the open ends in order to constrain all of the end nodes to displace an equal distance and at the same time yield a resultant axial force of zero. The structure (shown in Fig. 1a) was then cut into a quarter cylinder by two symmetry planes (one plane at mid-length perpendicular to its axis and another containing the axis). When the model was subjected to thermal loading, the linear buckling analysis showed that buckling occurs between the rings and stringers. The linear stress analysis showed a diamond pattern with high stresses along the stringers as seen in Fig. 2a.

The end nodes were constrained to equal displacements with a zero axial resultant force in the second domeless model pictured in Fig. 1b. The skin thickness, stringer spacing, and ring spacing remained the same. The results of the linear buckling analysis and linear stress analysis were the same as the previous model as shown in Fig. 2b.

In order to reduce the size and running time of the model, symmetry was used to reduce the model to a one ring, one stringer model, i.e. a single bay. The third model is still 180 degrees in circumference but contains only 1 ring. The fourth model containing one ring is 90 degrees in circumference. The fifth model is the single bay model, in this case it is an 18 degree segment. All models are shown in Fig. 1. The size and running time of the model is greatly reduced (as demonstrated by Table 1) without a loss in accuracy when the single bay model is used. The linear buckling analyses and linear stress analyses yield similar results as for the larger models (refer to Fig. 2). The smaller models yield the same displacements, stresses, and buckling temperatures, and exhibited similar stress patterns and buckling mode shapes as the larger models.

Table 1

Model	# of nodes	# of elements	# of dof's
1	1436	1670	8282
2	1278	1700	7317
3	294	340	1554
4	151	170	777
Single Bay Model	64	62	310

Parametric studies were performed on a single bay model with a finer mesh. The models had 288 nodes and 284 elements. In the first study, the stringer and ring spacings were 18 degrees and 24 inches, respectively. The skin thickness varied between 0.032 inches and 0.5 inches. The maximum Von Mises stress (on the inner skin surface at the center of the shell element) increases to an upper limit with increasing skin thickness as shown in Fig. 3a. The buckling temperature seems to increase without bound with increasing skin thickness as shown in Fig. 3b.

The skin thickness was 0.25 inches and the ring spacing was 24 inches in the second parametric study. The stringer spacing was varied between 5 degrees and 36 degrees. Fig.

4a shows that the maximum Von Mises stress increases to an upper limit with an increase in stringer spacing. Fig. 4b shows that: 1) as the stringer spacing becomes extremely small the buckling temperature approaches infinity, 2) as the spacing becomes large it approaches an upper limit, and 3) there is a minimum buckling temperature when the stringers are 10 to 15 degrees apart.

The third study investigated the effect of ring spacing on stress and buckling temperature. The results displayed in Figs. 5a and 5b are similar to those for stringer spacing with one exception. The buckling temperature reaches a minimum as the ring spacing is increased.

Since the analyses were linear, results of the analyses for any temperature gradient can be obtained by multiplying the results obtained by a factor equal to the desired temperature gradient divided by this temperature gradient of 200 degrees.

Preliminary models of cylinders with sandwich construction have been made. However, no results have been obtained.

Thermoelastic Beam Solution

To get solutions of the thermoelastic equations for a prismatic beam with an arbitrary cross-sectional shape, the thermoelastic equations are reduced to a set of plane strain problems. To demonstrate a relation between the straight beam and plane strain problems, the displacement form of the differential equations of thermoelasticity are derived for the plane strain problem. By incorporating the plane strain displacements into the displacements of the straight beam, the thermoelastic equations are satisfied for the straight beam. It is observed that the stress resultants, bending couples, and centroid displacements of the thermoelastic solution of the beam have a form similar to the strength of materials solution. By defining a fictitious thermal distribution, any strength of materials solver can be used to get thermoelastic solutions for beam structures. This suggests a new definition of the traditional thermal bending moments and end load. Finally, the displacement formulation is extended to orthotropic material properties.

This thermoelastic solution has been used on various examples. Consider a free pipe that lies along the z axis in a cylindrical coordinate system with a temperature distribution defined as:

$$T(r, \theta, z) = T_1(r) + z\,T_2(r)$$

where T_1 and T_2 are arbitrary functions of r. The ratio of the normal bending stress σ_{zz} calculated by thermoelasticity and strength of materials is:

$$\frac{\sigma_{zz}\,(elasticity)}{\sigma_{zz}\,(strength\ of\ materials)} = \frac{1}{(1 - \nu)}$$

where ν is Poissons ratio. The percent error of the strength of materials solution is:

$$Percent\ Error = \nu\,100\ .$$

Poissons ration varies between 0 and 0.5 for different materials. Hence the percent error of strength of materials is between 0 and 50.

Conclusions

The Response of Shell Structures

1. Thermal stresses in uniform unstiffened shells are predictable from a one-dimensional equation.
2. The single bay model greatly reduces the size of the model without losing too much accuracy. Thus, it is reasonable to use these single bay models for investigations until a need arises for the larger models.
3. Achievable temperature gradients can cause thermal buckling.
4. The maximum Von Mises stress approaches an upper limit as the skin thickness, stringer spacing, and ring spacing is increased.
5. The thermal buckling temperature increases parabolically with an increase in skin thickness. Thus, thermal buckling can occur at small thermal gradients for thin skins.
6. A certain range of stringer spacing exhibits a minimum buckling temperature at which point thermal buckling can occur for relatively small thermal gradients.
7. The thermal buckling temperature decreases with increasing ring spacing. Thus, thermal buckling would be more likely to occur when the rings are far apart.

Thermoelastic Beam Solution

8. The stresses for a thermally loaded beam produced by strength of materials can have up to 50 percent error. To overcome this, the thermoelastic equations can be satisfied by solving a simple set of problems.

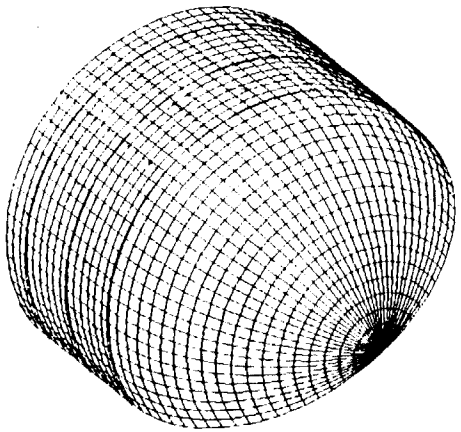

a. 8282-dof quarter cylinder domed model

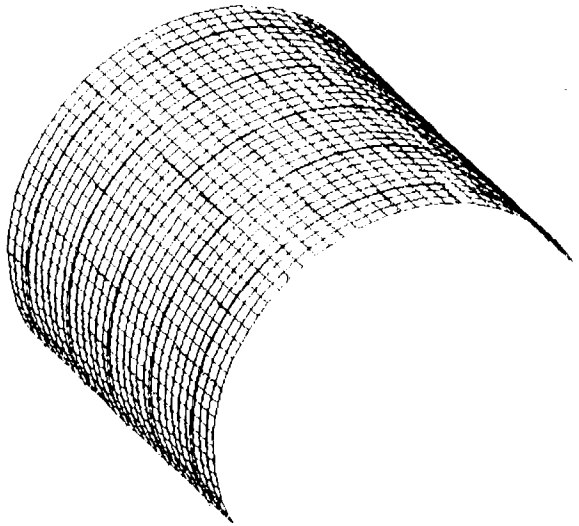

b. 7317-dof quarter cylinder model

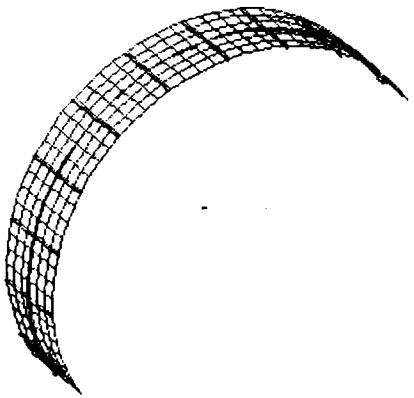

c. 1554-dof single ring quarter cylinder model

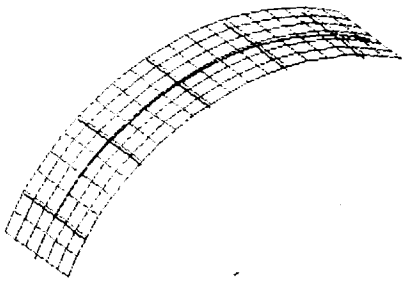

d. 777-dof single ring 90-degree model

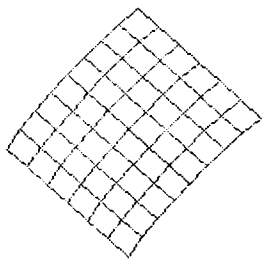

e. 310-dof single bay model

Figure 1
Reduction in Size of Finite Element Model

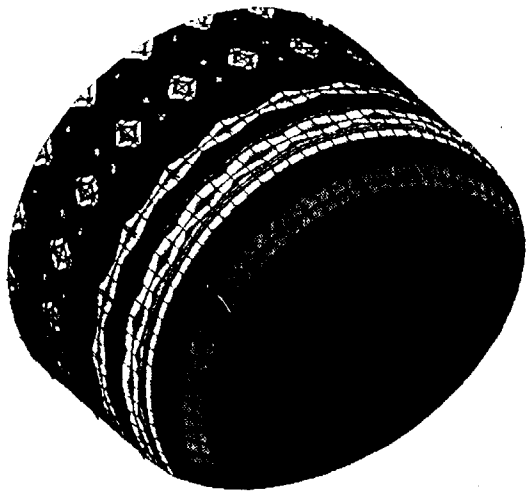

a. 8282-dof quarter cylinder domed model

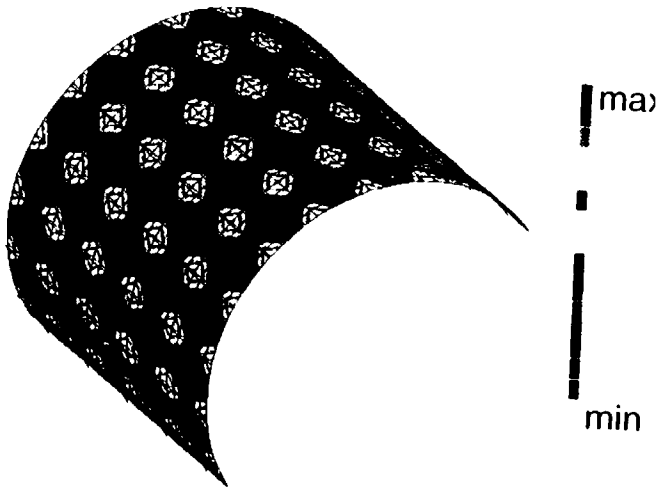

b. 7317-dof quarter cylinder model

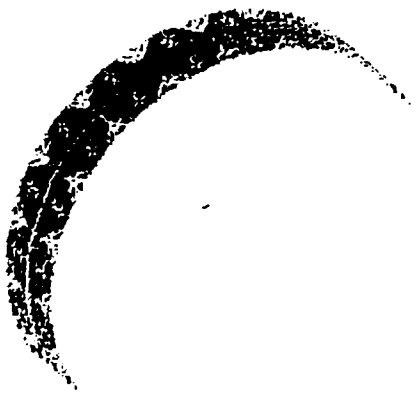

c. 1554-dof single ring quarter cylinder model

d. 777-dof single ring 90-degree model

e. 310-dof single bay model

Figure 2
Linear Stress Buckling Analyses

a. Skin Thickness vs Von Mises Stress

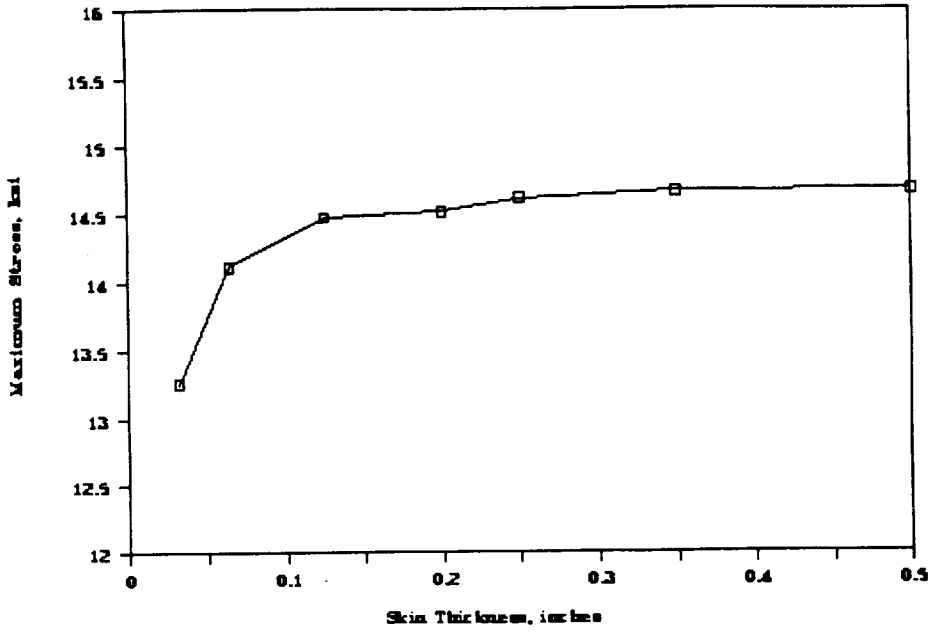

b. Skin Thickness vs Buckling Temperature

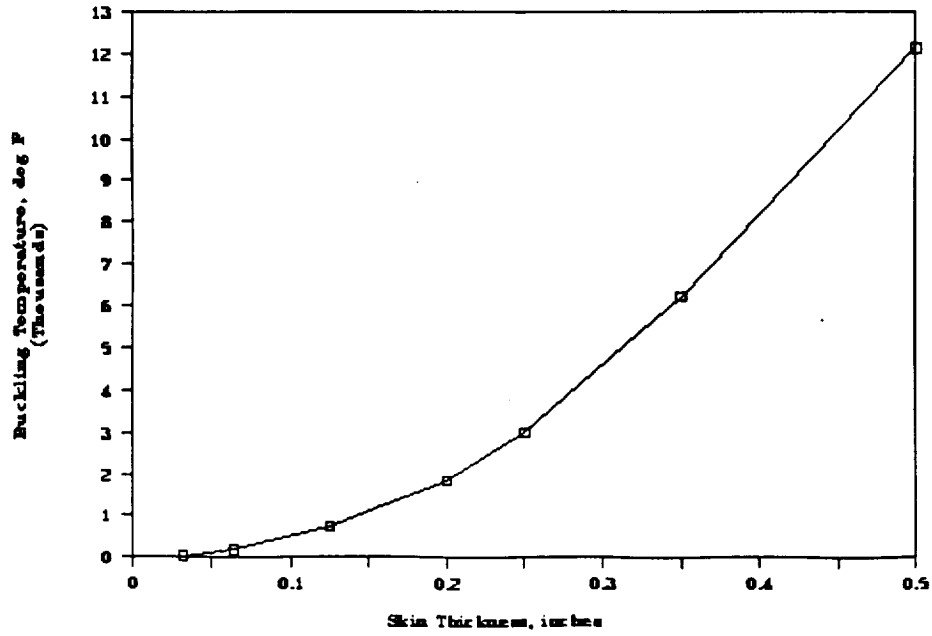

Figure 3
Single Bay Model: Response to Change in Skin Thickness

a. Stringer Spacing vs Von Mises Stress

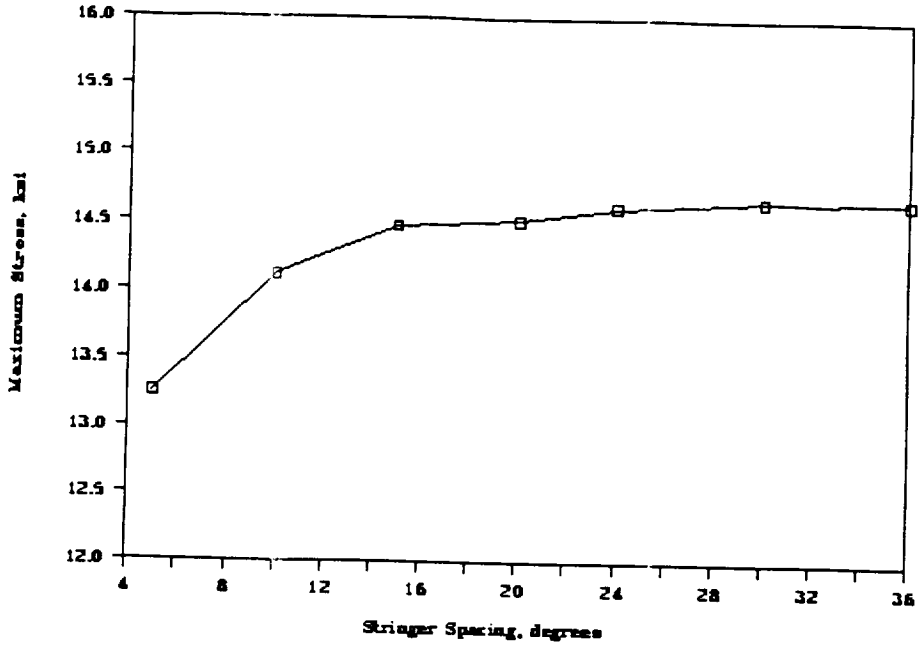

b. Stringer Spacing vs Buckling Temp

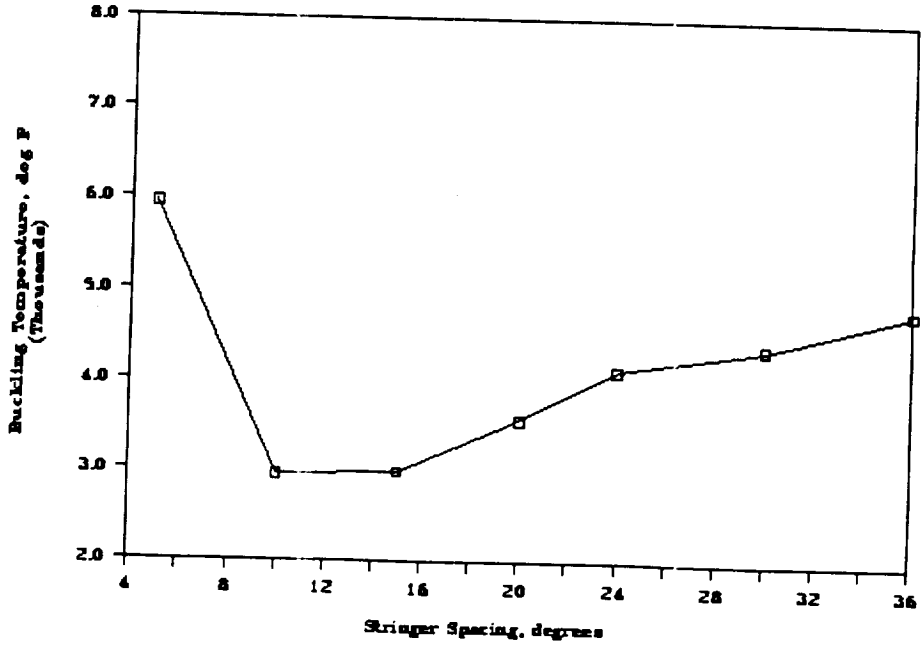

Figure 4

Single Bay Model: Response to Change in Stringer Spacing

a. Ring Spacing vs Von Mises Stress

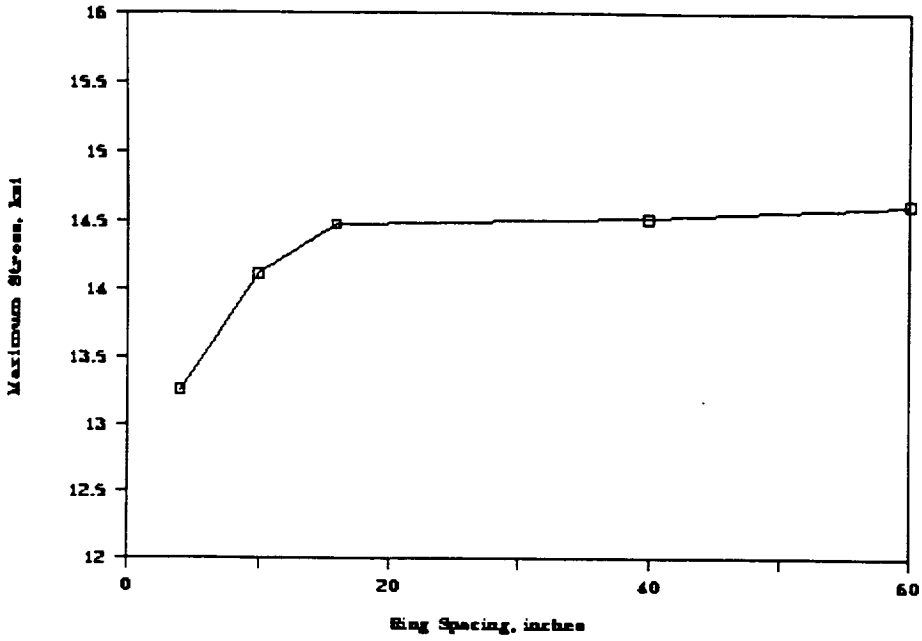

b. Ring Spacing vs Buckling Temperature

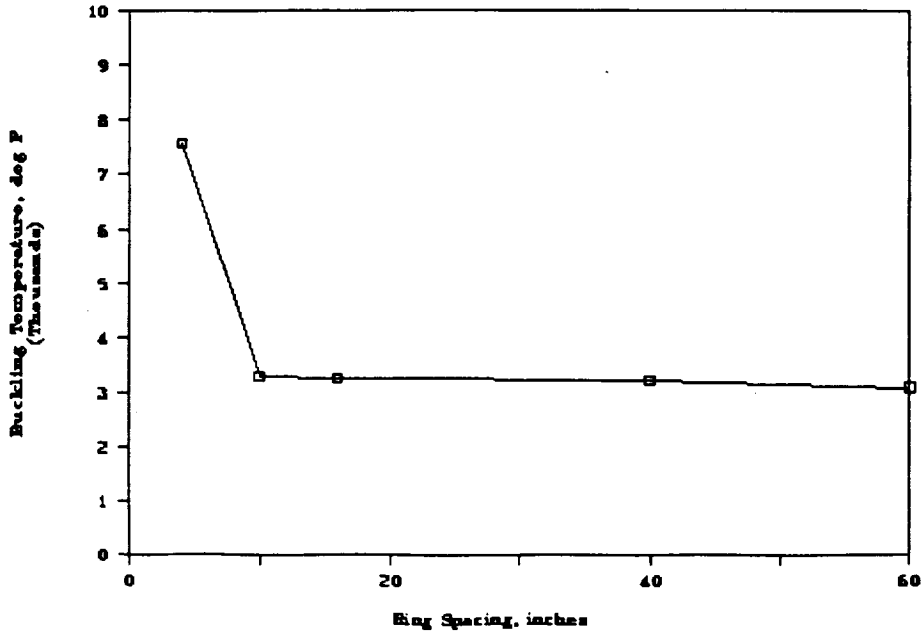

Figure 5
Single Bay Model: Response to Change in Ring Spacing

Project #14 **Experimental Study of the Nonlinear Viscoplastic Response of High Temperature Structures**

Marshall F. Coyle and E.A. Thornton

Objectives

The basic objective of this research program is to investigate experimentally the viscoplastic response of thermal structures for high speed flight. An additional objective of the experimental program is to provide high quality data for validation of finite element analysis using unified viscoplastic constitutive models.

Approach

Simplified structures of representative high temperature superalloys and/or advanced aluminum alloys will be designed and tested. These alloys will display typical biaxial stress states with appropriate temperatures and stress gradients. The simplified structures will provide well-defined thermal and structural boundary conditions.

Research Progress

Panel Tests

A series of experiments were conducted on three 1/8 in. thick 10 x 15 in. rectangular Hastelloy-X panels (panels No. 1, 2, and 3). The test panel configuration is shown in Figure 1. The test panel was supported at four points to provide well defined boundary conditions and to minimize heat losses. The supports were located 4 in. on either side of the transverse center line and 1/2 in. inside the transverse edge. A Research Inc. "High-Intensity Infrared Elliptical-Reflector" 16 in. long line heater (lamp) was used to heat the panel along the long transverse center line (X-Axis). The line heater produced a narrow (1/8 - 1/4 in.) heated strip along the X-Axis. The edges of the panel were cooled by running chilled water through polybutylene (PVC for panel No. 2) pipes adhesively bonded to opposite edges of the panel. Each edge of the panel was inserted and bonded in a slot machined into a polybutylene pipe. A chilled water system provided coolant at a constant temperature. The panel was fully insulated except for a tapered slot along the X-Axis to facilitate the heat flux from the line heater.

The first Hastelloy-X tests were performed on panel No. 2. This panel was instrumented with 18 type T thermocouples to measure the temperature distribution. The panel was also instrumented with 15 LVDTs to measure out-of-plane displacements. This panel was subjected to a series of tests at different heat flux levels. Results from these tests were reported in the 1991 progress report.

A second series of Hastelloy-X tests were performed on panel No. 3. This panel was instrumented with 29 type K thermocouples to measure the temperature distribution. Type K thermocouples were used on this panel so that tests could be run at temperatures above 700 °F (limit of type T thermocouples). The panel was also instrumented with 15 LVDTs to measure out-of-plane displacements. This panel was subjected to a series of five tests at increasing temperature levels. The first two tests were elastic. The last three tests induced increasing levels of permanent deformation in the panel. The test series is summarized in Table 1.

Table 1
Panel 3 Test Series

Test	P%	Max. Temp. (°F)	Behavior
1	5	250	Elastic
2	15	375	Elastic
3	15	500	Possibly Plastic
4	30	700	Plastic
5	70	1000	Plastic

Results from this test series are described in a paper presented at the 33rd Structures, Structural Dynamics, and Materials Conference on April of 1992 in Dallas Texas (Ref.1).

The third series of tests were conducted on panel No. 1. This panel was instrumented with 14 Measurements Group WK-series strain gages. A thermocouple was attached to the panel adjacent to each of the strain gages to measure the temperature at each gage. Additional thermocouples were combined with the previously mentioned thermocouples to document the panel's temperature distribution. This brought the total number of thermocouples used up to 20. The panel was also instrumented with 16 LVDTs to measure

out-of-plane displacements. Figure 2 is a schematic of the test setup. A Measurements Group System 4000 data acquisition was used to gather the strain and temperature data. A Keithley Metrabyte data acquisition system acquired LVDT the data.

Apparent strain curves were generated for each of the strain gages before testing. The instrumented panel (less LVDTs) was placed in an oven in a manner to permit free expansion. The oven was programmed to raise the panel's temperature from 75 °F to 500 °F in 10 hours and then, typically, back to 75 °F in about 16 hours. The long heating and cooling cycle was to prevent temperature gradients that would cause stresses. Thus, the panel was in a stress-free state. Strain and temperature data were recorded as the panel was thermally cycled. The panel was cycled until the strain gage's response became repeatable. This took several cycles. Strain and temperature data from the repeatable cycles were used to generate individual apparent strain curves for each gage.

This panel was subjected to a series of four tests at increasing temperature levels. The first test was elastic. The last three tests induced increasing levels of permanent deformation in the panel. The test series is summarized in Table 2.

Table 2
Panel 3 Test Series

Test	P%	Max. Temp. (°F)	Behavior
1	5	330	Elastic
2	15	375	Possibly Plastic
3	15	500	Plastic
4	30	700	Plastic

Results from test No. 1 will be used to illustrate some of the data that was collected. In this test, the lamp's output was set at 5% and the cooled edges were maintained at 70 °F. The panel reached a maximum steady state temperature of 330 °F at an elapsed time of 1 hr..

Figure 3 shows the temperature profile along the Y-Axis at 1 hr. It can be seen that the temperature profile is linear indicating steady-state temperatures. The through-the-thickness temperature gradient was found to be negligible. Figure 4 shows the top, middle, and bottom strains in the X direction along the Y-Axis. (Top refers to the heated side of the panel.) A strain gage could not be placed at Y = 0 on the top since it would be affected adversely by the incident heat flux. The mid-plane strain was calculated using strain information from the top and bottom strain gages. The mid-plane strain is both linear and symmetric about Y = 0 and agrees with the strain distribution expected for the given temperature distribution[2]. Note that significant bending strains are induced by panel bending. The displacements along the X-Axis at 1 hr. are shown in Figure 5. It should be noted that in this series of tests a positive displacement is towards the heat lamp. Figure 6 is a plot of temperature versus displacement at the center of the panel. This Figure shows an initial nonlinear response which becomes nearly linear in the middle temperature range. The out-of-plane displacements are initiated by the panel's initial shape and bending-buckling resulted from compressive thermal stresses. Tests 2-4 of panel 3 will be described in the next progress report. These tests document the transient, inelastic response of the panel.

Lamp Characterization Tests

The behavior of the Research Inc. "High-Intensity Infrared Elliptical-Reflector" 16 in. long line heater is very important to this test program. To understand the spatial variation of the heat flux on a deformed test panel, a special lamp test fixture was designed and fabricated. Figure 7 is a schematic of the test fixture. The quartz lamp is suspended above an array of heat flux calorimeters. The calorimeters are mounted on a water cooled table. A chiller provides coolant to the table in order to maintain a constant temperature. The table is indexed under the lamp with a X-Y motor driven actuator. The lamp's elevation is

controlled with a manual screw driven linear actuator. A data acquisition system is used to collect heat flux and temperature measurements from the calorimeters. A computer controls the X-Y position of the table along with data acquisition system, and it also stores the collected data. The system is programmed to perform a survey in the X-Y plane automatically.

Two series of lamp tests were conducted. In the first test series lamp power and incident heat flux were measured as a function of the control output percent. During a test, heat flux, lamp voltage and current were measured and recorded. The control output was maintained for a period of time to allow the lamp filament to equilibrate. Results from this test series showed that the heat flux varied nonlinearly with control output for levels of power less than 15%. Nevertheless, for higher power levels the lamp power and heat flux vary nearly linearly.

In the second series of tests, heat flux distributions in the X-Y plane were measured for three control output levels of 5%, 10% and 15%. Figure 8 shows heat flux variations with Y at the lamp centerline and X=0 for 5, 10, 15% lamp output power levels. Figure 9 shows non-dimensional average heat flux distributions f(x) along the X-Axis. These distributions show the variation of heat flux with both X and Y. Further discussion of the lamp characterization tests and results are given in Reference 1.

A device was designed and fabricated which will allow heat flux gages to be sent to NASA Langley for calibration. The device is a liquid cooled cylinder with interchangeable caps. On each cap a heat flux gage is permanently mounted. Once calibrated, the cap-gage combination can then be mounted directly into the copper surface. The surface serves as the incident heated surface for lamp calibration tests. Additional travel (approximately 2.5 in.) been added in the Z-Axis, allowing for an expanded 3-dimensional space calibration grid.

New lamp mounting brackets were designed and manufactured to allow for quick change of lamps between calibration stand and experimental setup. Finally, X and Y stepper motor routines were reprogrammed to allow for faster data acquisition as well as automating the entire test routine.

Plans for the Future Research

In the next six months, a Hastelloy-X panel with stiffeners will be designed and fabricated. This panel will then be instrumented with strain gages, thermocouples, and LVDTs. Initial tests will be conducted on the stiffened panel in the elastic range. A test will then be run with a flux level that will cause plastic deformation. Test preparation will begin on the 0.090 in. thick 8009 aluminum alloy panels received from NASA Langley.

Efforts will continue on the line heater surveys. Tests will be conducted to obtain the heat flux distribution in the Z direction. This information will be used in continued efforts to correlate the thermal behavior of the panel with given flux levels and panel deformations.

References

1. Thornton, E. A., Coyle, M. F., and McLeod, R. N., "Experimental Study of Plate Buckling Induced by Spatial Temperature Gradients," 33rd AIAA/ASME/ASCE/AHS/ASC Structures, Structural Dynamics, and Materials Conference, Dallas, TX, April 13-15, 1992, AIAA 92-2540.

2. Heldenfels, R. R. and Roberts, W. M., "Experimental and Theoretical Determination of Thermal Stresses in a Flat Plate", NACA TN 2769, 1952.

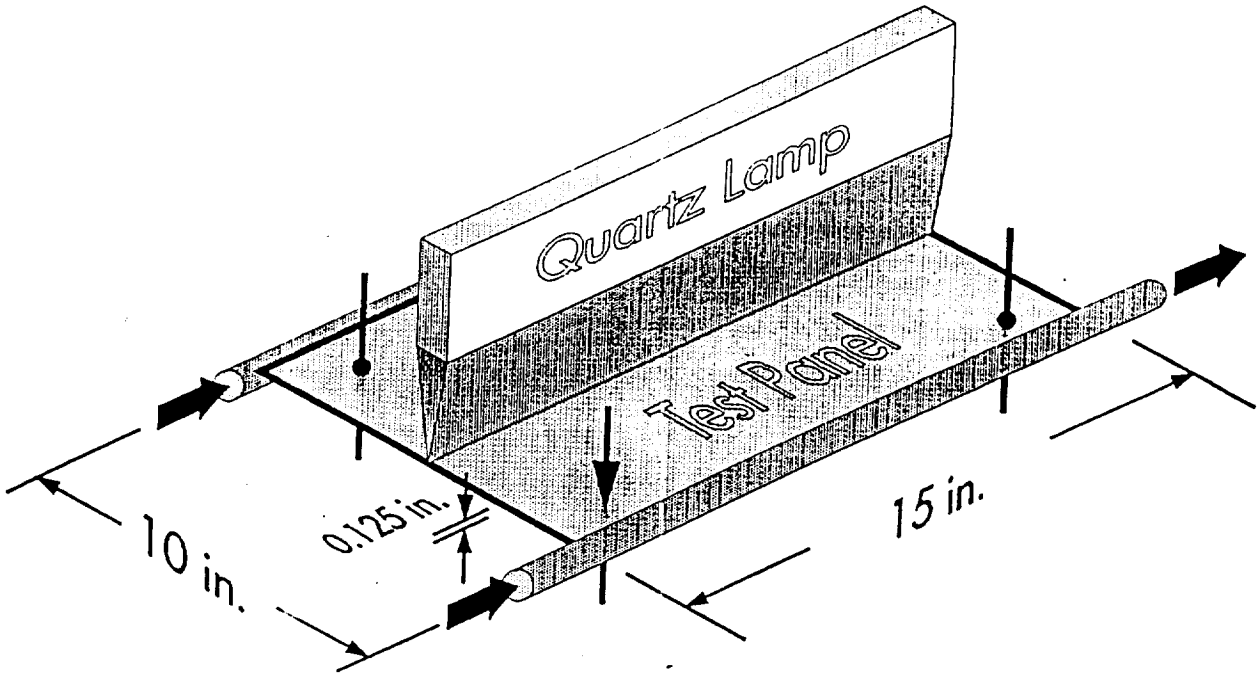

Figure 1: Test Panel Configuration

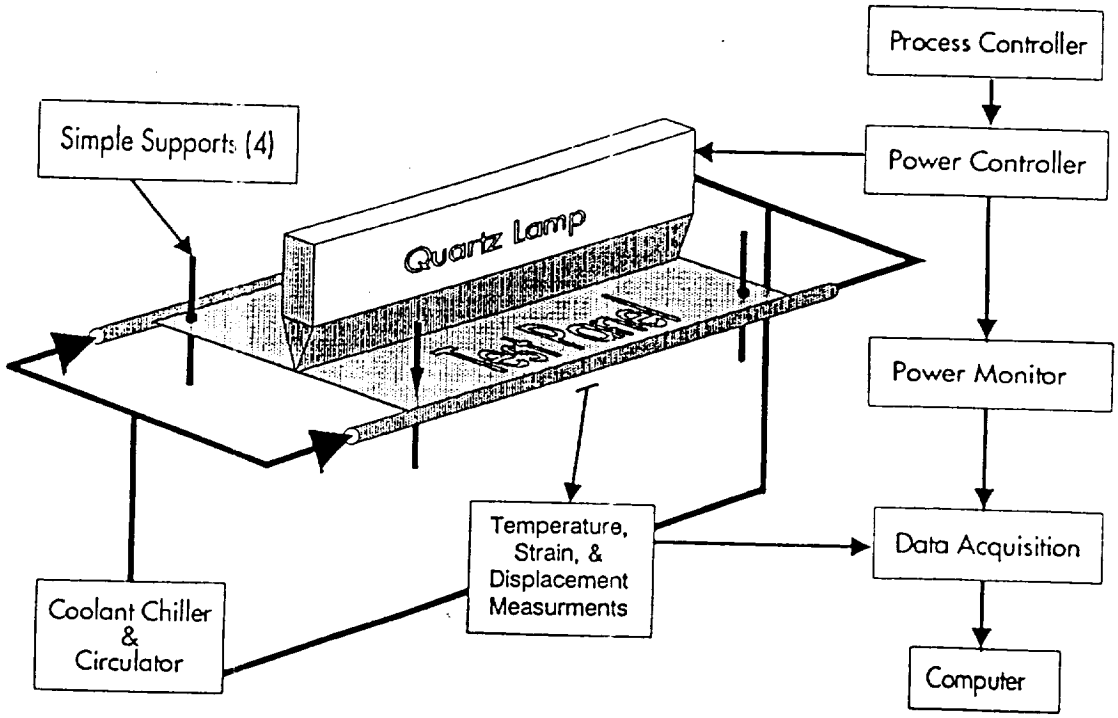

Figure 2: Panel Buckling Test Schematic

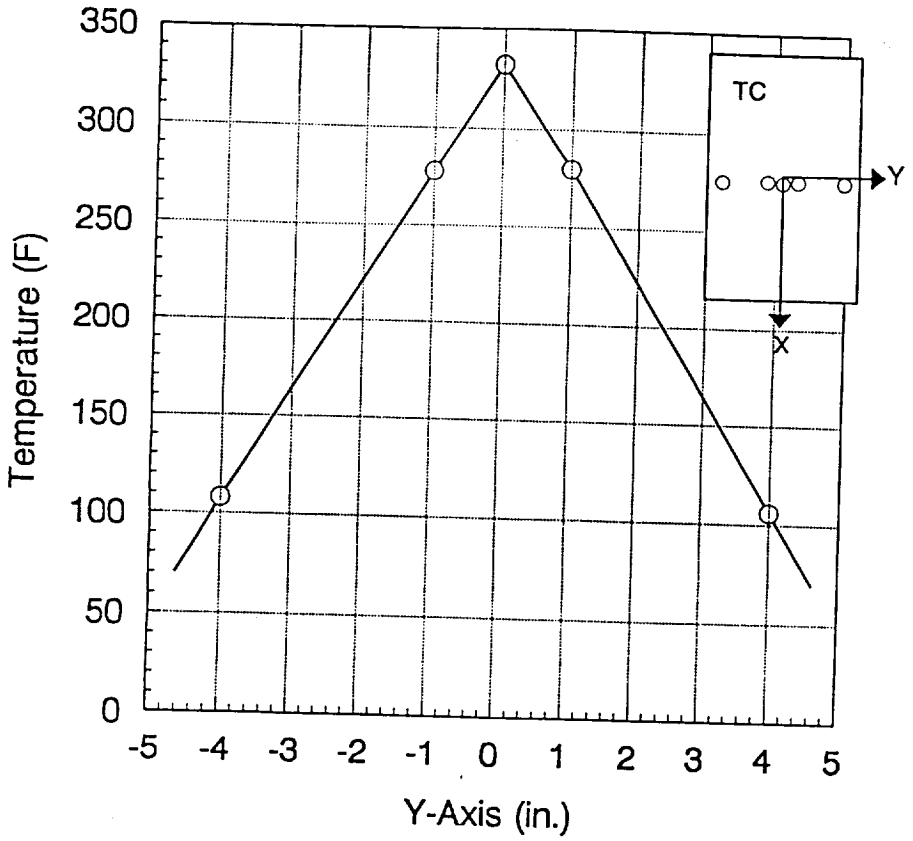

Figure 3: Panel Temperature Distribution

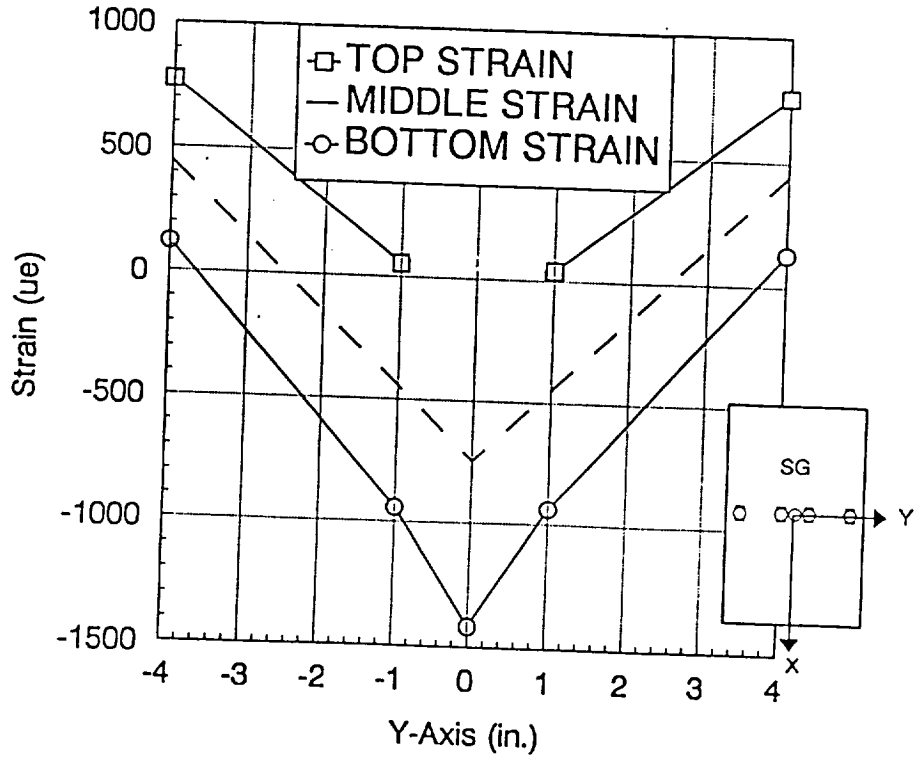

Figure 4: Panel Strain Distribution

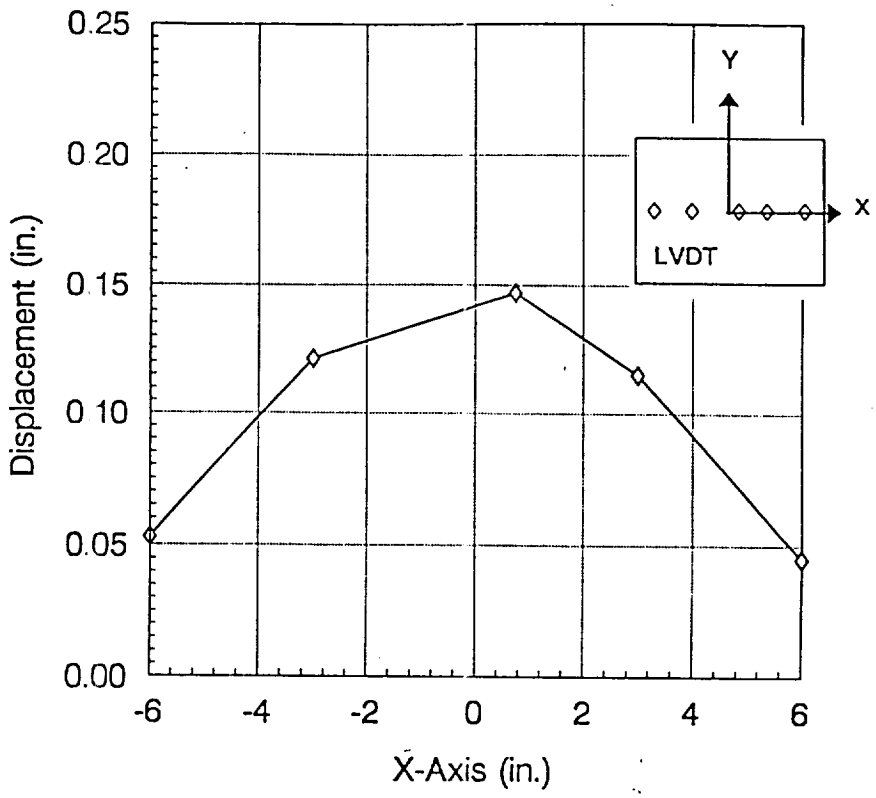

Figure 5: Panel Displacement Distribution

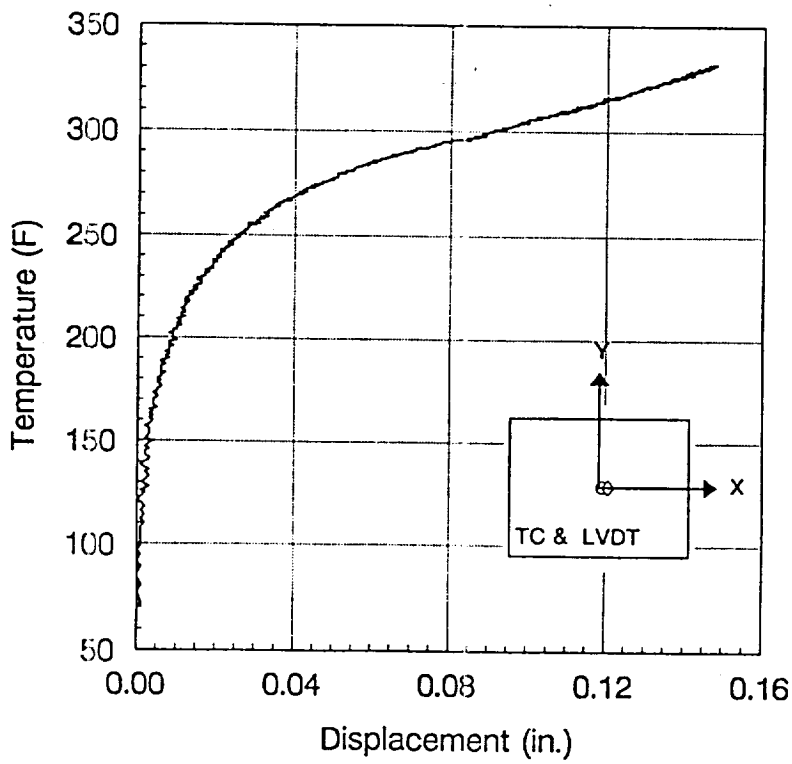

Figure 6: Panel Temperature versus Displacement Response at the Center

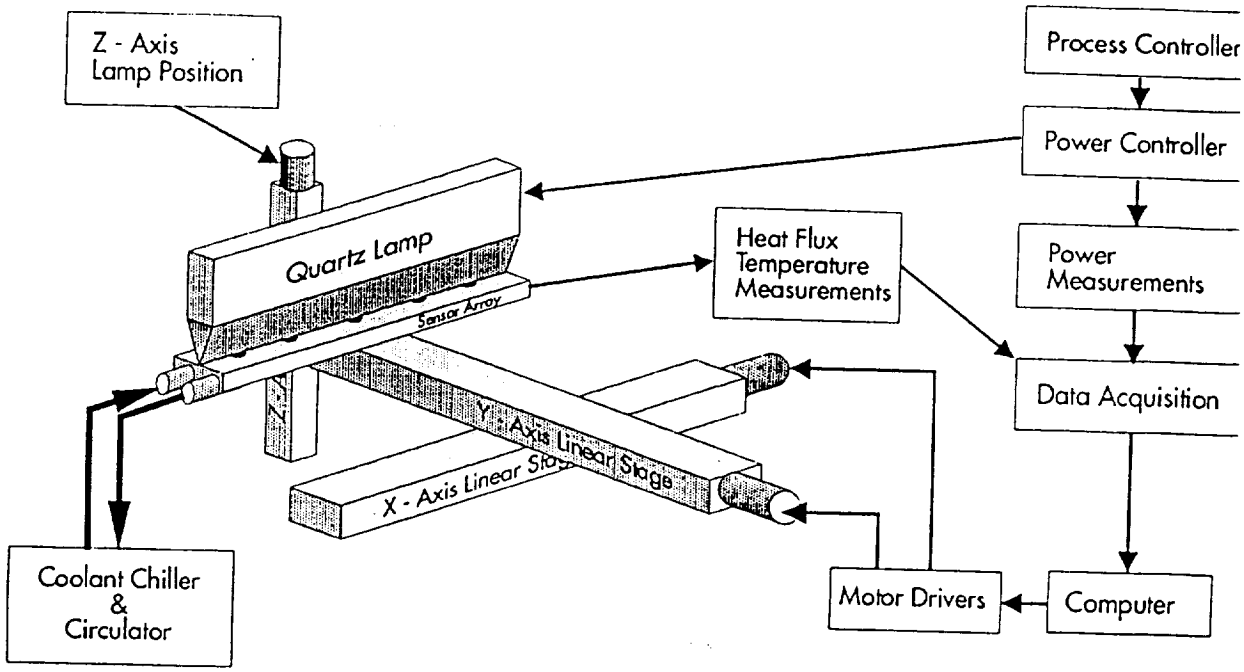

Figure 7: Lamp Characterization Test Schematic

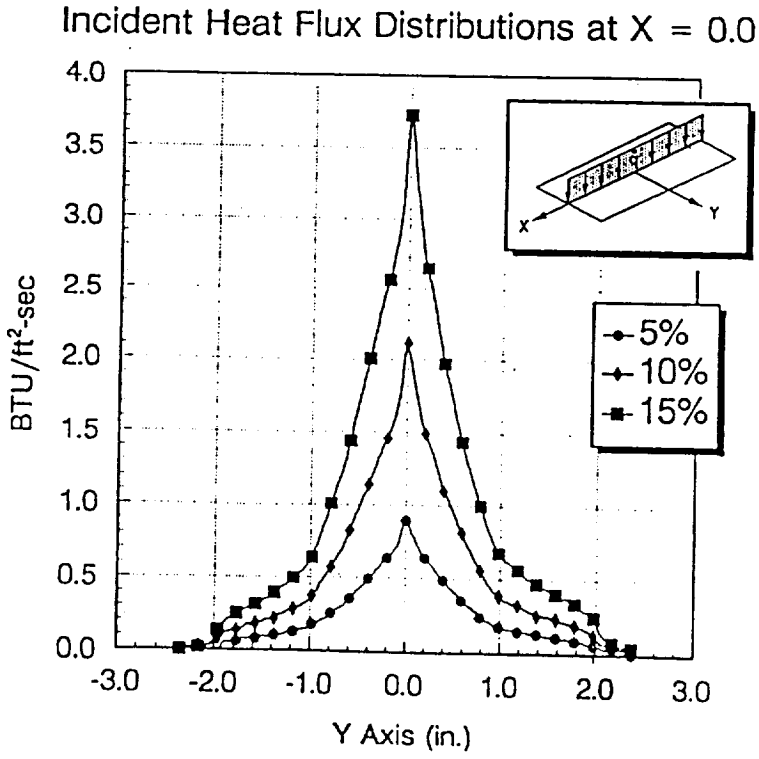

Figure 8: Incident Heat Flux Distribution at X = 0

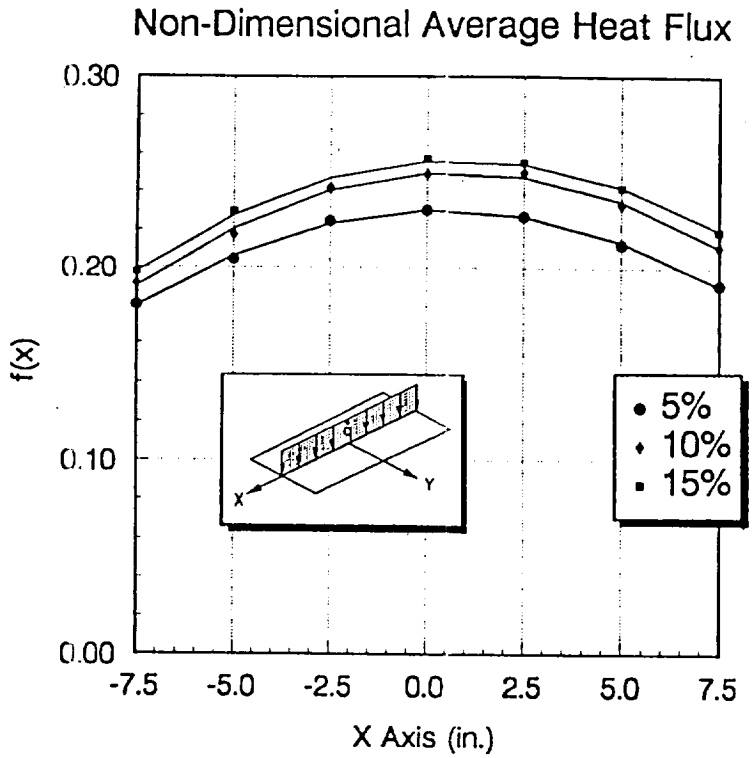

Figure 9: Non-Dimensional Average Heat Flux

Project 16 Characterization of the Viscoplastic Behavior of Materials

Mark A. Rowley and Earl A. Thornton

Introduction

An important aspect of understanding the inelastic behavior of structural components under severe heating is having a fundamental knowledge of the material behavior at elevated temperatures. To support the research funded by the Aircraft Structures Branch under Project 16, a material characterization project was initiated in the summer of 1991. The project involves close cooperation between the faculty and graduate students in the Mechanical and Aerospace Engineering and Materials Science and Engineering Departments at UVa. The experiments are being conducted using the testing facilities in the Materials Science Department. At present, Mr. Mark A. Rowley, an M.S. graduate student in the MAE Department, is being supported by the UVA Academic Enhancement Program through the Center of Light Thermal Structures.

Objective

The objective of this research is to characterize the viscoplastic behavior of materials that are being used in the thermal buckling tests. The approach has been divided into three tasks. The first task is to obtain accurate tensile or compressive data and accurate creep data for materials of interest from which model parameters for the Bodner-Partom constitutive model may be obtained. The second task is to develop procedures for obtaining the constitutive model parameters from the experimental data. The third task is to obtain and validate the parameters that provide an accurate modeling of the test materials.

Approach and Method

K.S Chan, S.R. Bodner, and U.S. Lindholm demonstrated[1] that nickel-based superalloys can be accurately modeled using a unified viscoplasticity constitutive model developed by S.R. Bodner and Y. Partom[2]. This model, summarized in Figures 1 and 2, implements the Prandtl-Reuss flow law, a kinetic equation relating the invariants of plastic strain rate and stress, and evolution equations for hardening.

A combined program of experimental and analytic procedures is used in developing the model parameters[1]. Previous research efforts by Chan et al.[1] showed that uniaxial tensile data and creep data are sufficient to develop a complete model over the temperature range of interest in the present buckling tests. Plastic work rate can be derived from the tensile data and used as the hardening measure. The model parameters are obtained through an iterative procedure involving calculations that incorporate saturation stresses, plastic strain rates, plastic work rates, and estimations of the yield stresses for each set of tensile data. An outline for the procedure for obtaining the Bodner-Partom parameters is as follows[1]:

1. Conduct a series of uniaxial tensile tests at multiple strain rates and temperatures.
2. Obtain a polynomial that approximates σ vs. ϵ_p.
3. Using the polynomial data, generate a plot of γ vs. σ where $\gamma = (1/\sigma)(d\sigma/d\epsilon_p)$.
4. Obtain m_1 and m_2 from the slopes of the bilinear curve of γ vs. σ.
5. Set D_0 (usually taken to be 1×10^4 sec^{-1}).
6. Obtain n from saturation stress (σ_s) vs. strain rate.
7. Calculate the sum of Z_1 and Z_3 from σ_s, n, and ϵ_p.
8. Obtain Z_0 from 0.2% offset yield stress ; Set $Z_2 = Z_0$.
9. Calculate Z_1 from σ_{yield} and σ_s; Obtain Z_3.
10. Conduct a series of creep tests at multiple strain rates and temperatures.
11. Obtain A and r from steady state creep data and previously determined parameters.

Steps 1 through 9 were implemented in the study of Hastelloy-X. Steps 10 and 11 were unnecessary due to the lack of response at the given temperature range. The parameters A and r are taken to be zero. 8009 aluminum, however, required creep testing to determine these recovery parameters.

Research Progress

Computer Program Development

A thorough investigation of the Bodner Partom viscoplasticity model was undertaken to gain familiarity with the model. A study of the experimental procedure developed by R.S. Chan, et al.[1] at SWRI proved to be very useful. Results for B1900-Hf were used in developing a working computer code that could expedite the procedure for obtaining the

model constants from tensile data.

Experimental Work

The experimental procedure involves a program of tests over a range of temperatures and strain rates. The first material under studied is Hastelloy-X, a nickel based, austenitic, solid solution strengthened alloy[4]. Tensile tests have been completed on twenty-two specimens of Hastelloy-X. These isothermal uniaxial tension tests were conducted at four temperatures ranging from 77 °F (25°C) to 1000 °F (538 °C). Strain data were collected at strain rates of 3.33×10^{-5} 1/s, 3.28×10^{-4} 1/s and 3.28×10^{-3} 1/s (Table 1). Experimental and model results are compared in Figure 3.

The second material of interest is 8009 Aluminum, a rapidly solidified, powder metallurgy aluminum-iron-vanadium-silicon alloy[5]. Tensile tests performed on a batch of eight specimens provided evidence of localized necking. This behavior prevented usable tensile data from being obtained and suggested compression testing as an alternate test method. Compression tests on small right cylinders, height of 0.375 in. and diameter of 0.240 in. (tolerance of +/- 0.005 in.), are being performed over a range of temperatures and strain rates (Table 2). These data will provide an acceptable alternative from which model parameters can be extracted. The compression tests are being performed on a screw driven ATS universal load frame. In addition to the compressive data, steady state creep data are required to give a complete model at elevated temperatures. As shown in Table 3, creep tests have been performed on several samples at varying loads and temperatures.

Future Work

Data Analysis

Following the outline provided above, the experimentally determined tensile data are modeled using the Fortran code previously mentioned. The model constants are optimized for the range of test conditions using an iterative procedure. Bodner-Partom model parameters for Hastelloy-X have been determined and the parameters for 8009 aluminum will be determined following the completion of the compression tests. Details of the experimental procedures and results of this research will be published in a Masters Thesis this spring.

Tests of Other Materials

Following the successful development of the constitutive models for Hastelloy-X and 8009 Al, the intention is to use the procedures developed here to obtain material

characteristics for other materials using the Bodner-Partom viscoplasticity model. The 8009 aluminum alloy is a candidate material for the High Speed Civil Transport. Among others, materials to be tested include 2618 Aluminum, an alloy used on the Concorde. An extensive tensile and creep test program has been conducted by Ms. Kristen Jones as part of her undergraduate senior thesis research.

References

1. Chan, K.S., Bodner, S.R., Lindholm, U.S., "Phenomenological Modeling of Hardening and Thermal Recovery in Metals", Journal of Engineering Materials and Technology, Vol. 110, Jan. 1988.

2. Miller, Alan K., Unified Constitutive Equations for Creep and Plasticity, Elsivier Applied Science, New York, NY, 1987.

3. Chan, K.S., Lindholm, U.S., Bodner, S.R., Constitutive Modeling for Isotropic Materials (HOST) Third Annual Report, NASA-CR 174980, 1986.

4. ATEK Metals Center Inc., Specification Report for Hastelloy-X, Cincinatti, OH, May 1990.

5. Allied Signal Inc., Specification Report for High Temperature Aluminum Alloy 8009, Morristown, NJ, May, 1991.

TABLE 1

Tension Testing for Hastelloy - X

STRAIN RATE	TEMPERATURE 25 C (77 F)	204 C (400 F)	371 C (700 F)	537 C (1000 F)
3.3×10^{-3} (sec^{-1})	2 tests	3	2	2
3.3×10^{-4} (sec^{-1})	3	3	2	2
3.3×10^{-5} (sec^{-1})	0	1	0	1

NOTE:

All tests are isothermal, constant strain rate, uniaxial tensile tests performed on an Instron screw driven load frame.

TABLE 2

Compression Testing for 8009 Aluminum

	TEMPERATURE				
STRAIN RATE	25C (77F)	100C (212F)	175C (347F)	225C (437F)	275C (527F)
2.67×10^{-5} (sec^{-1})	2 tests	2	1	1	1
2.67×10^{-4} (sec^{-1})	2	1	1	1	1
2.67×10^{-3} (sec^{-1})	1	1	1	1	1

NOTE:

All tests are isothermal, constant strain rate, uniaxial compression tests performed on an ATS screw driven load frame.

TABLE 3

Creep Testing for 8009 Aluminum

	TEMPERATURE			
STRAIN RATE	100C (212F)	175C (347F)	225C (437F)	275C (527F)
~1.0×10^{-6} (sec^{-1})	0 test	1	1	1
~5.0×10^{-7} (sec^{-1})	0	0	1	1
~1.0×10^{-7} (sec^{-1})	0	1	1	1
~5.0×10^{-8} (sec^{-1})	1	0	0	0
~1.0×10^{-8} (sec^{-1})	1	1	0	0

NOTES:

1. All tests are isothermal, constant load, uniaxial creep tests performed on an ATS creep load frame.

2. The strain rates listed are approximate. Load and temperature were the only specified parameters in the tests.

Essential Equations for the Uni-Directional Bodner - Partom Constitutive Model

1. Flow Law

$$\dot{\varepsilon}_T = \dot{\varepsilon}_E + \dot{\varepsilon}_P$$

2. Kinetic Equation

$$\dot{\varepsilon}_P = \frac{2}{\sqrt{3}} D_0 \left\{ \frac{\sigma}{|\sigma|} \right\} \exp\left\{ -\frac{1}{2} \left(\frac{Z}{\sigma} \right)^{2n} \right\}$$

3. Evolution Equations

$$Z = Z^I + Z^D$$

$$\dot{Z}^I = m_1 \left(Z_1 - Z^I \right) \dot{W}_P - A_1 Z_1 \left\{ \frac{\left(Z^I - Z_2 \right)}{Z_1} \right\}^{r_1}$$

$$\dot{Z}^D = m_2 \left(Z_3 - Z^D \right) \dot{W}_P - A_2 Z_1 \left\{ \frac{\left(Z^D - Z_2 \right)}{Z_1} \right\}^{r_2}$$

6. Rate of Plastic Work

$$\dot{W}_P = \sigma \left(\dot{\varepsilon}_P \right)$$

FIGURE 1

Material Constants in the Bodner - Partom Constitutive Model

TEMP. INDEPENDENT

D_0	Limiting Shear Strain Rate [sec^{-1}]
Z_1	Limiting (maximum) value of Z_I [psi]
Z_3	Limiting (maximum) value of Z_D [psi]
m_1	Hardening Rate Coeff. of Z_D [psi^{-1}]
m_2	Hardening Rate Coeff. of Z_I [psi^{-1}]

TEMP. DEPENDENT

Z_0	Initial Value of Isotropic Hardening Variable [psi]
Z_2	Fully Recovered (minimum) value of Z_I [psi]
n	Kinetic parameter
A_1	Recovery Coeff. for Z_I
A_2	Recovery Coeff. for Z_D
r_1	Recovery Exponent for Z_D
r_2	Recovery Exponent for Z_I

FIGURE 2

Hastelloy - X Model Comparison

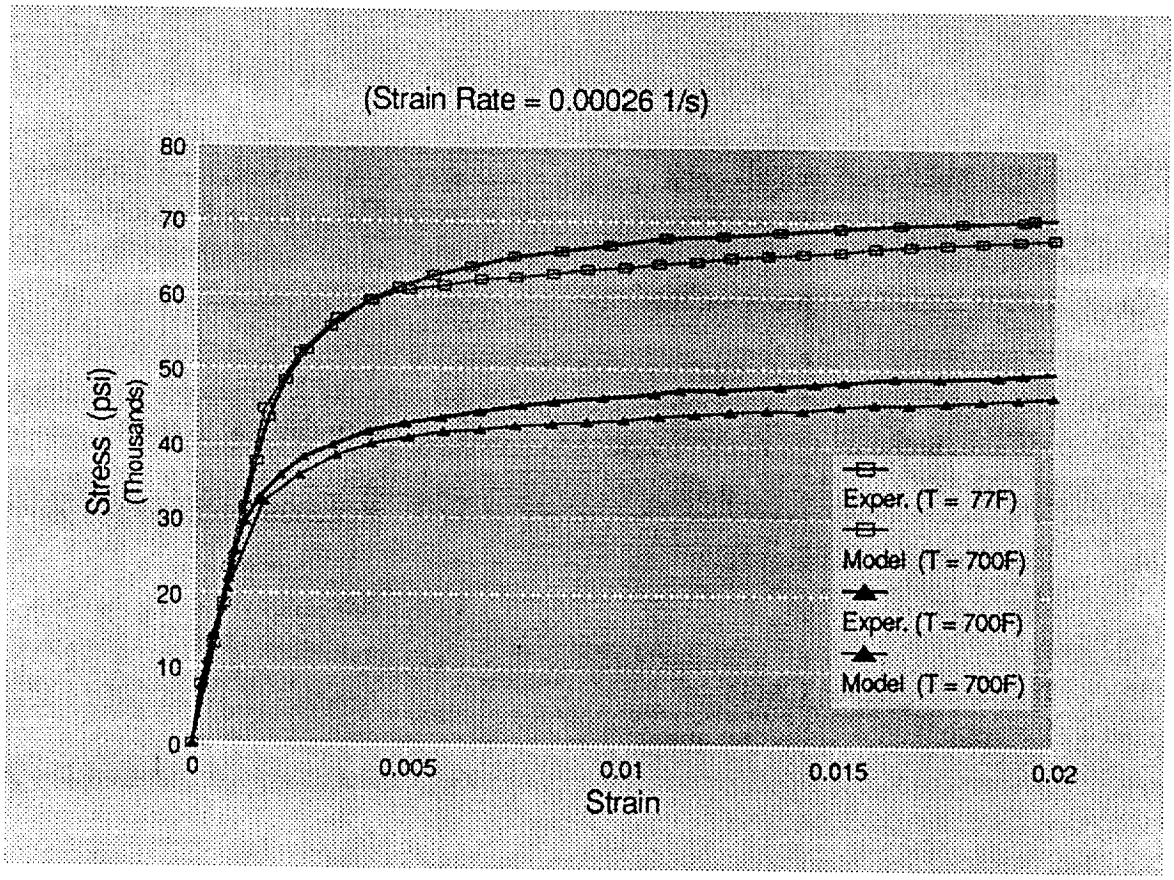

FIGURE 3

APPENDIX I: GRANT PUBLICATIONS (July 1 to December 31, 1992)

1. D.C. Slavik, J.A. Wert and R.P. Gangloff, "Determining Fracture Facet Crystallography Using Electron Back Scatter Patterns and Quantitative Tilt Fractography", Journal of Materials Research, in review (1992).

2. W.C. Porr, Jr. and R.P. Gangloff, "Elevated Temperature Fracture of RS/PM Alloy 8009: Part I-Fracture Mechanics Behavior", Metall. Trans. A, in review (1992).

3. D.C. Slavik, C.P. Blankenship, Jr., E.A. Starke, Jr. and R.P. Gangloff, "Intrinsic Fatigue Crack Growth Rates for Al-Li-Cu-Mg Alloys in Vacuum", Metall. Trans. A, in review (1992).

4. D.C. Slavik and R.P. Gangloff, "Microscopic Processes of Environmental Fatigue Crack Propagation in Al-Li-Cu Alloy 2090", in Fatigue '93, J.P. Bailon, ed., EMAS, West Midlands, UK, in press (1992).

5. S. Pride, J. Hudson and J.R. Scully, "Analysis of Electrochemical Transients Associated with the Metastable Pitting of Al and Al-2%Cu Alloys in Halide Solutions," in the ECS Proceedings on Corrosion in Electronic Materials, D. Sinclair and R. Comizzoli, eds., The Electrochemical Soc., Fall, in press (1992).

6. R.G. Buchheit, G.E. Stoner and G.J. Shiflet, "Corrosion Properties of a Rapidly Solidified $Al_{90}Fe_5Gd_5$ Alloy", Corrosion Science, in review (1992).

7. R.G. Buchheit, J.P. Moran and G.E. Stoner, "The Electrochemical Behavior of the T_1 (Al_2CuLi) Intermetallic Compound and Its Role in Localized Corrosion of Al-3Cu-2Li Alloys", Corrosion, in press (1992).

8. R.P. Gangloff and S.S. Kim, "Environment Enhanced Fatigue Crack Propagation in Metals: Inputs to Fracture Mechanics Life Prediction Models", SEAS Report No. UVA/528266/MSE93/111; University of Virginia, Charlottesville, VA, December (1992).

9. C.J. Lissenden, M-J. Pindera and C.T. Herakovich, "Response of SiC/Ti Tubes Under Biaxial Loading in the Presence of Damage," Damage Mechanics in Composites, D.H. Allen and D.C. Lagoudas, Eds., ASME-AMD-Vol. 150, pp. 73-90 (1992).

10. E.A. Thornton, M.F. Coyle, and R.N. McLeod, "Experimental Study of Plate Buckling Induced by Spatial Temperature Gradients," Journal of Thermal Stress, in press (1992).

APPENDIX II: PUBLICATION ABSTRACTS

INTRINSIC FATIGUE CRACK GROWTH RATES FOR Al-Li-Cu-Mg ALLOYS IN VACUUM

D.C. Slavik, C.P. Blankenship, Jr.[1],
E.A. Starke, Jr. and R.P. Gangloff
Department of Material Science and Engineering
University of Virginia
Charlottesville, VA 22903
Submitted to Metall. Trans. A

Abstract

The influence of precipitate microstructure and slip deformation mode on inert environment, intrinsic fatigue crack growth was investigated for Al-Li-Cu-Mg alloys 2090, 8090, and 2095 compared to 2024. The volume fraction of coherent shearable Al_3Li precipitate (δ'), and subsequent localized deformation, were reduced by composition (increased Cu/Li in 2095) and heat treatment (double aging of 8090). Tortuous crack profiles and large fatigue facets were observed for all aluminum-lithium alloys, independent of precipitate and localized deformation structures. Intrinsic crack growth rates, obtained at high constant K_{max} to minimize crack closure and in vacuum to minimize the environmental effect, were alloy dependent; da/dN varied up to 10-fold based on applied ΔK. Fatigue crack growth rates were less alloy dependent based on a crack tip strain range or cyclic crack tip opening parameter. Transitions in da/dN versus ΔK were modest without closure and environmental influences; FCP modeling, based on slip distance control of mechanical damage, is not strongly supported. Reduced FCP in 2095 compared to 2090 and 8090 does not correlate with increased crack path tortuosity or roughness induced crack closure. Surface roughness/reversible slip interactions which promote closure, and microstructure dependent damage accumulation, are suggested as possible mechanisms for alloy dependent FCP.

---

[1] Formerly Graduate Research Assistant, University of Virginia, presently Staff Scientist, General Electric Corporate Research and Development, Schenectady, NY, 12301.

MICROSCOPIC PROCESSES OF ENVIRONMENTAL FATIGUE CRACK PROPAGATION IN Al-Li-Cu ALLOY 2090

Donald C. Slavik and Richard P. Gangloff*
Submitted to FATIGUE '93

Intrinsic fatigue crack growth rates are increased, the da/dN versus ΔK relationship is altered, and microscopic crack paths are changed for 2090 in aqueous NaCl compared to vacuum. Unrecrystallized and large recrystallized grain microstructures exhibit identical power-law cracking kinetics for vacuum on a crack tip strain basis. NaCl rates are, however, increased by the presence of subgrains or higher strength. Based on electron backscattering patterns and quantitative tilt fractography, large vacuum fatigue facets form along {111} planes for Brass and random textured 2090. Smaller repeating facets are produced by fatigue in aqueous chloride, but they are not along a low index crystallographic plane. Results are inconsistent with hydride, lattice cleavage and slip plane cracking mechanisms for environmental FCP; and indicate the importance of intersecting slip damage interacting with absorbed hydrogen.

Submitted to J. of Materials Research

Determining Fracture Facet Crystallography Using Electron Back Scatter Patterns and Quantitative Tilt Fractography

D.C. Slavik, J.A. Wert, and R.P. Gangloff
Dept. of Materials Science and Engineering
University of Virginia
Charlottesville, VA 22903

Abstract

A methodology is presented to characterize the crystallography of individual fracture surface facets. Electron back scatter patterns (EBSPs) from a metallographic section through a facet identify grain orientation, and quantitative tilt fractography identifies facet orientation; these results are combined to establish fracture facet crystallography. For this technique, facet electropolishing is not required, the facet alignment procedure is accurate and quick, and the method can be generalized to different microstructures, test environments, or facet orientations. Method accuracy is illustrated for 25 to 50 μm fatigue crack surface facets in an unrecrystallized Al-Li-Cu alloy (AA2090) which has 5 μm thick subgrains in elongated grains which are 10 to 200 μm thick. The fine subgrain structure and tortuous fatigue crack profile precludes the use of other diffraction techniques for determining AA2090 facet crystallography. EBSP and tilt fractography results demonstrate that vacuum fatigue cracks in AA2090 are parallel to local {111} planes.

APPENDIX III: GRANT PRESENTATIONS (July 1 to December 31, 1992)

1. R.P. Gangloff and W.C. Porr, Jr., "Elevated Temperature of RS/PM Aluminum Alloys", Exxon Corporate Research-Science Laboratories, Clinton, NJ, October (1992).

2. R.P. Gangloff and W.C. Porr, Jr., "Elevated Temperature of RS/PM Aluminum Alloys", ALCOA Technical Center, Alcoa Center, PA, October (1992).

3. S.W. Smith and J.R. Scully, CORROSION/92, Student Poster Session, NACE Annual Conference and Corrosion Show, Nashville, TN, 1992.

4. S. Pride, "Analysis of Metastable Pitting Transients in Al and Al-Cu Thin Films," CORROSION/92 Student Poster Session (Fourth Place Award), NACE Annual Conference and Corrosion Show, Nashville, TN, 1992.

5. S. Pride, J. Hudson and J.R. Scully, "Analysis of Electrochemical Transients Associated with the Metastable Pitting of Al and Al-2%Cu Alloys in Halide Solutions," Presented at the Symposium on Corrosion in Electronic Materials, The Electrochemical Soc., Fall, 1992.

6. C.T. Herakovich and C.J. Lissenden, "Damage Induced Plasticity in MMC Tubes Subjected to Biaxial Loading", Society of Engineering Science 29th Annual Technical Meeting, University of California, San Diego, La Jolla, California, September, 1992.

7. C.T. Herakovich and C.J. Lissenden, "Response of SiC/Ti Tubes Under Biaxial Loading in the Presence of Damage", Winter Annual Meeting of the American Society of Mechanical Engineers, Anahiem, California, November, 1992.

APPENDIX IV: GRANT PROGRESS REPORTS (January, 1988 to July, 1992)

1. R.P. Gangloff, G.E. Stoner and R.E. Swanson, "Environment Assisted Degradation Mechanisms in Al-Li Alloys", University of Virginia, Report No. UVA/528266/MS88/101, January, 1988.

2. R.P. Gangloff, G.E. Stoner and R.E. Swanson, "Environment Assisted Degradation Mechanisms in Advanced Light Metals", University of Virginia, Report No. UVA/528266/MS88/102, June, 1988.

3. R.P. Gangloff, G.E. Stoner and R.E. Swanson, "Environment Assisted Degradation Mechanisms in Advanced Light Metals", University of Virginia, Report No. UVA/528266/MS89/103, January, 1989.

4. R.P. Gangloff, "NASA-UVa Light Aerospace Alloy and Structures Technology Program", UVa Report No. UVA/528266/MS90/104, August, 1989.

5. R.P. Gangloff, "NASA-UVa Light Aerospace Alloy and Structures Technology Program", UVa Report No. UVA/528266/MS90/105, December, 1989.

6. R.P. Gangloff, "NASA-UVa Light Aerospace Alloy and Structures Technology Program", UVa Report No. UVA/528266/MS90/106, June, 1990.

7. R.P. Gangloff, "NASA-UVa Light Aerospace Alloy and Structures Technology Program", UVa Report No. UVA/528266/MS91/107, January, 1991.

8. R.P. Gangloff, "NASA-UVa Light Aerospace Alloy and Structures Technology Program", UVa Report No. UVA/528266/MS91/108, July, 1991.

9. R.P. Gangloff, "NASA-UVa Light Aerospace Alloy and Structures Technology Program", UVa Report No. UVA/528266/MS92/109, January, 1992.

10. R.P. Gangloff, "NASA-UVa Light Aerospace Alloy and Structures Technology Program", UVa Report No. UVA/528266/MS93/111, July, 1992.

DISTRIBUTION LIST

1 - 2	Mr. D. L. Dicus Contract Monitor Metallic Materials Branch, MS 188A NASA Langley Research Center Hampton, VA 23665
3 - 4*	NASA Scientific and Technical Information Facility P. O. Box 8757 Baltimore/Washington International Airport Baltimore, MD 21240
5	Mr. Richard J. Siebels Grants Officer, M/S 126 NASA Langley Research Center Hampton, VA 23665
6	Dr. Darrel R. Tenney Materials Division NASA Langley Research Center Hampton, VA 23665
7	Dr. Charles E. Harris Mechanics of Materials Branch NASA Langley Research Center Hampton, VA 23665
8	Mr. W. Barry Lisagor Metallic Materials Branch NASA Langley Research Center Hampton, VA 23665
9	Mr. T.W. Crooker Code RM NASA Headquarters Washington, DC 20546
10	Dr. Robert S. Piascik Mechanics of Materials Branch NASA Langley Research Center Hampton, VA 23665
11	Mr. W. Brewer Metallic Materials Branch, MS 188A NASA Langley Research Center Hampton, VA 23665

12 Mr. Thomas T. Bales
Metallic Materials Branch, MS 188A
NASA Langley Research Center
Hampton, VA 23665

13 Dr. W.S. Johnson
Mechanics of Materials Branch
NASA Langley Research Center
Hampton, VA 23665

14 Dr. M.J. Shuart
Aircraft Structures Branch
NASA Langley Research Center
Hampton, VA 23665

15 Dr. James H. Starnes, Jr.
Aircraft Structures Branch
NASA Langley Research Center
Hampton, VA 23665

16 Mr. Dana Ward
Northrop Corporation
1 Northrop Avenue
Mail Zone 3872562
Hawthorne, CA 90250-3277

17 Dr. Santosh K. Das
Senior Manager
Metals and Ceramics Laboratory
Allied-Signal, Inc.
P. O. Box 1021
Morristown, NJ 07960

18 Dr. Michael Zedalis
Metals and Ceramics Laboratory
Allied-Signal, Inc.
P. O. Box 1021
Morristown, NJ 07960

19 Mr. E.A. Colvin
Alcoa Technical Center
Route 780, 7th Street Road
Alcoa Center, PA 15069

20 Dr. L.M. Angers
Alcoa Technical Center
Route 780, 7th Street Road
Alcoa Center, PA 15069

21	Dr. J. Andrew Walker Advanced Composite Materials Corporation 1525 South Buncombe Road Greer, SC 29651
22	Mr. Fred Casey Space Transportation Systems Division Rockwell International Dept. 289 MC/AC56 12214 Lakewood Blvd. Downey, CA 90241
23	Mr. Stephen G. Moran Lockheed Aeronautical Systems Company Georgia Division; Dept. 73-71 Zone 0160 86 South Cobb Dr. Marietta, GA 30063
24	E.A. Starke, Jr.; UVA
25-27	R.P. Gangloff; MS&E
28	G.E. Stoner; MS&E
29	J.A. Wert; MS&E
30	F.E. Wawner; MS&E
31	W.A. Jesser; MS&E
32	J.R. Scully; MS&E
33	W.D. Pilkey; MAE
34	E.A. Thornton; MAE
35	C.T. Herakovich; CE/Applied Mechanics
36-37	E.H. Pancake; Clark Hall
38	SEAS Preaward Administration Files
39	Mr. Gwyn Faile Code ED 24 Marshall Space Flight Center Huntsville, AL 35812

40 Mr. James Learned
Boeing Military Aircraft
Organization L-7109
Aerospace Group
Seattle, WA 98124

41 Mr. Brian McPherson
Code ED 24
Marshall Space Flight Center
Huntsville, AL 35812

42 Dr. Ken Garr
Rocketdyne Division, Rockwell International
6633 Canoga Ave.
Canoga Park, CA 91303

43 Mr. Michael Falugi
WRDC/FIBAA
Wright Patterson Air Force Base, OH 45433-6553

44 Mr. Peter Rimbos
Boeing Aerospace and Electronics
Aerospace Group
Seattle, WA 98124

45 Dr. Howard G. Nelson
NASA-Ames Research Center
EEM: 213-3
Moffett Field, CA 94035

46 Dr. R.G. Forman
Mail Code ES-5
NASA-L.B. Johnson Space Flight Center
Houston, TX 77058

47 Professor A.K. Noor
Center for Computational Structures Technology
NASA Langley Research Center
Hampton, VA 23665

48 Dr. M.J. Luton
Exxon Research and Engineering Company
Clinton Township, Route 22 East
Annandale, NJ 08801

49 Prof. A.K. Ghosh
Department of Materials Science and Engineering
University of Michigan
2102 Dow Building
Ann Arbor, MI 48109-2136

*One reproducible copy

Updated January, 1993